

## **INFORMATION TO USERS**

**This manuscript has been reproduced from the microfilm master. UMI films the text directly from the original or copy submitted. Thus, some thesis and dissertation copies are in typewriter face, while others may be from any type of computer printer.**

**The quality of this reproduction is dependent upon the quality of the copy submitted. Broken or indistinct print, colored or poor quality illustrations and photographs, print bleedthrough, substandard margins, and improper alignment can adversely affect reproduction.**

**In the unlikely event that the author did not send UMI a complete manuscript and there are missing pages, these will be noted. Also, if unauthorized copyright material had to be removed, a note will indicate the deletion.**

**Oversize materials (e.g., maps, drawings, charts) are reproduced by sectioning the original, beginning at the upper left-hand corner and continuing from left to right in equal sections with small overlaps. Each original is also photographed in one exposure and is included in reduced form at the back of the book.**

**Photographs included in the original manuscript have been reproduced xerographically in this copy. Higher quality 6" x 9" black and white photographic prints are available for any photographs or illustrations appearing in this copy for an additional charge. Contact UMI directly to order.**

# **UMI**

**A Bell & Howell Information Company  
300 North Zeeb Road, Ann Arbor MI 48106-1346 USA  
313/761-4700 800/521-0600**



**UNIVERSITY OF ALBERTA**

**DEPOSITION OF EMULSIONS IN AN IMPINGING JET CELL**

**BY**

**RALPH SEAN SIDDONS SANDERS**



**A thesis submitted to the Faculty of Graduate Studies and Research in partial  
fulfillment of the requirements of Doctor of Philosophy**

**Department of Chemical and Materials Engineering**

**Edmonton, Alberta**

**Spring 1997**



**National Library  
of Canada**

**Acquisitions and  
Bibliographic Services**

**395 Wellington Street  
Ottawa ON K1A 0N4  
Canada**

**Bibliothèque nationale  
du Canada**

**Acquisitions et  
services bibliographiques**

**395, rue Wellington  
Ottawa ON K1A 0N4  
Canada**

*Your file    Votre référence*

*Our file    Notre référence*

The author has granted a non-exclusive licence allowing the National Library of Canada to reproduce, loan, distribute or sell copies of his/her thesis by any means and in any form or format, making this thesis available to interested persons.

The author retains ownership of the copyright in his/her thesis. Neither the thesis nor substantial extracts from it may be printed or otherwise reproduced with the author's permission.

L'auteur a accordé une licence non exclusive permettant à la Bibliothèque nationale du Canada de reproduire, prêter, distribuer ou vendre des copies de sa thèse de quelque manière et sous quelque forme que ce soit pour mettre des exemplaires de cette thèse à la disposition des personnes intéressées.

L'auteur conserve la propriété du droit d'auteur qui protège sa thèse. Ni la thèse ni des extraits substantiels de celle-ci ne doivent être imprimés ou autrement reproduits sans son autorisation.

0-612-21628-4

# UNIVERSITY OF ALBERTA

## LIBRARY RELEASE FORM

NAME OF AUTHOR: Ralph Sean Siddons Sanders

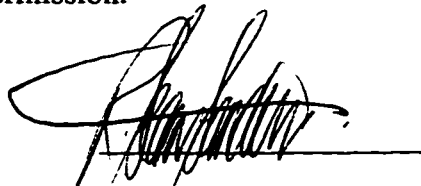
TITLE OF THESIS: Deposition of Emulsions in an Impinging Jet Cell

DEGREE: Doctor of Philosophy

YEAR THIS DEGREE GRANTED: 1997

Permission is hereby granted to the University of Alberta Library to reproduce single copies of this thesis and to lend or sell such copies for private, scholarly, or scientific research purposes only.

The author reserves all other publication and other rights in association with the copyright in the thesis, and except as hereinbefore provided, neither the thesis nor any substantial portion thereof may be printed or otherwise reproduced in any material form whatever without the author's prior written permission.



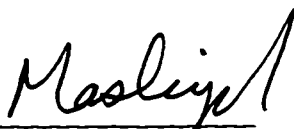
P. O. Box 118  
Manor, Saskatchewan  
S0C 1R0

January 30, 1997

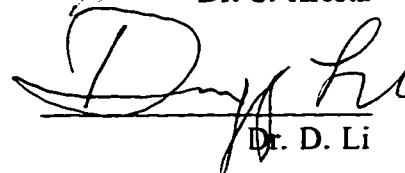
UNIVERSITY OF ALBERTA

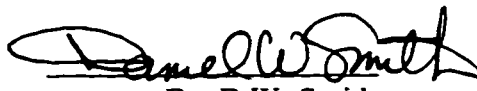
FACULTY OF GRADUATE STUDIES AND RESEARCH

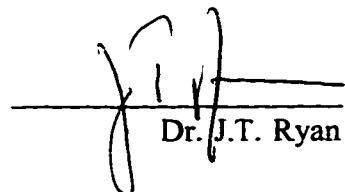
The undersigned certify that they have read, and recommend to the Faculty of Graduate Studies and Research for acceptance, a thesis entitled DEPOSITION OF EMULSIONS IN AN IMPINGING JET CELL submitted by Ralph Sean Siddons Sanders in partial fulfillment of the requirements for the degree of Doctor of Philosophy.

  
Dr. J.H. Masliyah

  
Dr. S. Kresta

  
Dr. D. Li

  
Dr. D.W. Smith

  
Dr. J.T. Ryan

  
Dr. R. Rajagopalan

December 5, 1996

**To my Mom and Dad.**

**Beverly Mae and David Lynne Siddons Sanders**

## **ABSTRACT**

The formation and subsequent breaking of emulsions play important roles in many industrial applications. Although the general mechanism by which emulsions are 'broken', or separated into their two constituent phases, has been well documented, there is a lack of fundamental, quantitative research describing emulsion behavior.

This study provides the means to describe, quantitatively, the effect of hydrodynamic and colloidal forces on a droplet deposition process that is analogous to droplet aggregation. Aggregation is the first stage in any demulsification process.

An impinging jet cell, in which droplets from a flowing emulsion are impinged on a glass microscope slide, was used to study a number of oil-in-water emulsions, as well as one type of nonaqueous (water-in-hydrocarbon) emulsion. The deposition experiments were modeled by solving the governing mass transfer and flow field equations, using analytical expressions from DLVO theory to describe the electric double layer and van der Waals forces.

The results of this study represent the development of a comprehensive data base of experimental measurements that describe:

- the effect of flow intensity on droplet deposition rates (expressed as Sherwood number, or dimensionless mass transfer).
- the effect of electrolyte concentration on droplet deposition rates.
- the effect of collector surface character (hydrophilic, hydrophobic, bitumen-coated) on droplet deposition rates.
- the effect of dispersed phase viscosity on droplet deposition rates.

- the effect of stabilizing agent concentration (Athabasca bitumen) on the deposition rates of water droplets suspended in a 4:1 (by volume) mixture of toluene and hexane.
- the collector surface coverage at high flowrates, using statistical analysis.
- the use of droplet coagulation studies to complement the results of droplet deposition experiments.

Numerical simulations showed that DLVO theory can provide reasonable predictions for complex emulsion systems. In some situations, such as the nonaqueous emulsion deposition experiments, DLVO theory could not be used to predict the variation of mass transfer rates with the bitumen concentration used to stabilize the emulsion.

This study emphasizes the importance of considering droplet surface structure and characteristics in the assessment of emulsion stability.

## **ACKNOWLEDGEMENTS**

A great number of people contributed a great deal to the completion of this thesis, either directly or indirectly through the maintenance of the author's well-being. I thank my parents for their unwavering and unconditional love and support. I would also like to thank my wife, April, who now knows first-hand that the only thing more difficult than writing a thesis is living with someone who is. She has shown me again and again the meaning of life and the beauty of love.

To my friends and family, especially Scott Lingley, Kelly Service, Linnea Zutz, Tracey and Lee Winter, and Larry and Kathy Beatty: while you may not know much about colloid science, you certainly know how to love and support someone who does. Thank you all. I thank Kelly Hill, Iain Walker, and Andrew Jenkins for their friendship and their remarkable scientific perspicacity.

I wish to thank Dr. Cliff Shook for inspiring in me the desire to teach and to conduct research, and as a result, the determination to complete this thesis. I thank Dr. Jacob Masliyah for his support and guidance, his regular pep-talks urging me to "live up to my potential", and most importantly, for believing in me.

I also wish to thank Ross Chow and Clare McCarthy for their technical and moral support. I am indebted to Cindy Heisler for her assistance and her words of encouragement.

I also appreciate the efforts of the following people who work in the department: my office mates, past and present; Kevin Dorma; Keith Faulder, Bob Scott and Ron van den Heuval; Bob Barton; Andree Koenig; Artin Afacan; Walter Boddez; Richard Cooper; Bev Walker; and Diane Reckhow.

Finally, I wish to thank the members of the examining committee (Dr. Raj Rajagopalan, Dr. D. Li, Dr. D. Smith, Dr. S. Kresta, Dr. J. Ryan, and Dr. K. Nandakumar) for their time and their consideration of this thesis.

## TABLE OF CONTENTS

	Page
<b><u>Chapter 1 Introduction</u></b>	<b>1</b>
1.1 Objectives of this work	2
1.2 Thesis overview	3
<b><u>Chapter 2 Colloidal deposition</u></b>	<b>4</b>
2.1 Previous studies using flow techniques	5
2.2 The impinging jet cell	6
2.3 Analysis of deposition experiments	9
2.4 Overview of experimental work	10
<b><u>Chapter 3 Theory</u></b>	<b>11</b>
3.1 Introduction	11
3.2 Description of the axisymmetric flow field	12
3.2.1 Governing equations	12
3.2.2 Boundary conditions	16
3.2.3 Numerical solution procedure	20
3.3 Description of the flow field in the stagnation region	20
3.3.1 Dependence of $\bar{\alpha}$ on Reynolds number	22
3.3.2 Evaluation of $\bar{\alpha}$ for this work	22
3.4 Solution of mass transfer equations	23
3.5 Development of the numerical model	28
3.5.1 Numerical method	28
3.5.2 Expressions for external forces	29
3.5.3 Prediction of Hamaker constant using Lifshitz theory	35
3.5.4 Prediction of $\zeta_c$ and $\zeta_p$ using the ISG Model	37

3.5.5 Analytical expressions for the universal hydrodynamic correction coefficients (UHCC's)	39
3.5.6 Summary: list of equations	41
3.6 Application of DLVO theory to nonaqueous suspensions	45
3.7 Sensitivity analysis	50
3.7.1 Effect of particle radius	51
3.7.2 Effect of Adhesion number	53
3.7.3 Effect of double layer strength	55
3.7.4 Summary	57
 <u>Chapter 4 Numerical model validation and testing of experimental apparatus</u>	 58
4.1 Review of previous studies	58
4.2 Model predictions	59
4.3 Results of deposition experiments using latex suspensions	62
 <u>Chapter 5 Experimental method</u>	 65
5.1 Emulsion preparation and characterization	65
5.2 Preparation of the glass microscope slides for deposition experiments	67
5.3 Flow chart describing experimental procedure	68
5.4 List of experiments conducted	68
 <u>Chapter 6 Deposition of oil-in-water emulsions</u>	 71
6.1 Bitumen-in-water emulsions	72
6.1.1 Emulsion preparation and characterization	72
6.1.2 Collector preparation and characterization	76
6.1.3 Effect of Reynolds number	76
6.1.4 Effect of electrolyte concentration	82

6.2	Bayol oil-in-water emulsions	85
6.2.1	Emulsion preparation and characterization	85
6.2.2	Effect of Reynolds number	87
6.3	Viscometry standard oil-in-water emulsions	91
6.3.1	Emulsion preparation and characterization	91
6.3.2	Effect of Reynolds number	96
6.3.3	Effect of electrolyte concentration	102
6.3.4	Droplet - droplet coagulation studies	103
6.4	Pentadecane-in-water emulsions	109
6.4.1	Emulsion preparation and characterization	109
6.4.2	Effect of Reynolds number	113
6.4.3	Effect of electrolyte concentration	117
6.5	Comparison of results: bitumen emulsions with low viscosity oil emulsions	119
6.5.1	Accuracy of model predictions	119
6.5.2	Analysis of surface coverage at high Reynolds numbers: bitumen and viscometry oil systems	121
6.5.3	Effect of dispersed phase viscosity	126
6.5.4	Summary	127

<b>Chapter 7</b>	<b><u>Deposition of bitumen-in-water emulsions on hydrophobic surfaces</u></b>	<b>130</b>
7.1	Introduction	130
7.2	Bitumen deposition experiments: hydrophobic collector	132
7.2.1	Collector preparation and characterization	132
7.2.2	Emulsion preparation and characterization	136
7.2.3	Effect of Reynolds number	138
7.2.4	Effect of electrolyte concentration	142

7.3 Bitumen deposition experiments: bitumen-coated collector	144
7.3.1 Collector preparation and characterization	144
7.3.2 Emulsion preparation and characterization	145
7.3.3 Effect of Reynolds number	146
7.4 Discussion: the nature of bitumen surface active agents	150
 <b><u>Chapter 8 Deposition of water-in-hydrocarbon emulsions</u></b>	 152
8.1 Introduction	152
8.2 Emulsion preparation and characterization	153
8.3 Collector preparation and characterization	156
8.4 Effect of Reynolds number	157
8.5 Effect of continuous phase bitumen concentration	164
8.6 Summary	171
 <b><u>Chapter 9 Summary and Recommendations</u></b>	 173
9.1 Validity of model: application of DLVO theory to oil-in-water emulsions	173
9.2 Significance of results of hydrophobic/coated collector deposition experiments	175
9.3 Significance of nonaqueous emulsion deposition experiments	176
9.4 Recommendations for future work	178
9.5 Major contributions made by this study	179
 References	 181
 <b>Appendix A Calculation of asphaltene concentration and water droplet         surface coverage for a water-in-hydrocarbon emulsion,         <math>b_0 = 1.22 \text{ g/L}</math></b>	   187

<b>Appendix B</b>	<b>Computer code for numerical solution of flow field equations</b>	<b>189</b>
<b>Appendix C</b>	<b>Computer code for numerical solution of mass transfer equations</b>	<b>197</b>
<b>Appendix D</b>	<b>Raw Data: SRCD data tables</b>	<b>202</b>

## LIST OF TABLES

	Page
<b>Table 3-1.</b> Dependence of $\bar{\alpha}$ on Reynolds number and capillary exit velocity profile, as determined by van de Ven <i>et al.</i>	22
<b>Table 3-2.</b> Curve - fitted coefficients for the universal hydrodynamic correction coefficients $f_1, f_2, f_3$ .	41
<b>Table 3-3.</b> Effective concentration of a 1:1 electrolyte in nonaqueous media, for a bulk electrolyte concentration of $m_0=0.001M$ .	48
<b>Table 4-1.</b> Characterization of latex deposition experiments.	62
<b>Table 6-1.</b> Characterization of bitumen emulsion deposition experiments I: 0.1M NaCl; $a=0.59 \mu m$ ; $c_0=7.2 \times 10^6$ droplets/ml.	78
<b>Table 6-2.</b> Characterization of bitumen emulsion deposition experiments II: pH=5; $Re=118$ ; $a=0.59 \mu m$ ; $c_0=7.2 \times 10^6$ droplets/ml.	83
<b>Table 6-3.</b> Characterization of Cannon standard viscometry oil emulsions deposition experiments.	95
<b>Table 6-4.</b> Characterization of pentadecane deposition experiments I: 0.01M NaCl; $a=0.42 \mu m$ ; $c_0=1.5 \times 10^7$ droplets/ml.	116
<b>Table 6-5.</b> Characterization of pentadecane deposition experiments II: pH=5; $Re=100$ ; $a=0.42 \mu m$ ; $c_0=1.6 \times 10^7$ droplets/ml.	117
<b>Table 6-6.</b> Particle distribution on the collector surface for bitumen and Cannon viscometry oil emulsions, $Re=800$ .	125
<b>Table 8-1.</b> Preparation of a number of different water-in-hydrocarbon emulsions.	153
<b>Table 8-2.</b> Water droplet concentration ( $c_0$ ) and continuous phase bitumen concentration ( $b_0$ ) for nonaqueous deposition experiments, Set A.	158
<b>Table 8-3.</b> Water droplet concentration ( $c_0$ ) and continuous phase bitumen concentration ( $b_0$ ) for nonaqueous deposition experiments, Set B.	165

## LIST OF FIGURES

		Page
<b>Figure 2-1.</b>	<b>Schematic diagram of experimental apparatus:</b> A - 345 kPa instrument air line      H - capillary casing B - 500 ml pressure vessel          I - collector (microscope slide) C - vessel injection port            J - external wall of cell D - flow controller (rotameter)      K - reservoir E - 60 cc. syringe pump            L - microscope F - interconnecting tubing          M - video camera G - impinging jet cell capillary	8
<b>Figure 3-1.</b>	Geometry of impinging jet cell: $R = 0.7$ mm; $h_0 = 0.84, 1.81$ mm; $L = 25$ mm.	13
<b>Figure 3-2.</b>	Dependence of dimensionless strength of stagnation point flow, $\bar{\alpha}$ , as a function of Reynolds number. Symbols represent results of numerical simulations: ( $\Delta$ ) $\bar{h}_0=2.59$ ; ( $\square$ ) $\bar{h}_0=1.21$ . Solid lines represent regression analysis. For $\bar{h}_0=2.59$ , $\bar{\alpha}=0.52Re^{1/2}$ . For $\bar{h}_0=1.21$ , $\bar{\alpha}=2.81Re^{1/2}$ .	24
<b>Figure 3-3.</b>	Variation of universal hydrodynamic correction coefficients (UHCC's), $f_i$ ( $i=1,2,3$ ), with dimensionless separation distance between a sphere and a planar surface.	40
<b>Figure 3-4.</b>	Debye length, $\kappa^{-1}$ , as a function of dielectric constant, $\epsilon$ , for bulk 1:1 electrolyte concentrations, $m_0$ , as shown. Values of $\kappa^{-1}$ calculated from Equation (3-49b), with $T=298$ K, and effective electrolyte concentrations, $m_i = m_i(\epsilon, m_0)$ , determined using Fuoss' theory [40,43].	47
<b>Figure 3-5.</b>	Effect of continuous phase dielectric constant, $\epsilon$ , on the electrostatic force, $F_R$ , between a droplet and the collector separated by a nonaqueous phase, with $a=0.5$ $\mu\text{m}$ , $\zeta_p=-60$ mV, $\zeta_c=-50$ mV and a bulk electrolyte concentration of 0.001 M. (—) $\epsilon=2.3$ ; (— —) $\epsilon=6$ ; (— — —) $\epsilon=15$ . Inset shows typical van der Waals force, $F_A$ , for a nonaqueous system, with $a=0.5$ $\mu\text{m}$ , $A_{132}=10^{-21}$ J, and $\lambda=10^{-7}$ m.	49

<b>Figure 3-6.</b>	Predicted variation of Sherwood number with particle radius for the model system described by: $\bar{h}_0=2.59$ ; $Ad=0.1$ ; $Dl=0$ ; $M_i=0.01M$ ; $q=1$ ; $Gr=0$ .	52
<b>Figure 3-7.</b>	Predicted variation of Sherwood number with Adhesion number for the model system described by: $a=0.5 \mu m$ ; $\bar{h}_0=2.59$ ; $Dl=0$ ; $M_i=0.01M$ ; $q=1$ ; $Gr=0$ .	54
<b>Figure 3-8.</b>	Predicted variation of Sherwood number with double layer strength for the model system described by: $a=0.5 \mu m$ ; $\bar{h}_0=2.59$ ; $Da=0.1$ ; $q=1$ ; $Gr=0$ . (a) $M_i=0.01M$ ; (b) $M_i=0.1M$ .	56
<b>Figure 4-1.</b>	Sherwood number as a function of Reynolds number for latex particles. Symbols represent experimental results. Solid line represents theoretical values. From Dabros and van de Ven [17].	60
<b>Figure 4-2.</b>	Model predictions of Sherwood number for latex particle deposition experiments conducted by Dabros and van de Ven. Parameters used in model: $a=0.5 \mu m$ ; $Ad=0.2$ ; $\bar{\lambda}=0.4$ ; $Dl=0$ ; $\bar{\alpha}=0.87Re^{1/2}$ . Symbols represent results of latex deposition experiments conducted by Dabros and van de Ven [17].	61
<b>Figure 4-3.</b>	Sherwood number as a function of Reynolds number for latex particles. Symbols represent experimental results. Solid line indicates theoretical results, obtained by solving Equation (3-30), with $a=0.416 \mu m$ , $Dl=0$ , $\bar{\alpha}=0.52Re^{1/2}$ , and $Ad=\{0.2, 0.8\}$ as shown.	64
<b>Figure 5-1.</b>	Flow chart description of the experimental method.	70
<b>Figure 6-1.</b>	Representative size distribution of a bitumen-in-water emulsion, with a mean droplet diameter of $1.18 \mu m$ and a standard deviation of $0.36 \mu m$ .	74
<b>Figure 6-2.</b>	Measured (symbols) and calculated (solid line) zeta potentials for the bitumen emulsion as a function of bulk pH in 0.1M NaCl. Theoretical zeta potentials calculated using the ISG model, with $N_s=2 \times 10^{18} m^{-2}$ , $pKa=4.5$ , $x_s=0.6 nm$ , $a=0.59 \mu m$ , and $ka=614$ .	75

- Figure 6-3.** Measured (symbols) and calculated (solid lines) zeta potentials for finely ground microscope slide particles as a function of bulk pH in 0.01M NaCl ( $\square$ ) and in 0.1M NaCl ( $\circ$ ). Theoretical zeta potentials calculated using the ISG model, with  $N_s=1 \times 10^{18} \text{ m}^{-2}$ ,  $pK_a=3.2$ ,  $x_s=1.4 \text{ nm}$ .  $\kappa a > 100$  for all data. 77
- Figure 6-4.** Stagnation region coating density as a function of time for  $1.18 \mu\text{m}$  bitumen droplets in 0.1M NaCl,  $\text{pH} = 4.7$ ;  $\zeta_p = -27.4 \text{ mV}$ ,  $\zeta_c = -20.2 \text{ mV}$ . 79
- Figure 6-5.** Dimensionless mass transfer (expressed as Sherwood number) as a function of Reynolds number for  $1.18 \mu\text{m}$  bitumen droplets in 0.1M NaCl ( $\kappa a = 614$ ). ( $\circ$ ) -  $\zeta_p = -27.4 \text{ mV}$ ,  $\zeta_c = -20.2 \text{ mV}$ ; ( $\square$ ) -  $\zeta_p = -53.2 \text{ mV}$ ,  $\zeta_c = -30.1 \text{ mV}$ ; ( $\blacktriangle$ ) -  $\zeta_p = -35.6 \text{ mV}$ ,  $\zeta_c = -23.4 \text{ mV}$ ; ( $\diamond$ ) -  $\zeta_p = -29.1 \text{ mV}$ ,  $\zeta_c = -21.6 \text{ mV}$ ; ( $\bullet$ ) -  $\zeta_p = -16.7 \text{ mV}$ ,  $\zeta_c = -19.9 \text{ mV}$ . Lines show theoretical mass transfer, obtained by solving Equation (3-30):  $Ad=0.11$ : (—)  $a=0.59 \mu\text{m}$ ; (— —)  $a \pm \sigma/2$  where  $\sigma=0.36 \mu\text{m}$ . 81
- Figure 6-6.** Experimentally determined effect of  $\kappa a$  parameter on mass transfer to collector surface for bitumen emulsions in various concentrations of NaCl solutions.  $Re=118$ ,  $\text{pH}=5$ . Solid line shows theoretical mass transfer. 84
- Figure 6-7.** Representative size distribution of a dilute Bayol oil-in-water emulsion, with a mean droplet diameter of  $\mu = 1.79 \mu\text{m}$ , and a standard deviation of  $\sigma = 0.89 \mu\text{m}$ . 86
- Figure 6-8.** Variation of zeta potential with bulk pH for Bayol oil emulsions suspended in 0.01M NaCl solution. Results obtained using a Malvern Zetasizer 3. 88
- Figure 6-9.** Dimensionless mass transfer (expressed as Sherwood number) as a function of Reynolds number for  $1.79 \mu\text{m}$  Bayol oil droplets in 0.01M NaCl ( $\kappa a=286$ ). Lines show theoretical mass transfer, obtained by solving Equation (3-30):  $Ad=0.11$ ; (—)  $a = 0.895 \mu\text{m}$ ; (— —)  $a \pm \sigma/2$ ,  $\sigma = 0.890 \mu\text{m}$ . 89

<b>Figure 6-10.</b>	Representative size distributions of: a) 7.67 mPa s mineral oil-in-water emulsion, with $\mu = 0.95 \mu\text{m}$ and $\sigma = 0.37 \mu\text{m}$ ; b) 3.39 mPa s mineral oil-in-water emulsion, with $\mu = 0.97 \mu\text{m}$ and $\sigma = 0.45 \mu\text{m}$ .	93
<b>Figure 6-11.</b>	Measured zeta potentials for the 7.67 mPa-s mineral oil-in-water emulsion ( $\circ$ ) and the 3.39 mPa-s oil-in-water emulsion ( $\blacktriangledown$ ) measured as a function of bulk pH in 0.01M NaCl.	94
<b>Figure 6-12.</b>	Stagnation region coating density as a function of time for viscometry standard oil emulsions, showing the coating densities for: (a) repulsive double layer force (System A); (b) attractive double layer force (System B).	97
<b>Figure 6-12.</b>	Stagnation region coating density as a function of time for viscometry standard oil emulsions. showing the coating densities for: (c) increased NaCl concentration (System C); (d) decreased dispersed phase viscosity (System D).	98
<b>Figure 6-13.</b>	Dimensionless mass transfer (expressed as Sherwood number) as a function of Reynolds number for viscometry standard oil emulsions. (a) - System A; (b) - System B. Experimental conditions listed in Table 6-3. Lines in each figure show theoretical mass transfer, calculated from numerical solution of Equation (3-30): using $Ad=0.11$ . (—) $a$ ; (— —) $a \pm \sigma/2$ .	100
<b>Figure 6-13.</b>	Dimensionless mass transfer (expressed as Sherwood number) as a function of Reynolds number for viscometry standard oil emulsions. (c) - System C; (d) - System D. Experimental conditions listed in Table 6-3. Lines in each figure show theoretical mass transfer, calculated from numerical solution of Equation (3-30): using $Ad=0.11$ . (—) $a$ ; (— —) $a \pm \sigma/2$ .	101
<b>Figure 6-14.</b>	Experimentally determined effect of $\kappa a$ parameter on mass transfer to collector surface for a 7.67 mPa s viscometry standard oil emulsion in various concentrations of NaCl solutions, $Re=118$ , $pH=9$ . Solid line shows theoretical mass transfer.	104

- Figure 6-15.** Droplet - droplet interaction energy diagrams for 0.95  $\mu\text{m}$  viscometry standard oil emulsion as a function of interdroplet separation distance,  $h$ . (a) NaCl solution: Curve 1, 0.01M; 2, 0.025M; 3, 0.05M. (b)  $\text{CaCl}_2$  solution: Curve 1, 0.001M; 2, 0.006M; 3, 0.009M. 106
- Figure 6-16.** Critical flocculation concentration experiments on viscometry standard oil emulsion. (left) The emulsion after it has been dispersed in 0.009M  $\text{CaCl}_2$  solution. No flocculation occurs. (right) The emulsion after it has been dispersed in 0.04M  $\text{CaCl}_2$  solution. Primary flocculation occurs (droplets do not redisperse even upon agitation). 108
- Figure 6-17.** Representative size distribution of pentadecane-in-water emulsion, with  $\mu=0.84 \mu\text{m}$  and  $\sigma = 0.39 \mu\text{m}$ . 111
- Figure 6-18.** Measured (symbols) and nonlinear regression analysis (solid lines) of the variation of pentadecane droplet zeta potential with a) bulk pH in a 0.01M NaCl solution and b)  $[\text{NaCl}]$  for a constant bulk pH ( $\text{pH}=5$ ). Analytical expression describing the variation of  $\zeta_p$  with pH given by Equation (6-5). Analytical expression describing the variation of  $\zeta_p$  with  $[\text{NaCl}]$  given by Equation (6-6). 112
- Figure 6-19.** Predicted variation of dimensionless mass transfer rate (expressed as Sherwood number) with solution pH for a pentadecane emulsion;  $\mu=0.84 \mu\text{m}$ ; 0.01M NaCl solution;  $\text{Re}=100$ ;  $\text{Ad}=0.11$ . 114
- Figure 6-20.** Dimensionless mass transfer (expressed as Sherwood number) as a function of Reynolds number and bulk pH for 0.84  $\mu\text{m}$  pentadecane droplets in 0.01M NaCl. ( $\circ$ ) - Set #1 ( $\text{pH}=3.6$ ); ( $\blacktriangledown$ ) - Set #2 ( $\text{pH}=5$ ). Experimental conditions described in Table 6-4. Lines show theoretical values of Sherwood number, obtained by solving Equation (3-30):  $\text{Ad}=0.11$ , ( $\text{—}$ )  $a = 0.42 \mu\text{m}$ ; ( $\text{— } \text{—}$ )  $a \pm \sigma/2$ ,  $\sigma = 0.39 \mu\text{m}$ . 115
- Figure 6-21.** Experimentally determined effect of  $\kappa a$  parameter on mass transfer to collector surface for a pentadecane emulsion in different concentrations of NaCl,  $\text{pH}=5$ ,  $\text{Re}=100$ . Solid line shows theoretical mass transfer. 118

- Figure 6-22.** Coverage of stagnation region at high flowrates ( $Re = 800$ ). 123  
Particle density given as particles/ $1500 \mu m^2$ : (a) 3-D representation of bitumen droplet deposition on collector surface ; (b) 3-D representation of viscometry oil droplet deposition (System A) on collector surface.
- Figure 6-23.** Distribution of droplets in  $185 \mu m^2$  areas at high flowrates 124  
( $Re = 800$ ) for (a) 0.1M NaCl bitumen emulsion, with  $s=1.93$  droplets/ $185 \mu m^2$  ; (b) viscometry oil emulsion (System A), with  $s=1.65$  droplets/ $185 \mu m^2$  . (●) - Experimental observations: (□) - Poisson distribution.
- Figure 7-1.** Schematic diagram of hydrophilic and silane-treated glass 133  
microscope slides, from Araujo *et al.* [45].
- Figure 7-2.** Measured (symbols) and nonlinear regression analysis 135  
(solid lines) of the variation of silane-treated microscope slide zeta potential with  $[NaCl]$  for a constant bulk pH ( $pH=4$ ). Analytical expression describing the variation of  $\zeta_c$  with  $[NaCl]$  given by Equation (7-1).
- Figure 7-3.** Representative size distribution of bitumen-in-water 137  
emulsions used in the deposition experiments involving silane-treated collectors. Mean droplet diameter shown as  $\mu = 1.24 \mu m$ , with  $\sigma = 0.18 \mu m$ .
- Figure 7-4.** Stagnation region coating density as a function of time for 139  
bitumen droplets attaching to a silane-treated (hydrophobic) collector surface in 0.1M NaCl,  $pH=4$ ;  $c_0=2.3 \times 10^6$  particles/ml.
- Figure 7-5.** Dimensionless mass transfer (expressed as Sherwood 140  
number) as a function of Reynolds number of  $1.24 \mu m$  bitumen droplets onto a silane-treated (hydrophobic) collector;  $pH=4$ , 0.1M NaCl;  $\zeta_c = 6.3$  mV;  $\zeta_p = -17.8$  mV. (○) -  $c_0 = 2.3 \times 10^6$  droplets/ml; (▼) -  $c_0 = 9.1 \times 10^6$  droplets/ml. Lines show theoretical mass transfer, obtained by solving Equation (3-30):  $Ad=0.11$ , (—)  $a = 0.62 \mu m$ ; (— —)  $a \pm \sigma/2$ ,  $\sigma = 0.18 \mu m$ .

- Figure 7-6.** Experimentally determined effect of  $\kappa a$  parameter on mass transfer rate of  $1.24\ \mu\text{m}$  bitumen droplets to a silane-treated (hydrophobic) collector,  $Re=100$ ,  $pH=4$ ,  $c_0=9.1 \times 10^6$  droplets/ml. Solid line shows mass transfer rates predicted using DLVO theory. Dotted line shows hypothetical mass transfer rates obtained when the hydrophobic force of attraction is estimated. 143
- Figure 7-7.** Representative size distribution of bitumen-in-water emulsions, used in the deposition experiments involving bitumen-coated collectors. Mean droplet diameter shown as  $\mu = 1.29\ \mu\text{m}$ , with  $\sigma = 0.15\ \mu\text{m}$ . 147
- Figure 7-8.** Dimensionless mass transfer (expressed as Sherwood number) as a function of Reynolds number of  $1.29\ \mu\text{m}$  bitumen droplets onto a bitumen-coated collector;  $0.1\text{M NaCl}$ ; ( $\circ$ ) -  $pH=4$ ; ( $\blacktriangledown$ ) -  $pH=10$ . Lines show theoretical mass transfer, obtained by solving Equation (3-30):  $Ad=0.07$ , ( $\text{—}$ )  $a = 0.645\ \mu\text{m}$ ; ( $\text{— } \text{—}$ )  $a \pm \sigma/2$ ,  $\sigma = 0.150\ \mu\text{m}$ . 148
- Figure 8-1.** Representative size distribution of water-in-hydrocarbon emulsions, with a mean droplet diameter of  $\mu = 1.39\ \mu\text{m}$  and  $\sigma = 0.34\ \mu\text{m}$ . 155
- Figure 8-2.** Dimensionless mass transfer (expressed as Sherwood number) as a function of Reynolds number for  $1.39\ \mu\text{m}$  water droplets suspended in 4:1 toluene/hexane (by volume) with added bitumen. Experimental conditions described in Table 8-2. ( $\bullet$ ) - set A-1; ( $\blacksquare$ ) - set A-2; ( $\nabla$ ) - set A-3. Lines show theoretical mass transfer, obtained by solving Equation (3-30):  $Ad=0.007$ . ( $\text{—}$ )  $a = 0.695\ \mu\text{m}$ ; ( $\text{— } \text{—}$ )  $a \pm \sigma/2$ ,  $\sigma = 0.340\ \mu\text{m}$ . 159
- Figure 8-3.** Variation of (a) stagnation region coating density curves for  $Re = 320$  and (b) initial flux to the collector surface as a function of  $c_0$  and  $b_0$  for water-in-hydrocarbon deposition experiments. Experimental conditions listed in Table 8-2. ( $\bullet$ ) - set A-1; ( $\square$ ) - set A-2; ( $\nabla$ ) - set A-3. 160

- Figure 8-4.** Dimensionless mass transfer rate (expressed as Sherwood number) as a function of Reynolds number for 1.39  $\mu\text{m}$  water droplets suspended in 4:1 toluene/hexane (by volume) with added bitumen. Experimental conditions described in Table 8-2. (●) - set A-4; (◇) - set A-5; (Δ) - set A-6. Lines show theoretical mass transfer, obtained by solving Equation (3-30):  $Ad=0.007$ , (—)  $a = 0.695 \mu\text{m}$ ; (— —)  $a \pm \sigma/2$ ,  $\sigma = 0.340 \mu\text{m}$ . 162
- Figure 8-5.** Dimensionless mass transfer rate (expressed as Sherwood number) as a function of Reynolds number and continuous phase bitumen concentration ( $b_0$ ) for 1.39  $\mu\text{m}$  water droplets suspended in 4:1 toluene/hexane (by volume) with added bitumen. (□) - set A-1  $\{b_0=6.4 \text{ g/L}\}$ ; (●) - set A-4  $\{b_0=1.22 \text{ g/L}\}$ ; (◇) - set A-5  $\{b_0=1.22 \text{ g/L}\}$ . Lines show theoretical mass transfer, obtained by solving Equation (3-30):  $Ad=0.007$ , (—)  $a = 0.695 \mu\text{m}$ ; (— —)  $a \pm \sigma/2$ ,  $\sigma = 0.340 \mu\text{m}$ . 163
- Figure 8-6.** Effect of continuous phase bitumen concentration ( $b_0$ ) on the dimensionless mass transfer rates (expressed as Sherwood number) of water droplets suspended in 4:1 toluene/hexane with added bitumen. For the upper band of results,  $b_0=1.22 \text{ g/L}$ : (◆) - set B-1; (Δ) - set B-2; (○) - set B-3; (■) - set B-4. For the lower band of results,  $b_0=3.00 \text{ g/L}$ : (●) - set B-5; (□) - set B-6; (∇) - set B-7. Solid line shows theoretical mass transfer, obtained by solving Equation (3-30):  $Ad=0.007$ ,  $a = 0.695 \mu\text{m}$ . 166
- Figure 8-7.** Variation of dimensionless mass transfer rate (expressed as Sherwood number) with continuous phase bitumen concentration ( $b_0$ ) for water-in-hydrocarbon emulsion deposition experiments:  $Re=320$ . 168
- Figure 8-8.** Schematic representation of possible mechanism to explain the deposition of water droplets (W) coated with asphaltene molecules (A) in the presence of 'free' asphaltenes (A), showing competition for collector adsorption sites between adsorbed and free asphaltenes. From [18]. 170

## NOMENCLATURE

$a$	droplet radius, m
$A_{132}$	Hamaker constant for materials {1} and {2} separated by medium {3}. J
$A_d$	Adhesion number
$b_0$	continuous phase bitumen concentration, g bitumen / L solution
$Bo$	Bond number, $4\Delta\rho ga^2/\sigma_t$
$c$	local particle or droplet concentration, $m^{-3}$
$c_0$	bulk particle or droplet concentration, $m^{-3}$
$Ca$	Capillary number, $2\eta Ga/\sigma_t$
$d_{\perp}$	diffusion coefficient correction factor normal to the surface
$d_{\parallel}$	diffusion coefficient correction factor parallel to the surface
$D$	diffusion coefficient tensor, $m^2 s^{-1}$
$D_x$	bulk particle or droplet diffusion coefficient, $m^2 s^{-1}$
$Da$	double layer asymmetry parameter
$DI$	double layer strength parameter
DLVO	Derjaguin-Landau-Verwey-Overbeek
$e$	elementary charge, $1.602 \times 10^{-19} C$
$f_i$	universal hydrodynamic correction coefficients [ $i=1,4$ ]
$F$	external force vector, N
$F_A$	van der Waals attractive force, N
$F_R$	double layer force, N
$G$	wall shear rate, $s^{-1}$
$Gr$	Gravity number
$h$	particle or droplet surface-to-collector surface separation distance, m
$h_0$	distance between capillary exit and collector surface, m
$\hbar$	Planck constant, $6.6256 \times 10^{-34} J s$
$H$	dimensionless particle or droplet-collector separation distance
HHF	Hogg-Healy-Furstenau
$j$	particle or droplet flux vector, $m^{-2} s^{-1}$
$J_0$	initial flux to collector surface, $m^{-2} s^{-1}$

$k$	Boltzmann constant, $1.381 \times 10^{-23} \text{ J K}^{-1}$
$L$	length of outflow region in impinging jet cell, m
$m_b$	mass of bitumen added to nonaqueous emulsion diluent, g
$m_i$	effective electrolyte concentration, $\text{mol L}^{-1}$
$m_0$	bulk electrolyte concentration, $\text{mol L}^{-1}$
$M_i$	molarity of ionic species $i$ , $\text{mol L}^{-1}$
$n$	refractive index of material
$n_c$	number of counterions per unit volume, $\text{m}^{-1}$
$N_A$	Avogadro number, $6.022 \times 10^{23} \text{ mol}^{-1}$
$N_s$	total surface density of functional groups, $\text{m}^{-2}$
$\text{pKa}$	surface group dissociation constant
$P_i$	probability of finding $i$ particles or droplets per given area of stagnation region
$\text{Pe}$	Peclet number, $2\alpha a^3/D_x$
$q$	valency of ionic species
$r, z$	radial and axial cylindrical coordinates
$R$	capillary radius, m
$\text{Re}$	Reynolds number, $\rho U R / \eta$
$s$	average number of particles or droplets per given area of stagnation region
$S$	stagnation region coating density (SRCD), $\text{m}^{-2}$
$\text{Sc}$	Schmidt number, $\eta / \rho D_x$
$\text{Sh}$	Sherwood number
$t$	time, s
$T$	absolute temperature, K
$u$	particle or droplet velocity vector, $\text{m s}^{-1}$
$U$	volume averaged bulk velocity, $\text{m s}^{-1}$
$v$	fluid velocity vector, $\text{m s}^{-1}$
$V_i$	volume of concentrated nonaqueous emulsion, L
$V_s$	volume of nonaqueous emulsion diluent, L
$x_s$	shear plane location, m
$X$	dimensionless particle or droplet flux to collector surface

$X_0$	dimensionless particle or droplet flux at the primary minimum (= Sh)
$y_0$	dimensionless zeta potential
$z$	particle or droplet centre-to-collector surface separation distance. m

### *Greek Symbols*

$\alpha$	strength of stagnation point flow, $\text{m}^{-1} \text{s}^{-1}$
$\delta_{\text{pm}}$	location of primary energy minimum, m
$\varepsilon$	dielectric constant
$\varepsilon_0$	permittivity of a vacuum, $8.854 \times 10^{-12} \text{ C}^2 \text{ N}^{-1} \text{ m}^{-2}$ or $\text{C V}^{-1} \text{ m}^{-1}$
$\zeta_{\text{c}}$	collector zeta potential, V
$\zeta_{\text{p}}$	particle or droplet zeta potential, V
$\eta$	continuous phase viscosity, Pa s
$\kappa$	inverse Debye length, $\text{m}^{-1}$
$\kappa a$	dimensionless double layer thickness parameter
$\lambda$	retardation parameter (London wavelength). m
$\mu$	mean particle or droplet diameter, m
$\nu$	frequency, $\text{s}^{-1}$
$\nu_{\text{e}}$	main electronic absorption frequency in UV spectra. $\approx 3 \times 10^{15} \text{ s}^{-1}$
$\rho$	density, $\text{kg m}^{-3}$
$\sigma$	standard deviation. m
$\sigma_{\text{t}}$	surface tension. Pa
$\phi$	interaction energy, J
$\bar{\psi}$	dimensionless stream function
$\bar{\omega}$	dimensionless vorticity
$\bar{\omega}^*$	ratio of dimensionless flow vorticity to dimensionless radial distance, $\bar{\omega} / \bar{r}$

# 1. Introduction

The interaction between a surface and a system of microscopic particles or droplets suspended in a liquid phase is complex and depends on the following parameters: particle size and shape; particle surface charge; continuous phase viscosity; dielectric permittivity of the continuous phase; hydrodynamic conditions; the nature of the surface; and the application of external forces. Even the aforementioned, incomplete list is overwhelming. Yet, an understanding of the behavior of suspensions and emulsions is crucial to the success of many industries, including those involved in the extraction of crude oil from underground reservoirs, the processing of oil sands to extract bitumen, pulp and paper processing, processed foods production, and biochemical and pharmaceuticals production.

Colloid science, which can very generally be defined as the study of the behavior of suspended particles and droplets, quantitatively describes flotation, demulsification, and filtration processes. Processes such as these are the basic building blocks of the aforementioned industrial applications. In this manner, colloid science provides a fundamental model of an applied process.

The work included in this thesis provides a quantitative method to describe the effect of hydrodynamic and short range forces on the mass transfer of colloidal droplets from a flowing emulsion to a collector surface. Although this study is fundamental in nature, it relates directly to the development and improvement of demulsification and filtration processes. The experimental apparatus used to conduct the deposition experiments is similar to the apparatus developed by Dabros and van de Ven [1]. A detailed description of the apparatus, known as the impinging jet cell, is given in Chapter 2. The corresponding numerical model is a simple, but clever, combination of colloidal, hydrodynamic, and mass transport theory. It is the product of a diverse cross-section of research, ranging from the development of the particle-surface interaction model of Derjaguin - Landau - Verwey - Overbeek (DLVO theory), to the study of particle motion near a surface [2 - 6], to the development of a

numerical method of solving mass transfer and fluid flow equations in stagnation flows [7].

### **1.1 Objectives of this work**

When this project was undertaken, one of the main goals of the author was to explore the ability of colloidal theory to describe deposition experiments involving dilute emulsions. After a number of years of research, that one sweeping statement of purpose is best reconstituted as:

1. The use of a well-established experimental technique that allows direct observation of deposition phenomena under strictly controlled conditions, so that a significant volume of reliable experimental data concerning the deposition behavior of emulsions may be accumulated;
2. The careful study of the effects of a number of parameters, such as particle surface charge, particle size, dispersed phase viscosity, nature of the collector surface. ionic strength, and flow intensity on both experimental and calculated results; and.
3. The study of both aqueous (oil-in-water) and nonaqueous (water-in-oil) emulsions using deposition experiments.

When the entire body of work contained within is considered, it represents the development of an extensive system of tests to study the behavior of different emulsion systems, and the parameters that most strongly influence the behavior of the emulsion droplets.

## **1.2 Thesis overview**

The present study can be divided into three major sections: a discussion and analysis of the experimental apparatus used to conduct the deposition experiments; an extensive discourse on the theory used to model the deposition experiments; and the experimental results and discussion. The experimental results and discussion represent the most significant portion of this work, including all of the experimental studies. from the initial model validation tests and calibration experiments, to the final experiments using water-in-hydrocarbon emulsions. The table of contents provides a detailed outline of the experimental results and discussion sections (Chapters 4 through 8).

## 2. Colloidal deposition

Deposition techniques are commonly used in research because they provide laboratory - scale models of coating, filtration, and demulsification processes. The relationship between deposition experiments and coating or filtration processes is self-explanatory: both are types of deposition processes. Demulsification can be studied using deposition experiments because the droplet - collector interactions observed in deposition experiments are analogous to droplet - droplet interactions that affect demulsification rates. The first step in any demulsification process involves droplet - droplet aggregation and is strongly dependent upon the nature and magnitude of the short range forces between droplets.

As Swanton [8] points out in an excellent review of experimental studies of colloid stability, deposition experiments can be categorized as "column experiments" or "flow techniques across a collector surface". Column experiments are really studies of deposition in packed beds, for which deposition rates are calculated from the change in dispersed phase concentration across the bed. Bulk-averaged information about the nature and strength of the particle - collector interactions is obtained from this type of experimental work.

Flow techniques focus more directly on the actual deposition process. Flow techniques generally allow for more rigorous control of the hydrodynamics, and also allow the researcher to study individual particle-collector interactions rather than the bulk-averaged information that is available from column experiments.

The impinging jet cell, such as the one used in this study, is similar to other flow technique deposition cells. However, the impinging jet cell was designed to allow the researcher to observe the deposition process directly, and thereby study deposition as a dynamic process of attachment and detachment. The analysis of impinging jet cell deposition experiments is relatively simple; the rate of particle deposition is calculated from number counts of attached particles as a function of time. Experimental results are directly compared with theoretical results obtained from a

model of the deposition process.

In this study, the impinging jet cell technique and corresponding theoretical model were used to observe and analyze the deposition behavior of different emulsions. Deposition experiments were conducted using bitumen-in-water emulsions, mineral oil-in-water emulsions, and nonaqueous, water-in-hydrocarbon emulsions to study the effect of droplet concentration, droplet size and surface charge, type of collector, electrolyte concentration, and flow intensity on the rates of droplet attachment to the collector.

## **2.1 Previous studies using flow techniques**

Some of the first deposition experiments were conducted by Marshall and Kitchener [9] and Hull and Kitchener [10], using the rotating disc technique. As the name implies, the collector surface is a disc that rotates at a constant velocity in order to create a diffusion boundary layer of constant thickness. Theoretical analyses of rotating disc experiments are well developed. Prieve and Lin [11] give a detailed description of a numerical model they used in conjunction with rotating disc experiments.

One of the shortcomings of this technique results from the movement of the collector surface: deposition cannot be observed directly, and evaluation of the coating density can only be accomplished once the experiment has been completed and the collector is removed and placed under a microscope. Furthermore, the extra handling of the surface could cause some doubt about the validity of the results.

Another widely used deposition technique eliminates the shortcomings associated with the rotating disc technique. A parallel plate flow chamber can be used to study particle deposition from a flowing suspension onto a collector surface situated parallel to the direction of flow. Bowen and Epstein [12] used this method to study the deposition of silica particles onto a glass plate. Parallel plate flow chambers have also been used to study polystyrene latex deposition [13 - 15] and microbial adhesion

[16]. The use of this technique is generally limited to applications where low flow rates are desired.

The theory that describes deposition in a parallel plate flow chamber is similar to the theory developed for the rotating disc technique, except that it must account for the fact that the particle coating density depends upon the distance from the chamber inlet [13].

## **2.2 The impinging jet cell**

A third deposition technique, developed by Dabros and van de Ven [1], is known as stagnation flow deposition, or the impinging jet technique. As was mentioned previously, an impinging jet cell was used in this study. Deposition in an impinging jet cell is similar to deposition onto a rotating disc, in that the diffusion boundary layer is of constant thickness over the entire stagnation region. The major difference between the two techniques is that the collector surface in the impinging jet cell is stationary, making it possible to focus a microscope on the stagnation region and then directly observe the deposition process.

The impinging jet cell has been used extensively to study particle attachment and detachment [17 - 22]. The advantages of this experimental setup are as follows:

- (i) it is possible to directly observe the deposition process in real time, from the onset of deposition to the conclusion of the experiment;
- (ii) the corresponding theoretical analysis is greatly simplified through the use of stagnation point flow within the deposition cell. In stagnation point flow, the flux to the collector surface is uniform and independent of radial distance in a small region surrounding the stagnation point; and,
- (iii) the hydrodynamic conditions can easily be controlled and reproduced for a wide range of Reynolds numbers.

The experimental apparatus is shown in Figure 2-1. The apparatus was designed so that the desired hydrodynamic conditions could be obtained in either of two ways: for Reynolds numbers greater than 100, a pressure driven flow is utilized, where 345 kPa from an instrument air line (A) was applied to a 500 ml pressure vessel (Whitey Co. Ltd.)(B), containing a known volume of the emulsion, which was previously loaded into the vessel through injection port (C). The resulting flow is measured with a rotameter (Matheson Gas Products Canada) (D) and controlled with a needle valve that is located at the rotameter inlet. For lower Reynolds number flows, a 60 cc. syringe pump (Sage Instruments, Model 341A)(E) is used. In either case, the flowing emulsion passes through approximately 0.1 m of 0.0032 m OD tubing (F) that is connected to the actual impinging jet cell. The cell itself consists of a 0.15 m length of stainless steel tubing (0.0014 m ID) (G), a length chosen to ensure that the flow is fully developed by the time it reaches the capillary exit. The capillary is completely encased in a thick cylindrical plug (0.05 m OD) (H) to eliminate any slight bends or vertical deviations in the inner capillary.

The emulsion then flows from the capillary and impinges on a glass microscope slide (I) held in place atop the external wall of the cell (J) {see inset, Figure 2-1}. The external wall of the cell can be moved upward or downward to change  $h_0$ , the distance from the capillary exit to the glass slide.

After the emulsion exits the capillary and impinges on the glass slide, it flows downward through the annulus between the external wall and the capillary casing, where it collects in the reservoir (K) so that it can be reused.

The deposition process was observed using a Rolyn Arcadia portable microscope (L), fitted with a Leitz-Wetzlar long distance 32X objective, and a Sony video camera adaptor instead of a conventional eyepiece. Dark field illumination was used to optimize the contrast between the particles and the background field. The microscope and adaptor were connected to a Sony SSC-M350 b/w video camera (M). The deposition experiments were video recorded with a Sony Betamax III for subsequent playback and analysis.

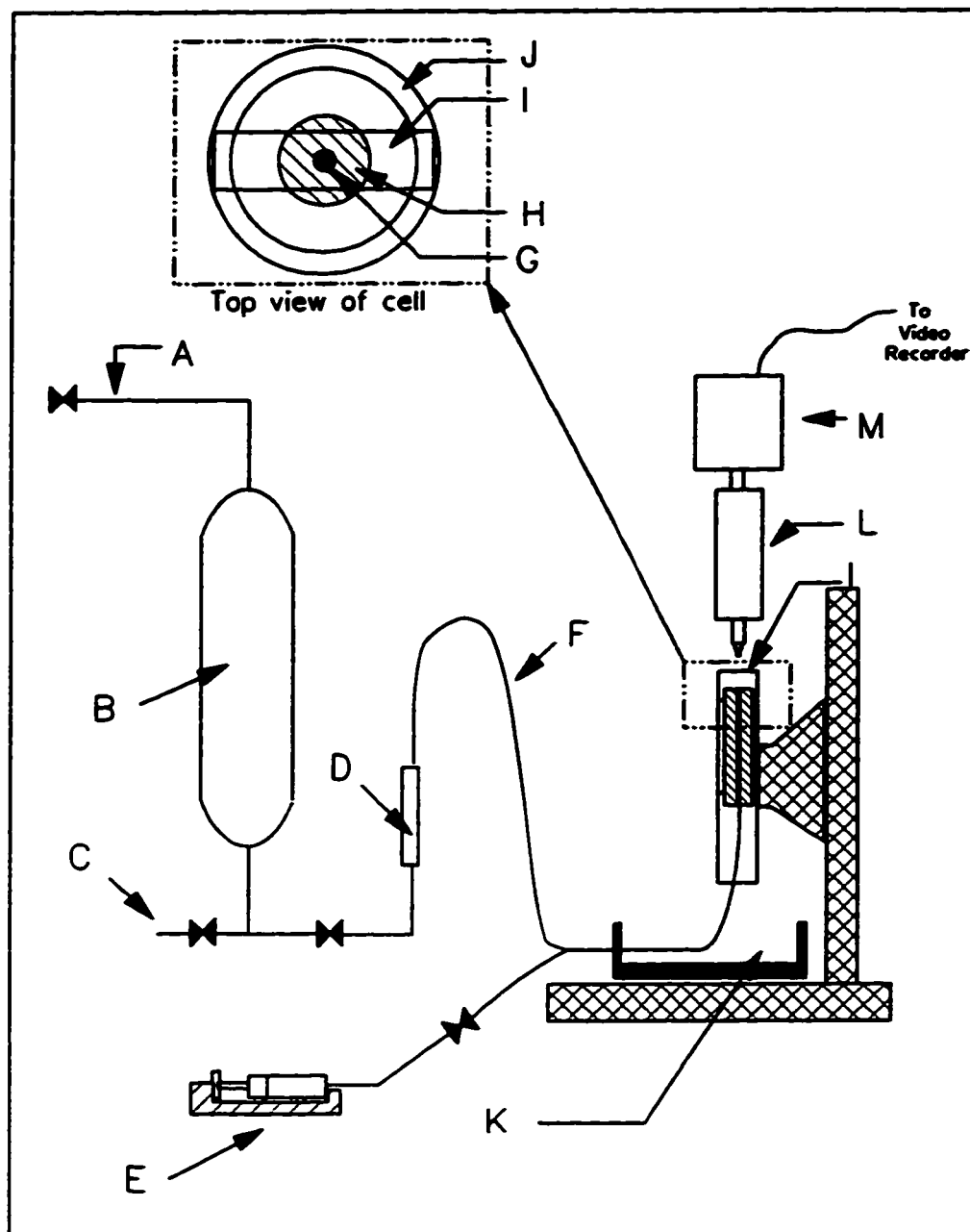


**Figure 2-1.** Schematic diagram of experimental apparatus:

- |                                  |                                  |
|----------------------------------|----------------------------------|
| A - 345 kPa instriner air line   | H - capillary casing             |
| B - 500 ml pressure vessel       | I - collector (microscope slide) |
| C - vessel injection port        | J - external wall of cell        |
| D - flow controller (rotameter)  | K - reservoir                    |
| E - 60 cc. syringe pump          | L - microscope                   |
| F - interconnecting tubing       | M - video camera                 |
| G - impinging jet cell capillary |                                  |

### 2.3 Analysis of deposition experiments

Once a set of deposition experiments has been completed, each experiment is analyzed by counting the number of particles deposited over the stagnation region as a function of time. The stagnation region (essentially the area of observation on the monitor screen) has the dimensions of 440  $\mu\text{m}$  by 330  $\mu\text{m}$ . The stagnation point, or the centre of the stagnation region, was set as near the centre of the screen as possible before any experiments were recorded. The stagnation region coating density (SRCD) is then determined by dividing the number of particles counted by the total area of the stagnation region. For nonuniform deposition, the observation area was divided into 96 equal areas and the number of particles in each area was determined as a function of time. Between 500 and 1000 particles were normally counted for each experiment, depending mostly on the bulk concentration of the emulsion being studied.

The initial slope of the SRCD line, shown on a graph as coating density as a function of time, was used to calculate the flux to the collector surface, where

$$J_0 = \left. \frac{dS}{dt} \right|_{t=0} \quad (2-1)$$

The dimensionless rate of mass transfer to the collector surface, given by the Sherwood number,  $Sh$ , was then calculated from

$$Sh = J_0 \frac{a}{D_\infty c_0} \quad (2-2)$$

Equations (2-1) and (2-2) illustrate that the experimentally determined Sherwood numbers are calculated directly from measurable quantities only: particle radius (both directly and in the calculation of  $D_\infty$  from the Stokes-Einstein equation), bulk concentration, flowrate, and coating density. Theoretical values of the Sherwood number are calculated from solving the Navier-Stokes, mass balance, and general convection-diffusion equations. The solution is discussed in detail in the next chapter.

## 2.4 Overview of experimental work

The impinging jet cell technique, along with its corresponding theoretical model, has been used extensively and is widely accepted as an excellent method for colloid science research. The focus of this study is not directed toward the impinging jet cell technique itself, but is concerned with the application of this technique to the study of emulsion droplet behavior.

The first part of this study focuses on the deposition behavior of bitumen-in-water emulsions onto a hydrophilic collector. The effect of bitumen droplet size and surface charge, collector surface charge, flow intensity, and electrolyte concentration on droplet deposition rates were studied and compared with theoretical predictions.

Deposition experiments were then conducted using low viscosity oils suspended in water. The following low viscosity oil-in-water emulsions were studied: mineral oil (Bayol-35) stabilized with nonionic surfactant (Triton-X); mineral oils (Cannon Standard Viscometry Oils, viscosity 7.67 mPa s and 3.39 mPa s) stabilized with asphaltenes separated from Athabasca bitumen; and pentadecane ( $C_{15}H_{32}$ ) stabilized with asphaltenes separated from Athabasca bitumen. The results of light oil emulsion deposition experiments were compared with (i) theoretical predictions, and (ii) with the results of the bitumen-in-water deposition experiments.

Bitumen-in-water emulsions were used to study the relationship between droplet deposition rates and the nature of the collector surface. In these experiments, the collector surface was treated to make it more hydrophobic. Subsequent experiments were conducted using a bitumen emulsion and a collector that had been coated with a thin layer of bitumen, in order to study bitumen - bitumen interactions.

The final set of experiments was conducted using a water-in-hydrocarbon emulsion. The continuous hydrocarbon phase consisted of a 4:1 (by volume) mixture of toluene and hexane. Bitumen was used to stabilize the emulsion. The effect of Reynolds number, bitumen concentration, and water droplet concentration on the droplet deposition rates were studied.

A detailed list of all of the experimental work that was conducted is given in Section 5.4.

## 3.Theory

### 3.1 Introduction

As mentioned earlier, stagnation flow deposition can be modelled by solving the governing flow field and mass transport equations. In this chapter, the governing equations are derived from fundamental fluid dynamics equations (continuity and Navier-Stokes equations), and from fundamental mass transfer equations (continuity and general convection-diffusion equations). All of the simplifications and assumptions that are used to develop a numerical model of the deposition process are outlined in this chapter. Although much of this work can be found elsewhere, it has not been presented in one complete, cohesive unit, as it is here.

The chapter can be divided into five sections. First, fluid flow in an impinging jet cell (stagnation flow) is characterized through the numerical solution of the continuity and Navier-Stokes equations in order to describe the flow profile in the region nearest the stagnation point. In the next section, analytical expressions used to approximate the radial and axial velocities are introduced, and their relationship to the flow profile generated by the numerical solution is discussed. The third section of the chapter provides a description of the governing mass transfer equations, and a step-by-step solution procedure that begins with the simplification of the general convection-diffusion equation, outlines the development of analytical expressions for the external forces acting on the droplets, and ends with the numerical method used to solve the final form of the mass transport equation. Section 3.6 discusses the application of DLVO theory to nonaqueous systems. In the last section of the chapter, the sensitivity of the numerical model to changes in particle size and the magnitudes of the van der Waals and electrostatic interactions is analyzed.

## 3.2 Description of the axisymmetric flow field

### 3.2.1 Governing equations

Figure 3-1 illustrates the geometry of the impinging jet cell. One of the inherent advantages of the impinging jet technique is the axisymmetric flow field that is produced in the stagnation point area. Because of this simplification, it is possible to solve the governing Navier-Stokes equations for incompressible, axisymmetric flow. Thus, the governing continuity and Navier-Stokes equations, in terms of dimensionless cylindrical components, have the form:

$$\frac{1}{\bar{r}} \frac{\partial}{\partial \bar{r}}(\bar{r} \bar{v}_r) + \frac{\partial \bar{v}_z}{\partial \bar{z}} = 0 \quad (3-1)$$

$$\bar{v}_r \frac{\partial \bar{v}_r}{\partial \bar{r}} + \bar{v}_z \frac{\partial \bar{v}_r}{\partial \bar{z}} = -\frac{\partial \bar{P}}{\partial \bar{r}} + \frac{1}{\text{Re}} \left[ \frac{\partial}{\partial \bar{r}} \left( \frac{1}{\bar{r}} \frac{\partial}{\partial \bar{r}}(\bar{r} \bar{v}_r) \right) + \frac{\partial^2 \bar{v}_r}{\partial \bar{z}^2} \right] \quad (3-2a)$$

$$\bar{v}_r \frac{\partial \bar{v}_z}{\partial \bar{r}} + \bar{v}_z \frac{\partial \bar{v}_z}{\partial \bar{z}} = -\frac{\partial \bar{P}}{\partial \bar{z}} + \frac{1}{\text{Re}} \left[ \frac{1}{\bar{r}} \frac{\partial}{\partial \bar{r}} \left( \bar{r} \frac{\partial \bar{v}_z}{\partial \bar{r}} \right) + \frac{\partial^2 \bar{v}_z}{\partial \bar{z}^2} \right] \quad (3-2b)$$

The dimensionless variables are defined as follows:

$$\bar{r} = \frac{r}{R} \quad (3-3a)$$

$$\bar{z} = \frac{z}{R} \quad (3-3b)$$

$$\bar{L} = \frac{L}{R} \quad (3-3c)$$

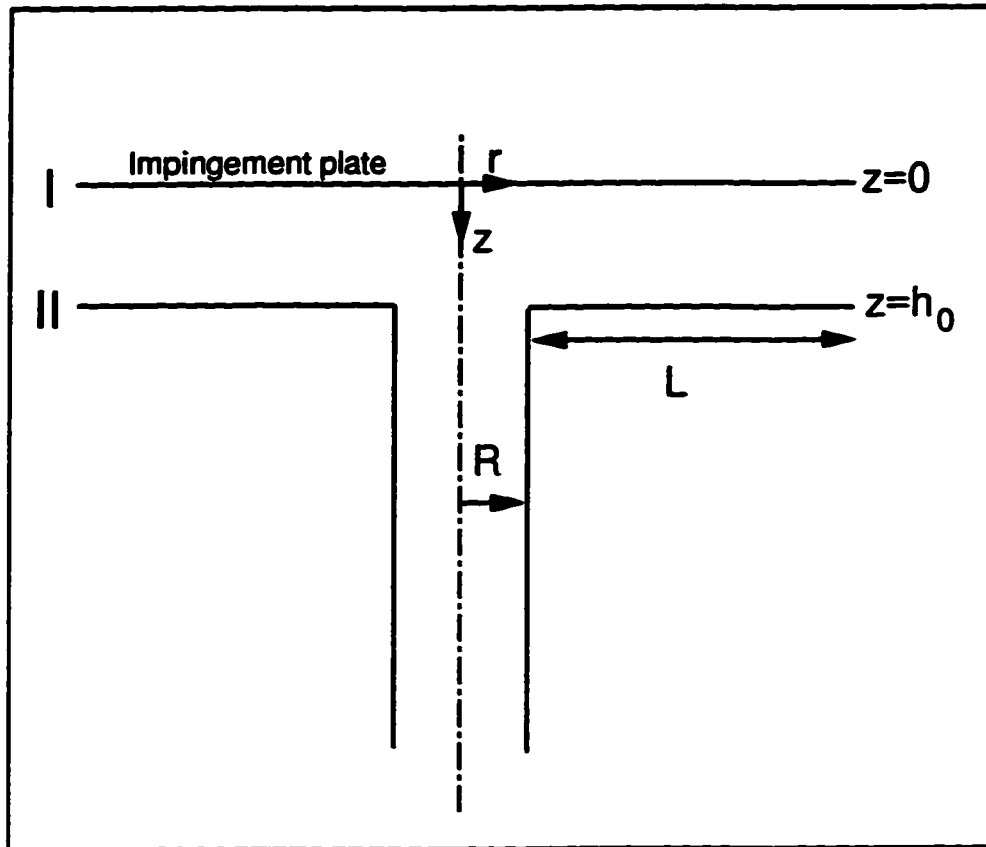


**Figure 3-1.** Geometry of impinging jet cell:  $R = 0.7$  mm:  $h_0 = 0.84, 1.81$  mm:  
 $L = 25$  mm.

$$\bar{h}_0 = \frac{h_0}{R} \quad (3-3d)$$

$$\bar{v}_r = \frac{v_r}{U} \quad (3-3e)$$

$$\bar{v}_z = \frac{v_z}{U} \quad (3-3f)$$

$$\bar{P} = \frac{PR}{\rho U^2} \quad (3-3g)$$

$$Re = \frac{\rho UR}{\eta} \quad (3-3h)$$

where the superscript '-' denotes a dimensionless parameter. In order to solve Equations (3-1) and (3-2), they are written in terms of vorticity and stream function, which are defined as

$$\bar{\omega} = \frac{\partial \bar{v}_r}{\partial \bar{z}} - \frac{\partial \bar{v}_z}{\partial \bar{r}} \quad (3-4a)$$

$$\bar{v}_z = \frac{1}{\bar{r}} \frac{\partial \bar{\psi}}{\partial \bar{r}} \quad (3-4b)$$

$$\bar{v}_r = -\frac{1}{\bar{r}} \frac{\partial \bar{\psi}}{\partial \bar{z}} \quad (3-4c)$$

Substitution of Equations (3-4b) and (3-4c) into Equation (3-1) satisfies the condition of continuity. Briefly, the solution of Equations (3-2) begins by differentiating Equation (3-2a) with respect to ' $\bar{r}$ ' and differentiating Equation (3-2b) with respect to ' $\bar{z}$ '. The second equation is then subtracted from the first. The difference can be

written, in terms of vorticity and stream function, as

$$\bar{r}^2 \left[ \frac{\partial}{\partial z} \left( \frac{\bar{\omega}}{\bar{r}} \frac{\partial \bar{\psi}}{\partial \bar{r}} \right) - \frac{\partial}{\partial \bar{r}} \left( \frac{\bar{\omega}}{\bar{r}} \frac{\partial \bar{\psi}}{\partial z} \right) \right] - \frac{1}{\text{Re}} \left[ \frac{\partial}{\partial z} \left( \bar{r}^3 \frac{\partial}{\partial z} \left( \frac{\bar{\omega}}{\bar{r}} \right) \right) + \frac{\partial}{\partial \bar{r}} \left( \bar{r}^3 \frac{\partial}{\partial \bar{r}} \left( \frac{\bar{\omega}}{\bar{r}} \right) \right) \right] = 0 \quad (3-5a)$$

The equation defining vorticity, Equation (3-4a), can also be written in terms of the stream function:

$$\bar{\omega} = \frac{1}{\bar{r}} \left[ - \left( \frac{\partial^2 \bar{\psi}}{\partial \bar{r}^2} + \frac{\partial^2 \bar{\psi}}{\partial z^2} \right) + \frac{1}{\bar{r}} \frac{\partial \bar{\psi}}{\partial \bar{r}} \right] \quad (3-5b)$$

By defining  $\bar{\omega}^*$  as

$$\bar{\omega}^* = \frac{\bar{\omega}}{\bar{r}} \quad (3-6)$$

Equations (3-5a) and (3-5b) can be written as

$$\begin{aligned} & \bar{r}^2 \left[ \frac{\partial}{\partial z} \left( \bar{\omega}^* \frac{\partial \bar{\psi}}{\partial \bar{r}} \right) - \frac{\partial}{\partial \bar{r}} \left( \bar{\omega}^* \frac{\partial \bar{\psi}}{\partial z} \right) \right] \\ & - \frac{1}{\text{Re}} \left[ \frac{\partial}{\partial z} \left( \bar{r}^3 \frac{\partial}{\partial z} (\bar{\omega}^*) \right) + \frac{\partial}{\partial \bar{r}} \left( \bar{r}^3 \frac{\partial}{\partial \bar{r}} (\bar{\omega}^*) \right) \right] = 0 \end{aligned} \quad (3-7a)$$

and

$$\bar{\omega}^* = \frac{1}{\bar{r}^2} \left[ - \left( \frac{\partial^2 \bar{\psi}}{\partial \bar{r}^2} + \frac{\partial^2 \bar{\psi}}{\partial z^2} \right) + \frac{1}{\bar{r}} \frac{\partial \bar{\psi}}{\partial \bar{r}} \right] \quad (3-7b)$$

Thus, the flow field is described by two nonlinear elliptic PDE's, given by Equations (3-7a) and (3-7b), above.

### 3.2.2 Boundary conditions

Conditions must be specified at all boundaries in order to solve the elliptic PDE's given by Equations (3-7a) and (3-7b). Therefore, the solution of governing equations given by Equations (3-7) is subject to the boundary conditions applied at

- (i) the capillary exit ( $\bar{z} = \bar{h}_0$ ,  $\bar{r} \leq 1$ );
- (ii) the axis of symmetry ( $\bar{r} = 0$ );
- (iii) the collector surface ( $\bar{z} = 0$ );
- (iv) the capillary exit plane ( $\bar{z} = \bar{h}_0$ ,  $\bar{r} > 1$ );
- (v) the outflow region, or the cell exit ( $\bar{r} = 1 + \bar{L}$ ).

These boundary conditions are outlined below.

- (i) At the capillary exit ( $\bar{z} = \bar{h}_0$ ,  $\bar{r} \leq 1$ ):

The radial and axial velocity components at the capillary exit are defined as follows:

$$\bar{v}_r = 0 \quad (3-8a)$$

$$\bar{v}_z = 2(\bar{r}^2 - 1) \quad (3-8b)$$

After substituting Equations (3-8) into Equations (3-4a) and (3-4b), the expressions for the vorticity and stream function become

$$\bar{\omega}^* = -4 \quad (3-9a)$$

and

$$\bar{\psi} = -\bar{r}^2 \left( 1 - \frac{\bar{r}^2}{2} \right) \quad (3-9b)$$

(ii) At the axis of symmetry ( $\bar{r} = 0$ ):

As Deshpande and Vaishnav [23] state, because of the condition of axial symmetry,

$$\begin{aligned} \bar{v}_r &= 0 \\ \bar{\omega} &= 0; \\ \bar{\psi} &= \text{constant} \end{aligned}$$

at  $\bar{r} = 0$ . Since the stream function is constant, it is acceptable to set  $\bar{\psi} = 0$  at the axis of symmetry. This still leaves  $\bar{\omega}^*$ , which is as yet undefined, but is nonzero at the symmetry axis. It can be calculated by assuming that the stream function  $\bar{\psi}$  has the form

$$\bar{\psi} = A(\bar{z})\bar{r}^2 + B(\bar{z})\bar{r}^4 \quad (3-10)$$

in the region surrounding the symmetry axis. When this equation defining the stream function is substituted into Equation (3-7b), the value of  $\bar{\omega}^*$  at  $\bar{r} = 0$  can be expressed as

$$\bar{\omega}^* \Big|_{\bar{r}=0} = - \left( 8B + \frac{\partial^2 A}{\partial \bar{z}^2} \right) \quad (3-11a)$$

where

$$A(\bar{z}) = \frac{1}{\bar{r}_2^2 - \bar{r}_1^2} \left( \frac{\bar{r}_2^2}{\bar{r}_1^2} \bar{\psi}_1 - \frac{\bar{r}_1^2}{\bar{r}_2^2} \bar{\psi}_2 \right) \quad (3-11b)$$

and

$$B(\bar{z}) = \frac{1}{\bar{r}_2^2 - \bar{r}_1^2} \left( \frac{\bar{\psi}_2^2}{\bar{r}_2^2} - \frac{\bar{\psi}_1^2}{\bar{r}_1^2} \right) \quad (3-11c)$$

It should be noted that  $\bar{\psi}_1$  and  $\bar{\psi}_2$  are the values of the stream functions at  $(\bar{r}_1, \bar{z})$  and  $(\bar{r}_2, \bar{z})$ , respectively.

(iii) At the collector surface (Surface I,  $\bar{z} = 0$ ):

The no-slip boundary condition is applied at the collector surface, meaning  $\bar{v}_r = \bar{v}_z = 0$ . Also,  $\bar{\psi} = 0$  at Surface I {recall the general expression defining  $\bar{\psi}$  given in (ii)}. The vorticity term  $\bar{\omega}^* = \bar{\omega} / \bar{r}$  is unknown, but can be approximated in the manner outlined below. Following [24],  $\bar{\psi}$  is expanded as a Taylor series, which yields the value of the stream function at the point nearest the wall,  $\bar{\psi}_i$ , as a function of the values of  $\bar{\psi}$  and  $(\delta^n \bar{\psi} / \delta \bar{z}^n)$ , where  $n=1$  to 3, at the wall. Briefly,  $(\delta \bar{\psi} / \delta \bar{z})_w = 0$  by the no-slip condition. The second derivative,  $(\delta^2 \bar{\psi} / \delta \bar{z}^2)_w$ , is written as

$$\left. \frac{\partial^2 \bar{\psi}}{\partial \bar{z}^2} \right|_w = -\bar{r} \bar{\omega}_w \quad (3-12a)$$

The third order derivative,  $(\delta^3 \bar{\psi} / \delta \bar{z}^3)_w$ , is simplified using the definition of vorticity,

Equation (3-4a), and the continuity equation, Equation (3-1). The resulting expression is

$$\left. \frac{\partial^3 \bar{\psi}}{\partial \bar{z}^3} \right|_w = \frac{-\bar{r}(\bar{\omega}_i - \bar{\omega}_w)}{\Delta \bar{z}} \quad (3-12b)$$

Equations (3-12a) and (3-12b) are then substituted into the original Taylor series expanding  $\bar{\psi}$  at  $\bar{\psi}_w$ . Rearrangement yields the following expression for  $\bar{\omega}^*$  at Surface I:

$$\bar{\omega}^* \Big|_I = \frac{3(\bar{\psi}_w - \bar{\psi}_i)}{(\bar{z}_i - \bar{z}_w)^2 \bar{r}^2} - \frac{\bar{\omega}_i}{2\bar{r}} \quad (3-13)$$

where the indices  $w$  and  $i$  refer to the wall and first internal grid points, respectively.

(iv) At the capillary exit plane (Surface II,  $\bar{z} = \bar{h}_0$ ,  $\bar{r} > 1$ ):

The stream function  $\bar{\psi}$  at Surface II is calculated as  $\bar{\psi} = -0.5$ , which is in accordance with the limiting value calculated from the expression for  $\bar{\psi}$  outlined in (i). The vorticity term  $\bar{\omega}^*$  can be calculated using the same method outlined in (iii) {Equation (3-13)}, except that now  $\bar{z} = \bar{h}_0$ .

(v) At the cell exit ( $\bar{r} = 1 + \bar{L}$ ):

The boundary conditions were set based on the assumption that the flow field at this point is stable [17], meaning

$$\frac{\partial v_r}{\partial \bar{z}} = 0 \quad (3-14a)$$

$$\frac{\partial \bar{\omega}}{\partial \tau} = 0 \quad (3-14b)$$

As others have suggested [17,25], the boundary conditions at the cell exit have no significant effect on the flow field near the stagnation point, as long as  $\bar{L} \gg \bar{h}_0$ .

For the impinging jet cell used in this study,  $\bar{L} = 35.7$ , and  $\bar{h}_0$  values are set at  $\bar{h}_0 = 2.59$  or  $\bar{h}_0 = 1.21$ , so that  $\bar{L} \gg \bar{h}_0$ .

### 3.2.3 Numerical solution procedure

Equations (3-7), along with boundary conditions described by Equations (3-8) through (3-14), were solved using a standard successive-substitution numerical technique [6]. A nonuniform grid, consisting of 41 points in the  $z$  direction and 28 points in the  $r$  direction, was used. The grid nodes near the collector surface and near the axis of symmetry were spaced closely together, with the distance between the nodes increasing with increasing  $r$  and  $z$ . Convergence criteria were taken from Dabros and van de Ven [1], where

$$\left( \frac{\theta^N - \theta^{N-1}}{\theta^N} \right)_{\max} < 10^{-3} \quad (3-15)$$

The variable  $\theta$  represents either  $\bar{\psi}$  or  $\bar{\omega}^*$  and  $N$  represents the iteration number.

### 3.3 Description of the flow field in the stagnation region

The sole purpose for the description of the flow field presented above (Section 3.2) is to determine the hydrodynamic conditions near the collector surface. The axial

and radial fluid velocities near the collector surface are integral to the solution of the mass transfer equations discussed in the next section. In fact, analytical expressions must be developed to describe the velocity components in the stagnation region.

As Dabros and van de Ven [1] point out, the Schmidt number ( $Sc = \eta/\rho D_0$ ) is usually very large for the mass transfer of colloidal particles. When  $Sc \gg 1$ , the diffusion boundary layer is much thinner than the hydrodynamic boundary layer. Consequently, only the portion of the flow field nearest the collector surface needs to be considered because the mass transfer process occurs entirely within the hydrodynamic boundary layer.

The flow field near the collector surface at the symmetry axis can be described by the axisymmetrical part of a general second order flow, where

$$\bar{v}_r = \bar{\alpha} \bar{r} \bar{z} \quad (3-16a)$$

$$\bar{v}_z = -\bar{\alpha} \bar{z}^2 \quad (3-16b)$$

where  $\bar{\alpha}$  is a constant. When Equations (3-16) are substituted into the definition of vorticity, Equation (3-4a), it can be seen that

$$\frac{\bar{\omega}}{\bar{r}} = \bar{\omega}^* = \bar{\alpha} \quad (3-17)$$

near the stagnation region. Dabros and van de Ven [1] have shown that this expression is valid for distances up to 20% of the capillary radius. It is evident that the numerical flow field model discussed in Section 3.2 can therefore be used to determine the constant,  $\bar{\alpha}$ , which is known as the "strength of stagnation point flow". The parameter  $\bar{\alpha}$  is dependent upon Reynolds number and the dimensionless distance between the capillary exit and the collector surface,  $\bar{h}_0$ .

### 3.3.1 Dependence of $\bar{\alpha}$ on Reynolds number

In their study of mass transfer due to a confined impinging jet, Law and Masliyah [25] showed that

$$\bar{\alpha} \propto Re^{1/2} \quad (3-18)$$

Equation (3-18) was confirmed experimentally by Dabros and van de Ven [17], and has been used in all of the modelling of stagnation flow deposition experiments that they have conducted. Table 3-1 shows some of the relationships between  $\bar{\alpha}$  and Reynolds number that they have developed, as a function of capillary exit velocity profile and collector - capillary exit separation distance.

**Table 3-1.** Dependence of  $\bar{\alpha}$  on Reynolds number and capillary exit velocity profile, as determined by van de Ven *et al.*

Reference	Velocity Profile	Re	$\bar{h}_0$	A $\bar{\alpha} = A Re^{1/2}$
Dabros and van de Ven [1]	parabolic	$0 < Re < 80$	1.0	3.09
Dabros and van de Ven [16]	flat	$10 < Re < 1500$	1.81	0.87
Varennnes and van de Ven [17]	flat	$100 < Re < 1500$	2.3	0.1

### 3.3.2 Evaluation of $\bar{\alpha}$ for this work

Values of  $\bar{\omega}^*$  were calculated as a function of Reynolds number and jet exit - collector surface separation distance,  $\bar{h}_0$ , using the numerical flow field model described in Section 3-2. As Equation (3-17) shows,  $\bar{\omega}^* = \bar{\alpha}$  near the stagnation point.

Thus, for each  $\bar{h}_0$ , values of  $\bar{\alpha}$  for different Reynolds numbers were determined using the model. Values of  $\bar{\alpha}$  for  $\bar{h}_0 = 2.59$  and  $\bar{h}_0 = 1.21$  are shown in Figure 3-2. Analytical expressions describing the curves shown in Figure 3-2 were obtained by performing regression analyses on the data. For  $\bar{h}_0 = 2.59$

$$\bar{\alpha} = 0.52 \text{ Re}^{1/2} \quad (3-19)$$

For  $\bar{h}_0 = 1.21$

$$\bar{\alpha} = 2.81 \text{ Re}^{1/2} \quad (3-20)$$

Equations (3-19) and (3-20) are used to simplify the solution to the governing mass transfer equations, which is discussed in the following section.

### 3.4 Solution of mass transfer equations

The mass transfer of spherical particles in a dilute suspension, assuming the absence of a source term, is described by:

$$\frac{\partial c}{\partial t} + \nabla \cdot \mathbf{j} = 0$$

For steady state, which is actually the case almost immediately after the onset of deposition, the general mass balance equation becomes

$$\frac{1}{r} \frac{\partial}{\partial r}(r j_r) + \frac{\partial j_z}{\partial z} = 0 \quad (3-21)$$

where  $j_r$  and  $j_z$  are the components of the flux vector  $\mathbf{j}$ . The flux vector  $\mathbf{j}$  is explicitly

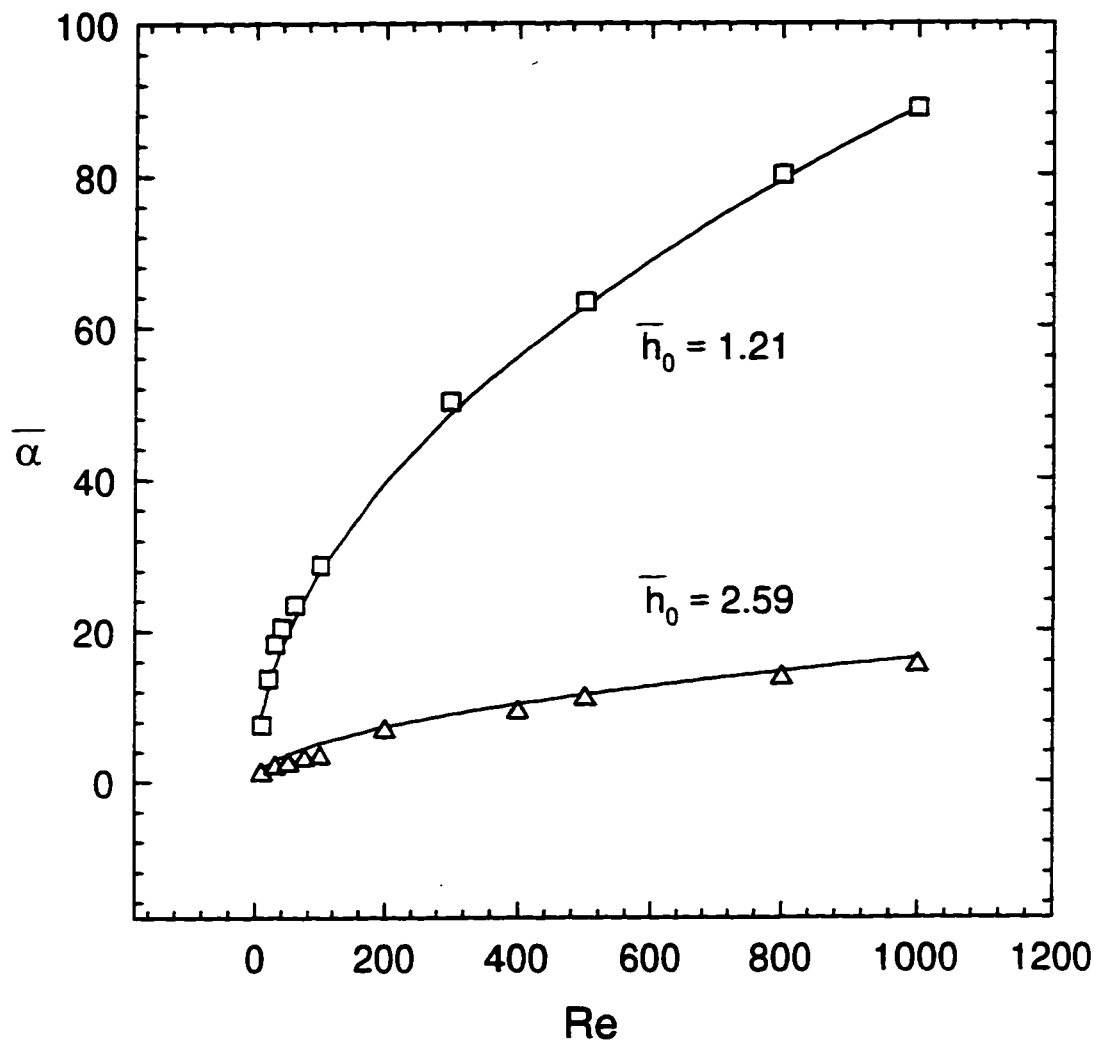


**Figure 3-2.** Dependence of dimensionless strength of stagnation point flow,  $\bar{\alpha}$ , as a function of Reynolds number. Symbols represent results of numerical simulations: ( $\Delta$ )  $\bar{h}_0 = 2.59$ ; ( $\square$ )  $\bar{h}_0 = 1.21$ . Solid lines represent regression analysis. For  $\bar{h}_0 = 2.59$ ,  $\bar{\alpha} = 0.52 \text{ Re}^{1/2}$ . For  $\bar{h}_0 = 1.21$ ,  $\bar{\alpha} = 2.81 \text{ Re}^{1/2}$ .

defined by the general convection-diffusion equation:

$$\mathbf{j} = \mathbf{u} \cdot \mathbf{c} - \underline{\mathbf{D}} \cdot \nabla \mathbf{c} + \frac{c}{kT} \underline{\mathbf{D}} \cdot \mathbf{F} \quad (3-22)$$

Following Spielman and Fitzpatrick [6], the relationships between the fluid velocity,  $\mathbf{v}$ , and particle velocity,  $\mathbf{u}$ , are

$$u_r = v_r f_3 \quad (3-23a)$$

$$u_z = v_z f_1 f_2 \quad (3-23b)$$

A diffusion coefficient tensor is used because the particle diffusion coefficient is a function of the particle position relative to another particle; where, following van de Ven [26] and Masliyah [27], this is expressed as

$$\underline{\mathbf{D}} = (D_1 + D_2)_{\infty} \begin{pmatrix} d_1 & 0 \\ 0 & d_{\perp} \end{pmatrix} \quad (3-24a)$$

For the case of a particle and a "large" collector, where the particle is much smaller than the collector,

$$\underline{\mathbf{D}} = D_{\infty} \begin{pmatrix} d_1 & 0 \\ 0 & d_{\perp} \end{pmatrix} \quad (3-24b)$$

where

$$D_{rr} = D_{\infty} d_1 = D_{\infty} f_4; \quad D_{rz} = D_{rz} = 0; \quad D_{zz} = D_{\infty} d_{\perp} = D_{\infty} f_1 \quad (3-24c)$$

The parameters  $f_1$  through  $f_4$  that are used in the above equations represent the universal hydrodynamic correction coefficients that were developed by Brenner [2], Goren and O'Neill [3], Goren [4], and Goldman et al [5]. These coefficients account for the deviations from Stokes flow and Stokes-Einstein equations caused by the presence of the collector surface.

If Equations (3-23) and (3-24b) are substituted into the general convection-diffusion equation, Equation (3-22), explicit expressions for  $j_r$  and  $j_z$  become

$$j_r = v_r f_3 c - D_\infty f_4 \frac{\partial c}{\partial r} + \frac{c}{kT} f_4 D_\infty F_r \quad (3-25a)$$

$$j_z = v_z f_1 f_2 c - D_\infty f_1 \frac{\partial c}{\partial z} + \frac{c D_\infty}{kT} f_1 F_z \quad (3-25b)$$

$F_z$  represents the sum of all external forces acting on the particles in the  $z$  direction: gravitational, van der Waals, electrostatic, and other (such as electromagnetic) forces, or

$$F_z = F_G + F_A + F_R + F_{\text{Other}} \quad (3-26)$$

Because of the experimental conditions, radial diffusion of particles in the stagnation region can be neglected. Substitution of Equations (3-16) into Equations (3-25) yields simplified expressions for  $j_r$  and  $j_z$ :

$$j_r = f_3 \alpha z r c \quad (3-27a)$$

$$j_z = -f_1 f_2 \alpha z^2 c - D_\infty f_1 \frac{dc}{dz} + D_\infty f_1 \frac{F_z}{kT} c \quad (3-27b)$$

The third term from Equation (3-25a) is necessarily zero because  $F_r=0$ . Otherwise, the deposition experiments are not axisymmetric. By defining  $j_r$  and  $j_z$  as shown in Equations (3-27), above, it is possible to rewrite the mass transport continuity equation, Equation (3-21) as

$$2f_3 \alpha z c - \frac{d}{dz}(f_1 f_2 z^2 \alpha c) - D_\infty f_1 \frac{d^2 c}{dz^2} + D_\infty f_1 \frac{F_z}{kT} \frac{dc}{dz} = 0 \quad (3-28)$$

The following dimensionless parameters are used:

$$\bar{c} = \frac{c}{c_0} \quad (3-29a)$$

$$H = \frac{z - a}{a} = \frac{h}{a} \quad (3-29b)$$

$$\overline{F_z} = F_z \frac{a}{kT} \quad (3-29c)$$

$$Pe = \frac{2\alpha a^3}{D_\infty} \quad (3-29d)$$

By multiplying through by  $(a^2/D_\infty c_0)$ , Equation (3-28) becomes

$$\frac{d}{dH} \left[ f_1 \frac{d\bar{c}}{dH} + \frac{1}{2} Pe f_1 f_2 (H + 1)^2 \bar{c} - f_1 \overline{F_z} \bar{c} \right] = Pe f_3 (H + 1) \bar{c} \quad (3-30)$$

subject to the boundary conditions

$$\bar{c} = 1 \quad \text{for } H \rightarrow \infty \quad (3-30a)$$

$$\bar{c} = 0 \quad \text{for } H = \frac{\delta_{pm}}{a} \quad (3-30b)$$

where  $\delta_{pm}$  represents the location of the primary minimum for the particle - collector interaction energy curve.

The solution of Equations (3-30) can be expected to yield an upper limit of the particle flux to the collector surface [17] because of the implications of the second boundary condition, Equation 3-30b. The hypothetical situation described by Equation (3-30b) indicates that the concentration of particles in the bulk flow will be zero once the flow passes through the primary minimum,  $\delta_{pm}$ . The flux is calculated based on the assumption that all particles that pass through the primary minimum attach to the collector surface. In practice, however, not all of the particles do attach to the collector surface.

Equation (3-30), subject to the boundary conditions described by Equations (3-30a) and (3-30b), was solved using a numerical procedure that is described in the next

section.

### 3.5 Development of the numerical model

#### 3.5.1 Numerical method

Equation (3-30) can be written as a system of two first-order ordinary differential equations, by defining the dimensionless flux,  $X$ , as

$$X = f_1 \frac{d\bar{c}}{dH} + \frac{1}{2} Pe f_1 f_2 (H+1)^2 \bar{c} - f_1 \bar{F}_z \bar{c} \quad (3-31)$$

so that Equation (3-30) becomes

$$\frac{dX}{dH} = Pe f_3 (H+1) \bar{c} \quad (3-32a)$$

and

$$\frac{d\bar{c}}{dH} = \frac{X}{f_1} - \frac{1}{2} Pe f_2 (H+1)^2 \bar{c} + \bar{F}_z \bar{c} \quad (3-32b)$$

The boundary conditions for Equation (3-30), described by Equations (3-30a) and (3-30b), are applicable to Equations (3-32). One additional boundary condition is necessary:

$$X = X_0 \quad \text{for} \quad H = \frac{\delta_{pm}}{a} \quad (3-33)$$

where  $X_0$  represents the dimensionless flux at the collector surface. In other words,

$$X_0 = Sh \quad (3-34)$$

It should be noted that  $X_0$  is defined at  $H = \delta_{pm}/a$  rather than at  $H = 0$  (the collector surface) to avoid difficulties with undefined terms in Equations (3-32) when  $H = 0$ .

For most solutions, the nondimensional primary minimum is generally located near  $H = 0.001$ , except when  $Re > 1500$ , in which case  $H < 0.001$ . As was mentioned in the previous section, defining  $X_0$  at  $H = \delta_{pm}/a$  yields an upper limit for the particle flux at the collector surface.

Equations (3-32), subject to the boundary conditions described by Equations (3-30a), (3-30b), and (3-33), were solved using a 4<sup>th</sup> order Runge-Kutta technique with a variable step size. The dimensionless flux at the collector surface,  $X_0$ , was determined using a method described by Prieve and Lin [10]. In this method, the boundary condition given by Equation (3-33), where  $X = X_0$  at  $H = \delta_{pm}/a$ , is initially satisfied by assigning an arbitrary value to  $X_0$ , represented here by  $X_0'$ . The solution of Equations (3-32) yields a value of the bulk concentration,  $\bar{c}'$ , for  $H \rightarrow \infty$ , that corresponds directly to the value assigned to  $X_0'$ . It is known from Equation (3-30a) that  $\bar{c} = 1$  for  $H \rightarrow \infty$ . Recognizing that Equations (3-32a) and (3-32b) are linear, one can determine the actual value of  $X_0$  from  $X_0'$  and  $\bar{c}'$ :

$$\frac{X_0}{\bar{c}} = \frac{X_0'}{\bar{c}'} \quad (3-35)$$

where  $\bar{c} = 1$ , as given by Equation (3-30a).

### 3.5.2 Expressions for external forces

It is assumed that in the systems studied here, the droplets are subjected to dispersion (van der Waals), electrostatic, and gravitational forces only. In order to incorporate these external forces into the numerical model, analytical expressions for each of the three constituent external forces must be developed.

The van der Waals potential between two molecules that are a distance  $h$  apart

has the form [28]

$$\phi_A(h) = - \text{constant} \cdot h^{-6}$$

Hamaker [29] combined all pairwise interactions between molecules to develop analytical expressions for the van der Waals interaction energy between two macroscopic bodies possessing different geometries. The van der Waals interaction energy can be expressed as a combination of a material dependent constant, known as the Hamaker constant, and a geometry dependent integral [27]:

$$\phi_A(h) = - \frac{A}{\pi^2} \int_{V_1} \int_{V_2} h^{-6} dV_1 dV_2 \quad (3-36)$$

where A is the Hamaker constant, h is the separation distance, and  $V_1$  and  $V_2$  are the volumes of the interacting bodies. The van der Waals, or dispersion force, can then be calculated from

$$F_A(h) = - \frac{d \phi_A(h)}{dh} \quad (3-37)$$

In his pioneering work, Hamaker developed analytical expressions for the van der Waals interactions between two spheres of equal and differing radii, and for flat plates. A number of other authors (see Mahanty and Ninham [30] or Israelachvili and Tabor [31], for example) have developed expressions for the attraction potential for other geometries.

In real systems, it is also necessary to account for the effect of the intervening medium and retardation effects. The existence of an intervening medium changes the value of the Hamaker constant, and must therefore be included in the calculation of  $A_{132}$ , the Hamaker constant for bodies 1 and 2 separated by medium 3. The nature of the retardation effect is succinctly described by Israelachvili [32]: "[The] van der Waals interaction is essentially electrostatic, arising from the dipole effect of an atom 'reflected back' by a second atom that has been polarized by this field...".

Israelachvili continues by noting that the time that it takes for the electric field of the first atom to reach the second and be 'reflected back' becomes comparable to the period of the fluctuating dipole of the first atom if the two atoms are separated by an 'appreciable' difference, roughly of the order of nanometers. Thus, by the time the electric field is transmitted back to the first atom, its instantaneous dipole is not the same as it was, and is consequently less likely to have as strong an attractive interaction with the second atom. The retardation effect is accounted for by including a retardation parameter [33], known as  $\lambda$ , in the calculation of the attraction potential between two separated bodies. This term is usually taken to be  $10^{-7}$  m [1,17,27,32], which is the distance travelled by light during one rotation of a Bohr atom electron [32].

The attractive force between a sphere and a flat plate must be calculated in this study. An expression developed by Suzuki [34] has been used to describe the attractive force  $F_A$  between a sphere and a flat plate:

$$F_A = - \frac{A_{132} a}{6} \frac{\lambda (\lambda + 22.232h)}{h^2 (\lambda + 11.116h)^2} \quad (3-38)$$

This expression can be nondimensionalized by multiplying it by  $a/kT$  and using dimensionless expressions for  $h$ , given in Equation (3-29b) and  $\lambda$ , where

$$\bar{\lambda} = \frac{\lambda}{a} \quad (3-39)$$

Thus, the dimensionless attractive force between a particle and the collector surface can be expressed as

$$\bar{F}_A = - A_d \frac{\bar{\lambda} (\bar{\lambda} + 22.232H)}{H^2 (\bar{\lambda} + 11.116H)^2} \quad (3-40)$$

where  $A_d$  is referred to as the Adhesion number and is defined as

$$A_d = \frac{A_{132}}{6kT} \quad (3-41)$$

and  $A_{132}$  is the Hamaker constant for interactions between phases 1 and 2 in medium 3.

The electrostatic interaction energy that occurs between two bodies is a result of the interaction of their so-called double layers. The "double layer" is actually a region immediately surrounding a charged surface where there are a higher number of counterions (ions possessing a charge opposite that of the surface). The electrostatic interaction energy,  $\phi_R$ , between two spheres can be calculated using Derjaguin's approach [27,35], for which

$$\phi_R(h) = \frac{2\pi a_1 a_2}{a_1 + a_2} \int_0^\infty \phi(h) dh \quad (3-42)$$

where  $\phi(h)$  is the interaction energy between two parallel flat plates. This integral was evaluated analytically for two spheres of unequal radii by Hogg, Healy, and Fuerstenau [36] to yield

$$\phi_R = \frac{\epsilon\epsilon_0 a_1 a_2 (\psi_1^2 + \psi_2^2)}{4(a_1 + a_2)} * \left[ \frac{2\psi_1 \psi_2}{(\psi_1^2 + \psi_2^2)} \ln \left( \frac{1 + \exp(-\kappa h)}{1 - \exp(-\kappa h)} \right) + \ln(1 - \exp(-2\kappa h)) \right] \quad (3-43)$$

The interaction between a sphere and a flat plate, where  $a_1$  is the sphere radius and  $a_2 \rightarrow \infty$  is

$$\phi_R = \epsilon\epsilon_0 a_1 (\psi_1^2 + \psi_2^2) \left[ \frac{2\psi_1 \psi_2}{(\psi_1^2 + \psi_2^2)} \ln \left( \frac{1 + \exp(-\kappa h)}{1 - \exp(-\kappa h)} \right) + \ln(1 - \exp(-2\kappa h)) \right] \quad (3-44)$$

Acknowledging that

$$F_R = - \frac{d\phi_R(h)}{dh} \quad (3-45)$$

and assuming that the particle and collector surface potentials can be represented by their zeta potentials ( $\psi_p = \zeta_p$  and  $\psi_c = \zeta_c$ ), the repulsive force between a particle and the collector surface can be expressed as [27]

$$F_R = \epsilon \epsilon_0 a \zeta_c \zeta_p \kappa \left[ \frac{\exp(-\kappa h)}{1 + \exp(-\kappa h)} - \frac{(\zeta_c - \zeta_p)^2}{2 \zeta_c \zeta_p} \frac{\exp(-2\kappa h)}{1 - \exp(-2\kappa h)} \right] \quad (3-46)$$

Equation (3-46) can be nondimensionalized by multiplying by  $a/kT$  and utilizing the definition of dimensionless separation distance from Equation (3-29b),  $H=h/a$ . The resulting equation describing the dimensionless electrostatic force between a particle and the collector surface is

$$\overline{F_R} = Dl \cdot \kappa a \left[ \frac{\exp(-\kappa a H)}{1 + \exp(-\kappa a H)} - Da \frac{\exp(-2 \kappa a H)}{1 - \exp(-2 \kappa a H)} \right] \quad (3-47)$$

where  $Dl$  is the double layer strength parameter and is defined as

$$Dl = \frac{\epsilon \epsilon_0 a \zeta_c \zeta_p}{kT} \quad (3-48a)$$

and  $Da$  is the double layer asymmetry parameter, which is given as

$$Da = \frac{(\zeta_c - \zeta_p)^2}{2 \zeta_c \zeta_p} \quad (3-48b)$$

and represents the portion of electric double layer force attributable to the difference between the surface charge of the collector and that of the particle. The Debye double layer parameter,  $\kappa$ , is defined as

$$\kappa = \left( \frac{1000 e^2 N_A}{\epsilon \epsilon_0 k T} \sum_i q_i^2 M_i \right)^{\frac{1}{2}} \quad (3-49a)$$

where the subscript  $i$  represents each ionic species present in the electrolyte solution and  $M_i$  is the molarity of each ionic species. For a symmetrical  $q:q$  electrolyte, Equation (3-49a) reduces to

$$\kappa = \left[ \frac{2000 e^2 q^2 N_A M}{\epsilon \epsilon_0 k T} \right]^{1/2} \quad (3-49b)$$

It should be noted that Equation (3-47) is the constant potential version of the HHF expression.

Finally, the force exerted on a particle by gravity is [27]

$$F_G = \frac{4}{3} a^3 \Delta \rho g \quad (3-50a)$$

This can be nondimensionalized with respect to the Brownian force,  $F_B$  exerted on a particle:

$$F_B = 6\pi\mu D_\infty \quad (3-50b)$$

The ratio of these forces is referred to as the Gravity number,  $Gr$ , and is given as

$$Gr = \frac{\text{Gravitational force}}{\text{Brownian force}} = \frac{2 \Delta \rho g a^3}{9 \mu D_\infty} \quad (3-51)$$

In this particular experimental set up, gravity acts against the deposition process, as the particles are flowing upward toward the collector. For the emulsions studied here, the gravity force is orders of magnitude smaller than the hydrodynamic force and is therefore neglected.

Equations (3-40), (3-47) and (3-51) show that the magnitude of the external

force is dependent upon the values of  $A_d$ ,  $\zeta_c$ ,  $\zeta_p$ ,  $\kappa a$ ,  $Da$ , and  $Gr$ .

### 3.5.3 Prediction of Hamaker constant using Lifshitz theory

Hamaker's predictions of van der Waals interactions were based on his assumptions that the interactions were nonretarded and additive. Retardation effects have already been discussed in the previous section. The assumption of additivity suggests that the van der Waals interactions between two macroscopic bodies are equal to the sum of the interactions between every pair of interacting atoms between the two bodies. Unfortunately, the calculation of van der Waals interactions is not nearly this simple. As Israelachvili [32] states, every pairwise interaction is affected by neighboring atoms. Thus, for macroscopic bodies, the effects of neighboring atom dipoles and multiple reflected electric fields make it almost impossible to evaluate pairwise interactions accurately.

Lifshitz theory, developed by Lifshitz in 1956, can be used to calculate van der Waals interactions between two macroscopic bodies based on bulk properties of the bodies and the properties of the intervening medium. In fact, since the geometric part of the van der Waals interaction remains unchanged from Hamaker's calculation method, the Lifshitz theory is actually used to calculate the Hamaker constant for any system where bodies 1 and 2 are separated by medium 3.

Rigorous application of Lifshitz theory requires knowledge of the variation of a material's dielectric permittivity with frequency, ranging from zero frequency permittivity to the UV frequency permittivity. The zero frequency permittivity is known as the dielectric constant of the material. For example,  $\epsilon(\nu=0) = 78.3$  for water at 25 °C [27]. Such extensive knowledge of quantum field theory, combined with a general lack of availability of such information, dissuaded most researchers from using this technique. However, the rigorous Lifshitz theory was greatly simplified by a number of researchers (see [30] and [31] for excellent reviews of this research). One of the simplest Lifshitz calculations, the modified additivity approach,

is discussed by Israelachvili [32]. He follows a series of arguments to show that the Hamaker constant,  $A_{132}$ , can be defined as

$$A_{132} = A_{132} \Big|_{v=0} + A_{132} \Big|_{v>0} \quad (3-52)$$

Israelachvili continues his analysis by showing that, to a good approximation, the contribution of the second term in Equation (3-52) can be evaluated at a single frequency, instead of being evaluated over a range of frequencies, as it would be using rigorous Lifshitz theory. The frequency of visible light is purposely chosen as the single frequency, specifically because  $\varepsilon(v=\text{visible}) = n^2$ , where  $n$  is the material's refractive index. This simplification is introduced to the general expression for  $A_{132}$  in Lifshitz theory, which is given as

$$A_{132} = \frac{3}{2}kT \sum_{n=0,1,\dots}^{\infty} \left[ \frac{\varepsilon_1(iv_n) - \varepsilon_3(iv_n)}{\varepsilon_1(iv_n) + \varepsilon_3(iv_n)} \right] \left[ \frac{\varepsilon_2(iv_n) - \varepsilon_3(iv_n)}{\varepsilon_2(iv_n) + \varepsilon_3(iv_n)} \right] \quad (3-53)$$

It can be shown that, using the appropriate substitutions and integration technique, the simplified version of Equation (3-53) is

$$A_{132} \approx \frac{3}{4}kT \left( \frac{\varepsilon_1 - \varepsilon_3}{\varepsilon_1 + \varepsilon_3} \right) \left( \frac{\varepsilon_2 - \varepsilon_3}{\varepsilon_2 + \varepsilon_3} \right) + \frac{3\hbar v_e (n_1^2 - n_3^2)(n_2^2 - n_3^2)}{8\sqrt{2} (n_1^2 + n_3^2)^{1/2} (n_2^2 + n_3^2)^{1/2} [(n_1^2 + n_3^2)^{1/2} + (n_2^2 + n_3^2)^{1/2}]} \quad (3-54)$$

Equation (3-54) expresses the nonretarded Hamaker constant for phases 1 and 2 across a medium 3, based on the dielectric constants and refractive indices of the three phases.

### 3.5.4 Prediction of $\zeta_c$ and $\zeta_p$ using the ISG Model

The Ionizable Surface Group (ISG) Model was initially developed to predict the electric double layer properties of inorganic oxides, clays, polymer latex colloids and biosurfaces, and was subsequently adapted by Takamura and Chow [37] to apply to bitumen, as well as those of glass or silica surfaces. This model can be used to predict the zeta potentials of bitumen and the glass collector surface in aqueous solutions at any pH and salt concentration.

The ISG model was developed as follows. First, the  $\psi_0$  -  $\text{pH}_b$  relationship is expressed as [37]

$$\text{pH}_b = \frac{-y_0}{2.303} + \text{pK}_a - \log \left[ \frac{\theta}{\sinh\left(\frac{qy_0}{2}\right)} - 1 \right] \quad (3-55)$$

where

$$y_0 = \frac{e\psi_0}{kT} \quad (3-56a)$$

and

$$\theta = \frac{-eN_s}{(8n_c\epsilon\epsilon_0kT)^{1/2}} \quad (3-56b)$$

The variable  $n_c$  in the above equation represents the number of counterions per unit volume and is related to the bulk salt concentration by

$$n_c = 1000[\text{salt}]N_A$$

where  $N_A$  is Avogadro's number. The dissociation constant for the active surface group is represented by  $\text{pK}_a$  in Equation (3-55), and  $N_s$  represents the total surface density of functional groups. Values of  $\text{pK}_a$  and  $N_s$  for bitumen were determined experimentally by Takamura and Chow [37]. Equations (3-55) and (3-56) were solved using a

method described by Healy and White [38]. The surface potential,  $\psi_0$ , is obtained as a function of bulk pH and salt concentration from the solution of Equations (3-55) and (3-56). The zeta potential is then calculated by assuming that

$$\zeta = \psi(x_s) \quad (3-57)$$

where  $x_s$  represents the location of the shear plane.  $\psi(x)$  is determined from the following expression:

$$\psi(x) = \frac{2kT}{eq} \ln \left( \frac{1 + \gamma_0 \exp(-\kappa x)}{1 - \gamma_0 \exp(-\kappa x)} \right) \quad (3-58)$$

where

$$\gamma_0 = \frac{\exp\left(\frac{qy_0}{2}\right) - 1}{\exp\left(\frac{qy_0}{2}\right) + 1} \quad (3-59)$$

By using an iterative procedure to solve the  $\psi_0$  - pH<sub>b</sub> relationship and then another to solve Equations (3-58) and (3-59), it is possible to calculate the zeta potential of bitumen as a function of bulk pH and salt concentration (and valence number).

A similar procedure was used to predict the zeta potential of the glass slide as a function of bulk pH and salt concentration. The three parameter ISG model described above was used to predict the glass zeta potentials because of its simplicity and relative accuracy. There are more complex dissociation models (see, for example, Buckley and Takamura [39]), but this model does provide reasonable predictions of the collector zeta potential as a function of pH and electrolyte concentration (see Figure 6-3).

This calculation scheme was incorporated in the numerical solution of the governing mass transfer equations (Section 3.5.1) so that the double layer force expression would be based upon accurate values of the glass and bitumen zeta

potential.

### 3.5.5 Analytical expressions for the universal hydrodynamic correction coefficients (UHCC's)

The UHCC's  $f_i$  ( $i=1,3$ ), used in the solution to the governing mass transfer equations, are given in tabular form by Brenner [2], Goren and O'Neill [3], Goren [4], and Goldman *et al.* [5]. In order to incorporate their values directly into the numerical model, it was advantageous to curve fit each of the UHCC's so that they could be represented by analytical equations that would provide values of the coefficients as a function of dimensionless droplet - collector separation distance,  $H$ . The results of these curve fits are:

$$f_1 = 1.00 + A_1 \exp(-B_1 H) + C_1 \exp(-D_1 H^{0.75}) \quad (3-60a)$$

$$f_2 = 1.00 + A_2 \exp(-B_2 H) + C_2 \exp(-D_2 H^{0.50}) \quad (3-60b)$$

$$f_3 = 1.00 + A_3 \exp(-B_3 H) + C_3 \exp(-D_3 H^{0.50}) \quad (3-60c)$$

Table 3-2, below, lists the values for constants  $A_i$  through  $D_i$  for each of the hydrodynamic correction coefficients. Curves for each of the coefficients  $f_1$ ,  $f_2$ , and  $f_3$  are shown in Figure 3-3.

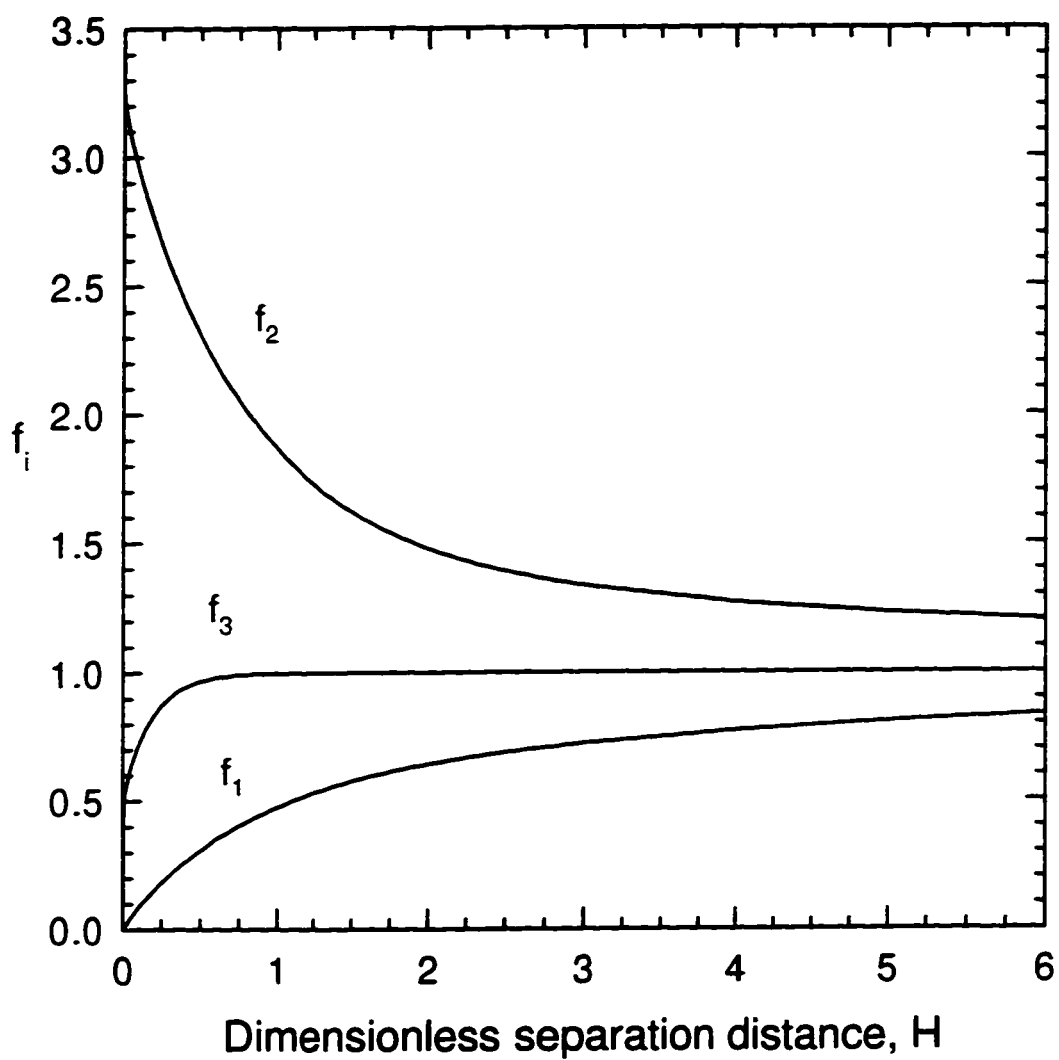


**Figure 3-3.** Variation of universal hydrodynamic correction coefficients (UHCC's),  $f_i$  ( $i=1,2,3$ ), with dimensionless separation distance between a sphere and a planar surface.

**Table 3-2.** Curve - fitted coefficients for the hydrodynamic correction coefficients  $f_1, f_2, f_3$ .

i	$A_i$	$B_i$	$C_i$	$D_i$
1	-0.4432	1.299	-0.5568	0.3198
2	1.455	1.259	0.7951	0.5597
3	-0.4873	5.423	-0.5905	37.83

### 3.5.6 Summary: list of equations

The numerical model, designed to calculate the theoretical rates of droplet attachment to the collector surface in an impinging jet cell, is based upon a flux balance and the general convection-diffusion equation, defined as:

$$\frac{1}{r} \frac{\partial}{\partial r}(r j_r) + \frac{\partial j_z}{\partial z} = 0 \quad (3-21)$$

and

$$j = u \cdot c - \underline{D} \cdot \nabla c + \frac{c}{kT} \underline{D} \cdot \underline{F} \quad (3-22)$$

The numerical model is developed through the incorporation of the following relationships in Equations (3-21) and (3-22):

$$u_r = v_r f_3 \quad (3-23a)$$

$$u_z = v_z f_1 f_2 \quad (3-23b)$$

$$D_{\pi} = D_{\infty} d_1 = D_{\infty} f_4; \quad D_{zx} = D_{xz} = 0; \quad D_{zz} = D_{\infty} d_{\perp} = D_{\infty} f_1 \quad (3-24c)$$

The resulting equation is non-dimensionalized and rewritten as a system of two first-order ordinary differential equations, so that the dimensionless particle flux to the collector surface, expressed as  $X_0$  or  $Sh$ , is determined by solving

$$\frac{dX}{dH} = Pe f_3 (H+1) \bar{c} \quad (3-32a)$$

and

$$\frac{d\bar{c}}{dH} = \frac{X}{f_1} - \frac{1}{2} Pe f_2 (H+1)^2 \bar{c} + \bar{F}_z \bar{c} \quad (3-32b)$$

subject to the boundary conditions

$$\bar{c} = 1 \quad \text{for } H \rightarrow \infty \quad (3-30a)$$

$$\bar{c} = 0 \quad \text{for } H = \frac{\delta_{pm}}{a} \quad (3-30b)$$

$$X = X_0 \quad \text{for } H = \frac{\delta_{pm}}{a} \quad (3-33)$$

where  $\delta_{pm}$  represents the location of the primary minimum for the particle - collector interaction energy curve and  $X_0$  represents the dimensionless flux at the collector surface. These equations are solved using a 4<sup>th</sup> order Runge-Kutta technique. An arbitrary value of  $X_0$ , denoted  $X_0'$ , is used to determine a corresponding value of the bulk concentration,  $\bar{c}'$ , for  $H \rightarrow \infty$ . Since Equations (3-32a) and (3-32b) are linear, the actual value of  $X_0$  is determined from

$$\frac{X_0}{\bar{c}} = \frac{X'_0}{\bar{c}'} \quad (3-35)$$

where  $\bar{c} = 1$ , as given by Equation (3-30a).

The following parameters are required for the numerical model of mass transfer of emulsion droplets to a collector surface in an impinging jet cell: droplet radius ( $a$ ), dimensionless capillary exit - collector surface separation distance ( $\bar{h}_0$ ), Reynolds number ( $Re$ ), Hamaker constant ( $A_{132}$ ), electrolyte concentration ( $M_i$ ) and valency ( $q_i$ ). The particle and collector zeta potentials,  $\zeta_p$  and  $\zeta_c$ , are also required. They can be taken directly from experimental measurements or calculated from the ISG model (discussed in Section 3.5.4). The Peclet number,  $Pe$ , which appears in Equations (3-32), is calculated from the values of  $a$ ,  $\bar{h}_0$ , and  $Re$ . The dimensionless external force term,  $\bar{F}_z$ , which appears in Equation (3-32b), is calculated from the values of  $a$ ,  $A_{132}$ ,  $\zeta_p$ ,  $\zeta_c$ ,  $M_i$ , and  $q_i$ .

The Peclet number is defined as

$$Pe = \frac{2\alpha a^3}{D_x} \quad (3-29d)$$

where

$$\alpha = \bar{\alpha} \frac{U}{R^2} \quad (3-61)$$

The term  $\bar{\alpha}$  represents the strength of stagnation point flow and is a function of Reynolds number and dimensionless capillary exit - collector surface separation distance,  $\bar{h}_0$ . The expression for  $\bar{\alpha}$  is

$$\bar{\alpha} = A Re^{1/2}$$

where A is determined by solving the governing Navier-Stokes equations, as discussed in Section 3.2.

The dimensionless external force term,  $\bar{F}_z$ , represents the sum of the dispersion (van der Waals) force,  $\bar{F}_A$ , and the electrostatic force,  $\bar{F}_R$ , acting between a droplet and the collector:

$$\bar{F}_z = \bar{F}_A + \bar{F}_R$$

The dimensionless van der Waals force that occurs between a droplet and the collector is given by

$$\bar{F}_A = -A_d \frac{\bar{\lambda} (\bar{\lambda} + 22.232H)}{H^2 (\bar{\lambda} + 11.116H)^2} \quad (3-40)$$

where  $\bar{\lambda} = \lambda/a$  and  $A_d$  is referred to as the Adhesion number and is defined as

$$A_d = \frac{A_{132}}{6kT} \quad (3-41)$$

The dimensionless electrostatic force that occurs between a droplet and the collector surface is

$$\bar{F}_R = Dl \cdot \kappa a \left[ \frac{\exp(-\kappa a H)}{1 + \exp(-\kappa a H)} - Da \frac{\exp(-2\kappa a H)}{1 - \exp(-2\kappa a H)} \right] \quad (3-47)$$

where  $DI$  is the double layer strength parameter and is defined as

$$DI = \frac{\epsilon \epsilon_0 a \zeta_c \zeta_p}{kT} \quad (3-48a)$$

and  $Da$  is the double layer asymmetry parameter, which is given as

$$Da = \frac{(\zeta_c - \zeta_p)^2}{2\zeta_c \zeta_p} \quad (3-48b)$$

and represents the portion of electric double layer force attributable to the difference between the surface charge of the collector and that of the particle. The Debye double layer parameter,  $\kappa$ , is defined as

$$\kappa = \left( \frac{1000 e^2 N_A}{\epsilon \epsilon_0 k T} \sum_i q_i^2 M_i \right)^{\frac{1}{2}} \quad (3-49a)$$

The numerical model thus provides theoretical values of Sherwood number as a function of  $a$ ,  $\bar{h}_0$ ,  $Re$ ,  $A_{132}$ ,  $\zeta_p$ ,  $\zeta_c$ ,  $M_i$ , and  $q_i$ .

### 3.6 Application of DLVO theory to nonaqueous suspensions

The body of work that discusses the application of DLVO theory to nonaqueous suspension behavior is very small compared with that which relates DLVO theory to aqueous systems. There are a number of excellent review articles that trace the history of nonaqueous studies. The reader is referred specifically to articles by van der Hoeven and Lyklema [40] and Morrison [41], both of which cover developments in nonaqueous suspension research since the seminal review written by Parfitt and Peacock [42] in 1978.

The theoretical treatment of deposition behavior discussed in this chapter does not change when nonaqueous suspensions are considered. In fact, the governing flow field and mass transfer equations remain exactly the same, DLVO theory is used to describe the attractive and repulsive interactions between a particle and the collector surface, and Lifshitz theory is still used to predict the Hamaker constants for the nonaqueous systems under study. There clearly will be slight differences in some of the parameters, caused almost entirely by changing the continuous phase and thereby altering the Reynolds number, Peclet number, and the bulk diffusion coefficient. The significant difference lies in the relative contributions of the attractive and repulsive forces defined by Equations (3-38) and (3-46), respectively. As van der Hoeven and Lyklema point out, any electrolyte present in a nonaqueous, low polar media will be poorly dissociated. This results in a low ionic strength, and therefore in a small value of  $\kappa$ , the Debye length parameter. Since  $\kappa$  is quite small, the Debye double layer thickness ( $\kappa^{-1}$ ) can be very large, often exceeding 1  $\mu\text{m}$  [40], which is at least three orders larger than it would be for an aqueous system. Figure 3-4 illustrates the effect of dielectric constant on the Debye double layer thickness. For the highest electrolyte concentration shown in Figure 3-4,  $\kappa^{-1}$  is at least two orders of magnitude larger than it would be in an aqueous system with a similar electrolyte concentration. As Figure 3-4 shows, the dielectric constant must be greater than 5 before the double layer is sufficiently compressed to provide any significant repulsive force. Extended double layers that are 100 nm or larger in size provide almost no electrostatic stabilization. As a result, there would be no electrostatic barrier to prevent particle attachment if deposition experiments were conducted using a continuous phase with a low dielectric constant.

In Figure 3-4, the Debye length,  $\kappa^{-1}$ , is calculated using bulk electrolyte concentrations of  $m_0 = 0.01\text{M}$ ,  $0.05\text{M}$ , and  $0.12\text{M}$ . Effective electrolyte concentrations, denoted  $m_i$ , are not this large, as electrolyte dissociation is notoriously incomplete when the continuous phase dielectric constant is less than 10, so that  $m_i < m_0$ . The actual extent of electrolyte dissociation can be derived from ion pair formation theory [40,43]. Values of effective electrolyte concentration,  $m_i$ , for a

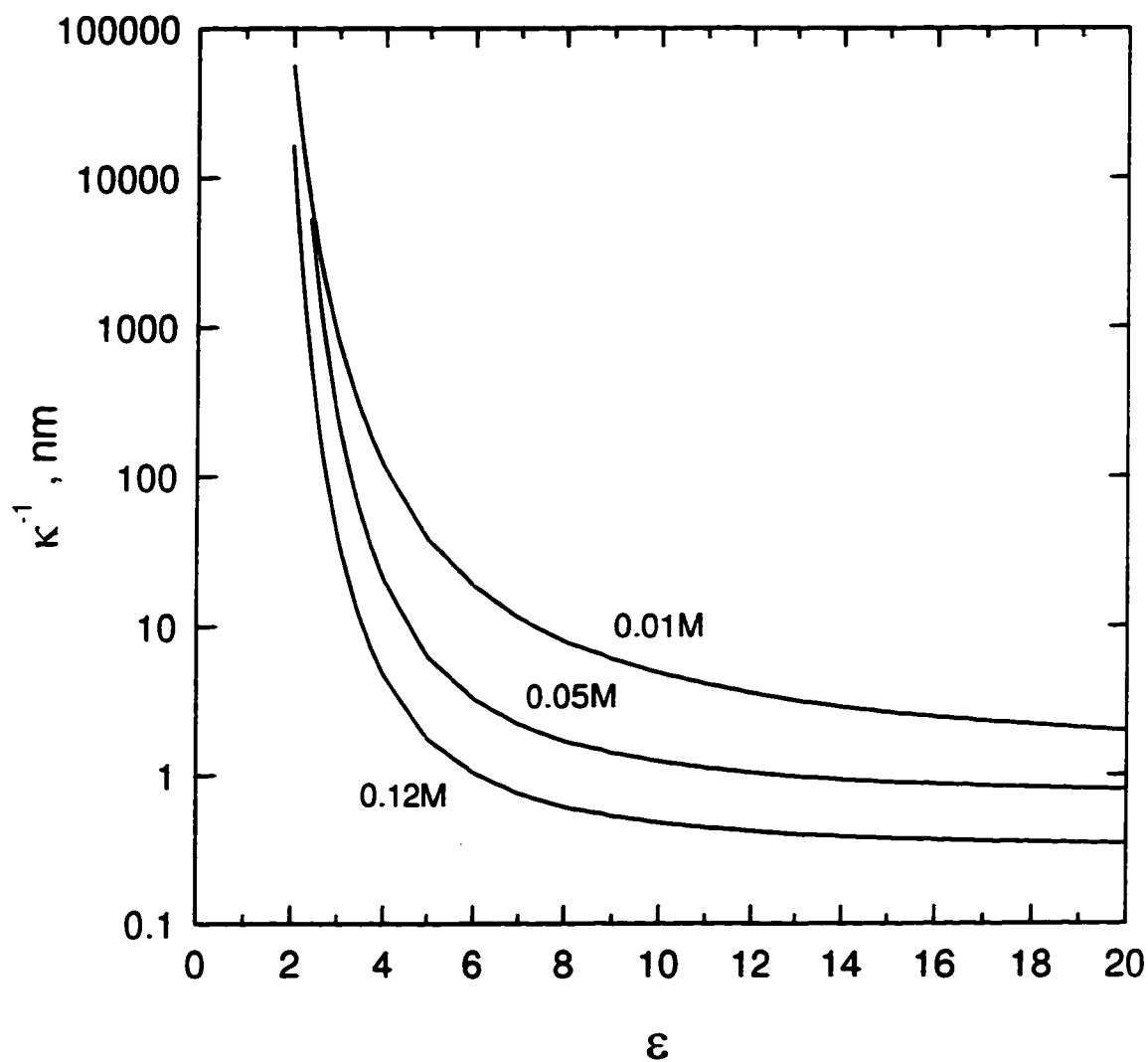


**Figure 3-4.** Debye length,  $\kappa^{-1}$ , as a function of dielectric constant,  $\epsilon$ , for bulk 1:1 electrolyte concentrations,  $m_0$ , as shown. Values of  $\kappa^{-1}$  calculated from Equation (3-49b), with  $T=298$  K, and effective electrolyte concentrations,  $m_i = m_i(\epsilon, m_0)$ , determined using Fuoss' theory [40,43].

**Table 3-3. Effective concentration of a 1:1 electrolyte in nonaqueous media, for a bulk electrolyte concentration of  $m_0=0.001$  M.**

$\epsilon$	$m_i$ (mol/L)
2.3	$1 \times 10^{-10}$
6	$8.4 \times 10^{-5}$
10	$9.7 \times 10^{-4}$

bulk concentration of  $m_0 = 0.001$ M, as reported by van der Hoeven and Lyklema [40], are shown in Table 3-3. As Table 3-3 illustrates, the lack of electrolyte dissociation in low polar (low permittivity) media is the main reason for the occurrence of the extended double layers shown in Figure 3-4.

Figure 3-5 shows the effect of continuous phase dielectric constant on the particle - collector electrostatic force, calculated using Equation (3-46). The electrostatic force is calculated for a range of dielectric constants, as shown in Figure 3-5, with  $a=0.5 \mu\text{m}$ ,  $\zeta_p = -60$  mV,  $\zeta_c = -50$  mV, and a bulk electrolyte concentration of 0.001M, so that the effective electrolyte concentrations,  $m_i$ , are the same as those listed in Table 3-3. The inset graph of Figure 3-5 shows the van der Waals force of interaction between a particle and a collector, calculated using Equation (3-38), with  $a=0.5 \mu\text{m}$ ,  $A_{132} = 10^{-21}$  J, and  $\lambda=10^{-7}$  m. For a hypothetical nonaqueous system that has a continuous phase dielectric constant of 2.3, represented by the solid line in Figure 3-5, the repulsive force,  $F_R$ , barely registers above zero. Compared with the attractive force shown in the inset graph, it is evident that this system could not be stabilized by electrostatic forces. The first dashed line in Figure 3-5 represents a system with  $\epsilon=6$ . The maximum electrostatic force in this system is nearly  $4 \times 10^{-12}$  N, or 4 pN, which is once again considerably smaller than the maximum van der

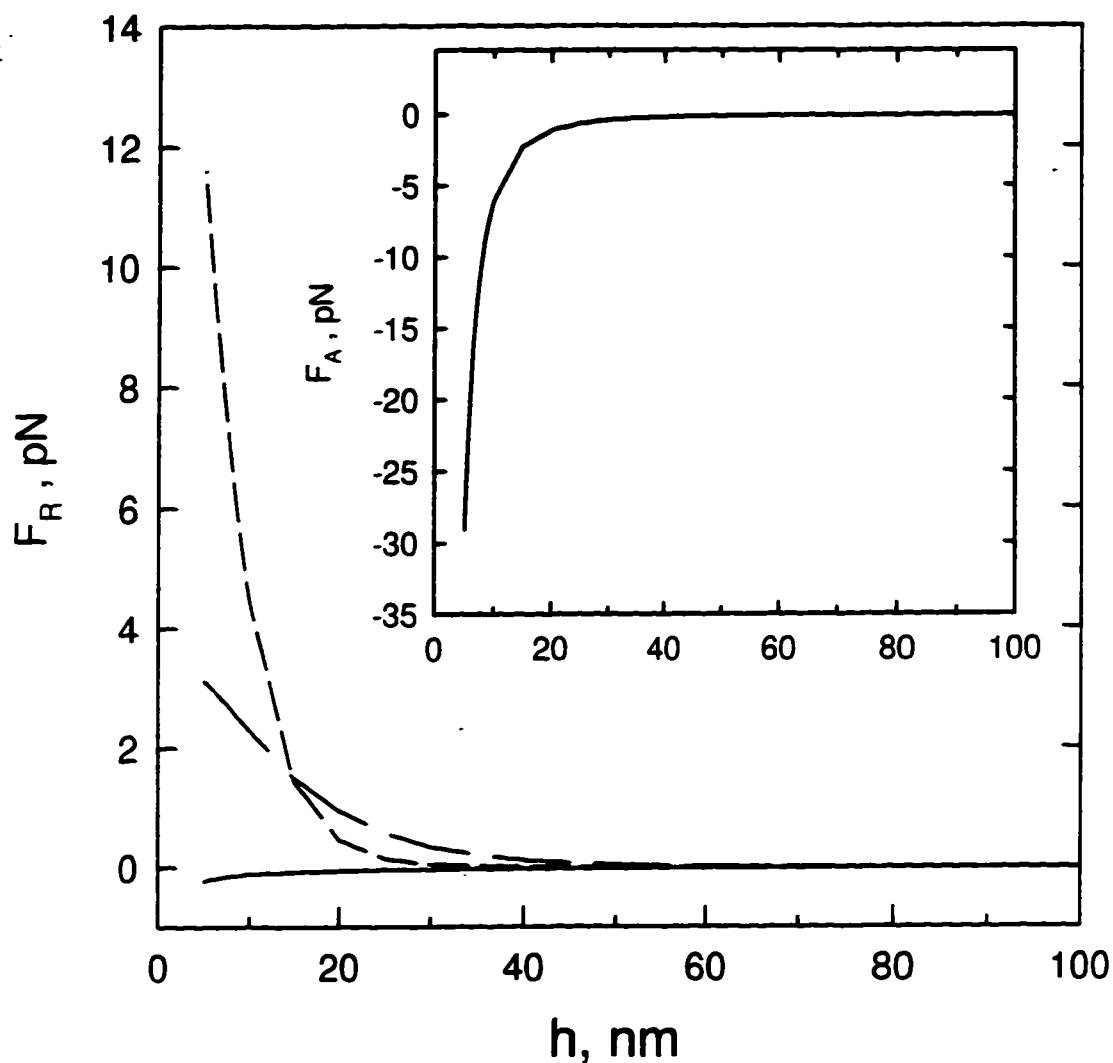


**Figure 3-5.** Effect of continuous phase dielectric constant,  $\epsilon$ , on the electrostatic force,  $F_R$ , between a droplet and the collector separated by a nonaqueous phase, with  $a=0.5 \mu\text{m}$ ,  $\zeta_p=-60 \text{ mV}$ ,  $\zeta_c=-50 \text{ mV}$  and a bulk electrolyte concentration of  $0.001 \text{ M}$ . (—)  $\epsilon=2.3$ ; (— —)  $\epsilon=6$ ; (— — —)  $\epsilon=15$ . Inset shows typical van der Waals force,  $F_A$ , for a nonaqueous system, with  $a=0.5 \mu\text{m}$ ,  $A_{132}=10^{-21} \text{ J}$ , and  $\lambda=10^{-7} \text{ m}$ .

Waals attractive force that would occur between a particle and the collector surface in this situation. Even the maximum repulsive force that occurs when  $\epsilon=15$  is less than half as large as the van der Waals attractive force. Figure 3-5 illustrates the degree of difficulty involved in stabilizing a nonaqueous suspension using electrostatic interactions, even when the particle and collector  $\zeta$ -potentials are quite large.

The relevance of this discussion is as follows: for the nonaqueous system studied here, it can be assumed that as long as the dielectric constant of the continuous phase is less than 6, the electrostatic force between a droplet and the collector is negligible, especially if no electrolyte is added to the system. As a result, the magnitude of the droplet  $\zeta$ -potential is irrelevant, and the total interaction between a droplet and the collector is equal to the van der Waals interactions only (since gravity forces are also negligible).

### 3.7 Sensitivity analysis

In this section, the sensitivity of the numerical model to changes in particle radius ( $a$ ), Adhesion number ( $Ad$ ), and double layer strength ( $DI$ ) is analyzed. A model system is used to illustrate the effect that each of these parameters has on the predicted values of Sherwood number. The model system is characterized by the following parameters:

$$\begin{aligned} a &= 0.5 \text{ } \mu\text{m} \quad (D_x = 4.367 \times 10^{-13} \text{ m}^2/\text{s}); \\ \bar{h}_0 &= 2.59; \\ Ad &= 0.1; \\ DI &= 0; \\ Da &= 0.1; \\ M_i &= 0.01\text{M (1:1 electrolyte, } q = 1); \\ \lambda &= 10^{-7} \text{ m}; \\ Gr &= 0. \end{aligned}$$

using three different values of  $a$  in the model while keeping the rest of the parameters constant. Particle radii of 0.25, 0.5 and 1.0  $\mu\text{m}$  are used in the model.

The effect of Adhesion number on predicted values of Sherwood number is analyzed by assigning values of  $Ad = 0.05, 0.1$  and  $1.0$ . The other parameters ( $a$ ,  $DI$ ,  $Da$ , and  $M_i$ ) remain constant.

Finally, the effect of particle and/or collector zeta potential variation is studied by changing the value of  $DI$  that is used in the model. Since the effect of the particle and collector surface charges (and therefore the effect of  $DI$ ) is highly dependent upon electrolyte concentration, the variation of Sherwood number with double layer strength is shown for electrolyte concentrations of  $0.01\text{M}$  and  $0.1\text{M}$ .

The sensitivity analysis shows that particle size has the most dramatic effect on the predicted mass transfer rates, as long as  $DI$  is less than a critical value that changes with electrolyte concentration.

### 3.7.1 Effect of particle radius

Figure 3-6 shows the predicted variation of Sherwood number with Reynolds number for 3 different values of particle radius:  $a = 0.25, 0.5$ , and  $1.0 \mu\text{m}$ . The results that correspond to  $a = 1.0 \mu\text{m}$  are nearly an order of magnitude larger than the results obtained for  $a = 0.5 \mu\text{m}$ ; similarly, the results of the  $a = 0.25 \mu\text{m}$  simulation are nearly an order of magnitude smaller than the results obtained for  $a = 0.5 \mu\text{m}$ . These results indicate that the numerical model is very sensitive to particle radius: a two-fold increase in particle size results in an eight-fold increase (approximately) in mass transfer rates.

The implications of the model's sensitivity to particle size are dramatic: first, the particle size must be accurately known, or else both theoretical predictions and experimental results will be erroneous. Second, the particle size distribution of any suspension used in deposition experiments should be very narrow. If it is not, a wide

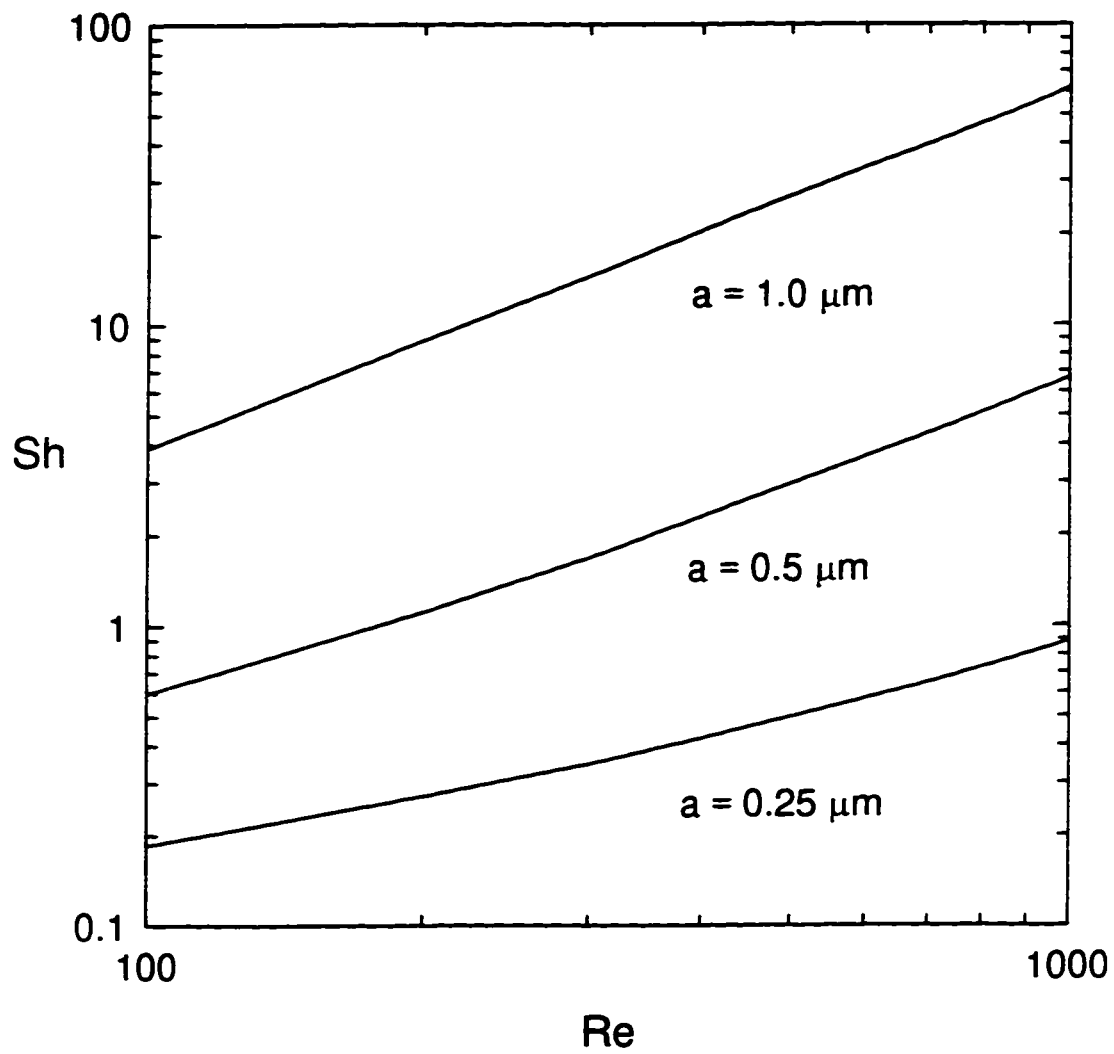


**Figure 3-6.** Predicted variation of Sherwood number with particle radius for the model system described by:  $\bar{h}_0 = 2.59$ ;  $Ad = 0.1$ ;  $DI = 0$ ;  $M_i = 0.01M$ ;  $q = 1$ ;  $Gr = 0$ .

range of mass transfer rates will be observed.

### **3.7.2 Effect of Adhesion number**

The Adhesion number can be considered to be a dimensionless Hamaker constant {see Equation (3-41)} and is therefore directly related to the strength of the van der Waals interaction between a particle and the collector. In essence, the sensitivity of the numerical model to changes in Adhesion number illustrates the degree to which uncertainty in the calculation of Hamaker constant is important: if small changes in Adhesion number cause large changes in calculated values of Sherwood number, then we must be very rigorous in calculating the Hamaker constants for the different systems studied here.

The variation of Sherwood number with Adhesion number is shown in Figure 3-7, for three different values of  $Ad$  ( $Ad = 0.05, 0.1$  and  $1.0$ ). As Figure 3-7 shows, an increase in Adhesion number from  $Ad = 0.05$  to  $Ad = 0.1$  has a negligible effect on the predicted mass transfer rates. In fact, the Sherwood number increases by less than 15% when the Adhesion number is doubled for any given value of Reynolds number. When the Adhesion number is increased to  $Ad = 1.0$  from  $Ad = 0.1$ , the Sherwood number increases by approximately 40%.

These results show that particle deposition rates are not sensitive to the value of the Adhesion number.

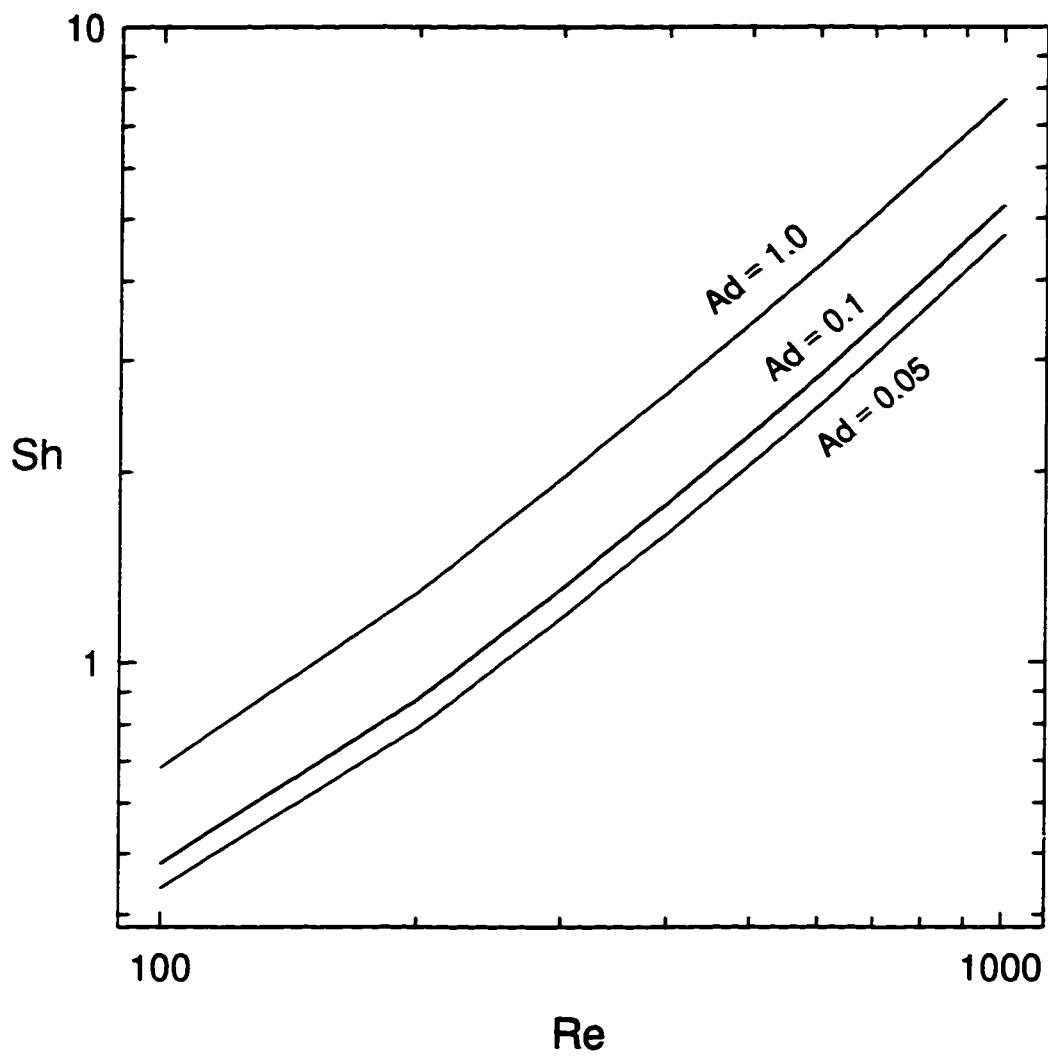


**Figure 3-7.** Predicted variation of Sherwood number with Adhesion number for the model system described by:  $a = 0.5 \mu\text{m}$ ;  $\bar{h}_0 = 2.59$ ;  $DI = 0$ ;  $M_i = 0.01M$ ;  $q = 1$ ;  $Gr = 0$ .

### 3.7.3 Effect of double layer strength

The double layer strength parameter,  $Dl$ , is related to the particle and collector zeta potentials:

$$Dl = \frac{\epsilon \epsilon_0 a \zeta_c \zeta_p}{kT} \quad (3-48a)$$

and is a direct measure of the strength of the electrostatic force between a particle and the collector. The effect that  $Dl$  will have on particle deposition rates is highly dependent upon the bulk electrolyte concentration. If the electrolyte concentration is low (0.001M, for example), then relatively small values of  $Dl$  will affect mass transfer rates. If the electrolyte concentration is greater than 0.1M, even large values of  $Dl$  would not be expected to affect droplet deposition rates. To illustrate this point, the effect of changes in the double layer strength parameter on predicted mass transfer rates was studied for two different concentrations of a 1:1 electrolyte ( $M_i = 0.01M$  and  $0.1M$ ).

Figure 3-8a shows the variation in Sherwood number with double layer strength for a 0.01M, 1:1 electrolyte at a constant Reynolds number ( $Re = 100$ ). The Sherwood number is constant ( $Sh = 0.594$ ) for  $Dl < 145$ . However, the Sherwood number decreases sharply when  $Dl > 160$ , and when  $Dl = 190$ ,  $Sh = 0.004$ . The results can be interpreted as follows: if  $Dl < Dl_{cr}$ , where  $Dl_{cr}$  represents the *critical* value of  $Dl$ , then changes in the double layer strength have no effect on the mass transfer rate. If  $Dl > Dl_{cr}$ , then changes in the double layer strength parameter will have a dramatic effect on droplet deposition rates.

The variation of Sherwood number with double layer strength in a 0.1M solution of 1:1 electrolyte, for  $Re = 100$ , is shown in Figure 3-8b. The curve shown in Figure 3-8b is similar to the curve shown in Figure 3-8a, meaning that any value of  $Dl < Dl_{cr}$  will not affect droplet deposition rates, while any change in  $Dl$ , where  $Dl > Dl_{cr}$ , will have a dramatic effect on the rate of mass transfer. The results shown in Figure 3-8b indicate that  $Dl_{cr} = 535$  for a system with a 1:1 electrolyte concentration

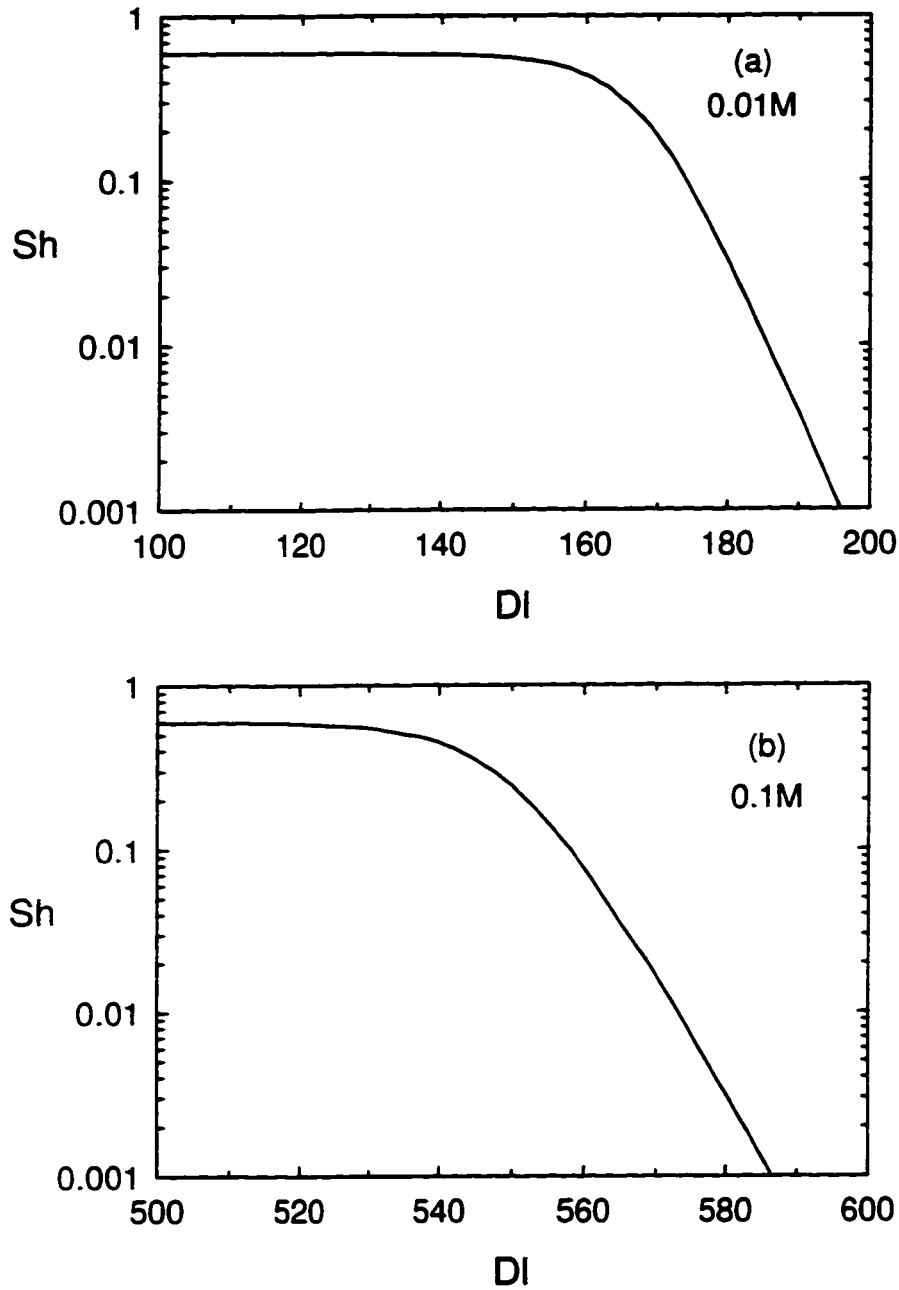


**Figure 3-8.** Predicted variation of Sherwood number with double layer strength for the model system described by:  $a = 0.5 \mu\text{m}$ ;  $\bar{h}_0 = 2.59$ ;  $Ad = 0.1$ ;  $Da = 0.1$ ;  $q = 1$ ;  $Gr = 0$ . (a)  $M_i = 0.01M$ ; (b)  $M_i = 0.1M$ .

of 0.1M.

### 3.7.4 Summary

Figures 3-6, 3-7, and 3-8 show the sensitivity of the numerical model (and therefore the sensitivity of the deposition experiments) to changes in particle size, Adhesion number, and double layer strength, respectively. It is evident from this analysis that changes in particle size have the most significant effect on predicted rates of droplet deposition, as long as  $DI < DI_{cr}$ . If the particle size is doubled, the mass transfer rates can be expected to increase by a factor of 10 (approximately). If the Adhesion number is doubled, the mass transfer rates will increase by approximately 15%. The effect of the double layer strength parameter is slightly more complex, as it is strongly dependent upon electrolyte concentration: at any given electrolyte concentration, a critical value of  $DI$ ,  $DI_{cr}$ , will exist. For  $DI < DI_{cr}$ , no change in Sherwood number will be observed with a change in  $DI$ . When  $DI > DI_{cr}$ , a change in  $DI$  could change the Sherwood number by 3 orders of magnitude.

## **4. Numerical model validation and testing of experimental apparatus**

It was necessary to test the numerical model and the experimental apparatus before proceeding with any new research. The impinging jet cell was tested by replicating experiments for which results had been published previously. The results obtained using the numerical model were validated by comparing them with results reported in the literature. The following sections describe the results of the verification tests.

### **4.1 Review of previous studies**

Studies of latex particle deposition conducted by Dabros and van de Ven [1,17] were the first results obtained using an impinging jet cell. In both studies, Dabros and van de Ven report the results of impinging jet experiments conducted using micron size polystyrene latex particles suspended in water. The results obtained in the first study showed the variation of the rate of mass transfer of the latex particles to the collector surface with Reynolds number, for values of Reynolds number ranging from 10 to 50. A parabolic flow profile at the jet exit was used to model the experimental results. Their second paper discusses the results of latex deposition experiments conducted at higher Reynolds numbers and for a flat velocity profile at the jet exit. A numerical model was used to obtain theoretical mass transfer rates for the latex particles. The results reported by Dabros and van de Ven suggest that latex suspensions do not follow DLVO theory, in that deposition is observed even when the numerical model predicts that the electrostatic forces are large enough to prohibit deposition. However, their results do indicate that the numerical model could be used to predict the maximum deposition rates, obtained when  $DI = 0$ . In other words, the predicted values of the maximum mass transfer rates compared favorably with

experimental results even when  $DI \gg 0$ .

The results obtained by Dabros and van de Ven were used as a basis for testing the experimental apparatus and numerical model to be used in this study. Neither set of results reported by Dabros and van de Ven could be duplicated with the experimental apparatus used in this study. Because of flowrate constraints ( $Re > 50$ ) and the nature of the jet exit velocity profile (parabolic), the verification tests were performed in two separate steps. First, the ability of the current model to predict the deposition results obtained by Dabros and van de Ven [17] was tested; and second, the ability of the model to predict the results of latex deposition experiments conducted by the author was verified.

## 4.2 Model predictions

The numerical model was tested by using it to calculate the mass transfer rates of latex particles based on results reported in Dabros and van de Ven's second paper. Figure 4-1 shows both their experimental and theoretical results for latex deposition experiments for  $40 < Re < 1000$ . The theoretical results were obtained using  $a=0.5 \mu\text{m}$ ;  $DI=0$ ;  $\bar{\lambda}=0.4$ ; and,  $\bar{\alpha} = 0.87 Re^{1/2}$  and three different values of  $Ad$ :  $Ad=0.05$ ;  $Ad=0.2$ ;  $Ad=0.8$ . The three different values of  $Ad$  were used by Dabros and van de Ven to represent the degree of uncertainty associated with Hamaker constant calculations. Figure 4-2 shows the theoretical values of Sherwood number obtained using the same parameters in the author's numerical model as were used by Dabros and van de Ven to produce the solid lines in Figure 4-1. The symbols in Figure 4-1 and Figure 4-2 represent the same experimental data, collected during experiments conducted by Dabros and van de Ven [17]. Although it is difficult to compare the theoretical curves shown in Figures 4-1 and 4-2 directly, it is evident that the theory line shown in Figure 4-2 fits the data collected by Dabros and van de Ven in the same way that their own theory line, shown in Figure 4-1, fits the data.

These results suggest that the numerical model used in this study is reliable.

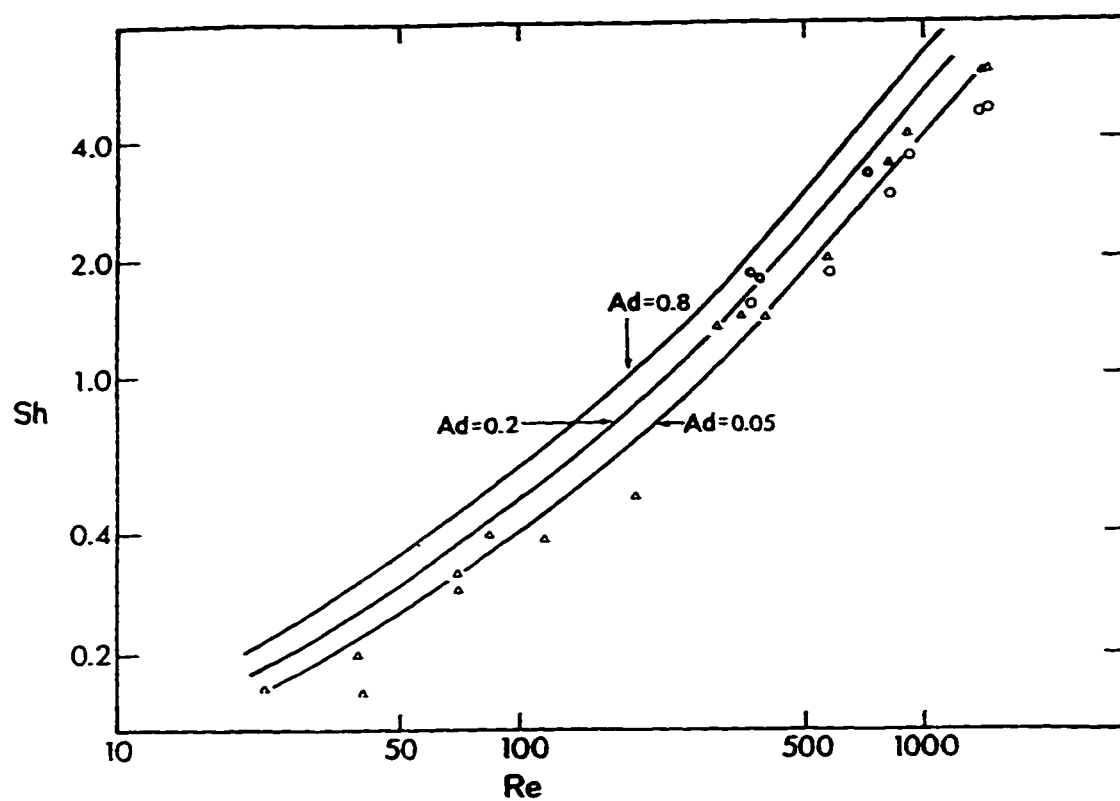


**Figure 4-1.** Sherwood number as a function of Reynolds number for latex particles. Symbols represent experimental results. Solid line represents theoretical values. From Dabros and van de Ven [17].

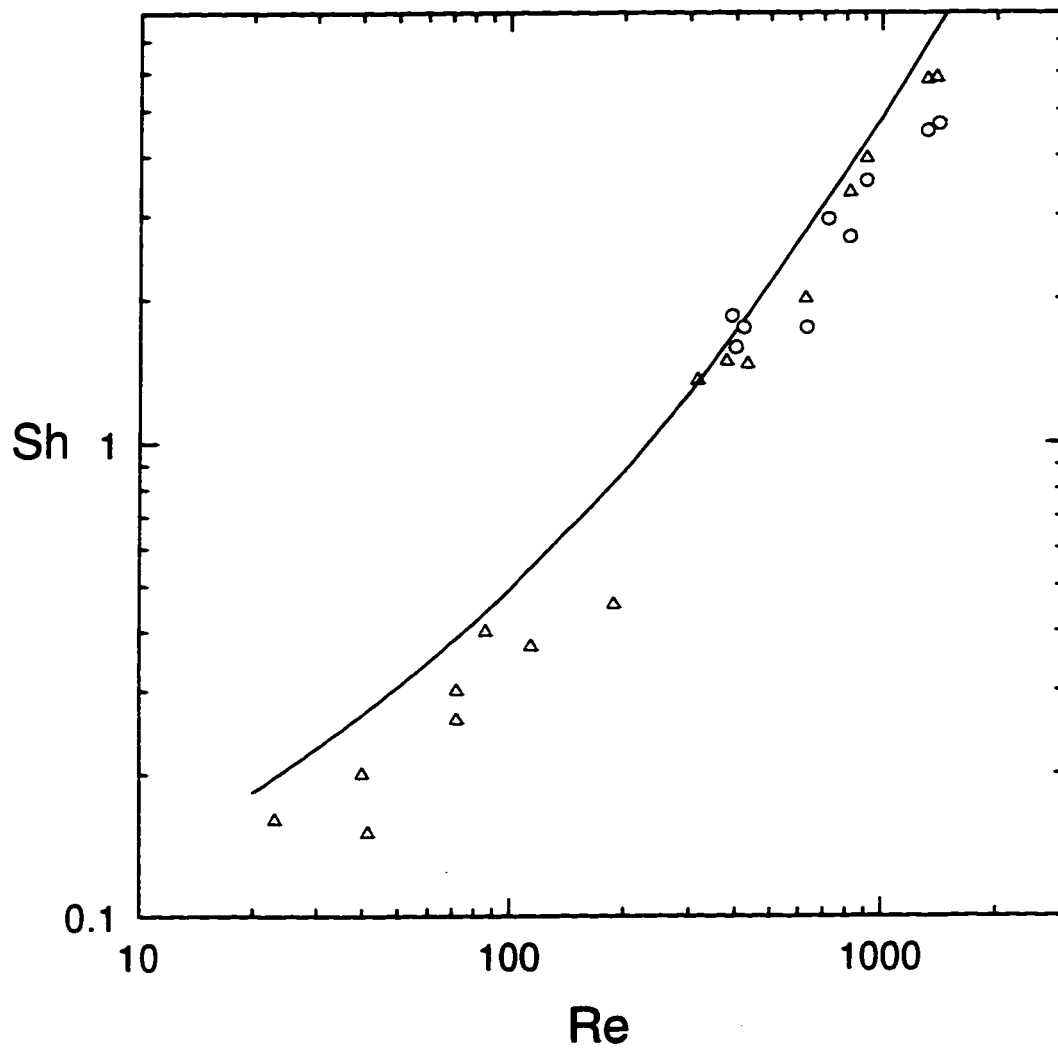


**Figure 4-2.** Model predictions of Sherwood number for latex particle deposition experiments conducted by Dabros and van de Ven. Parameters used in model:  $a=0.5$   $\mu\text{m}$ ;  $Ad=0.2$ ;  $\bar{\lambda}=0.4$ ;  $DI=0$ ;  $\bar{\alpha}=0.87\text{Re}^{1/2}$ . Symbols represent results of latex deposition experiments conducted by Dabros and van de Ven [17].

### 4.3 Results of deposition experiments using latex suspensions

A polystyrene latex suspension (Interfacial Dynamics Corporation, Portland, Oregon) was used to conduct deposition experiments similar to those conducted by Dabros and van de Ven, as discussed above. The latex particles had an average diameter of  $0.833\ \mu\text{m}$  with a very narrow size distribution ( $\pm 2\%$ ). The dilute latex suspension used in the deposition experiments was prepared from 850 ml of Milli-Q water, adjusted to  $\text{pH} = 7$ , and a sodium chloride concentration of  $0.01\text{M}$ . The average zeta potential of the latex particles was found to be  $-58\ \text{mV}$ . The particle zeta potential was measured using a Malvern Zetasizer 3 (Malvern Instruments, Inc.). The dimensionless jet exit - collector surface separation distance was set at  $\bar{h}_0 = 2.59$ . Table 4-1 lists the values of the parameters used to describe the latex suspension and the deposition experiments.

**Table 4-1.** Characterization of latex deposition experiments.

NaCl concentration, mol/L	0.01
bulk pH	7.0
particle diameter, $\mu\text{m}$	0.833
particle $\zeta$ -potential, mV	-58
collector $\zeta$ -potential, mV	-65
jet exit - collector separation, $\bar{h}_0$	2.59

Approximately 30 deposition experiments were conducted. The deposition experiments were conducted for a range of Reynolds numbers from 20 to 1000. Figure 4-3 shows the experimentally determined Sherwood numbers as a function of Reynolds number. The results shown in Figure 4-3 differ from the results presented by Dabros and van de Ven because the average particle size, the ionic strength, and the jet - collector spacing ( $\bar{h}_0$ ) are different. The results shown in Figure 4-3 do indicate that a Sherwood number - Reynolds number relationship similar to that reported by Dabros and van de Ven is followed.

The solid lines in Figure 4-3 represent the theoretical Sherwood number - Reynolds number relationship, calculated using the numerical model. The parameters used to generate the curves shown in Figure 4-3 are as follows:  $DI=0$ ;  $a=0.416 \mu\text{m}$ ;  $\bar{\lambda}=0.24$ ; and,  $\bar{\alpha} = 0.52 \text{ Re}^{1/2}$ . Two different values of Adhesion number,  $Ad$ , were used to show the effect of Hamaker constant on the predicted mass transfer rates. The top curve in Figure 4-3 corresponds to a value of  $Ad=0.8$ , while the lower curve corresponds to  $Ad=0.2$ . The agreement between the calculated values of Sherwood number, obtained using the numerical model, and the experimental results obtained using the impinging jet cell apparatus is within 20%.

The results of the verification tests using a well characterized latex suspension indicate that any disagreement between experiment and theory in this study cannot be attributed to the experimental apparatus or to the numerical model.

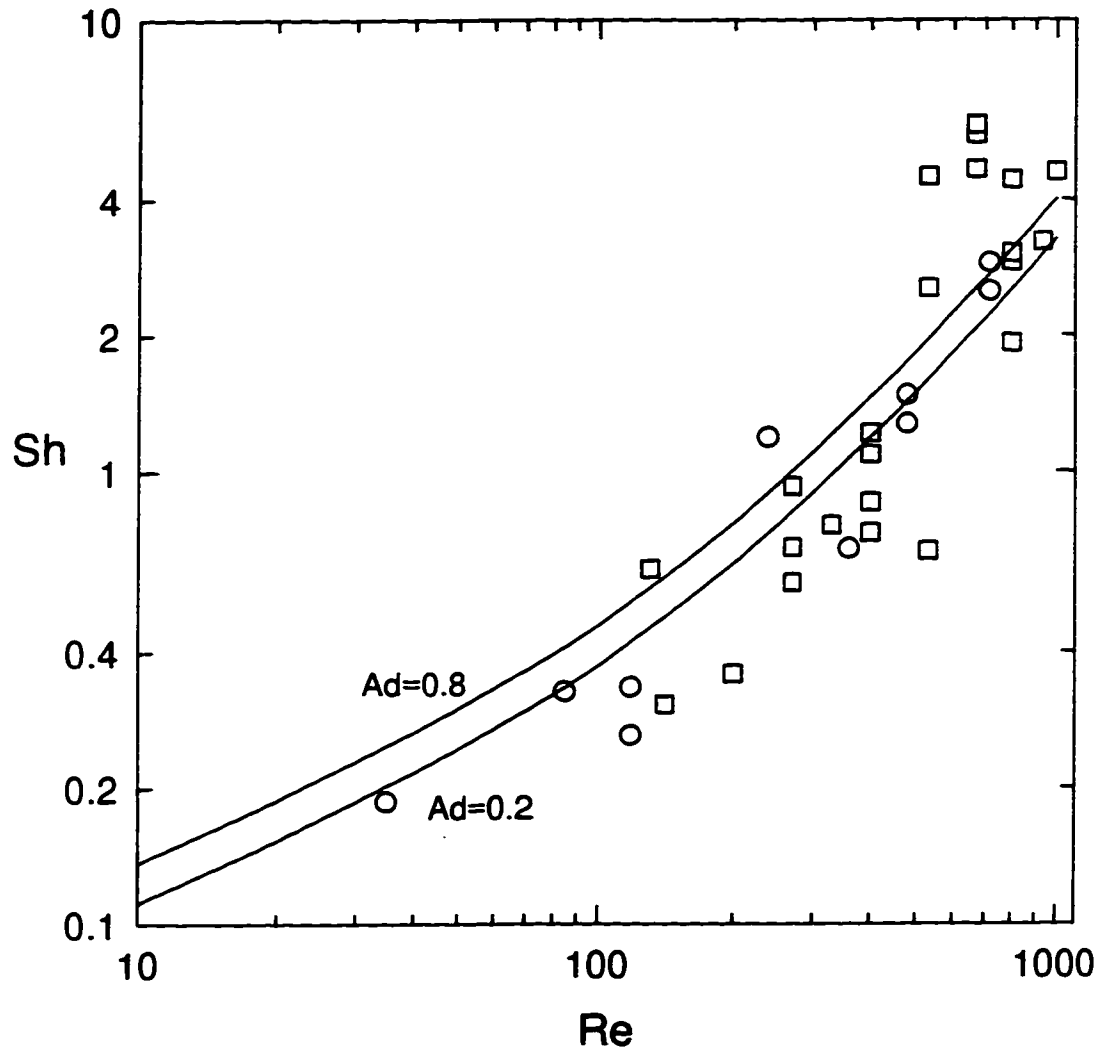


**Figure 4-3.** Sherwood number as a function of Reynolds number for latex particles. Symbols represent experimental results. Solid line indicates theoretical results, obtained by solving Equation (3-30), with  $a=0.416 \mu\text{m}$ ,  $Dl=0$ ,  $\bar{\alpha}=0.52\text{Re}^{1/2}$ , and  $Ad=\{0.2, 0.8\}$  as shown.

## **5. Experimental method**

The purpose of this chapter is to provide an outline of the experimental procedure that was followed. Although a number of different emulsions were studied and hundreds of experiments were conducted, a step-by-step procedure was followed at all times. In the following sections, the general procedure for emulsion preparation and characterization will be discussed. The method used to prepare the glass microscope slides will also be discussed. Changes or additions to the general procedure that are specific to any one set of experiments are discussed along with the presentation of results for that particular set of experiments.

### **5.1 Emulsion preparation and characterization**

Each emulsion used in this study was initially prepared in a much more concentrated form than that used in the experiments. The concentrated emulsions consisted of approximately 5% dispersed phase, by weight. Emulsions used in deposition experiments were very dilute, usually consisting of roughly 0.1% dispersed phase, by weight. There were a number of advantages associated with this method of emulsion preparation: first, the time spent characterizing an emulsion was minimized. Once a concentrated emulsion was prepared and its size distribution measured repeatedly, an average size distribution was calculated. Each time a set of experiments was conducted, another size distribution measurement was taken and then compared with the average size distribution for that sample. Consequently, an entire set of experiments was conducted from a single, well characterized emulsion. Second, nearly 2 litres of emulsion were required for each set of experiments. Preparing this volume of a dilute emulsion would have been extremely difficult.

After the concentrated emulsion was prepared, its size distribution was measured using a Malvern Zetasizer 3. A sample of the emulsion had to be diluted in

order to analyze it using the Zetasizer 3. Coincidentally, the dilution factors for the Malvern size analysis and for the deposition experiments were almost identical, so that any dependence of droplet size on dispersed phase concentration could be ignored. It must be pointed out, however, that a qualitative analysis of the concentrated and dilute emulsions using a high-powered microscope suggested that there was no dependence on dispersed phase concentration once the emulsion had been prepared.

Between 5 and 10 different samples were analyzed with the Zetasizer 3. The average droplet size was determined from the droplet size reported in each run. Only reproducible results were used in the calculation of the average droplet size. so that if too many inconsistent results were reported for one emulsion, it was not suitable for use in the deposition experiments and a new emulsion was prepared. Inconsistent size distribution results were normally observed during initial attempts to prepare an emulsion for a particular set of experiments, and once a recipe for a stable emulsion was arrived at, size distribution results tended to fall within a very narrow range, even for two emulsions prepared separately.

After the concentrated emulsion was prepared and its average size distribution was determined, droplet zeta potentials were measured as a function of bulk pH and NaCl concentration, using the Zetasizer 3. A number of different samples were analyzed to ensure that consistent values of zeta potential were reported for specific values of pH and [NaCl].

The average droplet size and zeta potential data were then used in the numerical model to determine the predicted range of conditions that would be favourable to droplet deposition. This information was used to choose different values of continuous phase pH and electrolyte concentration for the dilute emulsions used in the deposition experiments. Samples of the concentrated emulsion were then diluted in purified, double distilled water (Milli-Q water, Millipore Systems) that had been adjusted to the desired values of pH and [NaCl]. Droplet concentrations (expressed as particles/ml) were obtained using an optical hemacytometer (Reichert Bright-Line, Reichart Industries Ltd.). At least three different samples were used in the determination of droplet concentration. The average droplet concentration was

required to be within 5% of each individual droplet count. The droplet concentration was also measured at the end of each experiment to ensure that the droplet concentration did not change over the course of the experimental work.

## **5.2 Preparation of the glass microscope slides for deposition experiments**

As mentioned earlier, the experimental apparatus is designed so that the flowing emulsion impinges on a glass microscope slide. Precleaned, 20 mm x 50 mm microscope slides (Fisher Precleaned Superfrost, Fisher Scientific) were used in the experiments. Slides were used no more than twice each. The same rigorous cleaning procedure was followed for both new and used slides. First, the slides were soaked in concentrated HCl for at least two hours. They were then rinsed thoroughly with distilled water and placed in an ultrasonic bath of 70 °C distilled water and detergent (Sparkleen, Fisher Scientific) for 10 minutes. The slides were then rinsed thoroughly. The next step in the procedure depended upon the nature of the deposition experiments. For the experiments involving oil-in-water emulsions and a hydrophilic collector, the slides were simply stored in purified Milli-Q water until they were used. These slides were stored for less than 1 hour before they were used in order to minimize any aging effects that are known to occur when glass is immersed in water for any length of time [1,44].

For the experiments involving bitumen-in-water emulsions and a hydrophobic collector, the glass slides were removed from the ultrasonic bath, rinsed thoroughly, and placed in a drying oven at 60 °C for one hour. They were then coated with a 5% (w/w) solution of dichlorodimethylsilane in toluene, and allowed to dry. The slides, whose surfaces were now hydrophobic in nature [45,46], were then used in the hydrophobic deposition experiments. These slides were used only once.

For the experiments involving bitumen-in-water emulsions and a collector surface coated with a thin film of bitumen, the slides were silanated just as they were for the previous experiments. The slides were then soaked in a 10% (w/w) solution of

bitumen in methylene chloride for 1 hour. The slides were then removed from the dilute bitumen solution and were dried in an oven at 60° C for 1 hour before they were used in the deposition experiments. These slides were not reused.

For the experiments involving the water-in-hydrocarbon emulsions, the slides were removed from the ultrasonic bath, rinsed thoroughly, and placed in a drying oven at 60 °C for one hour. These slides were discarded after one use.

The microscope slides were prepared before each set of experiments. Slides that had been prepared but were not used were not kept for the next set of experiments. They were either sent through the cleaning procedure again or discarded, depending on the type of emulsion being studied.

### **5.3 Flow chart describing experimental procedure**

Figure 5-1 provides a general overview of the experimental method. Any changes to the procedure are discussed within the relevant section of Chapters 6, 7, and 8.

### **5.4 List of experiments conducted**

A comprehensive list of the deposition experiments conducted in this study is presented below. A brief description of each set of experiments is also provided. The chapter in which the results of each set of experiments are discussed is listed along with the description.

#### **Outline of experimental work**

##### **1. Latex suspensions (Chapter 4)**

- variation of Sherwood number with Reynolds number.

- used to test experimental apparatus and computer program.
2. Bitumen-in-water emulsions (Chapter 6)
    - variation of Sherwood number with Reynolds number.
    - variation of Sherwood number with dimensionless Debye length ( $\kappa a$ ).
    - analysis of surface coverage at high Reynolds numbers.
  3. Bayol oil-in-water emulsions (Chapter 6)
    - variation of Sherwood number with Reynolds number.
  4. Mineral oil (Cannon standard viscosity oil)-in-water emulsions (Chapter 6)
    - variation of Sherwood number with Reynolds number.
    - variation of Sherwood number with dispersed phase viscosity.
    - variation of Sherwood number with double layer strength ( $DI > 0$ ;  $DI < 0$ ).
    - variation of Sherwood number with dimensionless Debye length ( $\kappa a$ ).
    - analysis of surface coverage at high Reynolds numbers.
    - droplet coagulation experiments.
  5. Pentadecane-in-water emulsions (Chapter 6)
    - variation of Sherwood number with Reynolds number.
    - variation of Sherwood number with double layer strength ( $DI > 0$ ;  $DI < 0$ ).
    - variation of Sherwood number with dimensionless Debye length ( $\kappa a$ ).
  6. Bitumen-in-water emulsions on coated slides (Chapter 7)
    - silane-treated (hydrophobic) glass slides:
      - variation of Sherwood number with Reynolds number.
      - variation of Sherwood number with dimensionless Debye length ( $\kappa a$ ).
    - bitumen-coated glass slides:
      - variation of Sherwood number with Reynolds number.
      - variation of Sherwood number with bulk pH.
  7. Bitumen-stabilized water-in-hydrocarbon emulsions (Chapter 8)
    - variation of Sherwood number with Reynolds number.
    - variation of Sherwood number with continuous phase bitumen concentration.

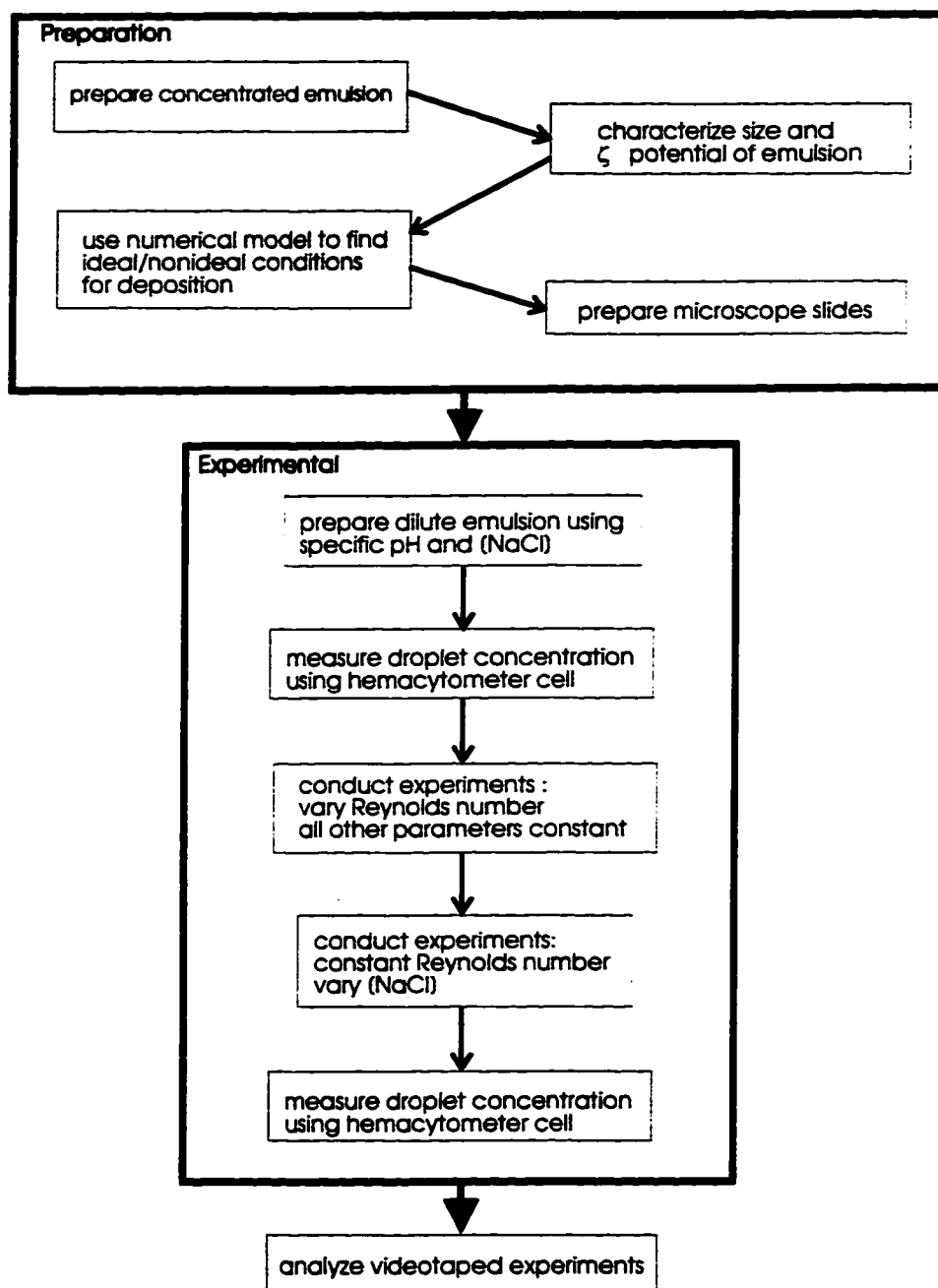


Figure 5-1. Flow chart description of the experimental method.

## 6. Deposition of oil-in-water emulsions

The experiments discussed in this chapter represent a major portion of the work completed for this thesis. With the exception of the deposition studies involving hydrophobic and bitumen coated collectors, all of the results of the oil-in-water-emulsion experiments are discussed in this chapter.

The bitumen-in-water emulsion deposition experiments were the primary focus of this part of the study because of the important role these emulsions play in oil sands extraction and processing problems. The variation of *bitumen* droplet deposition rates with *flow intensity* and *NaCl concentration* are discussed in Section 6.1.

Deposition experiments have been used extensively to study particulate systems. The stability of emulsions, on the other hand, has traditionally been studied using population balance experiments, or some other type of coagulation study. Consequently, there was no previous work with which the bitumen deposition studies could be compared. The success of the bitumen-in-water emulsion deposition experiments suggested that further experimentation was warranted. Thus, the remainder of this chapter focuses on the analysis of deposition experiments conducted using different oil-in-water emulsions. The effect of different dispersed phase characteristics, such as molecular structure, density, viscosity, and zeta potential, on droplet deposition rates were observed.

Initially, a refined mineral oil known as *Bayol-35* was used to prepare an oil-in water emulsion. Emulsions of Bayol-35 and water had been prepared previously by co-workers [52,53] and were known to be stable when a nonionic surfactant known as Triton-X was used. The Bayol-35 experiments show the variation of mass transfer rates with *Reynolds number*. They are discussed in Section 6.2.

The next sets of experiments were conducted using Cannon *Standard Viscosity Oils* (Cannon Instrument Co., State College, PA), which are refined mineral oils used for viscometer calibration. Two different oils were used for two different sets of experiments: a 7.67 mPa s sample and a 3.39 mPa s sample were used to prepare two

emulsions with *different dispersed phase viscosities*. The Cannon viscometry oil experiments are discussed in Section 6.3.

The last sets of experiments of this type were conducted using purified *pentadecane* (Aldrich Chemical Co., Inc.). The effects of *Reynolds number* and *electrolyte concentration* on droplet deposition rates were studied. The results are reported in Section 6.4.

In Section 6.5, the results of the *bitumen and low viscosity oil* deposition experiments are *compared*. First, the experimental results for each set of experiments are compared with theoretical predictions. The difference in surface coverage patterns at high flowrates between bitumen and Cannon viscometry oil deposition experiments is analyzed. Finally, the effect of dispersed phase viscosity on droplet deposition is discussed.

## 6.1 Bitumen-in-water emulsions

### 6.1.1 Emulsion preparation and characterization

A 5 g sample of toluene extracted Cold Lake bitumen was dispersed in 100 ml of 70 °C Milli-Q water using a hand-held homogenizer, following a procedure outlined by Chow and Takamura [47]. Physical properties of the bitumen are

viscosity (25°C) = 400 Pa s [47]

density (23°C) = 1010 kg/m<sup>3</sup> [47]

dielectric constant (24°C)  $\approx$  3 [48]

refractive index (25°C) = 1.45 [49]

The pH of the water was adjusted to 10 using a 1M solution of NaOH prior to the addition of the bitumen. The dispersion was passed through the homogenizer twice and then allowed to stand overnight in a refrigerator to promote settling of the largest

droplets and thereby reduce the average droplet size in the bulk phase. The size distribution of the sample was measured using a Malvern Zetasizer 3. The average particle diameter was 1.18  $\mu\text{m}$ . A representative size distribution is shown in Figure 6-1. The size distribution was measured before and after each set of experiments to ensure that no significant change in particle size occurred between the time the concentrated emulsion was prepared and the time that the deposition experiments were completed. The measured size distributions were consistently as narrow as the one shown in Figure 6-1, making the experiments less difficult to analyze and model.

The concentrated emulsion was diluted for use in the deposition experiments. Each time a set of experiments was conducted, a small volume of the concentrated emulsion was mixed with a large volume of Milli-Q that had previously been adjusted to the desired pH and electrolyte concentration. Dilution rates were approximately 7 ml of concentrated emulsion to 1000 ml of water. The bitumen droplet concentrations were determined for each set of experiments by physically counting the droplets under a microscope, using a hemacytometer cell, as was discussed in Section 5.1.

Zeta potentials of a dilute, 0.1 M NaCl bitumen emulsion were measured as a function of pH using a Malvern Zetasizer 3. These results are shown in Figure 6-2. The measured values of bitumen droplet zeta potential reported in Figure 6-2 correspond to values reported previously by Chow and Takamura [47]. The solid line shown in Figure 6-2 represents the calculated values of bitumen zeta potential in a 0.1M NaCl solution, determined using the ISG model.

The Hamaker constant for the bitumen emulsion and the glass collector was calculated from eq. (3-54), for the interaction of bitumen {phase 1} and glass {phase 2} across the continuous water phase {3}. The resulting value of the Hamaker constant was

$$A_{132} = 2.6 \times 10^{-21} \text{ J}$$

Takamura and Chow [50] reported a value of  $A_{132} = 1.0 \times 10^{-20} \text{ J}$  for a bitumen {1} - water {3} - sand {2} system. The larger value of  $A_{132}$  calculated by Takamura and Chow was obtained using the more rigorous Lifshitz continuous spectrum theory. In

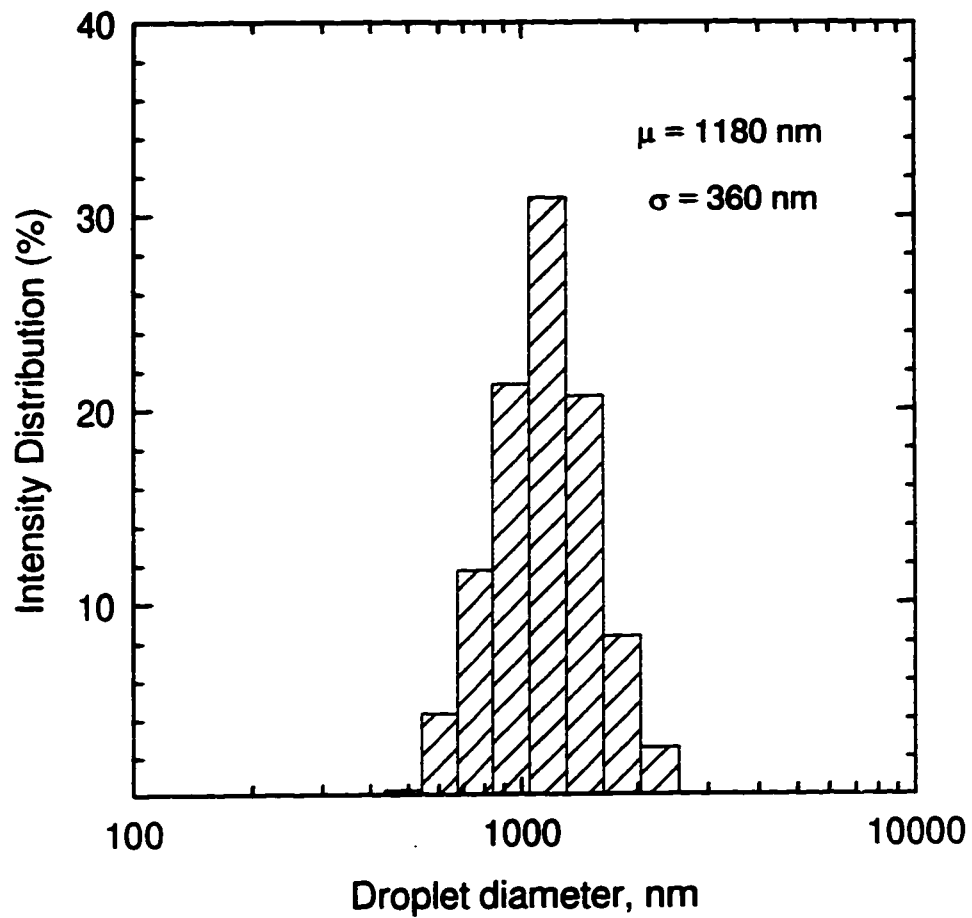


**Figure 6-1.** Representative size distribution of a bitumen-in-water emulsion, with a mean droplet diameter of 1.18  $\mu\text{m}$  and a standard deviation of 0.36  $\mu\text{m}$ .

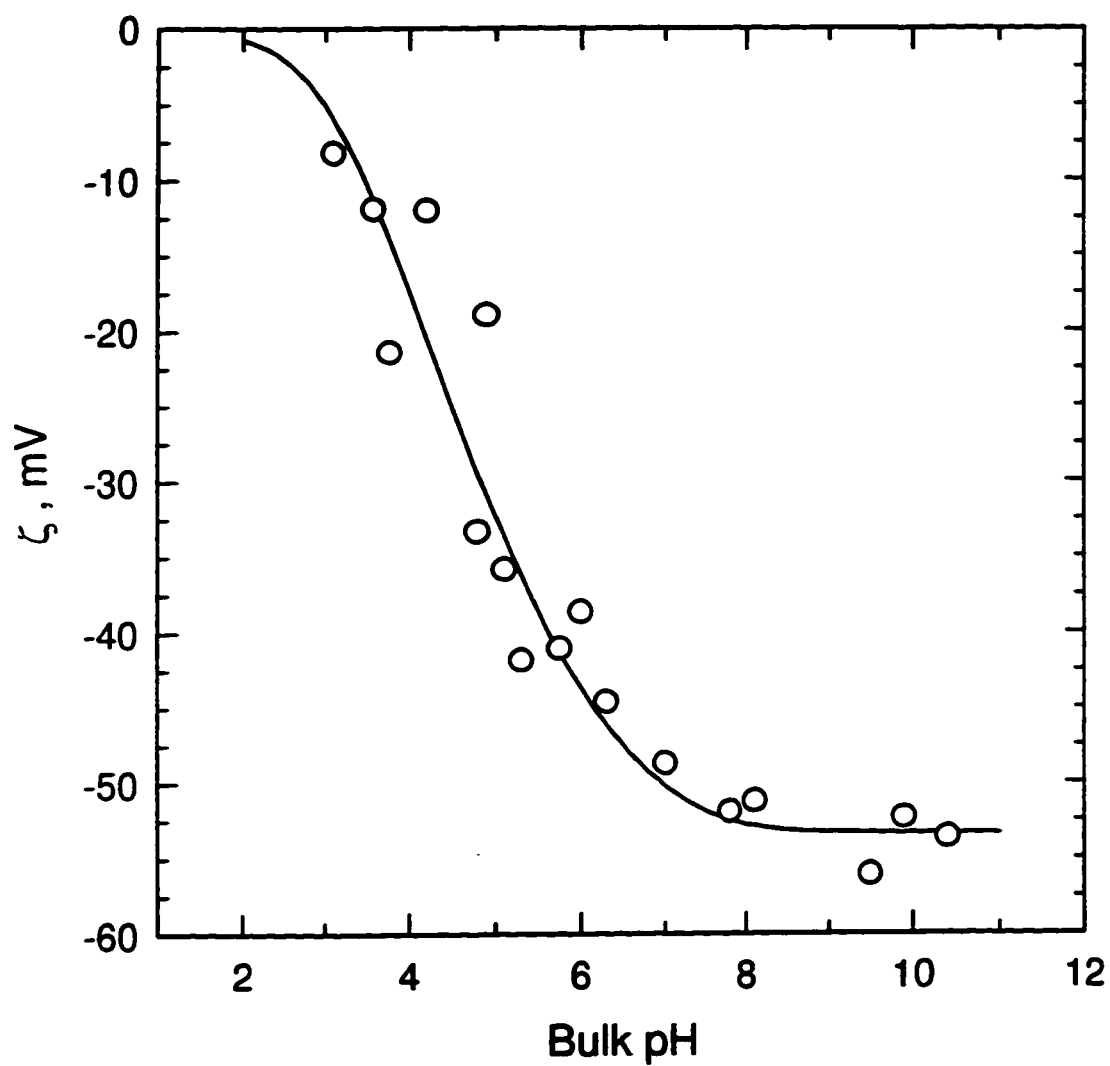


**Figure 6-2.** Measured (symbols) and calculated (solid line) zeta potentials for the bitumen emulsion as a function of bulk pH in 0.1M NaCl. Theoretical zeta potentials calculated using the ISG model, with  $N_s = 2 \times 10^{18} \text{ m}^{-2}$ ,  $\text{pKa} = 4.5$ ,  $x_s = 0.6 \text{ nm}$ ,  $a = 0.59 \text{ }\mu\text{m}$ , and  $\kappa a = 614$ .

the method employed by Takamura and Chow [50], the required values of the absorbance frequency spectra are available for alkanes with a maximum carbon length of 16. so they assumed that the value of the Hamaker constant becomes asymptotic beyond a C-16 alkane. In their calculations, it was assumed that the bitumen could be modelled as a long-chain alkane. Conversely, the bulk properties  $\epsilon$  and  $n$  are not always known and there is some degree of error associated with their estimation and with the use of eq. (3-54). Ultimately, both methods have been shown to yield good estimates of the three phase Hamaker constant [30,32,50].

If the Hamaker constant for this system is taken as  $A_{132} = 2.6 \times 10^{-21}$  J, then the Adhesion number,  $Ad = 0.11$ . If the Hamaker constant reported by Takamura and Chow is used, then  $Ad = 0.40$ . The numerical model is not particularly sensitive to the magnitude of the Adhesion number (as was demonstrated in Section 3.7). Thus, either value of Adhesion number is acceptable for use in the numerical model. A value of  $Ad = 0.11$  was used in this study.

### **6.1.2 Collector preparation and characterization**

The procedure outlined in Section 5.2 was used to prepare the microscope slides for the bitumen deposition experiments. The zeta potentials of the glass slides had been measured previously [51] by grinding a glass slide into a fine powder and dispersing it in water. Figure 6-3 shows the variation of  $\zeta_c$  with both pH and NaCl concentration. The solid lines shown in Figure 6-3 represent the values of  $\zeta_c$  calculated using the ISG model.

### **6.1.3 Effect of Reynolds number**

Experiments were conducted using bitumen emulsions solutions for a range of Reynolds numbers from 20 to 1000. For each experiment the coating density,  $S$

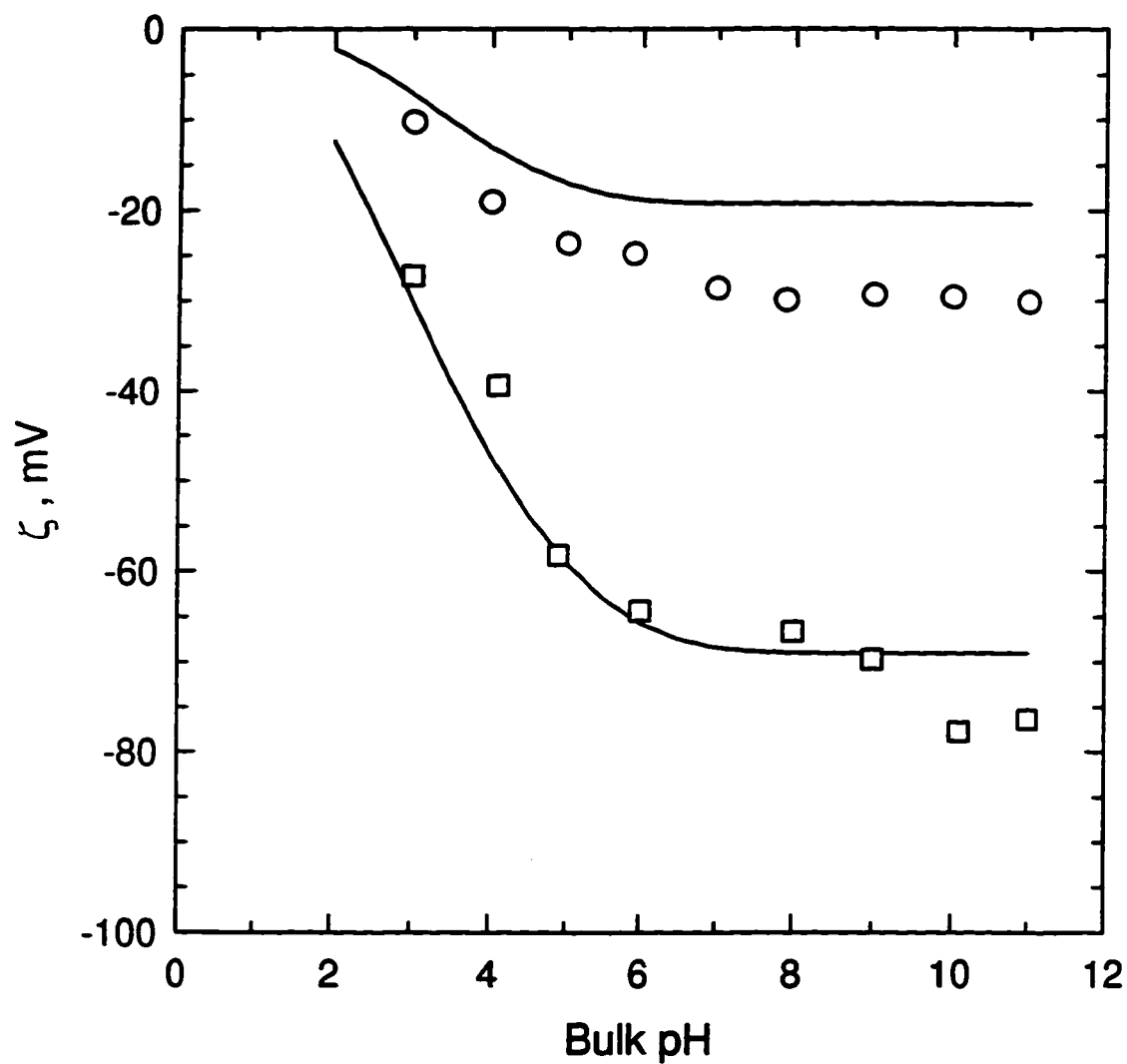


Figure 6-3. Measured (symbols) and calculated (solid lines) zeta potentials for finely ground microscope slide particles as a function of bulk pH in 0.01M NaCl ( $\square$ ) and in 0.1M NaCl ( $\circ$ ). Theoretical zeta potentials calculated using the ISG model, with  $N_s = 1 \times 10^{18} \text{ m}^{-2}$ ,  $\text{pKa} = 3.2$ ,  $x_s = 1.4 \text{ nm}$ .  $\kappa a > 100$  for all data.

(particles/mm<sup>2</sup>), was calculated at specific time intervals in order to study the relationship between the stagnation region coating density (SRCD) and the flow Reynolds number. Values of the SRCD were also used to calculate the dimensionless rate of mass transfer to the collector surface, as was discussed in Section 2.3. Five different sets of experiments were conducted. The NaCl concentration was 0.1M for each set of experiments, and the droplet concentration was fixed at  $7.2 \times 10^6$  particles/ml ( $\pm 5\%$ ), while  $\zeta_p$  and  $\zeta_c$  were changed for each set of experiments by changing the solution pH. Table 6-1 lists the droplet size, bulk pH, and the calculated values of  $\zeta_p$  and  $\zeta_c$  for each set of experiments.

**Table 6-1.** Characterization of bitumen emulsion deposition experiments I: 0.1M NaCl;  $a=0.59 \mu\text{m}$ ;  $c_0=7.2 \times 10^6$  droplets/ml.

Set #	bulk pH	$\zeta_p$ (mV)	$\zeta_c$ (mV)	DI
1	4.7	-27.4	-20.2	55.0
2	8.6	-53.2	-30.1	159
3	5.3	-35.6	-23.4	82.8
4	4.8	-29.1	-21.6	62.4
5	3.8	-16.7	-19.9	33.0

Figure 6-4 shows typical stagnation region coating densities for the bitumen deposition experiments, labelled Set 1 in Table 6-1. For these experiments,  $\zeta_p = -27.4$  mV and  $\zeta_c = -20.2$  mV. The symbols represent the observed stagnation region coating densities as a function of time. The straight lines represent linear regressions of the experimental data, showing that the bitumen coating densities were linear even at the highest Reynolds numbers. Although the other deposition experiments listed in Table 6-1 have different values of  $\zeta_p$  and  $\zeta_c$  than set 1, the SRCD curves were

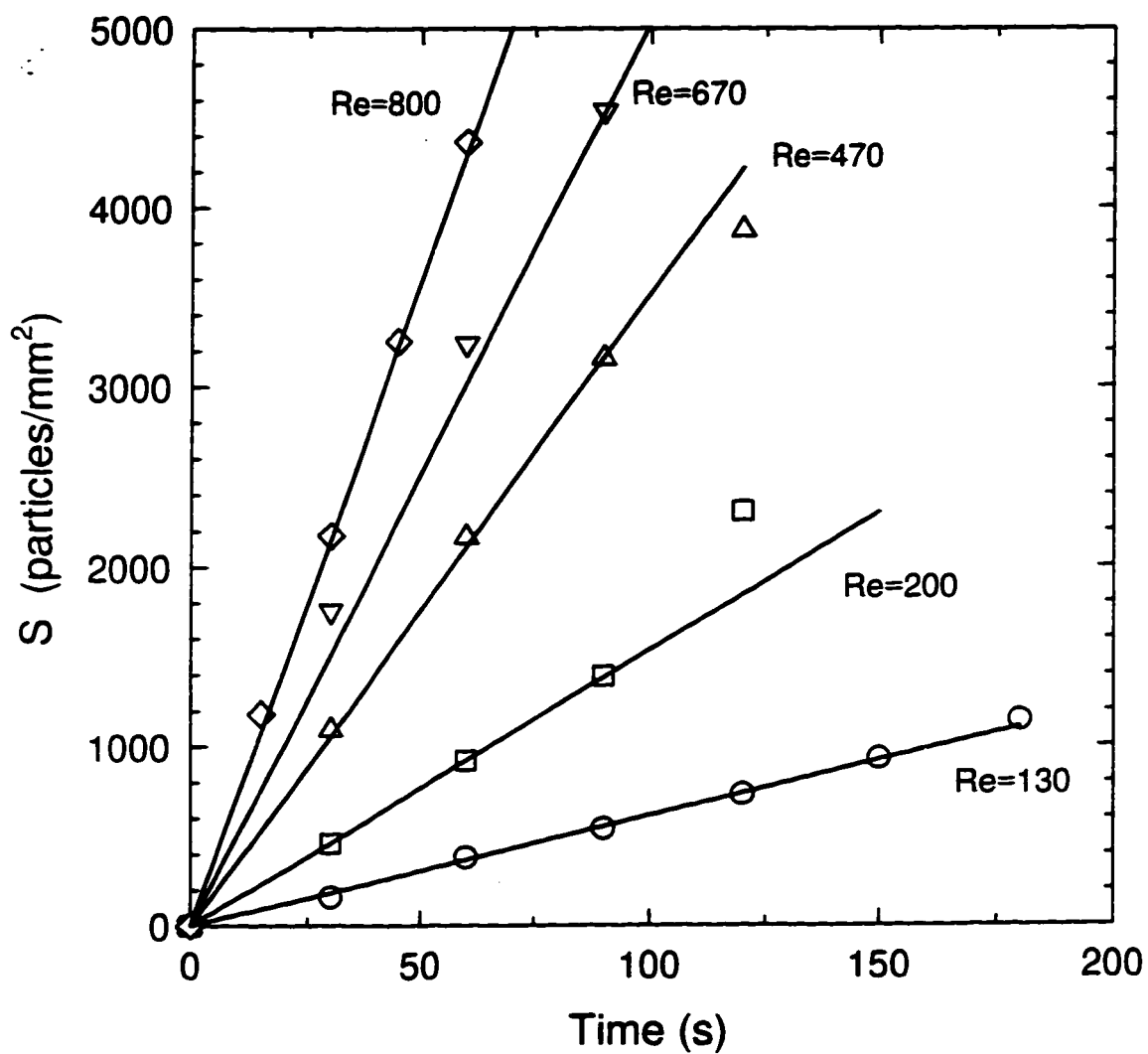


**Figure 6-4.** Stagnation region coating density as a function of time for 1.18  $\mu\text{m}$  bitumen droplets in 0.1M NaCl, pH = 4.7;  $\zeta_p = -27.4$  mV,  $\zeta_c = -20.2$  mV.

similar to those shown in Figure 6-4, in that they were linear even at high Reynolds numbers.

The initial slopes of the SRCD lines were used to calculate values of  $J_0$ , the flux to the collector surface, for each deposition experiment. The dimensionless rate of mass transfer to the collector surface was then calculated using eq. (2-2). Figure 6-5 shows the variation of the Sherwood number with Reynolds number for the bitumen deposition experiments. The results from all five sets of experiments are shown in Figure 6-5. The solid line in Figure 6-5 was obtained from the numerical solution of eq. (3-30) and represents the predicted values of Sherwood number as a function of Reynolds number for the mean bitumen particle radius ( $a = 0.59 \mu\text{m}$ ). The two dashed lines shown in Figure 6-5 represent the predicted values of Sherwood number as a function of Reynolds number for bitumen particle radii that are one standard deviation away from the mean ( $a \pm \sigma/2$ , where  $\sigma = 0.36 \mu\text{m}$ ). All of the bitumen deposition experiments described in Table 6-1 can be represented by the theoretical curves shown in Figure 6-5. Even though  $\zeta_p$  and  $\zeta_c$  changed for each set of experiments, the resultant value of the double layer strength parameter,  $DI = \epsilon\epsilon_0 a \zeta_c \zeta_p / kT$ , was never large enough to affect the calculated mass transfer rates. The relatively high NaCl concentration (0.1M) resulted in a large value of  $\kappa a$ , indicating that the double layer has been collapsed or compressed. The compressed double layer limited the effect that droplet and collector zeta potentials had on droplet deposition rates. As Figure 6-5 illustrates, there is excellent agreement between theory and experiment for the bitumen emulsions: the difference between observed and calculated mass transfer rates is generally less than 20%. These results indicate that bitumen deposition closely follows DLVO theory under the conditions studied here. It may seem surprising that DLVO theory provides such accurate predictions of bitumen deposition considering that for each set of experiments, the absolute values of  $\zeta_p$  and  $\zeta_c$  approach, and in some cases exceed those values normally considered acceptable for use with DLVO expressions. For example, the maximum absolute value of zeta potential for the HHF version of the double layer interaction equation is usually taken as 25 mV [27]. There are a number of possible explanations for the extended

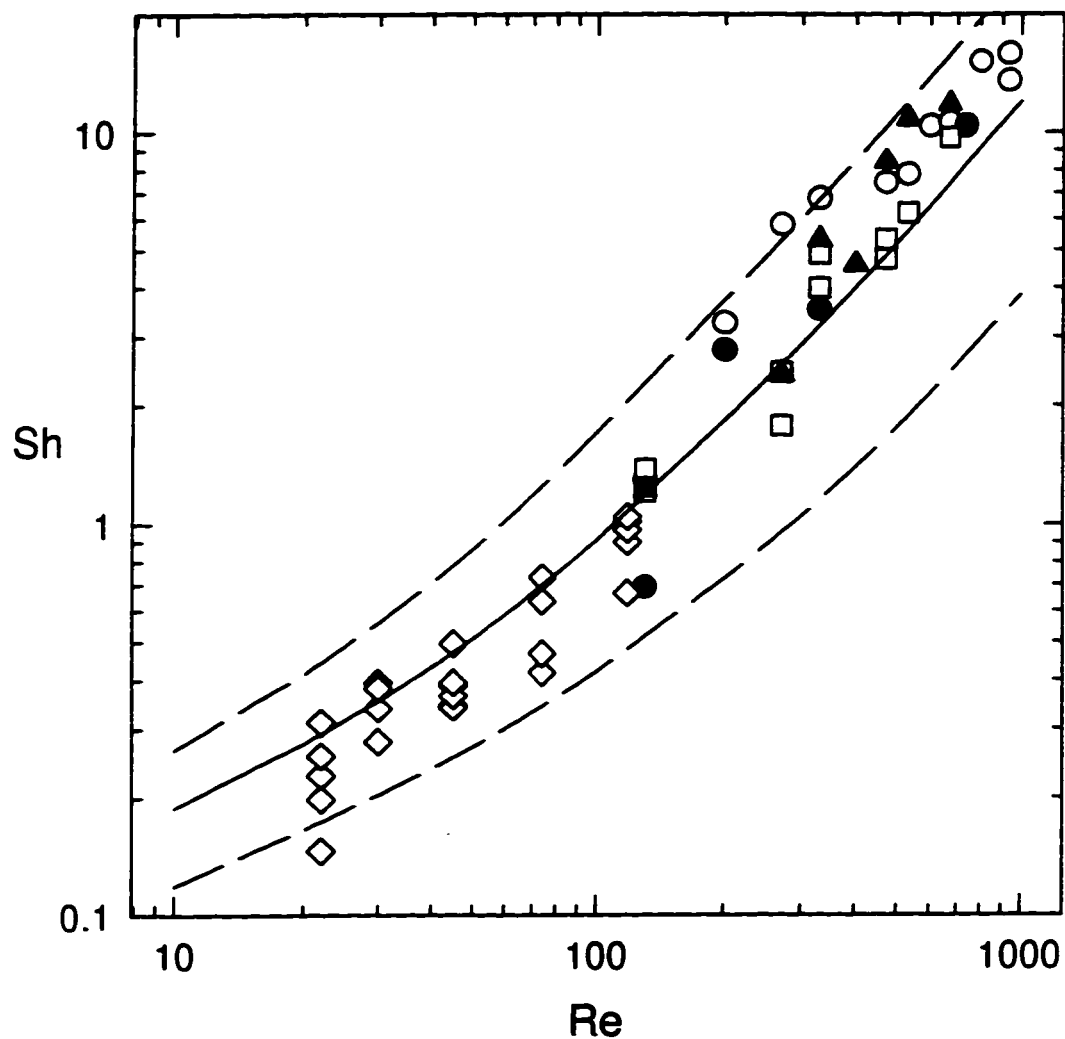


**Figure 6-5.** Dimensionless mass transfer (expressed as Sherwood number) as a function of Reynolds number for 1.18  $\mu\text{m}$  bitumen droplets in 0.1M NaCl ( $\kappa a = 614$ ). (○) -  $\zeta_p = -27.4$  mV,  $\zeta_c = -20.2$  mV; (□) -  $\zeta_p = -53.2$  mV,  $\zeta_c = -30.1$  mV; (▲) -  $\zeta_p = -35.6$  mV,  $\zeta_c = -23.4$  mV; (◇) -  $\zeta_p = -29.1$  mV,  $\zeta_c = -21.6$  mV; (●) -  $\zeta_p = -16.7$  mV,  $\zeta_c = -19.9$  mV. Lines show theoretical mass transfer, obtained by solving eq. (3-30):  $Ad=0.11$ ; (—)  $a=0.59$   $\mu\text{m}$ ; (- - -)  $a \pm \sigma/2$  where  $\sigma=0.36$   $\mu\text{m}$ .

applicability of DLVO theory. First, and perhaps most importantly, the effect of the high NaCl concentrations on the thickness of the double layers would certainly work to extend the applicability of DLVO theory to larger values of droplet and collector zeta potentials. The effect of the compressed double layers may be complemented by the difference in the wettabilities of the droplets and the collector. Previous studies have shown that for two hydrophilic surfaces (such as silica particles and glass microscope slides) in solutions possessing large electrolyte concentrations, a so-called solvation reaction occurs [32]. The solvation reaction creates an increased repulsive force between the two surfaces and would therefore lower the particle deposition rates. It is evident that the solvation effect does not occur in the bitumen deposition experiments, as the deposition rates are not lower than DLVO theory predicts even though the salt concentration is quite high. This may seem like a strange argument to present, in that bitumen is always thought of as a hydrocarbon, which is by definition hydrophobic. However, evidence suggesting that bitumen has some hydrophilic character will be presented in Chapter 7. The overall effect of NaCl concentration on the bitumen droplet mass transfer rates is discussed in the next section.

#### **6.1.4 Effect of electrolyte concentration**

Experiments were conducted in which  $\kappa a$  was changed by varying the bulk NaCl concentration, while keeping the pH constant at pH 5. In this way, both the dimensionless double layer thickness and the double layer parameter were varied for each set of experiments. The three parameter ISG model, discussed in Section 3.5.4, was used to model the change in both the bitumen and collector zeta potentials with pH and the different electrolyte concentrations. The values of  $\zeta_p$  and  $\zeta_c$ , calculated using the ISG model, were then imported to the numerical model so that the theoretical effect of  $\kappa a$  on the rates of bitumen droplet mass transfer could be predicted. Experiments were conducted at five different NaCl concentrations: 0.1M; 0.05M; 0.01M; 0.005M; and, 0.001M. The droplet and collector zeta potentials for

each set of experiments are reported in Table 6-2. The results of each set of experiments are shown as symbols in Figure 6-6. The theoretical results generated by the numerical model are shown as a solid line in Figure 6-6. Again, the difference between experiment and theory for the bitumen emulsion is, on average, less than 15% at salt concentrations of 0.1M, 0.05M, and 0.01M. The results of the experiments conducted at 0.01M NaCl are especially encouraging: as Figure 6-6 illustrates, the Sherwood number is extremely sensitive to electrolyte concentration in the region near

**Table 6-2.** Characterization of bitumen emulsion deposition experiments II: pH=5: Re=118:  $a=0.59\ \mu\text{m}$ :  $c_0=7.2 \times 10^6$  droplets/ml.

[NaCl] (mol/L)	$\kappa a$	$\zeta_p$ (mV)	$\zeta_c$ (mV)	DI	Da
0.001	61.3	-71.2	-67.1	474	0.004
0.005	137	-61.0	-64.9	393	0.004
0.01	194	-49.3	-58.3	286	0.028
0.05	434	-24.1	-31.0	74.2	0.064
0.1	614	-13.5	-23.1	31.0	0.30

0.01M, and yet the experimentally determined values fall on the theory line. Some deposition did occur at the lowest salt concentrations (0.005M and 0.001M), where DLVO theory predicts almost no deposition will occur. However, this behavior has been observed by other researchers [18,19]. Otherwise, the results suggest that the bitumen emulsion does conform to the DLVO model.

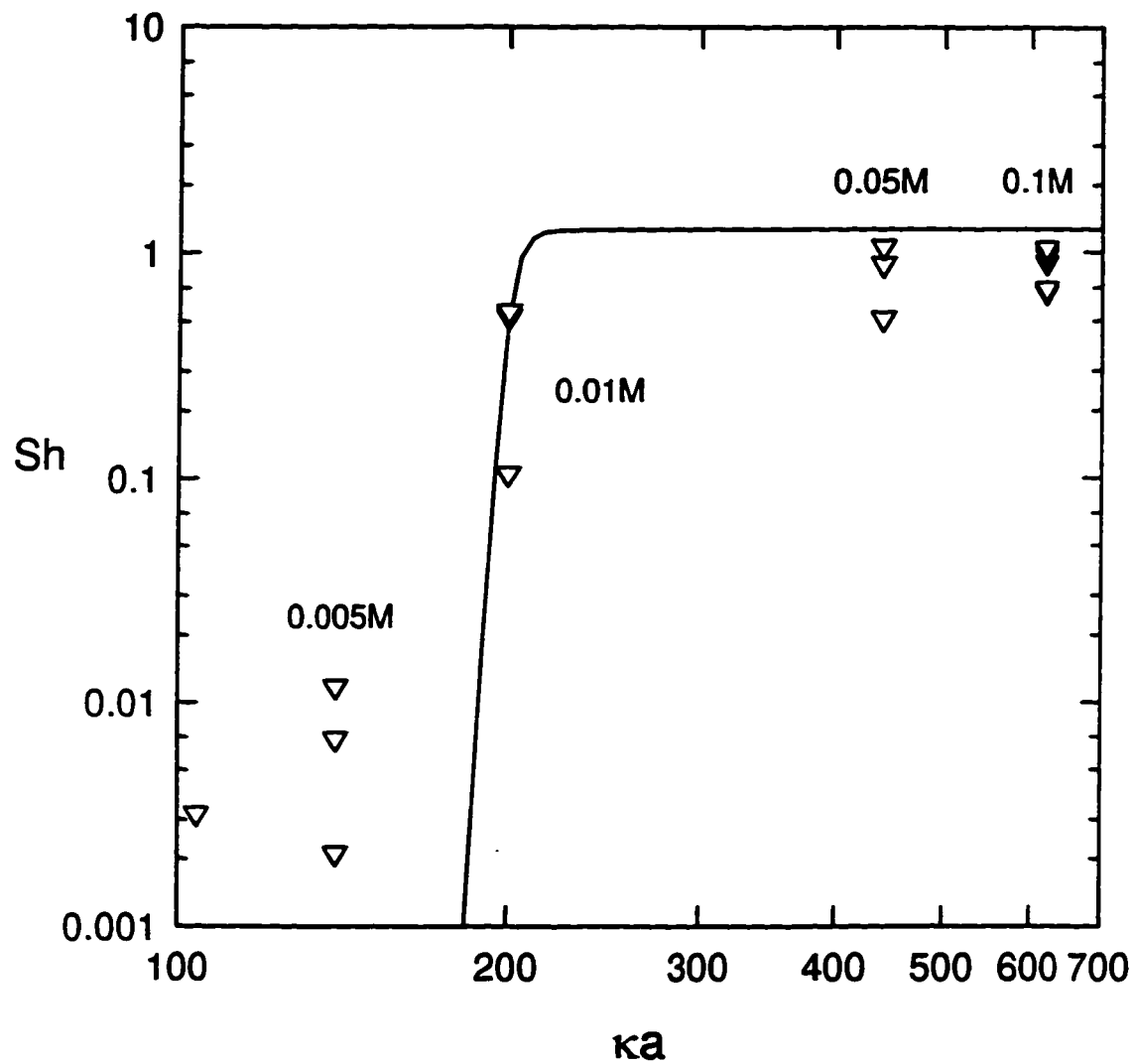


**Figure 6-6.** Experimentally determined effect of  $ka$  parameter on mass transfer to collector surface for bitumen emulsions in various concentrations of NaCl solutions,  $Re=118$ ,  $pH=5$ . Solid line shows theoretical mass transfer.

## 6.2 Bayol oil-in-water emulsion deposition experiments

### 6.2.1 Emulsion preparation and characterization

The Bayol-35 mineral oil, obtained from Esso Chemicals, has the following physical properties:

density (25°C) = 780 kg/m<sup>3</sup> [52]

viscosity (25°C) = 2.4 mPa s [52]

dielectric constant = 2.201 [48]

refractive index = 1.36 (measured)

The emulsion was prepared by following a procedure outlined by Yan *et al.* [52]. In this procedure, 1 g of Triton-X surfactant was mixed with 1 litre of water. 100 g of Bayol oil were then added to the water-surfactant mixture. The mixture was then emulsified using a shear homogenizer. The homogenizer was run for 10 minutes. Because of the emulsion's tendency to cream very quickly, it was doubtful that the size distribution and the droplet concentration would remain constant during the deposition experiments. In fact, it was found that the Bayol emulsion would start to cream in the pressure vessel before the deposition experiments had even begun. This problem was solved by placing the emulsion in a solvent extraction vessel overnight. The dispersed emulsion was then drawn from the bottom of the separatory flask, leaving the largest droplets behind in the creamed phase.

The size distribution of the separated emulsion was then analyzed using the Malvern Zetasizer 3. A typical example of the Bayol emulsion size distribution is shown in Figure 6-7. The average droplet size is slightly larger than that of the bitumen emulsion, and is less monodisperse. This emulsion was very stable as far as changes in size distribution are concerned.

Dilute emulsions were prepared by mixing 10 ml of the concentrated Bayol emulsion with 100 ml of Milli-Q water adjusted to a NaCl concentration of 0.01 M. The droplet concentration was found to be  $1.2 \times 10^6$  particles/ml. Zeta potentials of

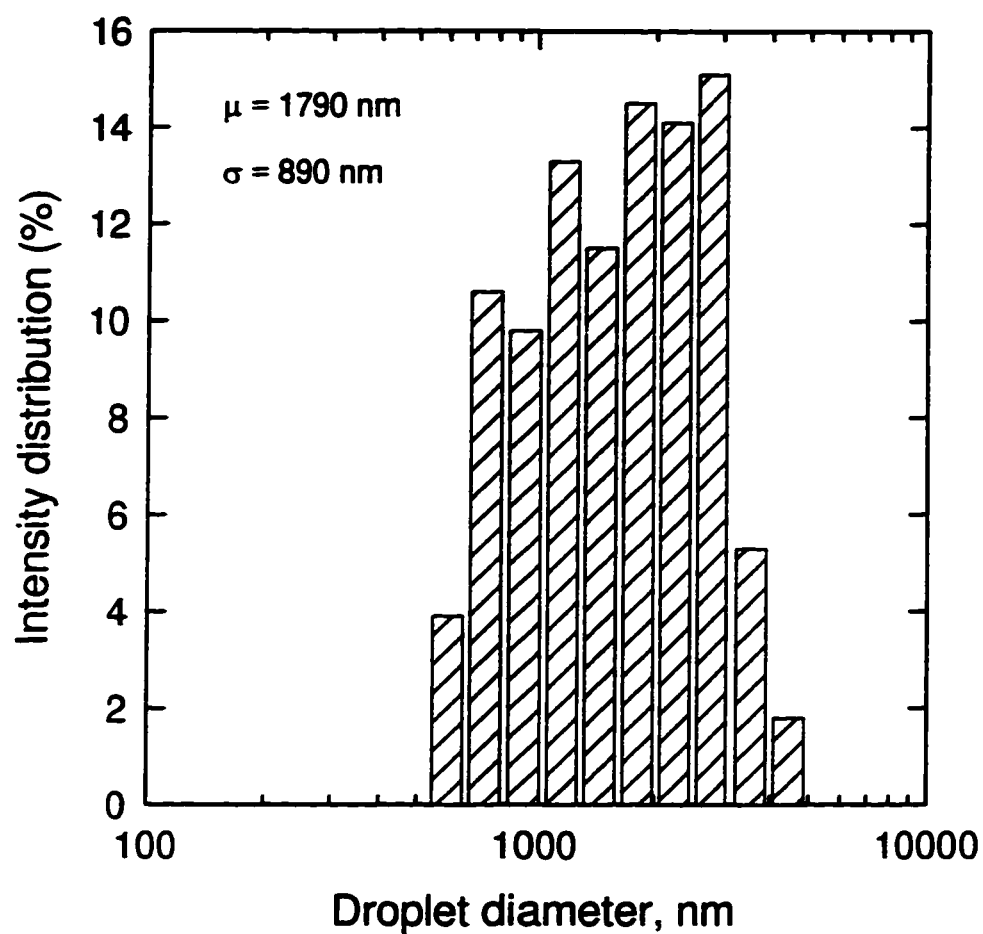


**Figure 6-7.** Representative size distribution of a dilute Bayol oil-in-water emulsion, with a mean droplet diameter of  $\mu = 1.79 \mu\text{m}$ , and a standard deviation of  $\sigma = 0.89 \mu\text{m}$ .

the droplets were measured as a function of bulk pH using the Malvern Zetasizer 3. Figure 6-8 shows the results of these measurements. The droplet zeta potential is effectively zero, considering the margin of error, and that changes in bulk pH had very little effect on the zeta potential measurements. It is believed that this is caused by the use of the Triton-X surfactant. Triton-X is a long chain nonionic surfactant; its nonionic character leads to the negligible droplet zeta potentials that were measured for this system [54].

The Hamaker constant for the Bayol oil {1} - water {3} - glass {2} system was calculated using Equation (3-53). It was found to be  $A_{132} = 2.6 \times 10^{-21}$  J. so that  $Ad=0.11$ .

### 6.2.2 Effect of Reynolds number

Deposition experiments were conducted using the Bayol oil-in-water emulsion described above. It was expected that the Bayol deposition experiments would yield values of Sherwood numbers comparable to the results of the bitumen deposition experiments because of the relatively large droplet size and the lack of a double layer repulsive force in this system. Nearly 30 different runs were conducted at a number of different Reynolds numbers. The syringe pump (shown in Figure 2-1) was used to produce flowrates yielding Reynolds numbers less than 100. The conventional pressure driven system was used for experiments characterized by Reynolds numbers larger than 100. The glass microscope slides were prepared as outlined in Section 5.2.

The results of these experiments are shown in Figure 6-9. The experiments at lower Reynolds numbers ( $10 < Re < 60$ ) yielded Sherwood numbers that were not significantly different from predicted values (the average variation between experiment and theory was less than 30%). At lower deposition rates, the data normally show a certain amount of scatter, suggesting that the Sherwood numbers observed at lower Reynolds numbers for the Bayol experiments are not unreasonable. The scatter in the data at low Reynolds numbers is likely caused by an irregular (pulse) flow that may

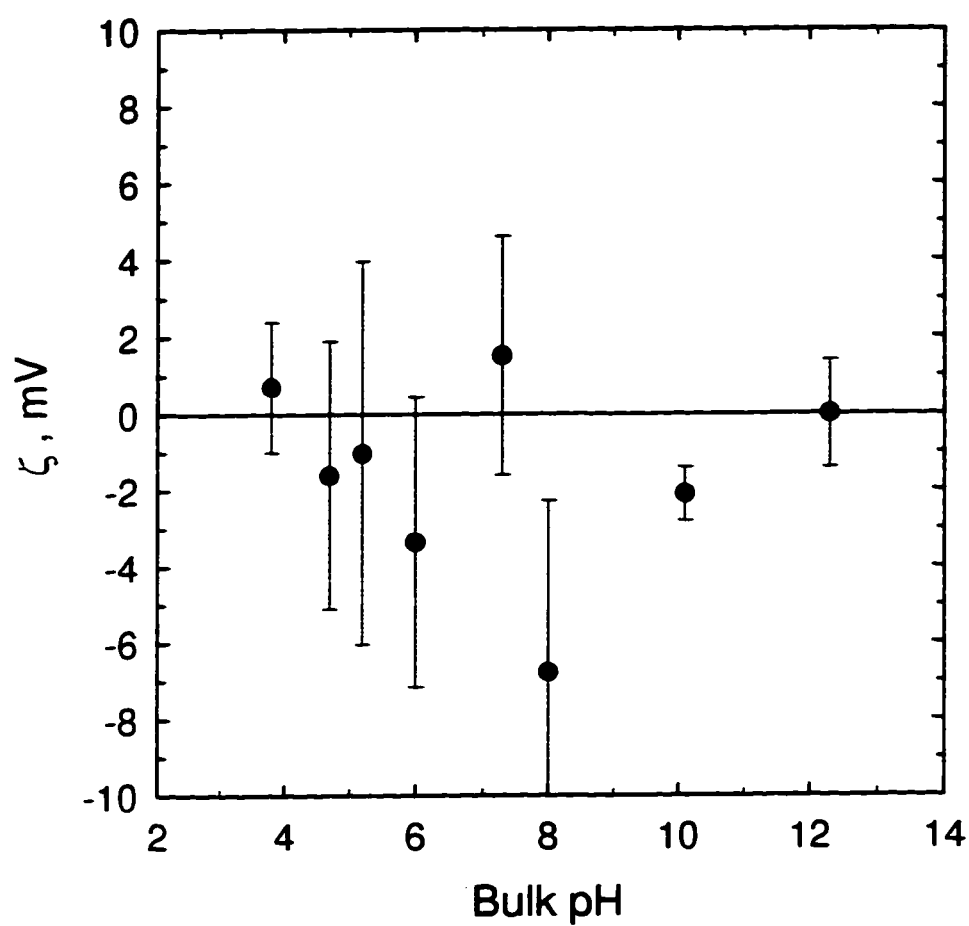


**Figure 6-8.** Variation of zeta potential with bulk pH for Bayol oil emulsions suspended in 0.01M NaCl solution. Results obtained using a Malvern Zetasizer 3.

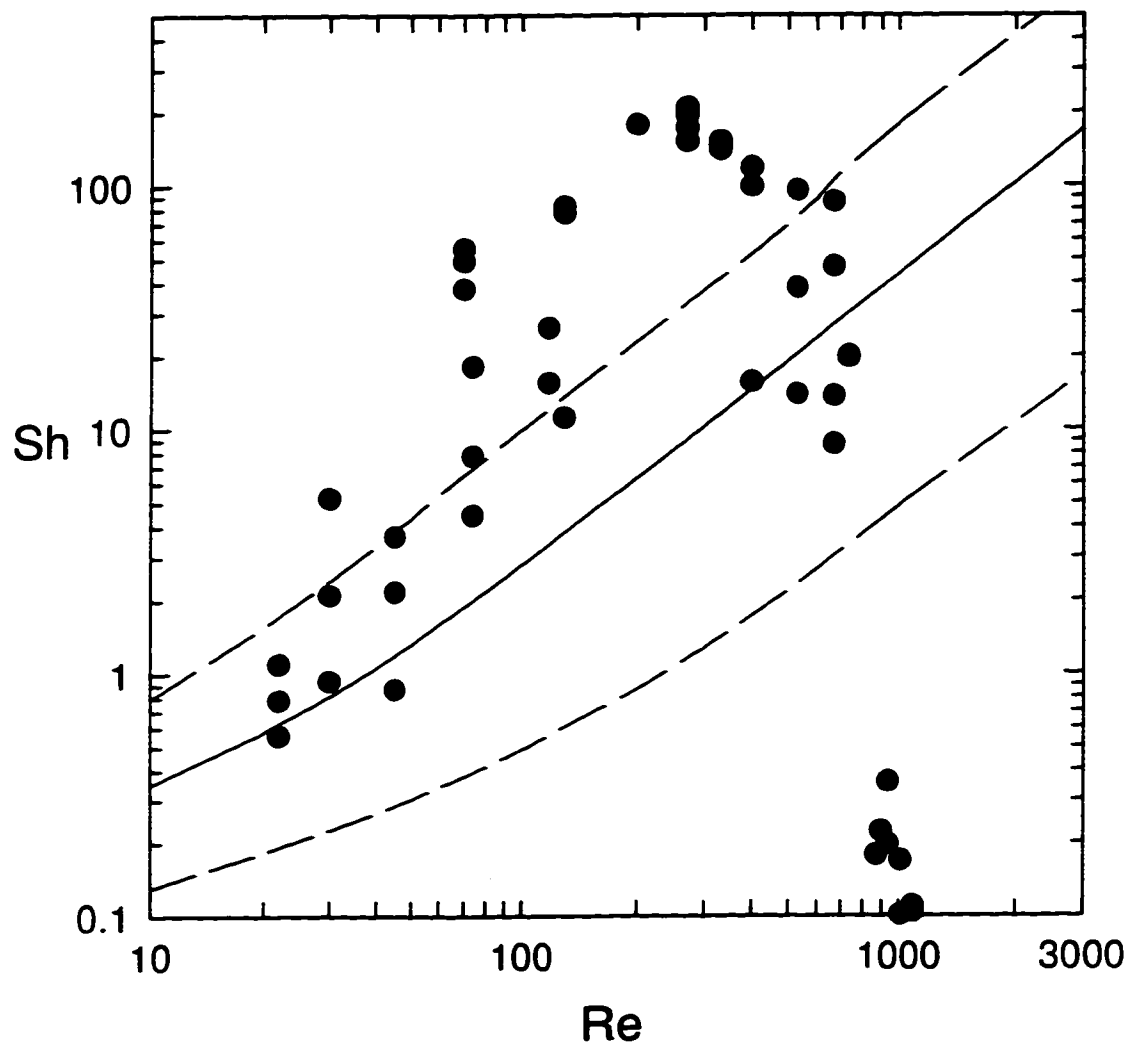


**Figure 6-9.** Dimensionless mass transfer (expressed as Sherwood number) as a function of Reynolds number for  $1.79\ \mu\text{m}$  Bayol oil droplets in  $0.01\text{M NaCl}$  ( $\kappa a = 294$ ). Lines show theoretical mass transfer, obtained by solving Equation (3-30):  $Ad = 0.11$ , (—)  $a = 0.895\ \mu\text{m}$ ; (---)  $a \pm \sigma/2$ ,  $\sigma = 0.890\ \mu\text{m}$ .

occur when the syringe pump is used to generate flow.

The mass transfer rates observed at intermediate Reynolds numbers are much higher. As Figure 6-9 shows, the experimentally determined values of Sherwood number are nearly 3 times larger than the predicted values at Reynolds numbers between 100 and 300. An unexpected trend in mass transfer rates is observed for Reynolds numbers larger than 400. The mass transfer rates begin to decrease as Reynolds number increases, so that the largest value of Sherwood number is observed at a Reynolds number of 280. This trend continues to hold until no deposition is observed at Reynolds numbers of 1100. The theoretical values of Sherwood number increase with increasing Reynolds number, reaching a predicted value of 270 at a Reynolds number of 1000, as is demonstrated in Figure 6-9.

The video tapes of the Bayol oil deposition experiments were reviewed to study the deposition characteristics at lower Reynolds numbers. The droplets did not appear to instantaneously "stick" to the collector surface. They appeared to roll a very short distance along the surface of the collector before they became stationary. The experiments that yielded the largest values of Sherwood number exhibited the lowest number of rolling particles, but were characterized by a very high particle "turnover", meaning that many particles attached for a fraction of a second and then were swept away in the flow. These particles were often replaced by particles that did attach to the collector indefinitely. Once the Reynolds number was increased past 400, the number of particles replacing the detached ones declined significantly. A review of the high Reynolds number experiments showed that most of the droplets attached to the surface in the first five seconds, indicating that the assumption that the flowrate instantaneously reaches its set value is invalid at the highest Reynolds numbers. After a high Reynolds number experiment runs for about 10 s, very little deposition occurs. Moreover, it is impossible to track single particles because the particle velocity is very large.

The behavior described above is very different from the behavior exhibited by the bitumen droplets. In the bitumen deposition experiments, there were almost no instances of particle detachment. Once a bitumen droplet hit the collector surface, it

stayed there, even at the highest Reynolds numbers. Previous studies have indicated that some suspensions exhibit some sort of "induction time" [18 - 20]. If a droplet can stay attached for this certain characteristic time, then it will stay attached indefinitely. Application of this analysis to the bitumen and Bayol oil emulsions would suggest that the bitumen droplets have a very short induction time, while the Bayol oil droplets have a very long induction time. This would account for the droplet movement and high detachment rates observed for the Bayol oil deposition experiments. The variables that would affect the characteristic induction time are not known, although it is certain that the surface characteristics of the dispersed phase are extremely important. The presence of the nonionic surfactant at the surface of the Bayol oil droplets certainly plays an important role in determining the rate of droplet deposition. Steric stabilization caused by nonionic surfactants has been well-documented [54,55]. The weak droplet - collector interactions observed for this system are attributable, at least in part, to the steric stabilization caused by the Triton-X surfactant.

### **6.3 Viscometry standard oil-in-water emulsions**

#### **6.3.1 Emulsion preparation and characterization**

Emulsions were prepared using Cannon Standard Viscometry Oil (Cannon Instrument Co., State College, PA), a refined mineral oil used for viscometer calibration. Two viscometry standard oils, each possessing a different viscosity, were used: a 7.67 mPa s sample and a 3.39 mPa s sample. The physical properties of the 7.67 mPa s sample are:

viscosity = 7.67 mPa s (at 20 °C)

density = 860 kg/m<sup>3</sup>

refractive index = 1.37 (measured)

dielectric constant = 2.2 [56]

The physical properties of the 3.39 mPa s sample are:

viscosity = 3.39 mPa s (at 20 °C)

density = 850 kg/m<sup>3</sup>

refractive index = 1.37 (measured)

dielectric constant = 2.2 [56]

The two different oils were used to prepare emulsions with different dispersed phase viscosities. The preparation method was adopted from research conducted by Schulman and Leja [57], Menon and Wasan [58], and Yan and Masliyah [59], in which fine particles were used to stabilize oil-in-water or water-in-oil emulsions. For each emulsion, 0.3 g of asphaltenes, separated using a procedure described by Menon and Wasan [58] and utilized by Yan and Masliyah [59], were dissolved in a nominal amount of reagent grade toluene (approximately 3 ml). The dissolved asphaltenes were added to a 10 g sample of the oil and mixed thoroughly to disperse the asphaltenes throughout the oil phase. The oil-asphaltene solution was then added to 100 ml of Milli-Q distilled water (pH 10), and this mixture was twice passed through a hand-held homogenizer. The dispersion was placed under a fume hood for an hour to remove any excess toluene, and was then allowed to stand overnight to facilitate creaming of the oversize droplets and thereby reduce the average droplet size in the bulk phase. The size distributions of these emulsions were determined using the Malvern Zetasizer 3, the results of which are shown in figs. 6-10a) and 6-10b).

Before each set of experiments was conducted, a standard, dilute emulsion was prepared by adding a known volume of concentrated emulsion to enough distilled water to make a 1 litre volume of dilute emulsion. The pH and salt concentration for each emulsion were controlled by adding the appropriate amount of 1M NaOH to increase pH (or 1M HCl to decrease pH) along with the appropriate amount of NaCl to the distilled water before the concentrated emulsion was added to the mixture.

The droplet zeta potentials for the dilute 7.67 mPa s mineral oil emulsion are shown as a function of bulk pH in Figure 6-11. The concentration of this emulsion was found to be  $5.8 \times 10^7$  particles/ml ( $\pm 5\%$ ). The concentration of the dilute 3.39

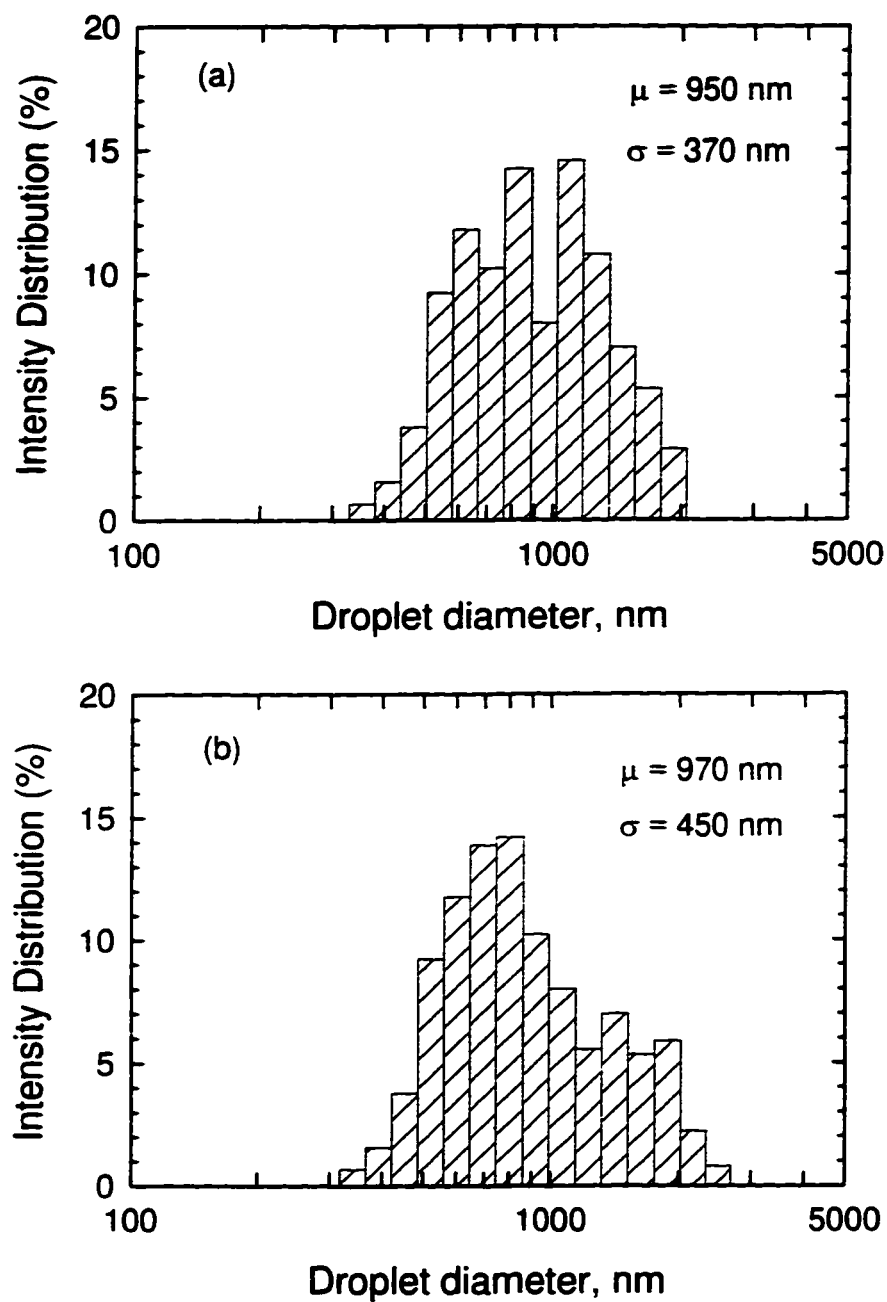


**Figure 6-10.** Representative size distributions of: a) 7.67 mPa s mineral oil-in-water emulsion, with  $\mu = 0.95 \mu\text{m}$  and  $\sigma = 0.37 \mu\text{m}$ ; b) 3.39 mPa s mineral oil-in-water emulsion, with  $\mu = 0.97 \mu\text{m}$  and  $\sigma = 0.45 \mu\text{m}$ .

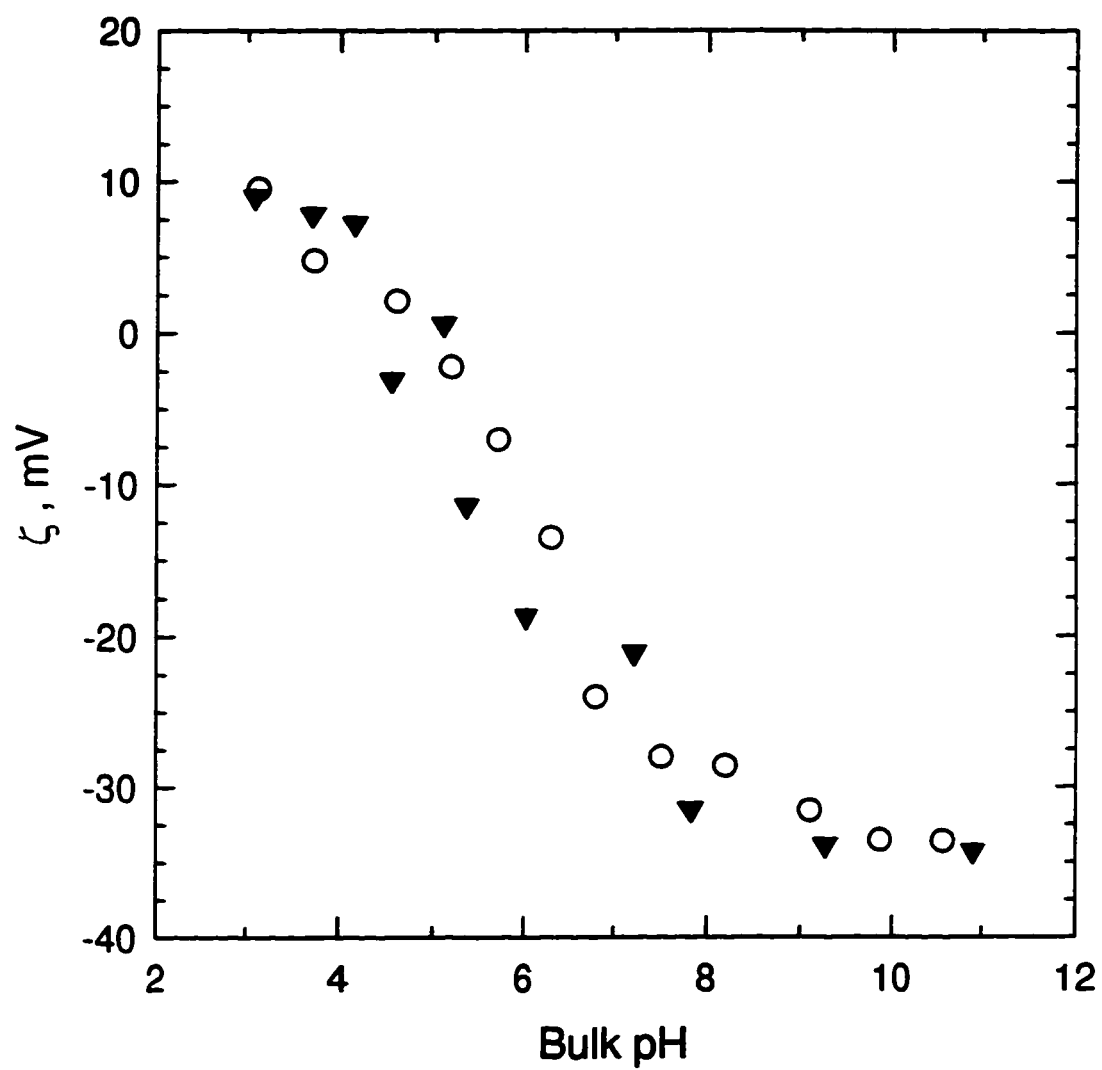


**Figure 6-11.** Measured zeta potentials for the 7.67 mPa-s mineral oil-in-water emulsion (○) and the 3.39 mPa-s oil-in-water emulsion (▼) measured as a function of bulk pH in 0.01M NaCl.

mPa s mineral oil emulsion was found to be  $5.8 \times 10^7$  particles/ml. The zeta potentials of the 3.39 mPa s mineral oil are also shown in Figure 6-11, as a function of bulk pH. As Figure 6-11 illustrates, the relationship between zeta potential and bulk pH is very similar for the two mineral oil emulsions.

The Hamaker constants for the two different viscometry oil systems, were calculated using Equation (3-54). For both systems,  $A_{132} = 2.6 \times 10^{-21}$  J, so that  $Ad=0.11$ .

Table 6-3 shows lists the properties of the 4 different systems studied in this set of experimental work. The different emulsions are labelled A through D. Three of the four emulsions were prepared using the 7.67 mPa s mineral oil emulsion. These emulsions will be referred to in the next section by the letter assigned to them in Table 6-3.

**Table 6-3.** Characterization of Cannon standard viscometry oil emulsions deposition experiments.

System	Oil Viscosity @ 25 C (mPa s)	Mean Particle Diameter ( $\mu\text{m}$ )	[NaCl] (mol/L)	$\kappa a$	Bulk pH	$\zeta_p$ (mV)	$\zeta_c$ (mV)	DI
A	7.67	0.95	0.01	156	7.3	-23.5	-65	122
B	7.67	0.95	0.01	156	3.1	+9.8	-26	-20.4
C	7.67	0.95	0.1	494	8.1	-14.3	-30	34.3
D	3.39	0.97	0.01	160	7.2	-22.3	-65	118

### 6.3.2 Effect of Reynolds number

Deposition experiments were conducted using the viscometry standard oils, for the conditions described in Table 6-3. Figure 6-12 shows the SRCD diagrams for the viscometry oil emulsions. Systems A, B, and C (figs. 6-12a - 6-12c) had the same dispersed phase viscosity; System D (Figure 6-12d) had a lower dispersed phase viscosity. Systems A, C, and D all exhibited positive values of  $DI$ , meaning that the electric double layer force between a droplet and the collector was repulsive. System B had a negative value for  $DI$ , indicating that  $\zeta_p$  and  $\zeta_c$  had opposite signs, and thus there was an attractive double layer interaction between a droplet and the collector. For the cases in which  $DI$  was positive, the deposition rate decreased with time at high Reynolds numbers. This is clearly shown for  $Re \geq 800$  in figs. 6-12a, 6-12c, and 6-12d, where it can be seen that the coating densities become nonlinear with time at high Reynolds numbers, by comparing the position of the symbols with the position of the linear regression that represents the initial slope of each experiment. The nonlinearity of the high Reynolds number runs is normally attributed to particle blocking effects that occur when the coating density is very high. However, in these experiments, there is evidence that suggests that some other mechanism causes the nonlinearity in the coating densities with time at high Reynolds numbers. Consider figs. 6-12a and 6-12b: the maximum coating density shown in either diagram is approximately  $20,000 \text{ particles/mm}^2$ , corresponding to  $Re=800$  in Figure 6-12b. The coating density does not become nonlinear with time for this run, even though the coating density is nearly 5 times larger than the maximum coating density attained in the experiments conducted at the same Reynolds number ( $Re=800$ ) using System A, as shown in Figure 6-12a. If particle blocking effects were important in these experiments, they should be most significant for System B, which has the largest observed coating densities of any of the four viscometry oil systems. It is therefore more appropriate to describe the nonlinearity that occurs in Systems A, C, and D in terms of a characteristic induction time, as was discussed previously when the Bayol oil emulsion experiments were analyzed. If the characteristic induction time

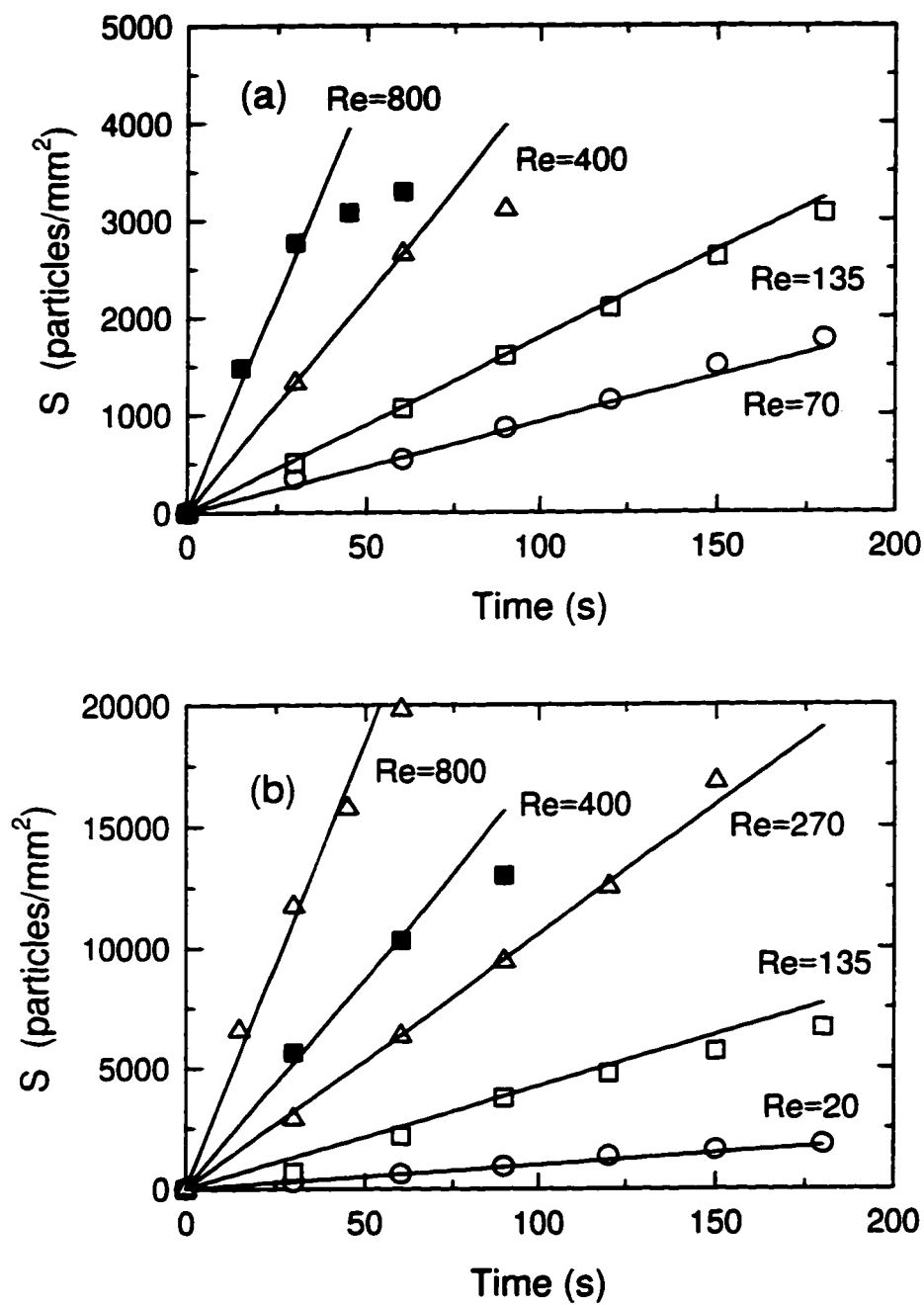


**Figure 6-12.** Stagnation region coating density as a function of time for viscometry standard oil emulsions: (a) repulsive double layer force (System A); (b) attractive double layer force (System B).

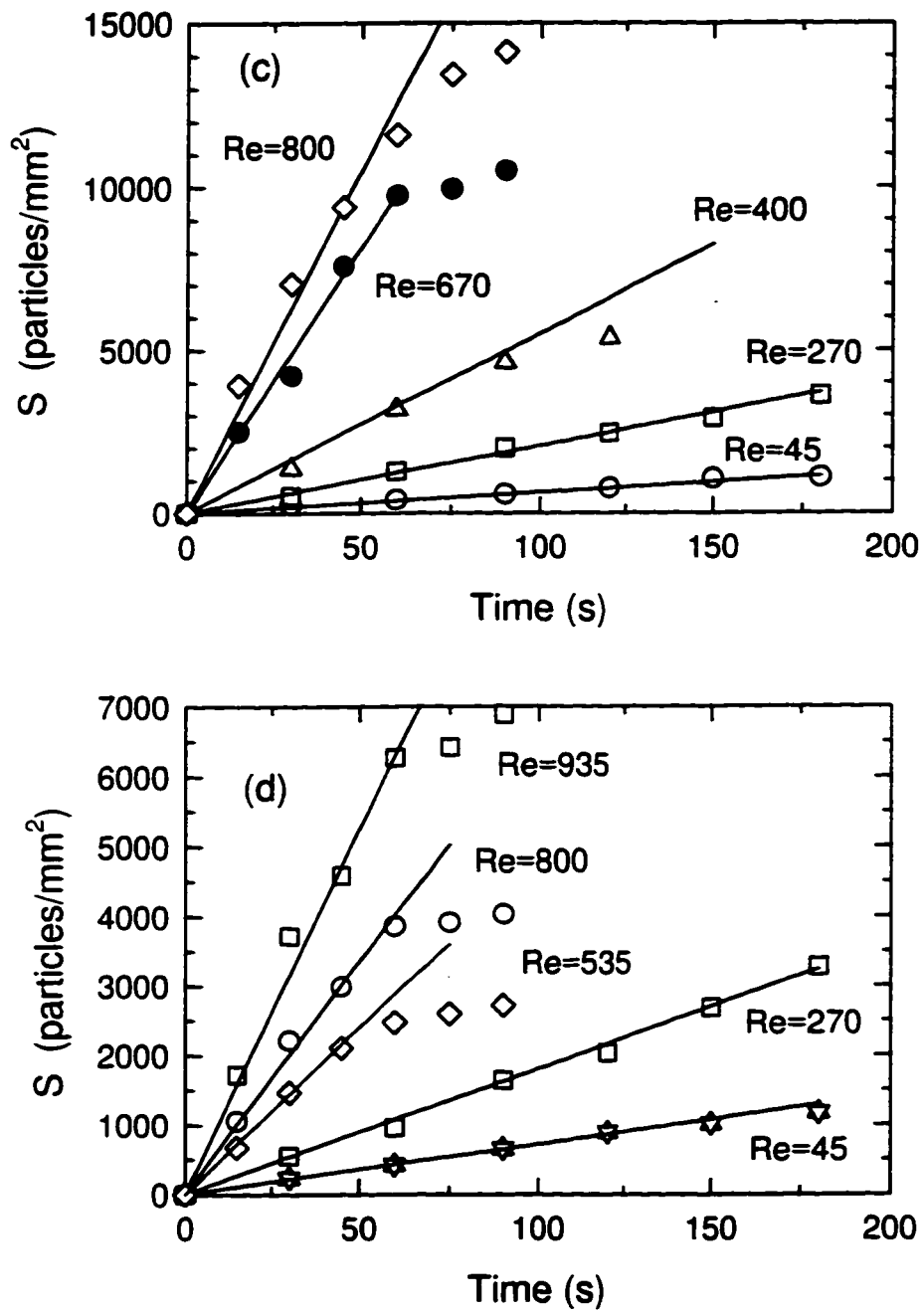


**Figure 6-12.** Stagnation region coating density as a function of time for viscometry standard oil emulsions: (c) increased NaCl concentration (System C); (d) decreased dispersed phase viscosity (System D).

assumption is valid, it would make sense that the attractive double layer force present in System B would shorten the induction time, thus creating the possibility for the higher coating densities shown in Figure 6-12b.

The Sherwood number - Reynolds number relationship for the viscometry oil emulsions is shown in figs. 6-13a through 6-13d for systems A through D (as characterized in Table 6-3). The lines shown in figs. 6-13 were determined by solving Equation (3-30). The difference between the theoretical predictions for all four sets of experimental conditions were negligible, meaning that theoretically, there should be no difference in deposition rates for all four systems. This prediction is not surprising for Systems A and D, as there is no part of the model that accounts for dispersed phase viscosity. Comparison of System A (Figure 6-13a) with System D (Figure 6-13d) shows that there is no recognizable dependence of the deposition rate on the dispersed phase viscosity. The Sherwood numbers for the lower viscosity runs (System D) were very similar to those having almost twice the dispersed phase viscosity (System A). All other parameters for Systems A and D were almost identical.

For system B (Figure 6-13b), where  $\zeta_p$  and  $\zeta_c$  had opposite signs, good agreement between the observed and theoretical results was obtained. The average difference between experimental results and predicted mass transfer rates was less than 30%. For the other three sets of experiments (figs. 6-13a, 6-13c, and 6-13d), the deposition rates predicted by DLVO theory were significantly higher than the observed deposition rates. The experimental results for System A were, on average, only 1/2 as large as predicted values of Sherwood number. The observed mass transfer rates for System D were in most cases nearly five times lower than predicted values of Sherwood number at any given Reynolds number. Salt concentration did have some effect on the deposition rate, as larger Sherwood numbers were observed for the 0.1M concentration of System C (Figure 6-13c) than for Systems A or D, which had salt concentrations of 0.01M. The experimental results and the corresponding theoretical predictions for System C differed by approximately 60%. The experimental results obtained for Systems A, C, and D contradict the theoretical predictions of droplet deposition rates for these systems: the experimentally determined deposition rates are

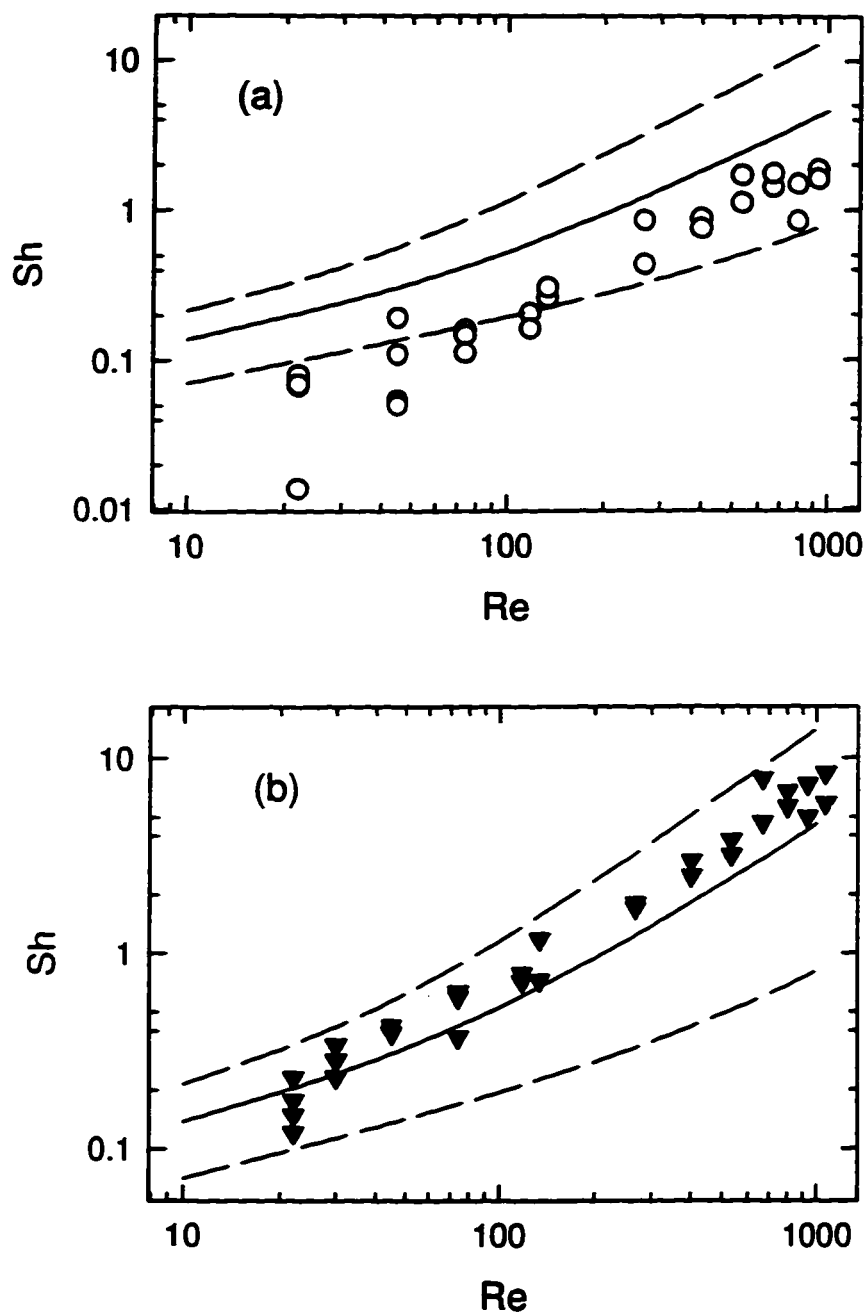


**Figure 6-13.** Dimensionless mass transfer (expressed as Sherwood number) as a function of Reynolds number for viscometry standard oil emulsions. (a) - System A; (b) - System B. Experimental conditions listed in Table 6-3. Lines in each figure show theoretical mass transfer, calculated from numerical solution of Equation (3-30):  $Ad=0.11$ , (—)  $a$ ; (---)  $a \pm \sigma/2$ .

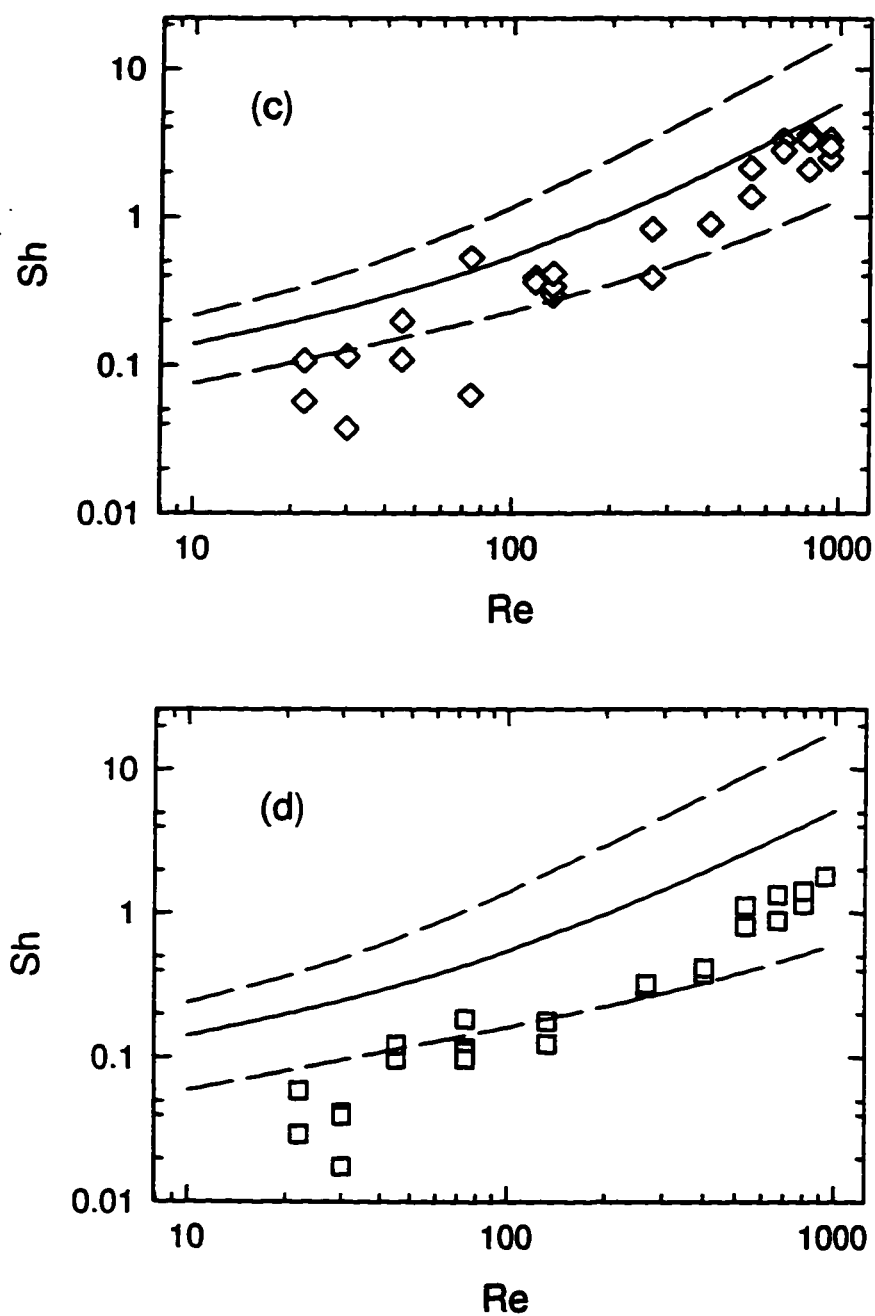


**Figure 6-13.** Dimensionless mass transfer (expressed as Sherwood number) as a function of Reynolds number for viscometry standard oil emulsions. (c) - System C; (d) - System D. Experimental conditions listed in Table 6-3. Lines in each figure show theoretical mass transfer, calculated from numerical solution of Equation (3-30):  $Ad=0.11$ , (—)  $a$ ; (---)  $a \pm \sigma/2$ .

different for each system. Theoretical predictions indicate that there should be no difference in droplet deposition rates among all four systems. The results of these experiments suggest that the deposition behavior of the viscometry oil emulsions is more complicated than the relatively straightforward DLVO theory can account for.

Systems A, C, and D exhibited a much greater incidence of particle detachment than did System B. For Systems A and D, particle detachment became so pronounced at higher Reynolds numbers that deposition seemed to nearly cease beyond a certain Reynolds number (see figs. 6-12a and 6-12d). A more extensive analysis of the rate of particle detachment occurring in System A and in the bitumen deposition experiments will be presented in Section 6.5.2. Particle blocking effects and further comments concerning characteristic induction times will also be discussed in Section 6.5.2.

### **6.3.3 Effect of electrolyte concentration**

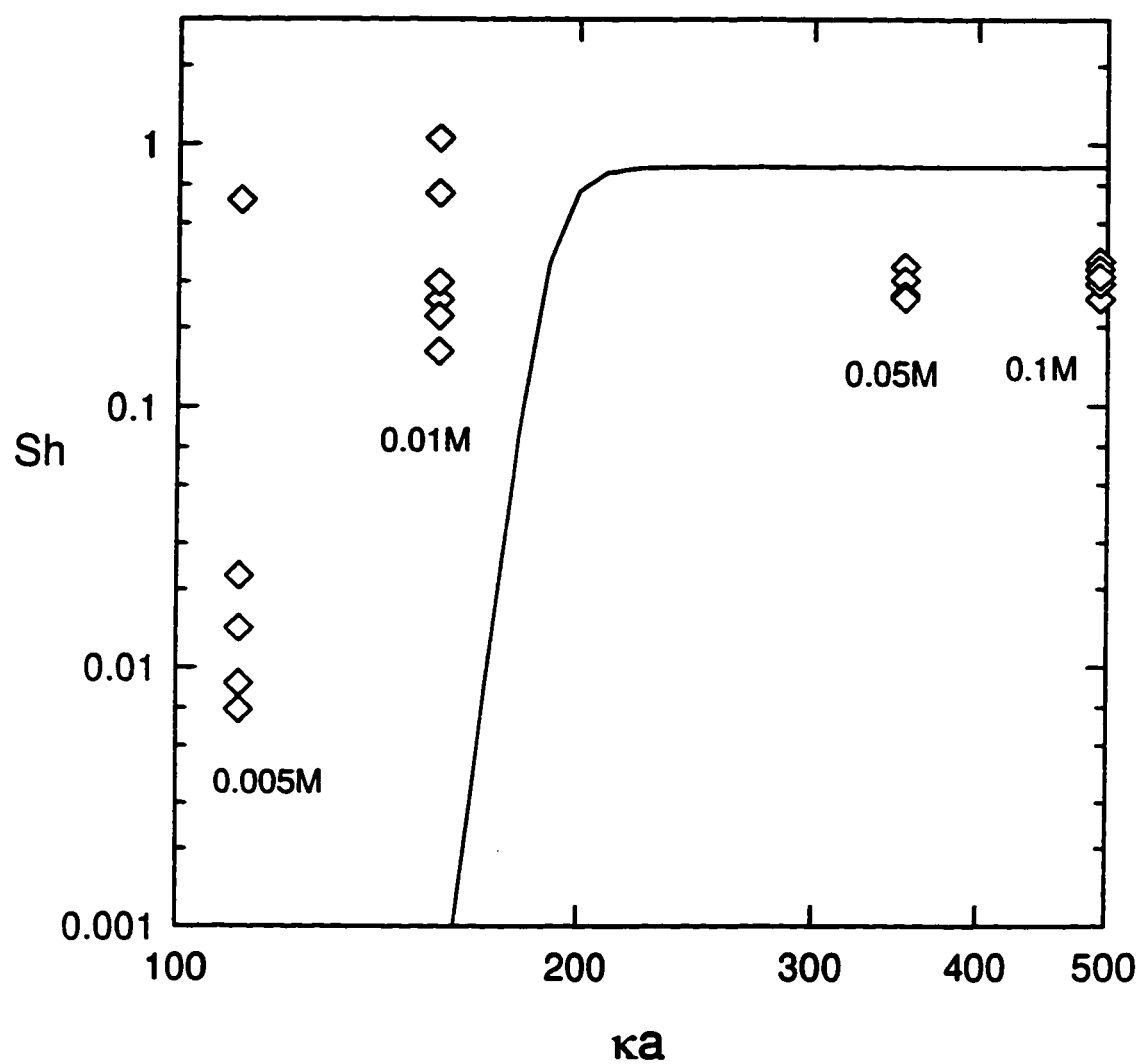
Experiments were conducted in which  $\kappa a$  was changed by varying the bulk NaCl concentration, while keeping the pH constant. The experiments are exactly the same as those conducted using bitumen emulsions, discussed in Section 6.1.4. Only one viscometry standard oil, the 7.67 mPa s sample, was used in these experiments. The change in NaCl concentration for each set of experiments meant that  $\kappa a$ ,  $\zeta_p$ , and  $\zeta_c$  were different for each set of experiments. The three parameter ISG model was used to predict the change in collector zeta potential. It was not used to predict changes in the viscometry oil zeta potential because the range of values exhibited by the viscometry oil was rather narrow (see Figure 6-11) and the relationship between the parameters of the ISG model and the surface properties of the viscometry oil droplets could not be verified. Instead, the viscometry oil zeta potentials were measured with the Malvern Zetasizer 3 each time the salt concentration was changed and then entered directly into the computer model.

Figure 6-14 shows how the deposition of viscometry oil droplets varied with changes in electrolyte concentration. Although deposition rates decreased at very low  $[\text{NaCl}]$ , overall there seems to be a weak relationship between the flux to the collector surface and the double layer parameter ( $\kappa a$ ) for the viscometry oil emulsion. The solid line in Figure 6-14 shows the calculated relationship between  $Sh$  and  $\kappa a$ . As the theory line indicates, deposition rates should fall off sharply below  $\kappa a=200$ , and should be 3 orders of magnitude lower than the maximum deposition rate once  $\kappa a=160$ . The experimental results do not follow this pattern. The symbols in Figure 6-14 show that there is a weak dependence of Sherwood number on  $\kappa a$ . For  $\kappa a=110$  (0.005M NaCl), it is true that the deposition rates have decreased by an order of magnitude; however, theory predicts that no deposition should occur at all. The discrepancy between observed and calculated viscometry oil droplet deposition rates in experiments where the NaCl concentration was changed is consistent with the lack of agreement that occurs between theory and experiment for the Sherwood number - Reynolds number runs discussed in the previous section. Both types of experiments indicate that the behavior of the viscometry oil emulsions is too complex to be accurately modelled using DLVO theory.

#### 6.3.4 Droplet - droplet coagulation studies

The discrepancies between the results calculated using DLVO theory and the results of the viscometry standard oil emulsion deposition experiments suggest that the viscometry oil emulsion system cannot be described by DLVO theory; more specifically, that some other mechanism or non-DLVO forces control the rate of deposition of the oil droplets.

It was decided that further tests were required to determine the applicability of DLVO theory to the mineral oil emulsions. Following the work of Takamura *et al.* [60] and Takamura and Chow [61] for bitumen systems, stability diagrams for the



**Figure 6-14.** Experimentally determined effect of  $ka$  parameter on mass transfer to collector surface for a 7.67 mPa s viscometry standard oil emulsion in various concentrations of NaCl solutions,  $Re=118$ ,  $pH=9$ . Solid line shows theoretical mass transfer.

viscometry oil emulsion were calculated using DLVO theory. These diagrams, Figures 6-15a and 6-15b, represent the total interaction potential ( $\phi_T$ ) between two viscometry oil emulsion droplets as calculated from the following expressions:

$$\phi_T(h) = \phi_A(h) + \phi_R(h) \quad (6-1)$$

where

$$\phi_A(h) = \frac{-A_{132}a}{12h} \left[ 1 - \frac{5.32h}{\lambda} \ln \left( 1 + \frac{\lambda}{5.32h} \right) \right] \quad (6-2)$$

and

$$\phi_R = 2\pi a y^2 \frac{nkT}{\kappa^2} \left[ \ln \frac{1 + \exp(-\kappa h)}{1 - \exp(-\kappa h)} + \ln(1 - \exp(-2\kappa h)) \right] \quad (6-3)$$

The dimensionless potential,  $y$  is defined as

$$y = \frac{e\zeta_p}{kT} \quad (6-4)$$

The expressions for  $\phi_A$  and  $\phi_R$  shown above are the same as those used by Takamura and Wallace [62].

The stability diagrams given in Figures 6-15a and 6-15b show how the interaction potential between two particles changes when the particles approach one another, as a function of electrolyte concentration and valence number. The diagrams can be interpreted as follows [60]:

- (i) For  $\phi_T > 25$  kT, a stable emulsion exists and the droplets will not flocculate (Curves 1 in Figures 6-15a and 6-15b).
- (ii) For  $\phi_T > 25$  kT, and a secondary minimum deeper than -5 kT, the emulsion will become weakly coagulated, meaning that the droplets will flocculate but will be redispersed by vigorous shaking (Curve 2 in Figure 6-15a).

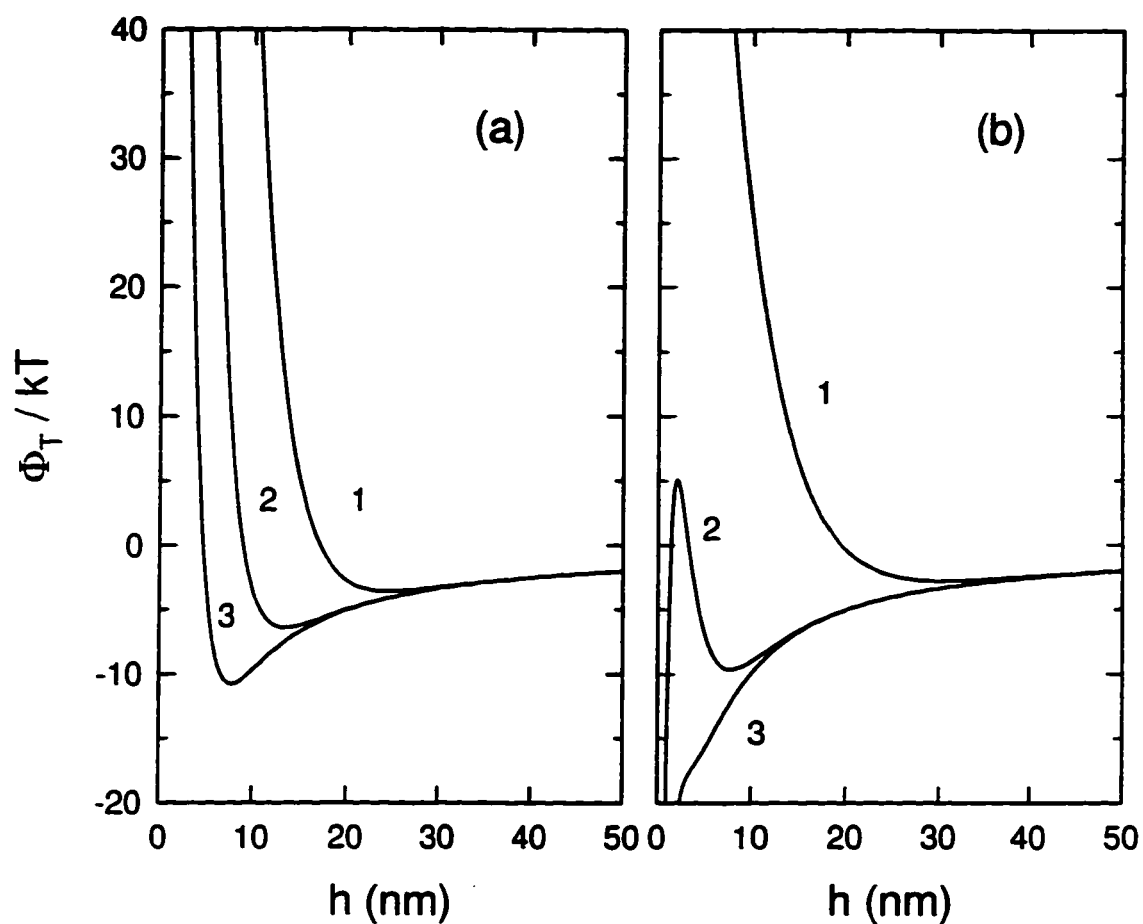


**Figure 6-15.** Droplet - droplet interaction energy diagrams for 0.95  $\mu\text{m}$  viscometry standard oil emulsion as a function of interdroplet separation distance,  $h$ . (a) NaCl solution: Curve 1, 0.01M; 2, 0.025M; 3, 0.05M. (b)  $\text{CaCl}_2$  solution: Curve 1, 0.001M; 2, 0.006M; 3, 0.009M.

(iii) For  $\phi_T < 25$  kT, the oil droplets will become strongly coagulated, meaning that the droplets will not redisperse, even with vigorous shaking (Curve 3 in Figure 6-15b).

The results of the viscometry oil emulsion coagulation experiments can thus be interpreted using the stability criteria defined above and by Figure 6-15. In the coagulation experiments, a sample of the concentrated emulsion is dispersed in a vial containing an electrolyte solution of known concentration. The sample is then shaken and allowed to stand. The stability of the emulsion is judged as follows:

- (i) Stable: no coagulation occurs, and the sample remains cloudy.
- (ii) Weakly coagulated: sample becomes transparent as droplets flocculate and rise to the surface of the continuous phase; however, if the sample is shaken again, the droplets are redispersed and the sample becomes cloudy once again.
- (iii) Strongly coagulated: the emulsion becomes transparent almost immediately upon the cessation of shaking. Coagulated droplets can actually be seen at the air-water interface, and a second shaking only momentarily redisperses the droplets.

The results of coagulation experiments using  $\text{CaCl}_2$  are shown in Figure 6-16. The vial on the left in Figure 6-16 shows a sample of the emulsion dispersed in a 0.009M  $\text{CaCl}_2$  solution. The sample remained cloudy, even upon shaking. This appears to be a stable emulsion, even though the stability diagram (Curve 3 in Figure 6-15b) predicts that strong coagulation should occur. Since the emulsion did not coagulate at the predicted  $\text{CaCl}_2$  concentration, further experiments were conducted in order to determine the critical coagulation concentration for the viscometry oil emulsion. It was discovered that the emulsion became strongly coagulated in a 0.04M  $\text{CaCl}_2$  solution, as indicated by the transparency of the sample in the vial shown on the right in Figure 6-16. The critical coagulation concentration of the viscometry oil emulsion was much higher than that predicted by DLVO theory.



**Figure 6-16.** Critical flocculation concentration experiments on viscometry standard oil emulsion. (left) The emulsion after it has been dispersed in 0.009M  $\text{CaCl}_2$  solution. No flocculation occurs. (right) The emulsion after it has been dispersed in 0.04M  $\text{CaCl}_2$  solution. Primary flocculation occurs (droplets do not redisperse even upon agitation).

This analysis provides some information about the viscometry oil emulsion system. It seems evident that some non-DLVO force is acting on the oil droplets, providing them with increased stability.

## **6.4 Pentadecane-in-water emulsions**

### **6.4.1 Emulsion preparation and characterization**

Initially, 5 g of pentadecane was blended with 100 ml of Milli-Q water using a hand held homogenizer, producing a pure, surfactant-free oil-in-water emulsion. The properties of the pentadecane are

$$\text{density} = 688 \text{ kg/m}^3$$

$$\text{viscosity} = 2.9 \text{ mPa s}$$

$$\text{refractive index} = 1.431 \text{ [63]}$$

$$\text{dielectric constant} = 2.04 \text{ [63]}$$

Unfortunately, the emulsion was not stable enough to use in the deposition experiments. The average droplet size changed too quickly with time for the first 7 - 8 hours. When the droplet size did stabilize, the droplets were too small to be observed clearly in the deposition experiments.

A stable pentadecane-in-water emulsion was prepared by following a procedure similar to the one used to produce stable viscometry oil-in-water emulsions. Briefly, the procedure is as follows: a 5 g of pentadecane was combined with an asphaltene solution made from 0.15 g of dried asphaltene {see Yan and Masliyah [59]} and ca. 1 ml of toluene. The pentadecane-asphaltene-toluene solution was stirred continuously for an hour to promote the transfer of asphaltene to the pentadecane. This mixture was placed under a fume hood for one hour in order to remove the toluene from the mixture. At this point the pentadecane-asphaltene mixture showed some signs of asphaltene aggregation in the form of sediment in the bottom of the beaker. Samples

of the pentadecane were observed under a microscope to check for further signs of asphaltene aggregation. No aggregates were visible at 400 X magnification, indicating that any asphaltene aggregates present in the continuous pentadecane phase were less than 100 nm in size.

The pentadecane-asphaltene solution was then mixed with 50 g Milli-Q. A pentadecane-in-water emulsion was then prepared using the hand held homogenizer. The pentadecane-water mixture was put through the homogenizer three times. The resulting emulsion was placed in a separatory vessel and allowed to stand for 8 hours, after which time the bottom 3/4 of the separatory vessel's contents was removed and placed in a clean, dry container. The size distribution of this emulsion was measured several times over a period of 8 hours. No significant change in size distribution occurred. A typical size distribution analysis, conducted using the Malvern Zetasizer 3, is shown in Figure 6-17.

Dilute pentadecane emulsions were prepared using the same procedure used to prepare the dilute bitumen and viscometry oil emulsions, where a small sample of the concentrated emulsion was added to a large volume of pH adjusted, electrolyte solution. A number of emulsions possessing different pH values and NaCl concentrations were prepared and the droplet zeta potentials of each emulsion were measured with the Malvern Zetasizer 3. Figures 6-18a and 6-18b show the results of these measurements. Figure 6-18a shows the change in droplet zeta potential with pH, in a 0.01M solution. Figure 6-18b shows the change in droplet zeta potential with [NaCl], for pH=5. The solid lines in Figures 6-18a and 6-18b depict regression analyses that were conducted on the data so that analytical expressions for the  $\zeta_p$  - pH and  $\zeta_p$  - [NaCl] relationships could be developed. The resulting analytical expressions are

$$\zeta_p = -60(1 - 4.3 \exp(-0.37 \text{pH})) \quad (6-5)$$

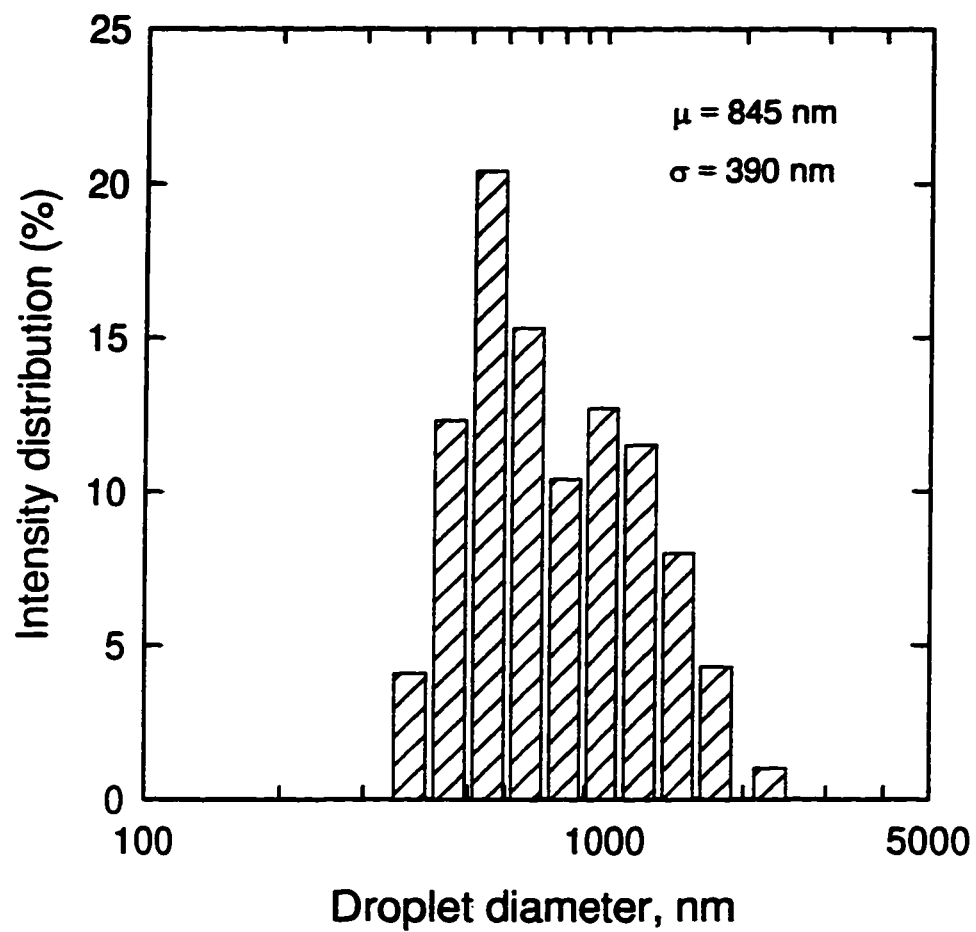


**Figure 6-17.** Representative size distribution of pentadecane-in-water emulsion, with  $\mu=0.84 \mu\text{m}$  and  $\sigma = 0.39 \mu\text{m}$ .

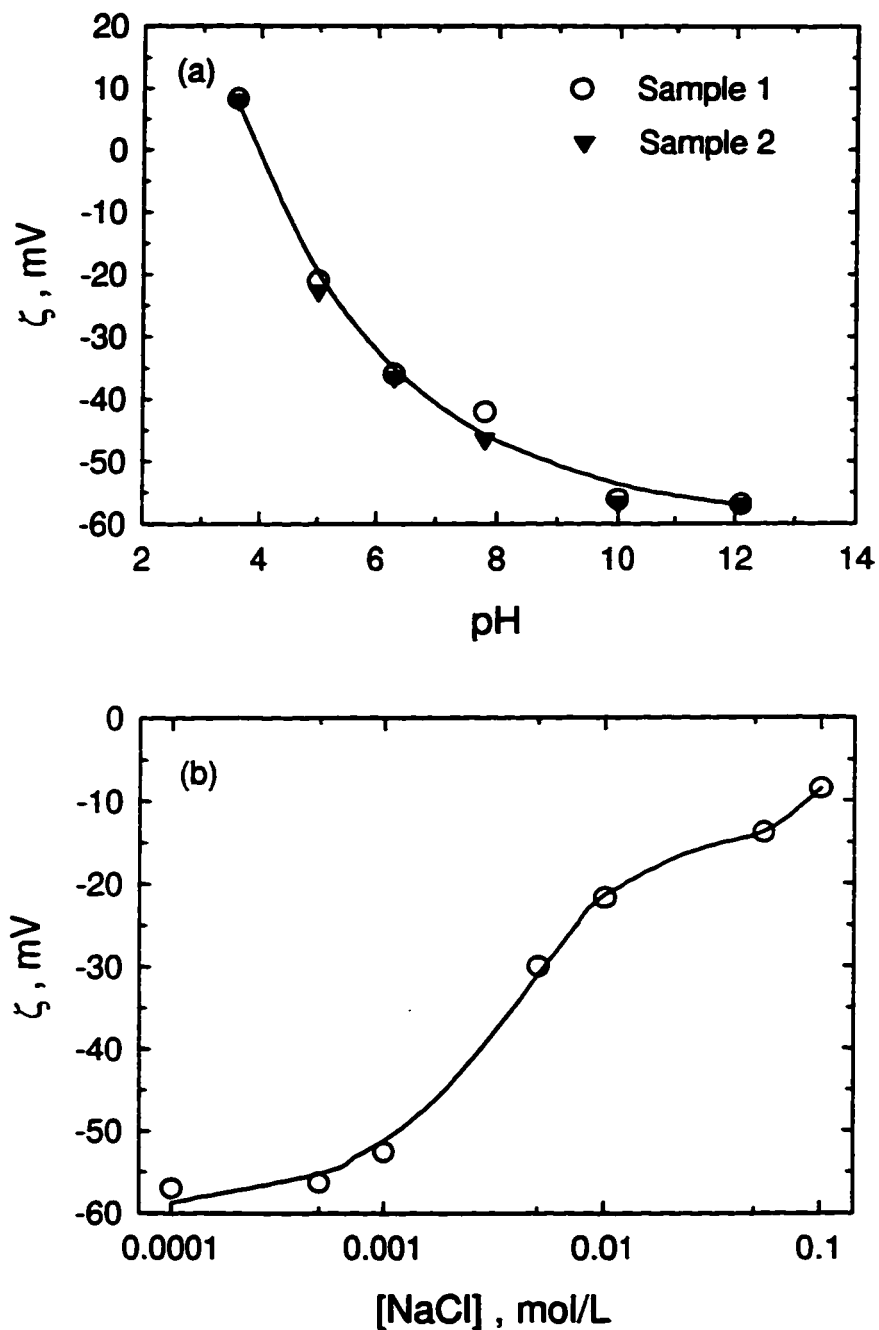


**Figure 6-18.** Measured (symbols) and nonlinear regression analysis (solid lines) of the variation of pentadecane droplet zeta potential with a) bulk pH in a 0.01M NaCl solution and b) [NaCl] for a constant bulk pH (pH=5). Analytical expression describing the variation of  $\zeta_p$  with pH given by Equation (6-5). Analytical expression describing the variation of  $\zeta_p$  with [NaCl] given by Equation (6-6).

for bulk pH values from 4 to 12, inclusive, in a 0.01M NaCl solution; and

$$\zeta_p = -43 \exp(-220[\text{NaCl}]) - 16.7 \exp(-66.9[\text{NaCl}]^2) \quad (6-6)$$

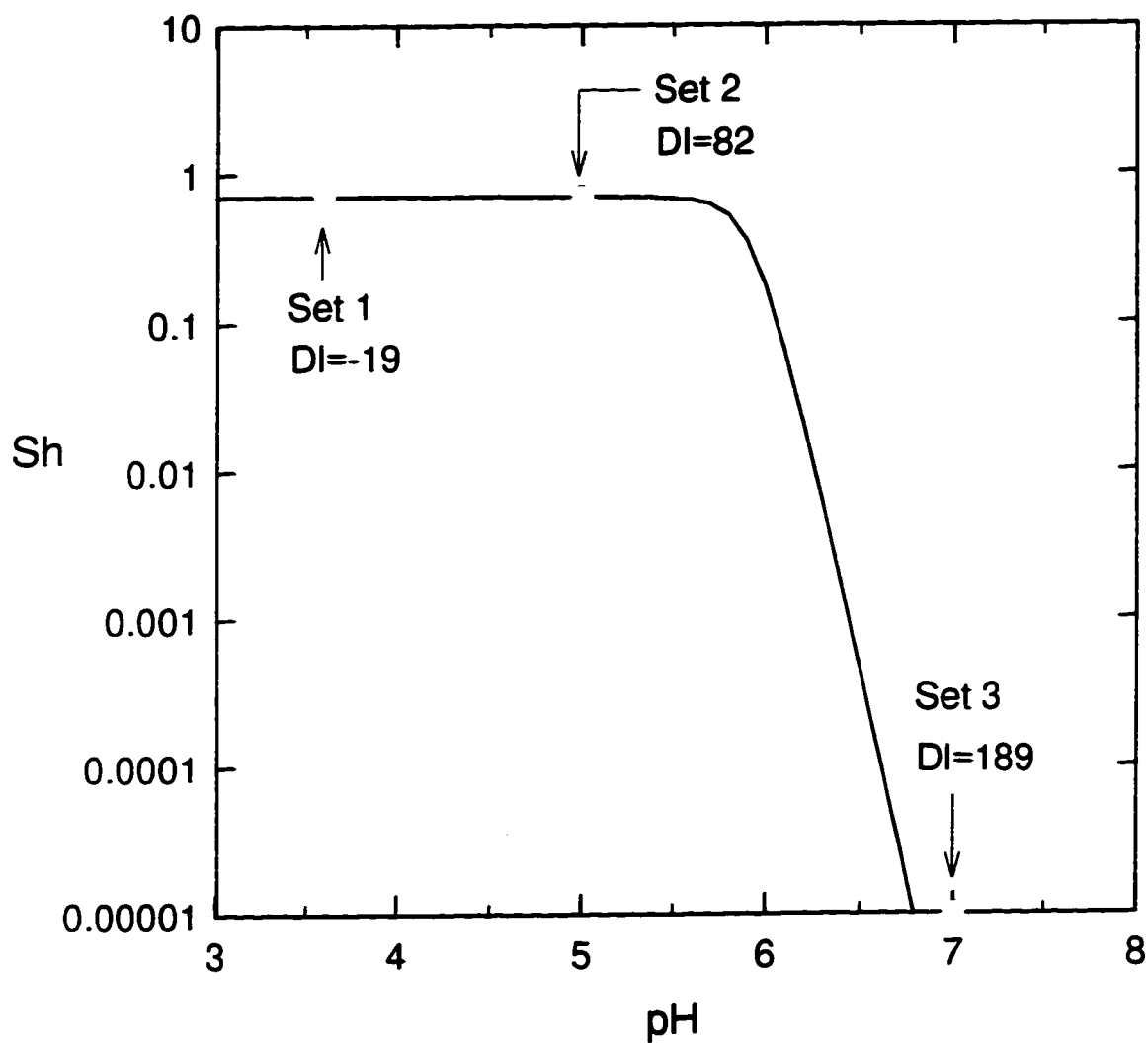
for NaCl concentrations from 0.0001 to 0.1M, inclusive, with a bulk pH of 5.

Equations (6-5) and (6-6) were used in the computer model.

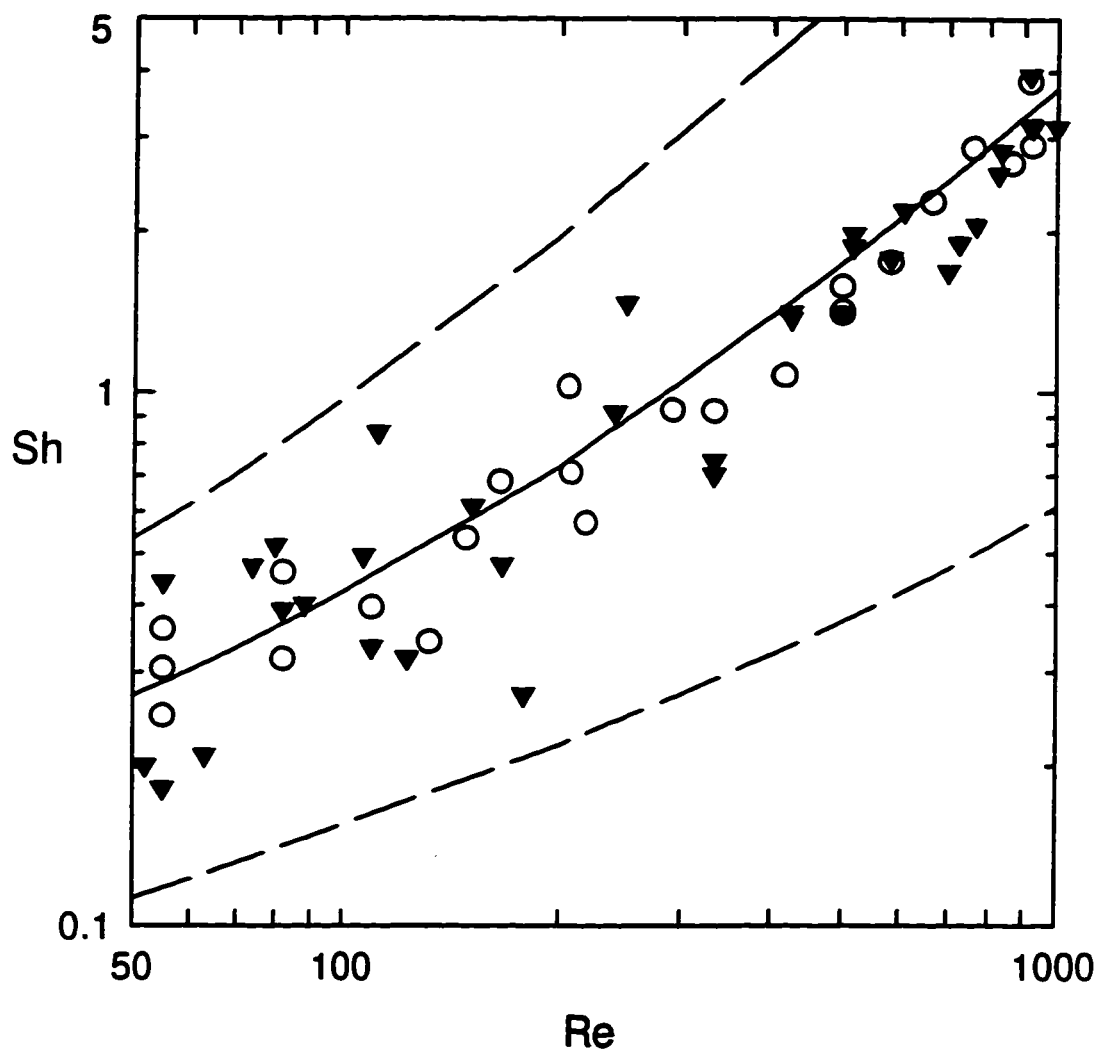
#### 6.4.2 Effect of Reynolds number

Figure 6-19 shows the results of a numerical simulation using the  $\zeta_p$  - pH relationship described by Equation (6-5), for a 0.01M NaCl solution and a mean droplet diameter of 0.84  $\mu\text{m}$  at a Reynolds number of 100. The changing zeta potentials of the collector surface were accounted for using the ISG model. From Figure 6-19, it is clearly seen that the theory predicts a constant deposition rate below a bulk pH of 6, beyond which the deposition rate rapidly decreases. Using these results, we determined the experimental conditions that would most clearly illustrate the ability of our theoretical analysis to predict actual results.

Based on the predictions shown in Figure 6-19, three sets of experiments were conducted to allow us to study the relationship between the experimentally determined values of Sherwood number and the Reynolds number. The characteristic data describing each set of experiments (sets #1 through #3) are given in Table 6-4. The results of sets #1 and #2 are shown in Figure 6-20. The solid line in Figure 6-20 represents the theoretical prediction of the Sherwood number using the average particle radius; the dashed lines represent one standard deviation above and below the average particle radius. The experimental conditions described in Table 6-4 for sets #1 and #2 yield identical theoretical predictions of Sherwood number, meaning that the set of lines shown in Figure 6-20 accurately represent both sets of experiments. A number of observations can be drawn from Figure 6-20: first, the mass transfer rates for both sets #1 and #2 exhibit a dependence on Reynolds number that is very similar to that predicted by theory. Second, Figure 6-20 indicates that there is no significant



**Figure 6-19.** Predicted variation of dimensionless mass transfer rate (expressed as Sherwood number) with solution pH for a pentadecane emulsion;  $\mu=0.84 \mu\text{m}$ ;  $0.01\text{M}$  NaCl solution;  $Re=100$ ;  $Ad=0.11$ .



**Figure 6-20.** Dimensionless mass transfer (expressed as Sherwood number) as a function of Reynolds number and bulk pH for 0.84  $\mu\text{m}$  pentadecane droplets in 0.01M NaCl. (○) - Set #1 (pH=3.6); (▼) - Set #2 (pH=5). Experimental conditions described in Table 6-4. Lines show theoretical values of Sherwood number, obtained by solving Equation (3-30):  $Ad=0.11$ , (—)  $a = 0.42 \mu\text{m}$ ; (---)  $a \pm \sigma/2$ ,  $\sigma = 0.39 \mu\text{m}$ .

**Table 6-4.** Characterization of pentadecane deposition experiments I: 0.01M NaCl:  $a=0.42\ \mu\text{m}$ ;  $c_0=1.5 \times 10^7$  droplets/ml.

Set #	pH	$\zeta_p$ (mV)	$\zeta_c$ (mV)	DI	Da
1	3.6	7.62	-35.3	-19.3	-2.85
2	5	-19.7	-58.9	82.1	1.32
3	7	-40.6	-65.9	189	0.239

difference between the two sets of results, even though the two sets are characterized by electrostatic forces that are opposite in sign. For set #1, the electric double layer force between a droplet and the collector is attractive ( $DI = -19$ ), while the particle-collector interaction is repulsive for set #2 ( $DI=80$ ). Without the benefit of Figure 6-19, one would most likely expect set #1 to show higher rates of mass transfer than set #2. However, as Figure 6-19 shows, the theory predicts otherwise.

The final set of experiments, set #3, has not yet been discussed. It should be noted that the results of these experiments are not shown in Figure 6-20. The data are absent from the figure because no deposition was observed at any Reynolds number. This result is in agreement with the theoretical predictions: as Figure 6-19 illustrates, a pentadecane emulsion dispersed in 0.01M NaCl solution ( $pH=5$ ), should exhibit no deposition.

It appears that the results from the three sets of experiments provide evidence to support the use of DLVO theory to describe the forces that exist between a pentadecane droplet and the glass collector surface.

### 6.4.3 Effect of electrolyte concentration

Another set of experiments (set #4) was conducted in order to compare the predicted and experimentally determined mass transfer rates for a system in which the dimensionless double layer thickness ( $\kappa a$ ) was varied. The predicted effect of  $\kappa a$  on the mass transfer rate is shown in Figure 6-21, for a constant Reynolds number of 100. The solid line shows that deposition is not predicted to occur when  $\kappa a < 125$ , but as long as  $\kappa a$  is larger than that limiting value, deposition rates should not be affected.

Five different NaCl concentrations were used to test the theoretical predictions. The experimental conditions for set #4 are listed in Table 6-5.

**Table 6-5.** Characterization of pentadecane deposition experiments II: pH=5; Re=100;  $a=0.42 \mu\text{m}$ ;  $c_0=1.6 \times 10^7$  droplets/ml.

[NaCl] (mol/L)	$\kappa a$	$\zeta_p$ (mV)	$\zeta_c$ (mV)	DI	Da
0.001	43.7	-51.2	-67.1	243	0.074
0.005	97.7	-31.0	-64.9	142	0.571
0.01	138	-21.3	-58.3	87.8	1.10
0.05	309	-14.1	-31.0	30.9	0.653
0.1	437	-8.55	-23.1	14.0	1.07

For these experiments, the Reynolds number was held constant at 100 and the solution pH was kept constant at 5. The results of these experiments are shown in Figure 6-21. The results for the three largest values of  $\kappa a$  (corresponding to NaCl concentrations of 0.1M, 0.05M and 0.01M, respectively) compare favourably with the predicted results, differing by less than 20% (on average). For the experiments conducted using a 0.001M solution ( $\kappa a=58$ ), no deposition is observed, as is predicted by theory. The

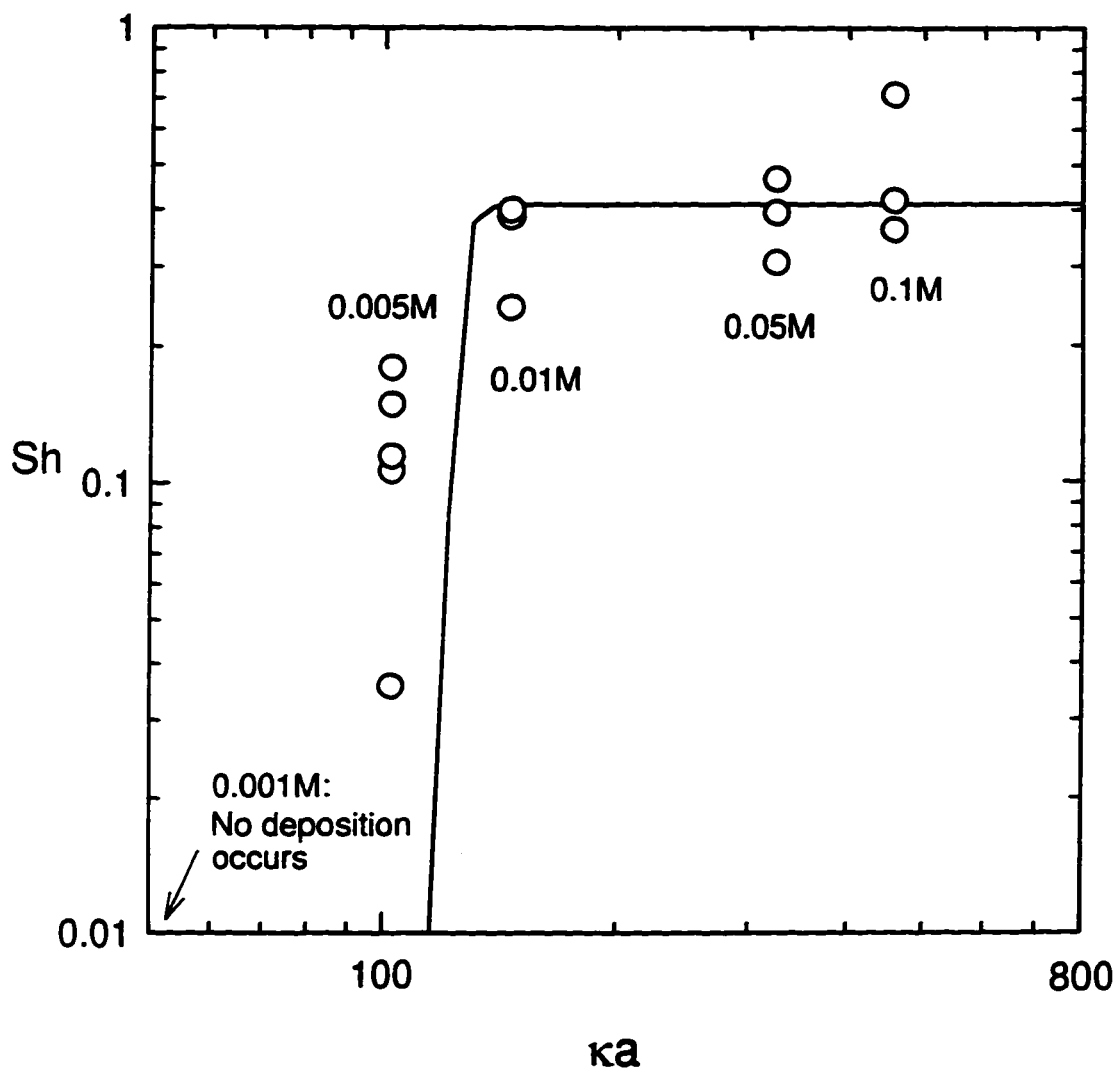


**Figure 6-21.** Experimentally determined effect of  $ka$  parameter on mass transfer to collector surface for a pentadecane emulsion in different concentrations of NaCl, pH=5, Re=100. Solid line shows theoretical mass transfer.

results of the experiments conducted using the 0.005M solution ( $\kappa a = 102$ ) are more difficult to analyze, mostly because mass transfer rates in this region are extremely sensitive to electrolyte concentration. The results of the 0.005M experiments show a wide margin of error {see Figure 6-21}. Although the results seem to deviate from the theoretical predictions, they do fall close enough to the vertical portion of the theory line to suggest that the agreement is better than a first glance would indicate. In light of the fact that no deposition occurs at 0.001M NaCl concentrations, the spread of the results for the 0.005M experiments may be an indication that deposition is very unstable at that salt concentration, which would then be in support of the theoretical predictions shown in Figure 6-21.

## **6.5 Comparison of results: bitumen emulsions with low viscosity oil emulsions**

General comments regarding the agreement between theoretical predictions of Sherwood number and experimental results for each emulsion system are presented below. A more extensive comparison of specific deposition behavior is also discussed in Section 6.5.2: the distributions of bitumen and 7.67 mPa s viscometry oil droplets on the collector surface at high flowrates are compared. In Section 6.5.3, the effect of dispersed phase viscosity on the results of the oil-in-water emulsion deposition experiments is discussed. The results presented in this chapter are summarized in Section 6.5.4.

### **6.5.1 Accuracy of model predictions**

Deposition experiments showing the dependence of Sherwood number on Reynolds number were conducted for each of the bitumen, Bayol oil, viscometry oil, and pentadecane systems. Further experiments showing the effect of electrolyte concentration on Sherwood number were conducted using each of the emulsions

except the Bayol oil and one of the viscometry oil samples (the 3.39 mPa s sample). Theoretical predictions were provided for each set of experiments.

Good agreement between theory and experiment was observed for the bitumen emulsion experiments, for the entire range of Reynolds numbers and NaCl concentrations. The strongest evidence that suggests correlation between the bitumen deposition results and the theoretical model is exhibited in the experiments where the NaCl concentration is changed for each set of experiments {shown in Figure 6-6}. These experiments cover a wide range of conditions favorable to deposition and the agreement between the observed and calculated Sherwood numbers is very good.

The results of the pentadecane deposition experiments also agree favourably with theoretical predictions for both types of experiments. The deposition experiments illustrating the effect of Reynolds number were conducted using three different pentadecane emulsions. Theoretical predictions indicated that the experimental conditions for the first two sets of experiments should yield similar results, and that the third set should show almost negligible rates of droplet deposition. These predictions were verified experimentally, as shown in Figure 6-20. The experiments showing the dependence of Sherwood number on salt concentration also compared favourably with theory {see Figure 6-21}.

The experiments using Bayol oil and viscometry oil systems did not yield such favourable results. The Bayol emulsion deposition experiments {shown in Figure 6-9} appear to follow the predicted Reynolds number - Sherwood number relationship at low Reynolds numbers. Once a certain Reynolds number is reached, the droplet deposition rates decrease, a result not accounted for in the theoretical analysis. By studying specific droplets in the deposition experiments, and noting the high rates of droplet detachment, it seems possible that some mechanism other than the one proposed in the theoretical model is determining droplet deposition rates in the Bayol oil system.

Droplet deposition rates for the viscometry oil emulsions are lower than predicted at all flowrates, by more than a factor of 5 in most cases, when the zeta potentials of a droplet and the collector have the same sign. The low deposition rates

are observed for two different NaCl concentrations and two different dispersed phase viscosities {see Figure 6-13}. The results of experiments involving positively charged viscometry oil droplets agree favourably with predicted mass transfer rates. The results of the deposition experiments involving the variation of salt concentration at a constant Reynolds number are inconclusive at best, in that some relationship between salt concentration and Sherwood number is observed, but the results do not match the predicted values of Sherwood number.

### **6.5.2 Analysis of surface coverage at high Reynolds numbers: bitumen and viscometry oil systems**

As was mentioned in the discussion of the viscometry oil deposition experiments (Section 6.3), the rate of deposition became nonlinear with time at high Reynolds numbers. This behavior was not observed in the bitumen experiments, where the SRCD data was linear with time, even at the highest flowrates {see Figure 6-4}. The nonlinearity in the viscometry oil SRCD data could not be initially attributed to particle blocking effects. A study of the actual distribution of particles on the collector surface had to be conducted first.

The distribution of particles on the collector surface provides important information about the nature of the deposition process when particle deposition becomes nonuniform with time, or with radial distance from the stagnation point. Nonuniform deposition is not predicted by mass transfer theory; in fact, mass transfer theory predicts that deposition will be uniform over the stagnation region, meaning that, on average, the number of particles per given area will be constant [1]. Consequently, the number of particles deposited on a given fraction of the stagnation region should be random, and should be described by a Poisson distribution, where the probability of finding  $i$  particles on a given area would be

$$P_i = \frac{s^i}{i!} e^{-s} \quad (6-7)$$

where  $s$  represents the average number of particles per unit area. Dabros and van de Ven [1] used this technique to analyze the distribution of latex particles on a collector surface.

A similar method has been used here to analyze the distributions of bitumen and viscometry oil droplets over the stagnation region at high flowrates ( $Re=800$ ). These distributions are shown qualitatively in Figures 6-22a and 6-22b. Figures 6-22a and 6-22b represent three dimensional graphs of the stagnation region coating density for bitumen and 7.67 mPa s viscometry oil, respectively. The two diagrams show the difference between the bitumen and the viscometry oil runs. It can be seen that in the case of the bitumen droplet distribution, the particles seem to be more spread out over the entire stagnation region than the viscometry oil droplets are. Figure 6-22b shows a localized area of high particle density that occurred in the viscometry oil experiment. A similar area of high concentration is not observed for the bitumen experiment {see Figure 6-22a}. Figures 6-22a and 6-22b clearly indicate the qualitative difference between the two runs.

A quantitative analysis was conducted for the two runs shown in Figures 6-22 by dividing the centre of the field of view into 384 equal areas of approximately  $185 \mu\text{m}^2$  per area and counting the number of particles in each smaller area. The probability of finding  $i$  particles in each  $185 \mu\text{m}^2$  region was then calculated and compared with a random (Poisson) distribution, calculated from Equation (6-7). The results are shown in Figures 6-23a and 6-23b.

A  $\chi^2$  test was conducted to measure the goodness of fit between the experimentally determined distribution and a Poisson distribution. The results of the  $\chi^2$  test are shown in Table 6-6.

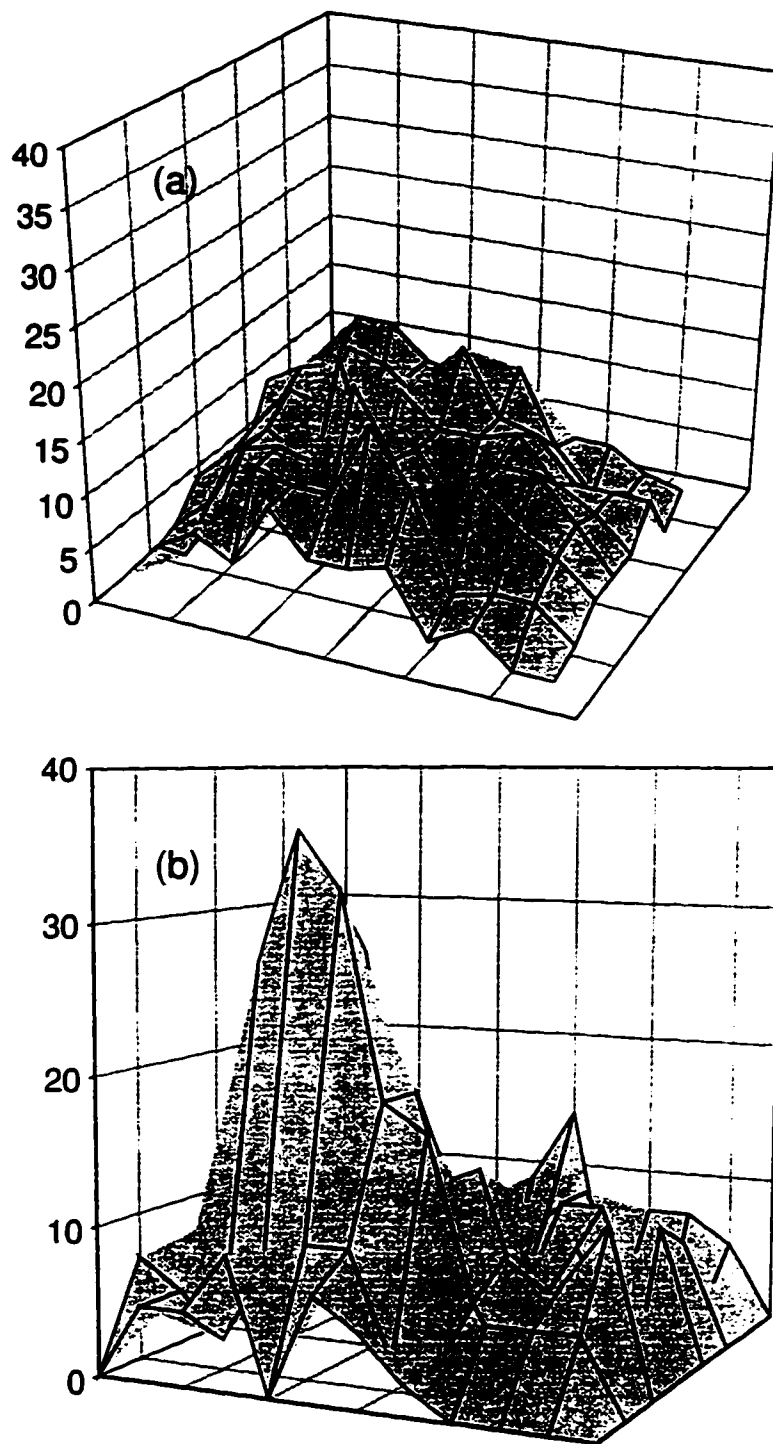


**Figure 6-22.** Coverage of stagnation region at high flowrates ( $Re = 800$ ). Particle density given as particles/ $1500 \mu\text{m}^2$ : (a) 3-D representation of bitumen droplet deposition on collector surface ; (b) 3-D representation of viscometry oil droplet deposition (System A) on collector surface.

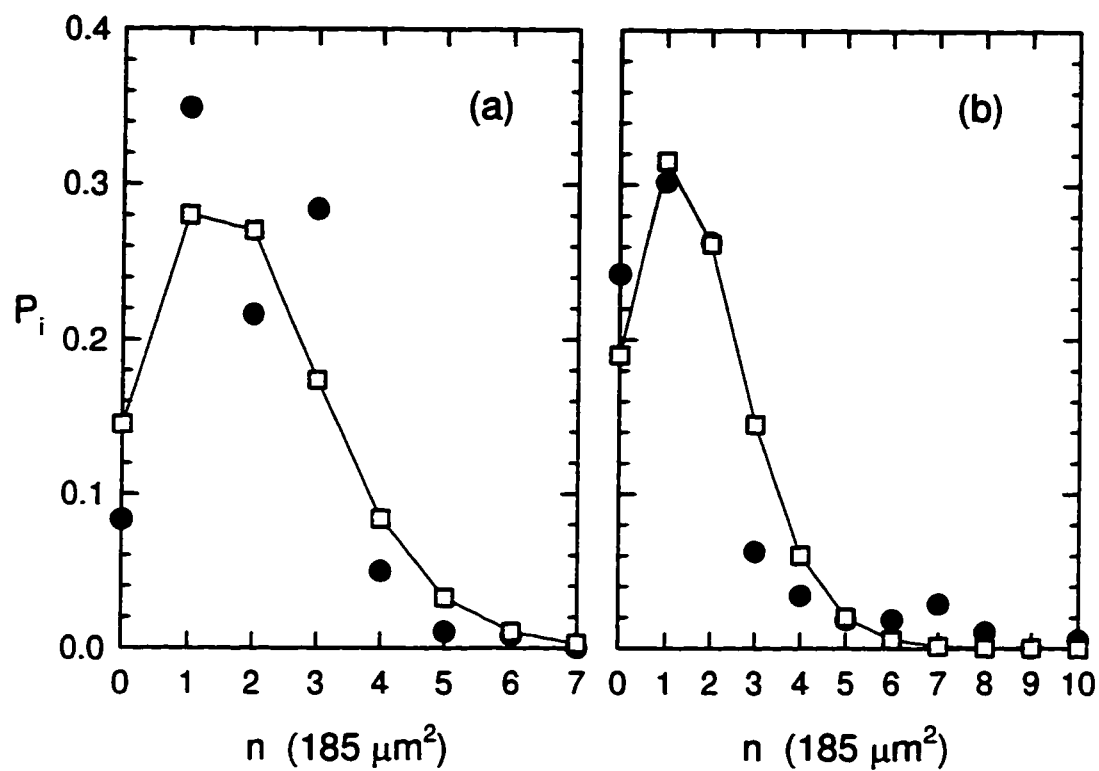


**Figure 6-23.** Distribution of droplets in  $185 \mu\text{m}^2$  areas at high flowrates ( $Re = 800$ ) for (a) 0.1M NaCl bitumen emulsion, with  $s=1.93$  droplets/ $185 \mu\text{m}^2$ ; (b) viscometry oil emulsion (System A), with  $s=1.65$  droplets/ $185 \mu\text{m}^2$ . (●) - Experimental observations; (□) - Poisson distribution.

**Table 6-6.** Particle distribution on the collector surface for bitumen and Cannon viscometry oil emulsions,  $Re=800$ .

System	s <u>particles</u> 185 $\mu\text{m}^2$	$\chi^2$ (Expt'l)	Degrees of Freedom	$\chi^2 _{\alpha=0.01}$
Bitumen	1.93	59.9	5	15.1
Viscometry oil	1.65	403	8	20.1

The goodness of fit analysis shows that at a 1% level of significance, the distribution of bitumen droplets on the collector surface is significantly different from a Poisson distribution. At the same level of significance, it appears that the viscometry oil droplets were not randomly distributed on the collector surface either [see Figure 6-23b]. The two systems exhibit opposite deviations from random behavior: the bitumen droplets tend to spread over the collector surface, while the viscometry oil droplets tend to cluster near the stagnation point. It should be noted that this behavior occurs only at high Reynolds numbers.

The particle distribution analysis conclusively shows that the deposition process is different for the two systems. Moreover, the clustering that was observed in the viscometry oil experiments suggests that particle blocking effects are important after all; in other words, the 'effective' area of deposition is very small and therefore a limiting particle coating density will be reached more quickly than anticipated, because the 'effective' area of deposition is much smaller than the actual stagnation region. An unanswered question remains: why do the bitumen droplets attach over such a large portion of the stagnation region, while the viscometry oil droplets do not? There is evidently something different about the mechanism that causes the droplets to attach to the collector surface. This mechanism is poorly understood even though it is often mentioned.

### 6.5.3 Effect of dispersed phase viscosity

The most important effect of dispersed phase viscosity is droplet deformation. Droplet deformation can lower droplet deposition rates and create additional repulsive forces between the collector and the droplet [64,65]. It is known that small, isolated droplets are much less likely to deform than larger droplets [66], as described by the Bond number:

$$Bo = \frac{4\Delta\rho g a^2}{\sigma_t} \quad (6-8)$$

The Bond number is of the order of  $10^{-2}$  for oil droplets that are 1 mm in diameter. Droplet deformation does not occur until  $Bo \geq 0.1$ . The droplets observed in this study are definitely spherical. According to studies by Mahe *et al.* [66], these droplets would continue to be almost perfectly spherical even when they were attached to the collector surface, at least under conditions where there is no flow in the system. Since the droplets attached to the collector surface are exposed to flow, the effect of shear forces on the droplets must be taken into consideration. In this case, the capillary number, defined as

$$Ca = \frac{2\eta G a}{\sigma_t} \quad (6-9)$$

can be used as a measure of the shear forces to the surface tension forces. Work conducted by Varennes and van de Ven [18] showed that, for an impinging jet cell, the wall shear rate can be expressed as

$$G = \frac{\partial v_r}{\partial z} = \alpha r \quad (6-10)$$

where

Equation (6-10) shows that the shear rate at the collector surface will vary linearly with radial distance from the stagnation point ( $r = 0$ ).

$$\alpha = \frac{D_x Pe}{2a^3} = \bar{\alpha} \frac{U}{R^2} \quad (6-11)$$

Assuming a droplet is 0.25 mm from the stagnation point, and the experiment is conducted with a Reynolds number of 600, then the shear rate  $G$  is equal to  $130 \text{ s}^{-1}$ . For the bitumen emulsion,  $Ca=0.0024$ . For the pentadecane emulsion,  $Ca=0.007$ . The low values of capillary number suggest that droplet deformation is not a concern for these experiments. Any differences in deposition behavior among different emulsions cannot be attributed to differences in dispersed phase viscosity, insofar as droplet deformation is concerned.

#### 6.5.4 Summary

The combination of (i) providing experimental results that show the variation of droplet deposition rates with flow intensity and electrolyte concentration and (ii) comparing these results with theoretical predictions (iii) for a number of different oil-in-water emulsions has produced a reasonably extensive initial study on the behavior of oil droplets in an impinging jet cell apparatus.

The bitumen emulsion experiments indicate that bitumen droplets behave in a way that can be modelled by DLVO theory. Calculated and observed results of deposition experiments were in good agreement, over a range of Reynolds numbers from 50 to 1000 and for a range of NaCl concentrations from 0.001M to 0.1M. The bitumen emulsions were also very monodisperse and easy to prepare. The bitumen emulsions exhibit a wide range of zeta potential that changes drastically with salt concentration and solution pH. Overall, the bitumen emulsions were excellent systems to work with, even though bitumen is the most complex material studied here, as far as molecular structure of the dispersed phase is concerned. One would suspect that the DLVO model would be too simplified to accurately predict bitumen droplet behavior; yet, the results of this study, along with the bitumen droplet coagulation

studies conducted by Takamura, Chow, and Tse [60] and Takamura and Chow [61], show that bitumen droplet coagulation and adhesion can be predicted using this simple model. The analysis of nonuniform coverage at high Reynolds numbers hints at the existence of some non-DLVO mechanism that may actually increase the rate of deposition. The non-random droplet distributions at the collector surface for high Reynolds numbers indicates that there may be some affinity between a bitumen droplet and the collector surface that is not accounted for in the theoretical model.

The Bayol oil deposition experiments did not provide such favourable results. While it appears that experimental results and theoretical predictions are in good agreement at low Reynolds numbers, further analysis shows that some mechanism other than that predicted by DLVO theory is governing the rate of Bayol oil droplet deposition. The high rates of droplet detachment that were observed in these experiments are attributed to the effect of the long-chain, nonionic surfactant (Triton-X) used to stabilize the emulsion. Other research has shown that nonionic surfactants often create steric stabilization in systems where they are used. It is also surmised that the nature of the surfactant causes larger characteristic induction times in the Bayol oil deposition experiments. The induction time is defined as the time it takes for a strong bond to form between the droplet and the collector surface. Systems with large induction times exhibit very high rates of droplet or particle detachment. Very little is known about the nature of the bond that occurs between a droplet and the collector, except that once it forms, it is very stable, and droplet detachment will not occur unless very high shear rates are used [66].

The observed mass transfer rates for the viscometry oil deposition experiments were consistently lower than the predicted rates under all experimental conditions except when the emulsion and the collector surface possessed surface charges of opposite sign. The two viscometry oil emulsions with different dispersed phase viscosities exhibited similar rates of mass transfer. According to the analysis shown in the previous section, two dispersed phase viscosities varying by a factor of 2 would not alter droplet deformation tendencies for the droplet sizes considered here. In both cases the droplets would not be deformed. The droplet coagulation study conducted

using a 7.67 mPa s sample of the viscometry oil confirmed that the behavior of this system could not be predicted using DLVO theory. The analysis of the nonuniform coverage of the collector surface at high Reynolds numbers observed during the viscometry oil deposition experiments showed that the droplets tend to cluster near the stagnation point instead of adhering in a random (Poisson) distribution. An equilibrium coating density is reached more quickly because the area of stagnation region available for deposition is decreased by the clustering effect. It is highly likely that viscometry oil droplet deposition rates decrease with time at high Reynolds numbers because of particle blocking effects.

The results of the pentadecane deposition experiments are in excellent agreement with theoretical predictions. Both the effect of Reynolds number and NaCl concentration were modelled accurately using DLVO theory. The results of the viscometry oil and pentadecane deposition experiments, considered together, are difficult to interpret. Why do the viscometry oil and pentadecane emulsions behave differently in deposition experiments? Both were stabilized with asphaltenes separated from Athabasca bitumen. The difference in their behavior should not be a result of different dispersed phase viscosities. Conversely, particle zeta potentials for the two emulsions are not affected by [NaCl] and bulk pH in the same way. The zeta potentials of the viscometry oil droplets did not vary over as wide a range as they did for the pentadecane droplets. The difference in zeta potential variation between the two emulsions is not large enough to affect the predicted values of Sherwood number, but may suggest that the dissimilar deposition behavior of the emulsions is somehow related to their surface characteristics. It is results such as these, where two emulsions should behave in a similar way but do not, that expose the falliability of a model whose only description of surface characteristics is based exclusively on zeta potential measurements.

## 7. Deposition of bitumen-in-water emulsions on hydrophobic surfaces

### 7.1 Introduction

The deposition experiments discussed in the previous chapters were all conducted using the same type of collector. In the experiments discussed in this chapter, the nature of the collector surface is altered by coating it with different substances. The coating process changes the glass slides from being hydrophilic to being hydrophobic in nature. The terms 'hydrophilic' and 'hydrophobic' refer to the wetting properties of the surface: a hydrophilic surface will be water-wet and have a three phase contact angle less than  $90^\circ$ , as measured through the water phase when a water droplet is attached to the solid surface. A hydrophobic surface will be oil-wet and have a three phase contact angle of greater than  $90^\circ$ , again measured through a water droplet placed on the solid surface.

DLVO theory does not account for the additional forces that can occur between two hydrophobic materials or two hydrophilic materials. These non-DLVO forces can be extremely large, often exceeding the forces predicted by DLVO theory by 10 to 100 times [67]. The repulsive forces that occur between two interacting, strongly hydrophilic bodies ( $\theta < 20^\circ$ ) have been well-documented by a number of researchers [68 - 73]. The existence of these repulsive forces, known as solvation forces (or *hydration* forces in water-continuous systems), has been "proven" experimentally using an atomic force microscope (AFM), which measures the force of interaction between two molecularly smooth surfaces (see studies presented by Pashley [72 - 75], and Pashley and Israelachvili [76], for example). Hydration forces were also measured by Rabinovich *et al.* [77] for glass fibre - silica surface interactions in water, and by Yotsumoto and Yoon [78] in aqueous  $\text{TiO}_2$  (rutile) systems. Attempts to explain the nature of hydration forces have caused a great deal of controversy among colloid scientists [32]. Generally, though, hydration forces occur when water molecules from

the continuous phase can bind to the materials in question. Thus, materials possessing H-bonding groups will potentially exhibit repulsive hydrophilic interactions, depending on the number of active hydrophilic surface groups present [32]. An excellent review of this material is given by Israelachvili [32].

The forces between two strongly hydrophobic objects suspended in water are known to be attractive, based on surface force measurements [79 - 82] and from coagulation experiments involving suspensions of finely ground coal and methylated (hydrophobic) silica particle suspensions [83,84]. One of the most important consequences of the existence of the hydrophobic force is the attachment of hydrophobic particles to air bubbles in flotation processes [67].

The attractive hydrophobic forces are much larger in magnitude and range than the van der Waals attractive force calculated from DLVO theory [32,67,82,83,84]. Once again, the origin of the hydrophobic force is contested [79]: some researchers suggest that the force arises from the reconfiguration of water molecules trapped between two hydrophobic surfaces [79,85]. Others believe that the hydrophobic force is a result of a phase change in the interfacial layer between the two hydrophobic bodies [81,86]. Another hypothesis relates the hydrophobic force to the polarization of water molecules near a hydrophobic surface [80,87]. The reader is referred to the textbook by Israelachvili [32] for a complete review of the nature of hydrophobic interactions and the experimental work that has been conducted in this area.

The study of bitumen deposition on methylated (hydrophobic) and bitumen-coated glass surfaces presented here is relevant to the bitumen extraction/flotation process, and is also applicable to the breaking of bitumen-in-water emulsions. The deposition experiments are no different than those described in Chapter 6, except that the nature of the collector surface has been changed. The first sets of experiments presented in this chapter show how bitumen droplet deposition rates are affected when a methylated (silane-treated) glass slide is used. The methylation, or silanation, process has been used extensively [45,46,88,89,90] to impart a hydrophobic character to glass slides and other silica surfaces. The process is described in Section 7.2.1. In Section 7.3, deposition experiments involving the attachment of bitumen droplets to a bitumen-

coated slide are discussed. This work complements studies conducted by Dabros *et al.* [91], in which the attachment of air bubbles to methylated and bitumen-coated slides was discussed, and more recently by Alexander and Li [92], in which the dynamic formation of a bitumen film on an air bubble is discussed.

## **7.2 Bitumen deposition experiments: hydrophobic collector**

### **7.2.1 Collector preparation and characterization**

Glass microscope slides similar to those used in the previous experiments (Fisher Precleaned Superfrost, 20 mm x 50 mm) were prepared following the cleaning procedure outlined in Section 5.2. The slides were soaked in concentrated HCl, rinsed thoroughly, placed in a hot ultrasonic bath with detergent, and then rinsed thoroughly. The slides were then dried in an oven at 60°C for 1 hour. The microscope slides were imparted with a hydrophobic character by soaking them in a 5% (by weight) solution of dichlorodimethylsilane in toluene for 4 hours. They were then removed from the solution and rinsed thoroughly with toluene, and then with isopropyl alcohol (IPA).

The use of 'organofunctional silanes' [45] to artificially change the nature of a water-wet surface has been well documented. A comprehensive review of silanisation and its practical applications is provided by Anderson [93]. Araujo *et al.* [45] studied the changes in wettability (contact angle) and surface composition for a number of glass slides treated with different silane coupling agents, including dichlorodimethylsilane. The change in surface composition was determined using X-ray photoelectron spectroscopy (XPS). Both the contact angle measurements and the analysis of surface composition showed that the silane-treated glass slides became hydrophobic through chemisorption of organic matter. Figure 7-1 illustrates the configuration of carbon groups adsorbed on a glass surface, as proposed by Araujo *et al.* [45].

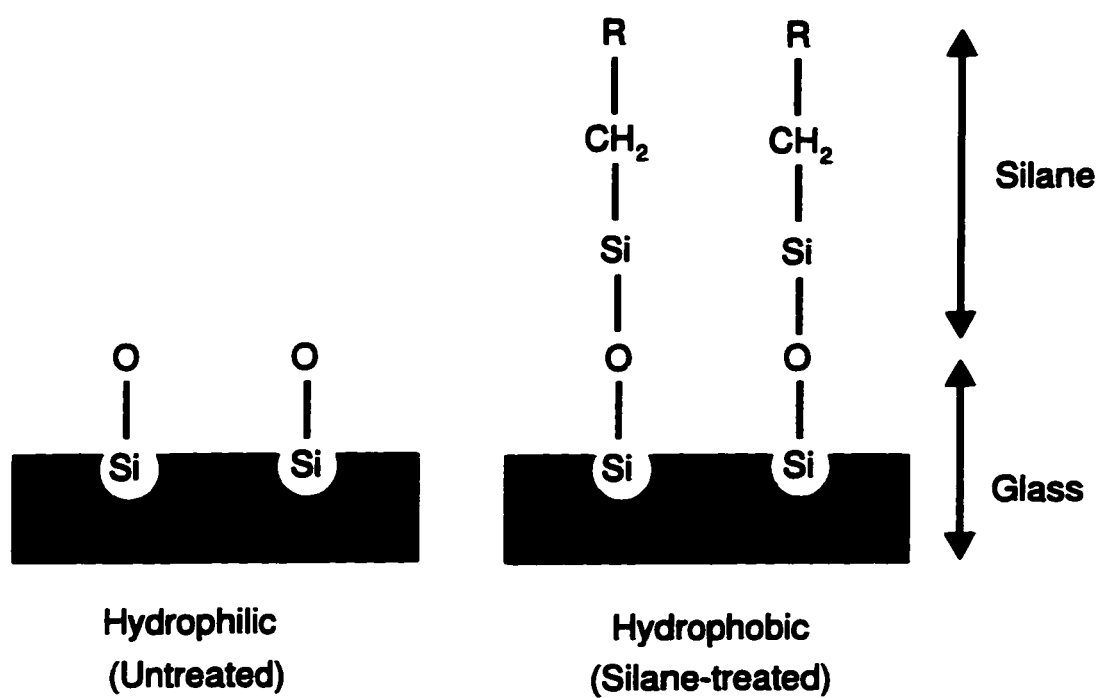


**Figure 7-1.** Schematic diagram of hydrophilic and silane-treated glass microscope slides. from Araujo *et al.* [45].

A silanation process similar to the one used in the present study was also used by Dabros *et al.* [91] to study the deposition of air bubbles onto a hydrophobic surface in an impinging jet cell. The solid-water-air contact angle, measured through the liquid phase, was found to be  $84 \pm 4^\circ$ , and was independent of electrolyte concentration. A contact angle of this magnitude indicates a strongly hydrophobic surface. Although contact angles were not measured in this study, the work presented by Araujo *et al.* and Dabros *et al.* indicates that the silanated glass slides used here are indeed hydrophobic in nature.

The zeta potentials of the silanated slides were measured by soaking a sample of finely ground microscope slide in the dichlorodimethylsilane solution overnight. The silanated ground glass was then rinsed thoroughly with toluene and then dried in an oven at  $60^\circ\text{C}$  for 1 hour. Samples of the ground glass were then dispersed in different electrolyte solutions and the zeta potentials were measured with the Malvern Zetasizer 3. It should be noted that it was very difficult to suspend the ground glass in water. The suspensions were stirred continuously for nearly 2 hours in order to completely disperse the glass particles in the aqueous phase.

Figure 7-2 shows the results of the zeta potential measurements for different NaCl concentrations, with a constant bulk pH, set at pH=4. The solid line shown in Figure 7-2 represents a regression analysis of the zeta potential data that was used to provide an analytical expression for the relationship between the silanated glass zeta potential and the bulk NaCl concentration. The variation of  $\zeta_c$  with [NaCl], for pH=4, can be described by the following equation:

$$\zeta_c = 5 - 13.7e^{-86[\text{NaCl}]} - 27e^{10[\text{NaCl}]^2} \quad (7-1)$$

Equation (7-1) is applicable for NaCl concentrations from 0.001M to 0.1M, inclusive.

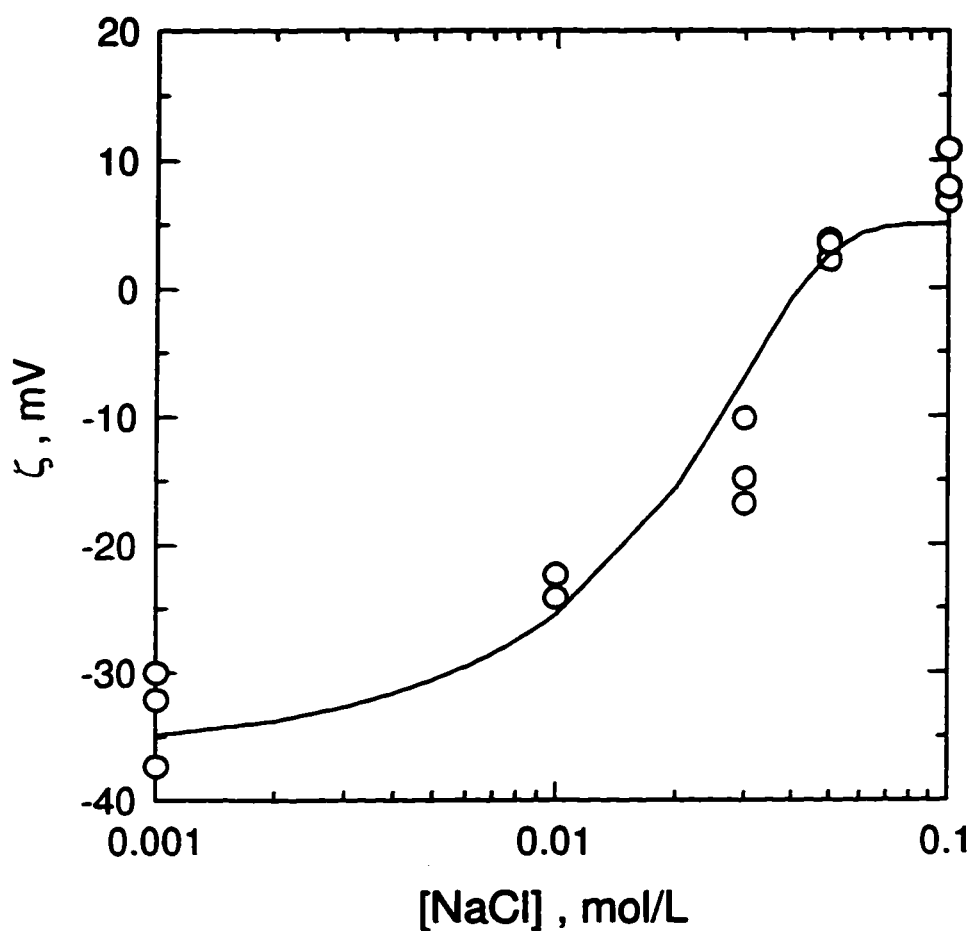


**Figure 7-2.** Measured (symbols) and nonlinear regression analysis (solid lines) of the variation of silane-treated microscope slide zeta potential with  $[\text{NaCl}]$  for a constant bulk pH (pH=4). Analytical expression describing the variation of  $\zeta_c$  with  $[\text{NaCl}]$  given by Equation (7-1).

### 7.2.2 Emulsion preparation and characterization

The bitumen-in-water emulsions used in deposition experiments involving silane-treated glass slides were prepared exactly as described in Section 6.1.1. The size distribution of each dilute emulsion used in this set of experiments was measured to ensure that the size distribution did not change with time. A typical size distribution result is shown in Figure 7-3. The mean particle diameter of this sample was 1.29  $\mu\text{m}$  with a standard deviation of 0.18  $\mu\text{m}$ .

No new zeta potential measurements were taken. The results of the initial bitumen zeta potential measurements, presented in Figure 6-2, were used in the numerical model.

The Hamaker constant was assumed to be the same as it was for the bitumen deposition experiments using hydrophilic glass slides, ie.  $A_{132} = 2.6 \times 10^{-21}$  J. This may not be the actual value of the Hamaker constant for this system. Any adsorbed material on the surface of an object is known to affect the Hamaker constant of the object [94]. However, it is difficult to estimate the effect of the adsorbed layer accurately. In this case, an attempt to estimate the effect of the adsorbed organic layer would only increase the degree of uncertainty associated with the calculation of the Hamaker constant. The Hamaker constant is therefore taken to be the same as for the hydrophilic collector, with a parenthetical comment on its relative inaccuracy. As was mentioned in Section 3.7, the Hamaker constant can change by more than a factor of 4 with little effect on the results generated by the numerical model. In other words, if an attractive hydrophobic force occurs between the bitumen droplets and the silanated microscope slide, the increase in the resulting deposition rates would be far greater than any margin of error caused by an inaccurate choice of Hamaker constant.

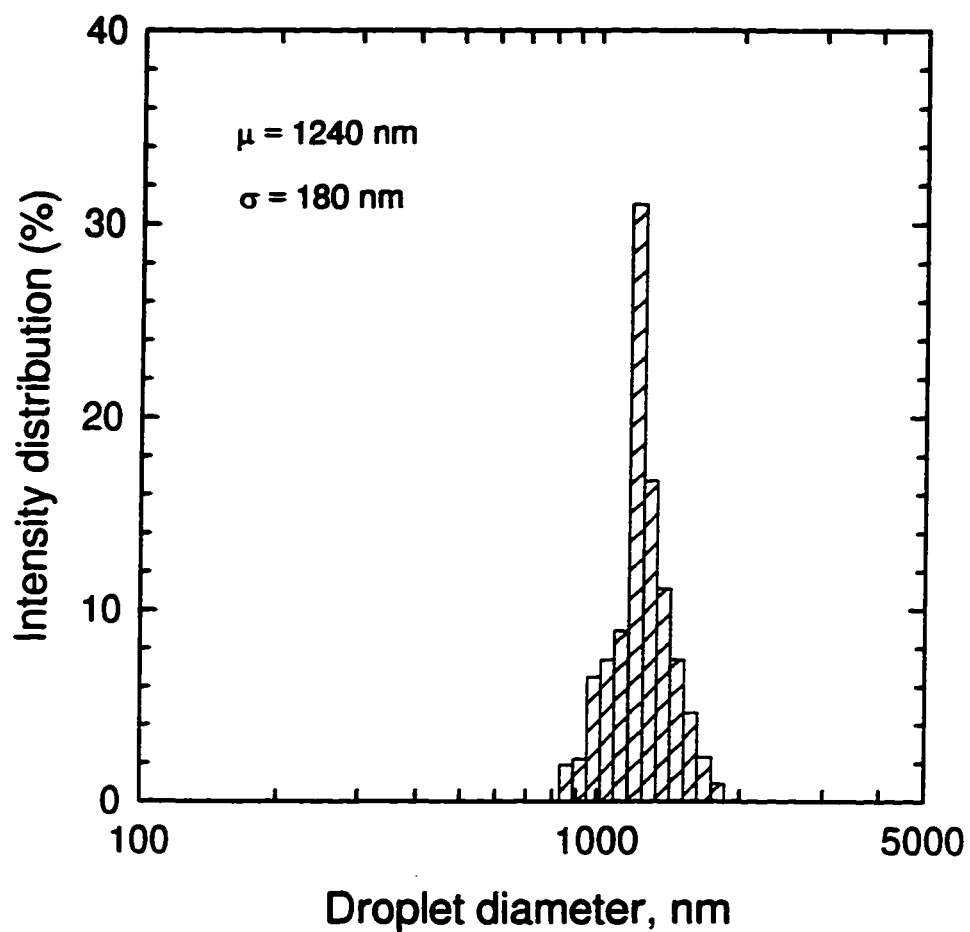


**Figure 7-3.** Representative size distribution of bitumen-in-water emulsions used in the deposition experiments involving silane-treated collectors. Mean droplet diameter shown as  $\mu = 1.24 \text{ }\mu\text{m}$ , with  $\sigma = 0.18 \text{ }\mu\text{m}$ .

### 7.2.3 Effect of Reynolds number

Deposition experiments were conducted for a range of Reynolds numbers from 50 to 1000. The dimensionless jet exit-to-collector surface distance,  $\bar{h}_0$ , was set at 1.21 for these experiments. The bulk pH and NaCl concentration were held constant at 4 and 0.1M, respectively, for all of the experiments. Two different bitumen concentrations were used: the first emulsion used in the experiments had a bitumen concentration of  $9.1 \times 10^6$  particles/ml, while the concentration of the second emulsion was determined to be  $2.3 \times 10^6$  particles/ml. The zeta potentials of the glass slide and the bitumen were measured as  $\zeta_c = +6.3$  mV and  $\zeta_p = -17.8$  mV for the conditions described above (pH=4, 0.1M NaCl).

Thirty experiments were conducted using the greater bitumen droplet concentration. Representative SRCD results for these runs are given in Figure 7-4. The solid lines in Figure 7-4 correspond to linear regression analyses of the SRCD data. It is evident that the deposition process becomes nonlinear with time at higher Reynolds numbers. The SRCD data is nearly linear with time at lower Reynolds numbers. Comparison of the SRCD data shown in Figure 7-4 with the SRCD data from the bitumen deposition experiments with a hydrophilic collector surface {Figure 6-4} provides relatively little information about the differences between the two sets of experiments. The SRCD data for the higher Reynolds numbers shown in Figure 6-4 are more linear than the high Reynolds number SRCD data shown in Figure 7-4.

Figure 7-5 shows the variation of Sherwood number with Reynolds number for both the lower and higher bitumen droplet concentrations. As would be expected, the results of the experiments collapse onto each other even though two different bitumen droplet concentrations were used. The collapse of the results onto each other is to be expected because the initial flux,  $J_0$ , increases when the droplet concentration,  $c_0$ , increases. Equation (2-2) shows that the Sherwood number is proportional to  $J_0$  but inversely proportional to  $c_0$ , so that different droplet concentrations should yield the same values of Sherwood number as long as all other parameters are held constant.

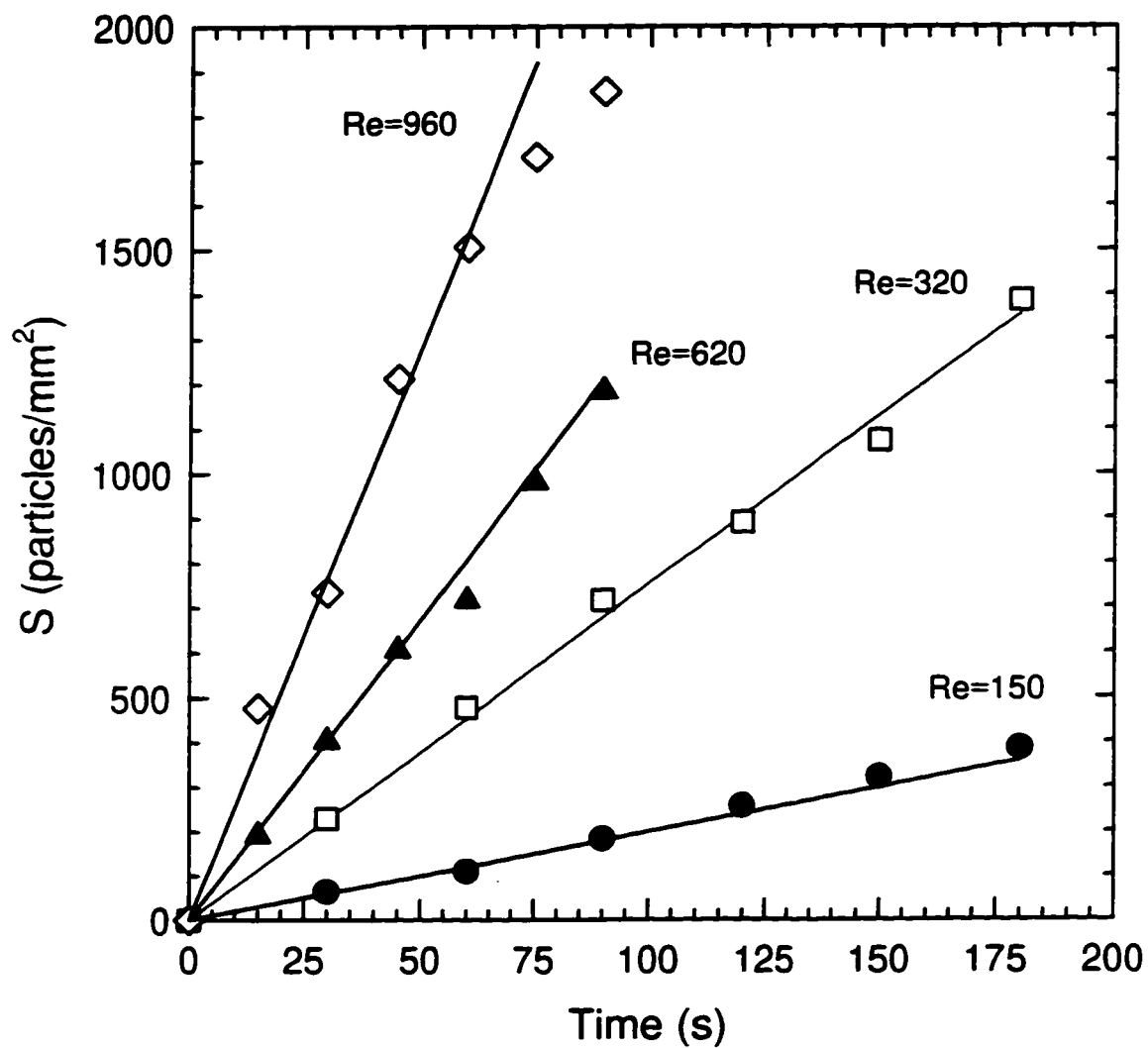


**Figure 7-4.** Stagnation region coating density as a function of time for bitumen droplets attaching to a silane-treated (hydrophobic) collector surface in 0.1M NaCl. pH=4;  $c_0=2.3 \times 10^6$  particles/ml.

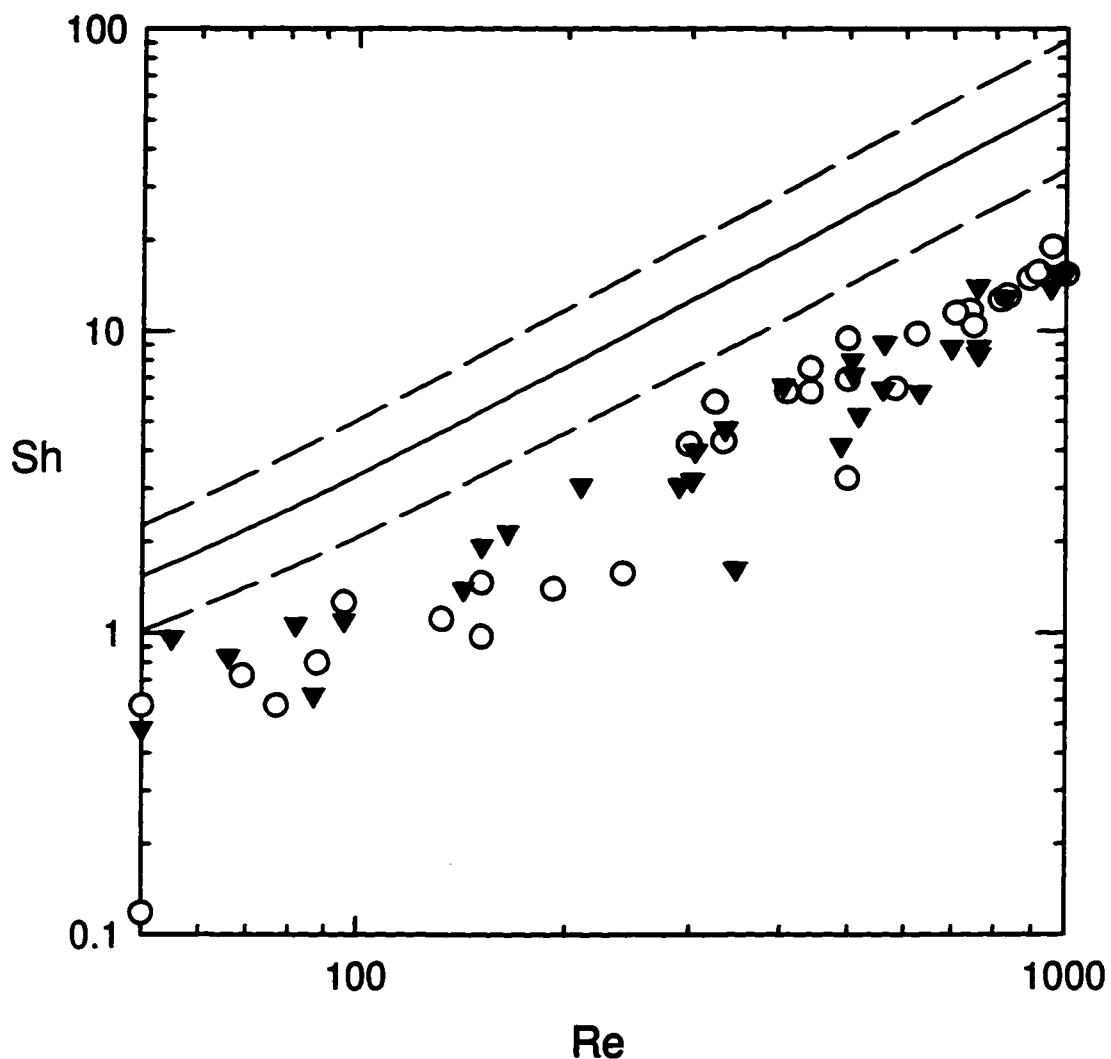


**Figure 7-5.** Dimensionless mass transfer (expressed as Sherwood number) as a function of Reynolds number of 1.24  $\mu\text{m}$  bitumen droplets onto a silane-treated (hydrophobic) collector; pH=4, 0.1M NaCl;  $\zeta_c = 6.3$  mV;  $\zeta_p = -17.8$  mV. (○) -  $c_0 = 2.3 \times 10^6$  droplets/ml; (▼) -  $c_0 = 9.1 \times 10^6$  droplets/ml. Lines show theoretical mass transfer, obtained by solving Equation (3-30):  $Ad=0.11$ , (—)  $a = 0.62$   $\mu\text{m}$ ; (---)  $a \pm \sigma/2$ ,  $\sigma = 0.18$   $\mu\text{m}$ .

This behavior indicates consistency within the measurements of the stagnation region coating density.

The solid line shown in Figure 7-5 represents the predicted values of Sherwood number as a function of Reynolds number for the bitumen deposition experiments for the conditions  $\bar{h}_0=1.21$ ;  $a=0.63 \mu\text{m}$ ;  $Ad=0.11$ ;  $\zeta_c=+6.3 \text{ mV}$ ; and,  $\zeta_p=-17.8 \text{ mV}$  (pH=4, 0.1M NaCl). The dashed lines represent the predicted values of Sherwood number based on a droplet radius that is one standard deviation above and below the mean. The predicted values of Sherwood number are between 2 and 3 times as large as the observed values of Sherwood number. The experimental results do seem to follow the same Sherwood number - Reynolds number trend as the theoretical results, but are lower than the theoretical results. If there were significant hydrophobic interactions between the bitumen droplets and the hydrophobic collector, the experimentally determined values of Sherwood number would have been larger than the predicted values at all Reynolds numbers.

The experimental results shown in Figure 7-5 cannot be directly compared with the results of the hydrophilic collector experiments, shown in Figure 6-5, because the jet exit to collector surface distance,  $h_0$ , is different for the two sets of experiments ( $\bar{h}_0=1.21$  for the results shown in Figure 7-5, and  $\bar{h}_0=2.59$  for the results shown in Figure 6-5). The results of the two different experiments must be analysed by comparing the relative agreement between theory and experiment for each of the two experiments. Figure 6-5 illustrates the good agreement between theory and experiment for the hydrophilic collector experiments. As mentioned previously, the predicted values of Sherwood number are significantly larger than the observed values for the hydrophobic collector experiments.

### 7.2.4 Effect of electrolyte concentration

A third set of experiments were conducted, in which the deposition rate of bitumen droplets on a hydrophobic collector was studied as a function of NaCl concentration for a constant Reynolds number of 100. The bulk pH was kept at a constant value of 4. The bitumen concentration was  $9.1 \times 10^6$  particles/ml and the mean droplet radius was  $0.64 \mu\text{m}$ . Twenty two experiments were conducted using five different NaCl concentrations (0.001M; 0.005M; 0.03M; 0.05M; 0.1M).

The results of these experiments, along with the theoretical results calculated from the numerical model, are shown in Figure 7-6. The symbols in Figure 7-6 represent the experimentally determined Sherwood numbers. No deposition occurred when the NaCl concentration was 0.001M. Figure 7-6 shows that the observed deposition rates do not follow the Sherwood number -  $ka$  relationship that is described by the numerical model. The experimentally determined values of Sherwood number seem to increase with increasing  $ka$ , although the scatter in the data make it difficult to say whether the Sherwood numbers are increasing or have approximately the same value. Regardless, there is poor agreement between theory and experiment for the bitumen deposition experiments conducted using a hydrophobic collector.

If there were a hydrophobic component to the attractive force between a droplet and the collector, the experimental results would not follow the solid line shown in Figure 7-6. Instead of exhibiting the sharp drop in deposition rate that is predicted by mass transfer theory and represented by the solid line in Figure 7-6, the experimental data should remain at a constant value of Sherwood number, as indicated by the dotted line. The constant Sherwood number indicated by the dotted line in Figure 7-6 is arbitrary in the sense that it is not possible to say how the hydrophobic force would affect the droplet deposition rates in this situation. The dotted line in Figure 7-6 was obtained by setting the hypothetical hydrophobic force at the same value (but opposite sign) as the maximum repulsive force  $F_R$  for the 0.01M solution. This method was used by Xu and Yoon [83] to estimate the value of the hydrophobic force between methylated silica particles in coagulation experiments. The dotted line

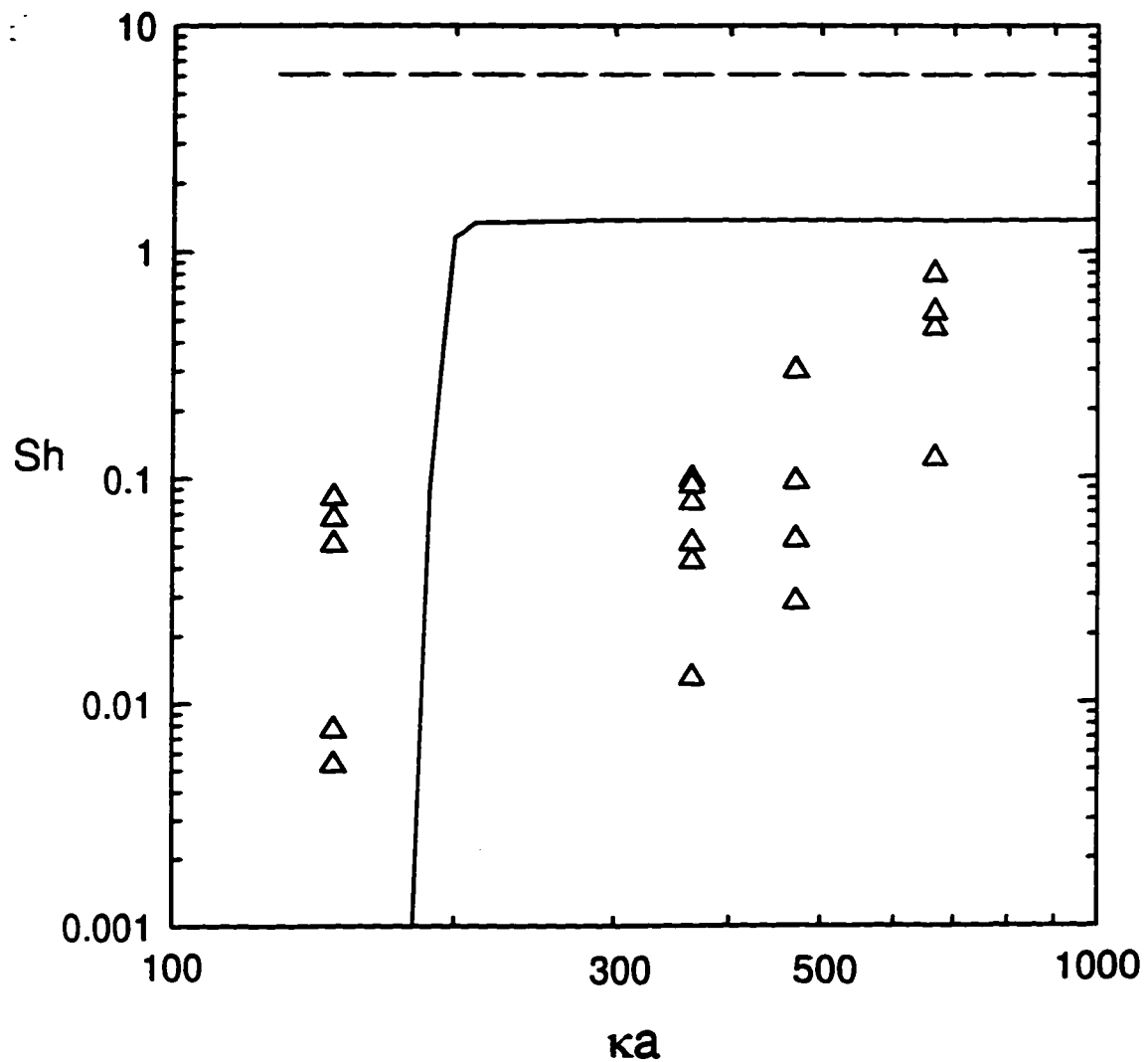


**Figure 7-6.** Experimentally determined effect of  $ka$  parameter on mass transfer rate of  $1.24 \mu\text{m}$  bitumen droplets to a silane-treated (hydrophobic) collector,  $Re=100$ ,  $pH=4$ ,  $c_0=9.1 \times 10^6$  droplets/ml. Solid line shows mass transfer rates predicted using DLVO theory. Dotted line shows hypothetical mass transfer rates obtained when the hydrophobic force of attraction is estimated.

is included to emphasize the difference between the results of the experiments and the results that would be expected if hydrophobic forces were important.

It is reasonable to suggest that the experimentally determined Sherwood numbers are increasing with increasing  $\kappa a$  (or increasing  $[\text{NaCl}]$ ) because the values of  $\zeta_c$  and  $\zeta_p$  tend toward zero as the  $[\text{NaCl}]$  increases, which lowers the magnitude of the repulsive force,  $F_R$ . Moreover, the double layer becomes more compressed as the NaCl concentration increases, meaning that there is less double layer interaction between a droplet and the collector. The trend followed by the data shown in Figure 7-6 supports the following two statements:

- (i) No hydrophobic force of an attractive nature occurs between the bitumen droplets and the collector surface in these experiments; and,
- (ii) some non-DLVO interaction that is repulsive in nature occurs between the bitumen droplets and the collector surface.

Statement (i) has already been discussed. Statement (ii) is believed to be true because the data shown in Figure 7-6 do not follow the Sherwood number -  $\kappa a$  relationship described by DLVO theory, while the same experiments using a hydrophilic collector did yield results described by DLVO theory (cf. Figure 6-6 with Figure 7-6).

### **7.3 Bitumen deposition experiments: bitumen-coated collector**

#### **7.3.1 Collector preparation and characterization**

Bitumen-coated slides were prepared in two steps. First, by following the procedure described in Section 7.2.1, a number of microscope slides were rendered hydrophobic. The silanated (hydrophobic) glass slides were then dried as per the procedure listed in Section 7.2.1, and then soaked in a 10% (by weight) bitumen in methylene chloride solution for 1 hour. The slides were allowed to dry in an oven at

60 °C for 1 hour. The slides were then stored in Milli-Q (pH=10) until they were used. All slides were used the same day they were prepared so that no slides were stored longer than 12 hours. Once the slides were to be used, they were removed from the storage solution and the top side of the slide was wiped clean with a disposable lint-free towel (Kimwipes) dipped in toluene.

The procedure described above is very similar to the method used by Dabros *et al.* [91] to coat a glass microscope slide with bitumen. In their method, the bitumen was dissolved in naphtha, and the slides were immersed and immediately removed from a 20% solution of bitumen in naphtha. To the author's knowledge, the two procedures were developed independently even though they are quite similar.

Dabros *et al.* also measured the contact angle of an air bubble attached to a bitumen-coated slide surrounded by water. They found that the contact angle, as measured in the liquid phase, was  $77 \pm 1^\circ$  for a 0.01 M NaCl, pH=6 solution. For a 0.01 M, pH=9 solution, the contact angle was found to be  $75 \pm 2^\circ$ . When the pH was held at 9 and the NaCl concentration increased to 0.1 M, the contact angle was  $64 \pm 2^\circ$ . These contact angle measurements indicate that the bitumen became less hydrophobic at higher pH values. The same relationship seems to hold between contact angle and NaCl concentration, at least at pH 9. It should be noted that the contact angle for an air bubble on a clean, hydrophilic glass slide was found to be  $0^\circ$ .

The zeta potentials of the bitumen-coated slide were assumed to be the same as the bitumen droplets. Since it was not possible to determine the actual zeta potentials of the collector surface, the deposition experiments were conducted in a 0.1 M NaCl solution so that the values of  $\zeta_c$  and  $\zeta_p$  would not affect the droplet deposition rates.

### 7.3.2 Emulsion preparation and characterization

The bitumen emulsions used in this set of experiments were prepared from the same concentrated emulsion used in the previous experiments, as described in Section 7.2.2. Consequently, the measured size distributions were not significantly different

than those reported in Section 7.2.2. A representative size distribution is shown in Figure 7-7. Again, the mean droplet radius was taken to be  $0.63\ \mu\text{m}$ . The zeta potentials of the bitumen emulsions used here are satisfactorily described by Figure 6-2.

The Hamaker constant of the bitumen-coated slide - water - bitumen droplet system was calculated using the dielectric constant and refractive index of bitumen to describe both phase 1 {the collector} and phase 3 {the bitumen droplet}. The Hamaker constant was

$$A_{132} = A_{232} = 1.8 \times 10^{-21}\ \text{J}$$

The discussion that was presented in Section 7.2.2, regarding the uncertainty associated with Hamaker constant calculation, especially when one of the phases possesses an adsorbed layer of a different material, also applies here. Again, while the actual value of the Hamaker constant may be a source of error in modelling the deposition experiments, it is not expected to be large enough to significantly affect the theoretical outcome.

### 7.3.3 Effect of Reynolds number

Deposition experiments were conducted using a bitumen-coated collector for a range of Reynolds numbers from 50 to 1000. Two different sets of experiments were conducted. The first set of experiments was conducted with a 0.1M NaCl aqueous phase and pH=4. The second set of experiments were also conducted with a 0.1 M NaCl aqueous phase, but with a bulk pH of 10. The results of the two sets of deposition experiments are shown in Figure 7-8. The solid line in Figure 7-8 represents the predicted values of Sherwood number based on the mean bitumen droplet radius. The dashed lines represent the predicted values of Sherwood number for a bitumen droplet radius one standard deviation above and below the mean. The predicted values of Sherwood number are the same for both sets of experiments

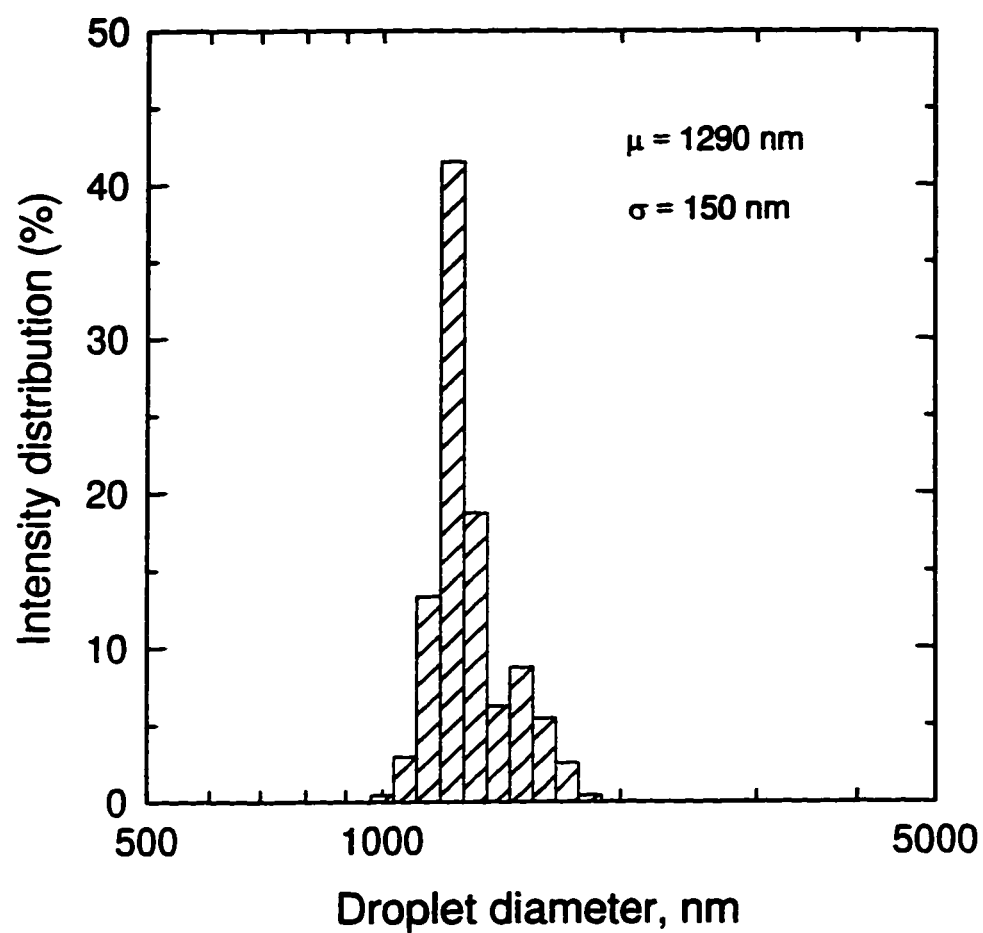


**Figure 7-7.** Representative size distribution of bitumen-in-water emulsions used in the deposition experiments involving bitumen-coated collectors. Mean droplet diameter shown as  $\mu = 1.29 \text{ }\mu\text{m}$ , with  $\sigma = 0.15 \text{ }\mu\text{m}$ .

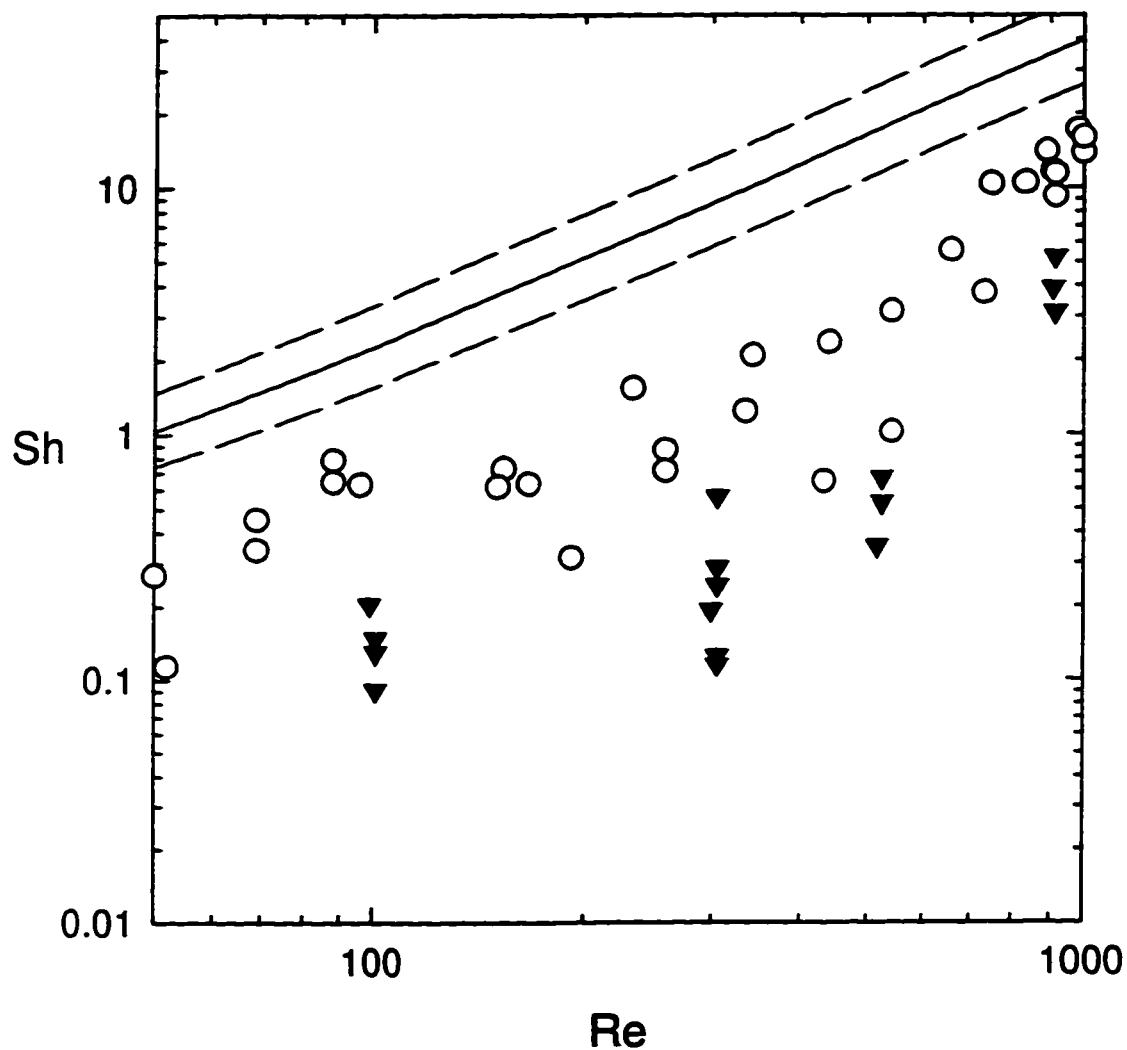


**Figure 7-8.** Dimensionless mass transfer (expressed as Sherwood number) as a function of Reynolds number of  $1.29\ \mu\text{m}$  bitumen droplets onto a bitumen-coated collector;  $0.1\text{M NaCl}$ ; ( $\circ$ ) -  $\text{pH}=4$ ; ( $\blacktriangledown$ ) -  $\text{pH}=10$ . Lines show theoretical mass transfer, obtained by solving Equation (3-30):  $\text{Ad}=0.07$ , (—)  $a = 0.645\ \mu\text{m}$ ; (---)  $a \pm \sigma/2$ ,  $\sigma = 0.150\ \mu\text{m}$ .

despite the fact that  $\zeta_c$  and  $\zeta_p$  change when the bulk pH is changed because the high NaCl concentration corresponds to very compressed double layers ( $\kappa a = 671$ ).

According to DLVO theory, there should be no difference in droplet deposition rates for the experiments conducted at pH 4 and pH 10. However, the observed droplet deposition rates for the pH 10 experiments are noticeably lower than the rates observed at pH 4. In fact, Figure 7-8 shows that both sets of experimental results are nearly an order of magnitude lower than predicted values of Sherwood number. There are now two issues to address:

- (i) the decrease in deposition rates with increasing pH; and,
- (ii) the discrepancy between observed and calculated Sherwood numbers for the deposition of bitumen droplets onto a bitumen-coated collector.

The data presented in Figure 7-8 indicate that the droplet deposition rate decreases with increasing pH. According to contact angle measurements reported by Dabros *et al.* [91], the bitumen becomes less hydrophobic with increasing pH. Based solely on the data presented in Figure 7-8, it would seem reasonable to assume that deposition rates are higher at pH 4 because the bitumen has a stronger hydrophobic character at this pH. The hydrophobic (attractive) interaction between a bitumen droplet and the bitumen-coated collector is therefore stronger at pH 4, which could increase the deposition rates.

Unfortunately, when the experimental results shown in Figure 7-8 are examined alongside the results presented in Sections 6.1.3 and 7.2.3, the preceding analysis is shown to be highly suspect. The results presented in Section 6.1.3 indicate that high deposition rates were observed for bitumen droplets attaching to a plain glass microscope slide (a hydrophilic surface). The results presented in Section 7.2.3 indicate that deposition rates that are lower than predicted were observed for bitumen droplets attaching to a silane-treated microscope slide (a hydrophobic surface). In other words, the difference in deposition onto a bitumen-coated collector at pH 4 and at pH 10 cannot be explained by the existence of an attractive hydrophobic force.

The discrepancy between observed and calculated deposition rates for the bitumen emulsion - bitumen-coated collector is not any easier to explain. Comparison of Figure 7-8 with Figure 6-5 indicates that there is much better agreement between experiment and theory for the bitumen emulsion deposition experiments conducted with a hydrophilic collector surface (Figure 6-5) than with a bitumen-coated collector (Figure 7-8). The results of the bitumen-coated collector experiments compare favourably with the results of the silane-treated collector results (cf. Figure 7-8 with Figure 7-5), although the observed mass transfer rates are lower than the predicted values of mass transfer for both sets of experiments. The results of the experiments involving bitumen emulsions and the three different collectors indicate that the nature of the collector has an important effect on deposition behavior. These results cannot be explained on the basis of DLVO theory alone.

#### **7.4 Discussion: the nature of bitumen surface active agents**

The results of the bitumen deposition experiments using both silane-treated (hydrophobic) slides and bitumen-coated slides indicate that no significant hydrophobic interactions occur between the bitumen droplets and the collector surface in this study. The higher deposition rates to the bitumen-coated slide in a pH 4, 0.1M NaCl solution than in a pH 10, 0.1M solution cannot be considered to be the result of weak hydrophobic forces, since the bitumen deposition experiments using a hydrophilic collector resulted in high mass transfer rates.

The results of the bitumen deposition experiments using silane-treated slides strongly suggest that no attractive, hydrophobic interactions occur between the bitumen droplets and the collector. The predicted values of Sherwood number, obtained from DLVO theory, are nominally 4 to 5 times larger than the observed values of Sherwood number for the entire range of Reynolds numbers used in the study. In fact, there was a larger discrepancy between experiment and theory for the bitumen - hydrophobic slide experiments than there was for the bitumen - hydrophilic slide experiments

discussed in Section 6.1.

It is by definition that all oils (hydrocarbons) are assumed to be strongly hydrophobic in nature. The wettability of bitumen and crude oils is influenced by the naturally occurring surface active agents that give these oils their negative surface charges [37,39,95]. The surface active agents in bitumen are widely accepted to be carboxyl groups, whose dissociation behavior at the bitumen/water interface affects both the surface charge and wettability of the bitumen [37]. It is for this reason that the Ionizable Surface Group Model can be used to predict the surface charge of bitumen as a function of bulk pH and electrolyte concentration, because it predicts the dissociation behavior of carboxyl groups. The study conducted by Xu and Yoon [83], in which oxidized coal samples were shown to exhibit no hydrophobic particle-particle interactions, suggests that the presence of oxygen-containing groups (such as carboxyl groups) is related to the absence of hydrophobic interactions.

Recent publications by Yaminsky *et al.* [96] and Attard [97] use a thermodynamic analysis of energy versus distance plots to study the interaction of hydrophobic surfaces. Yaminsky *et al.* suggest that for purely nonpolar surfaces in water, such as silane-treated glass, no long range hydrophobic forces of attraction can be measured (within the limits of the accuracy of the surface force apparatus used to measure the force). For the case of nonpolar surfaces in ionic surfactant solutions, which is analogous to the experiments discussed in this chapter, Yaminsky *et al.* state that attractive interactions can be larger than predicted because of increasing surfactant adsorption with decreasing separation distance between two surfaces, at separation distances less than 100 nm. In other words, the hydrophobic interactions are determined by the nature of the surfactant and not by the hydrophobic nature of the surfaces. This observation may explain the apparent absence of extra attractive forces due to hydrophobic interactions in the bitumen deposition experiments discussed in this chapter.

## **8. Deposition of water-in-hydrocarbon emulsions**

### **8.1 Introduction**

Water-in-hydrocarbon emulsions are commonly encountered in the petroleum industry. The presence of salts in the dispersed aqueous phase can cause serious damage to petroleum processing equipment through corrosion. Water droplets suspended in a hydrocarbon phase can result in costly shutdowns due to catalyst deactivation and may be involved in reactor plugging and subsequent pressure drop increases. The problem with breaking these emulsions is that only a small fraction of colloid science research has been directed toward nonaqueous suspensions, and only a fraction of that to nonaqueous emulsions.

Some of the more recent (and thorough) studies involving water-in-oil or water-in-hydrocarbon emulsions were published by Mousa and van de Ven [64,65]. They studied the stability of water-in-oil emulsions, as measured by tracking the change in droplet size with time in a simple shear flow. In studying the orthokinetic collection efficiency of a set of water-in-silicon oil emulsions, they found that the presence of solid particles at the water/oil interface greatly increased emulsion stability.

The water-in-hydrocarbon emulsions studied here are also believed to be stabilized by the presence of particles, specifically bitumen surface active agents, at the water-oil interface. The results of deposition experiments conducted using water droplets dispersed in a 4:1 (by volume) mixture of toluene and hexane are reported here. A small amount of solvent-extracted Athabasca bitumen was used to stabilize the nonaqueous emulsions. Two sets of experiments were conducted in order to analyze the effect of hydrodynamic forces (flowrate) on the deposition rates. The results also show that the deposition rates are highly dependent upon the amount of bitumen added to the continuous phase.

## 8.2 Emulsion preparation and characterization

Recent work conducted by Yarranton and Masliyah [98] concerning the stability of water droplets dispersed in a hydrocarbon phase consisting of different ratios of toluene and hexane provided the basis for the emulsion preparation procedure described below. Yarranton and Masliyah's work showed how droplet size, asphaltene precipitation, and emulsion stability are determined by the ratios of toluene and hexane present in the continuous phase. A number of different emulsions were prepared, using different toluene/hexane ratios, different amounts of bitumen dissolved in the continuous phase, and different values of pH for the water phase. Table 8-1 lists the compositions of the different emulsions.

**Table 8-1.** Preparation of a number of different water-in-hydrocarbon emulsions.

Sample #	Toluene (ml)	Hexane (ml)	Bitumen (g)	Water (g)
1	80	20	6	9.9
2	80	20	5.9	9.9**
3	80	20	1.18	9.0
4	50	50	1.09	9.9**
5	50	50	5.45	9.5

\*\* pH =10 (adjusted using 1M NaOH).

All the emulsions were prepared in the same way. The bitumen was first added to a measured volume of toluene. The toluene-bitumen mixture was blended using a Ware-Coming Industrial two speed blender for less than a minute to increase the dissolution rate of the bitumen in the toluene. A measured volume of hexane was then added to the toluene-bitumen mixture. This mixture was blended until it became homogeneous,

which took less than 30 s. The blender was operated continuously at low speed and a measured volume of water was added dropwise using a disposable pipette. The addition of the water took approximately 10 min. The mixture was blended at low speed for an additional 5 minutes after all the water had been added.

Samples of each emulsion were studied under the microscope at time intervals of  $t=0$  (immediately after preparation),  $t=30$  min, 1 h, 2h, 5 h, 8 h, 18 h, 22 h, and 72 h. The most stable emulsion was emulsion #2 (listed in Table 8-1). The droplet size of this emulsion did not appear to change with time over the 72 hour period. Samples of this concentrated emulsion were diluted in a 4:1 mixture of toluene/hexane and the size distribution was measured using a Malvern Zetasizer 3. The viscosity and refractive index of the continuous phase were required in order to measure the droplet size distribution. The viscosity was measured using a Poiseuille - type viscometer (Cannon-Fenske Routine Viscometer). Repeated measurements yielded an average viscosity of 8.87 mPa s at 25 °C. The refractive index was measured using a benchtop refractometer (Baush and Lomb) which measures the refractive index at 589.3 nm. The average refractive index was found to be 1.40.

Approximately 18 size distribution measurements were taken. A typical size distribution is shown in Figure 8-1. The mean droplet size was calculated by taking the mean of the measured samples. The average droplet diameter was found to be 1.39  $\mu\text{m}$  with a standard deviation of 0.34  $\mu\text{m}$ . Size distributions were measured three times before and after each set of experiments.

The Hamaker constant for the water-hydrocarbon-glass system was calculated using Equation (3-54). A dielectric constant of 4 was used for the hydrocarbon phase [99]. The Hamaker constant was determined to be

$$A_{132} = 1.7 \times 10^{-22} \text{ J}$$

so that  $A_d = 0.007$  for the water {1} - hydrocarbon {3} - glass {2} system.

Droplet zeta potentials were not measured because, as was mentioned in Section 3.6, the values of droplet zeta potential are irrelevant as long as the electrolyte concentration is negligible, because of the low dielectric constant of the continuous

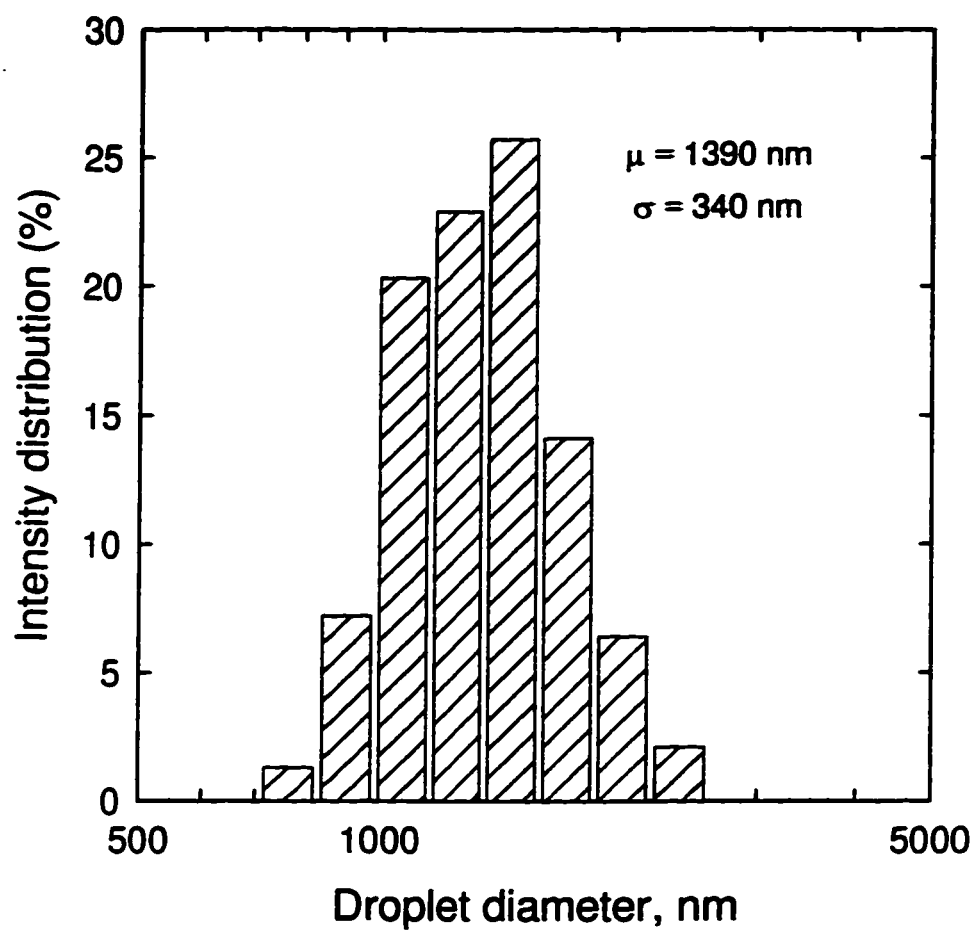


**Figure 8-1.** Representative size distribution of water-in-hydrocarbon emulsions, with a mean droplet diameter of  $\mu = 1.39 \text{ }\mu\text{m}$  and  $\sigma = 0.34 \text{ }\mu\text{m}$ .

phase. The low dielectric constant hinders the double layer interactions of two surfaces because the double layers are very dispersed.

Dilute emulsions were used for the deposition experiments. They were prepared by adding a specific volume of the concentrated emulsion to a much larger volume of premixed 4:1 (by volume) toluene/hexane solution. Bitumen was added to the toluene/hexane solution as necessary, in order to produce a dilute emulsion that had the desired continuous phase bitumen concentration,  $b_0$ . The value of  $b_0$  for each emulsion, expressed as *g bitumen / L solution*, was calculated as follows:

$$b_0 = \frac{59 V_i + m_b}{V_i + V_s} \quad (8-1)$$

where  $b_0$  = continuous phase bitumen concentration (g bitumen / L solution)

$V_i$  = volume of concentrated emulsion used to prepare the dilute emulsion (L)

$m_b$  = mass of bitumen added to the 4:1 toluene/hexane diluent (g)

$V_s$  = volume of 4:1 (by volume) toluene/hexane diluent (L).

As Equation (8-1) shows, the value of  $b_0$  for each set of experiments was determined by (a) the dilution rate of the concentrated emulsion, and (b) the amount of extra bitumen added to the toluene/hexane diluent.

Different dilutions yielded different water droplet concentrations. Droplet concentrations were measured using a hemacytometer cell (as described in Section 5.1).

### 8.3 Collector preparation and characterization

Untreated (hydrophilic) glass slides were used for the water-in-hydrocarbon deposition experiments. A rigorous cleaning procedure was used in the preparation of all glass slides. The procedure was outlined in Section 5.2 but is repeated here. The glass slides were soaked in concentrated HCl for 3 h. They were then rinsed

thoroughly with distilled water and placed in an ultrasonic bath containing hot ( $70^{\circ}\text{C}$ ) water and detergent for 10 minutes. The slides were then removed from the bath, rinsed thoroughly with Milli-Q, and then dried in an oven at  $60^{\circ}\text{C}$  for 1 h. The slides were used only once, and if some slides were left over from a set of experiments, they were put through the cleaning procedure again to be used in the next set of experiments.

The zeta potentials of the glass slides immersed in the hydrocarbon phase were not measured because the double layer force between a droplet and the glass slide would be very small regardless of the magnitude of  $\zeta_c$ .

#### 8.4 Effect of Reynolds number

Deposition experiments were conducted using a number of different water-in-hydrocarbon emulsions for a range of Reynolds numbers from 80 to 1000. The characteristic water droplet concentration ( $c_0$ ) and the continuous phase bitumen concentration ( $b_0$ ) of the different sets of experiments, labelled set 'A', are listed in Table 8-2. The 6 sets of experimental conditions listed in Table 8-2 were chosen based on water droplet concentration. The continuous phase bitumen concentration was simply a result of the dilution of the concentrated emulsion: it was not specifically controlled in this set of experiments. The different water droplet concentrations were chosen to make sure the experimental results were reproducible: the Sherwood number should be independent of water droplet concentration at any given Reynolds number, so that the experimental results of all 6 sets of experiments should collapse into a single band of data. If all other parameters remain the same, then the initial flux to the collector surface ( $J_0$ ) should decrease with decreasing water droplet concentration, so that the ratio of  $J_0/c_0$  remains the same. Thus, the Sherwood number, as defined by Equation (2-2), should be the same. It was necessary to conduct deposition experiments using emulsions with different droplet concentrations in order to have complete confidence in the experimental data.

**Table 8-2.** Water droplet concentration ( $c_0$ ) and continuous phase bitumen concentration ( $b_0$ ) for nonaqueous deposition experiments. Set A.

Set #	Water concentration $c_0$ (droplets/ml)	Bitumen concentration $b_0$ (g/L)
A-1	$7.3 \times 10^6$	6.40
A-2	$7.3 \times 10^7$	12.2
A-3	$3.1 \times 10^7$	6.00
A-4	$7.15 \times 10^6$	1.22
A-5	$7.15 \times 10^6$	1.22
A-6	$2.7 \times 10^6$	0.617

The results of experiments A-1 through A-3 are shown in Figure 8-2. The solid line shown in Figure 8-2 represents the predicted values of Sherwood number, with  $a=0.695 \mu\text{m}$ ,  $Ad=0.007$ ,  $DI=0$ , and  $\bar{\alpha}=2.81\text{Re}^{1/2}$ . The dashed lines represent the predicted values of Sherwood number using a droplet radius that is one standard deviation above and below the mean. Nearly all of the experimental data fall outside the area bounded by the two dashed lines, indicating that the observed mass transfer rates are significantly lower than the calculated mass transfer rates.

Figure 8-2 also shows that the observed values of Sherwood number do not fall in a single band, even though Equation (2-2) indicates that they should (as discussed previously). The failure of the results to collapse into a single band is shown more clearly by Figures 8-3a and 8-3b. Figure 8-3a shows the SRCD diagram for sets A-1 through A-3, for  $\text{Re}=320$ . The water droplet concentrations for these three sets of experiments differ by an order of magnitude; yet, the SRCD data fall on a single line, meaning that

$$J_0|_{\text{set } 1} \cong J_0|_{\text{set } 2} \cong J_0|_{\text{set } 3} \quad (8-2)$$

as is illustrated in Figure 8-3b. As Figure 8-3b shows, the initial flux to the collector

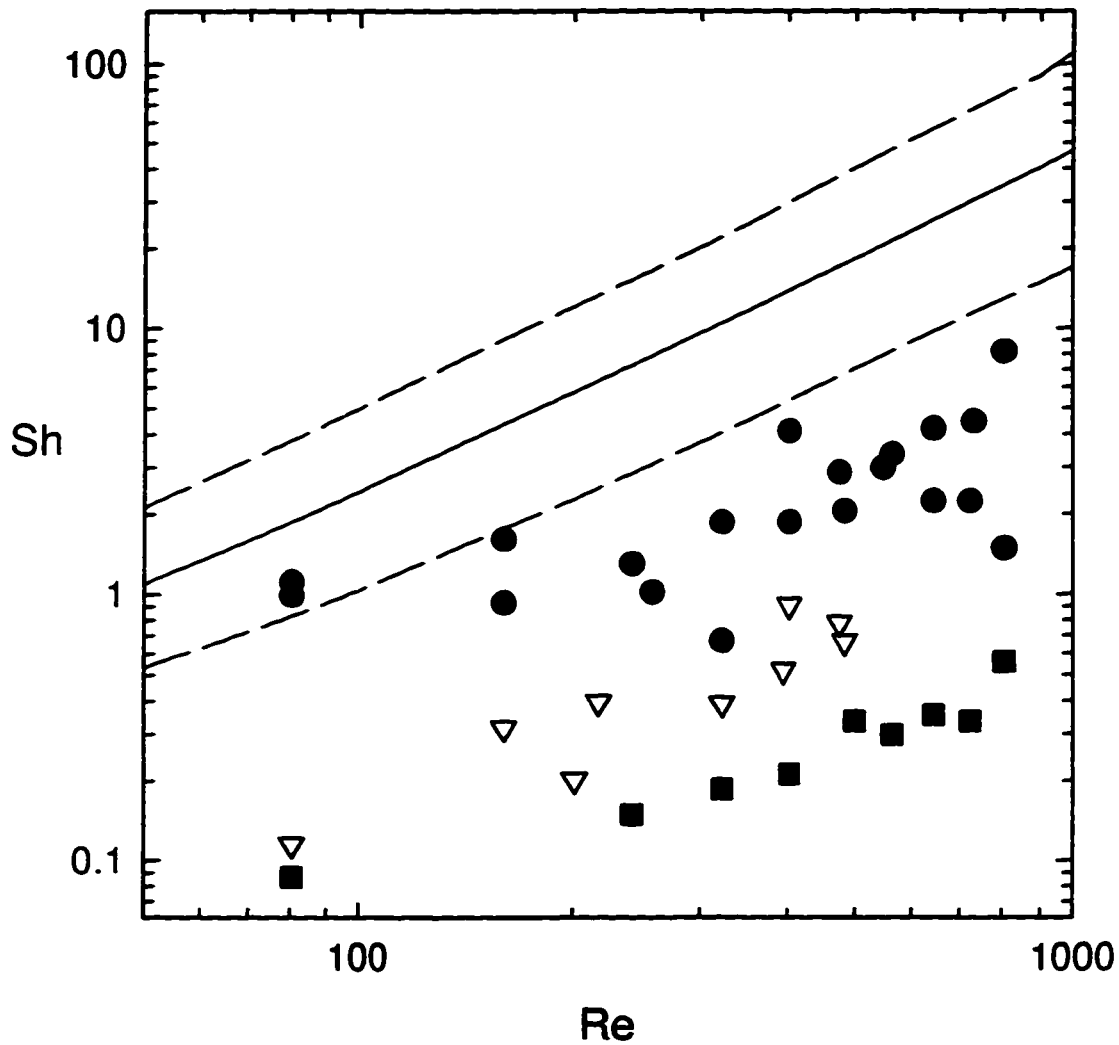


**Figure 8-2.** Dimensionless mass transfer (expressed as Sherwood number) as a function of Reynolds number for 1.39  $\mu\text{m}$  water droplets suspended in 4:1 toluene/hexane (by volume) with added bitumen. Experimental conditions described in Table 8-2. (●) - set A-1; (■) - set A-2; (▽) - set A-3. Lines show theoretical mass transfer, obtained by solving Equation (3-30):  $Ad=0.007$ , (—)  $a = 0.695 \mu\text{m}$ ; (— —)  $a \pm \sigma/2$ ,  $\sigma = 0.340 \mu\text{m}$ .

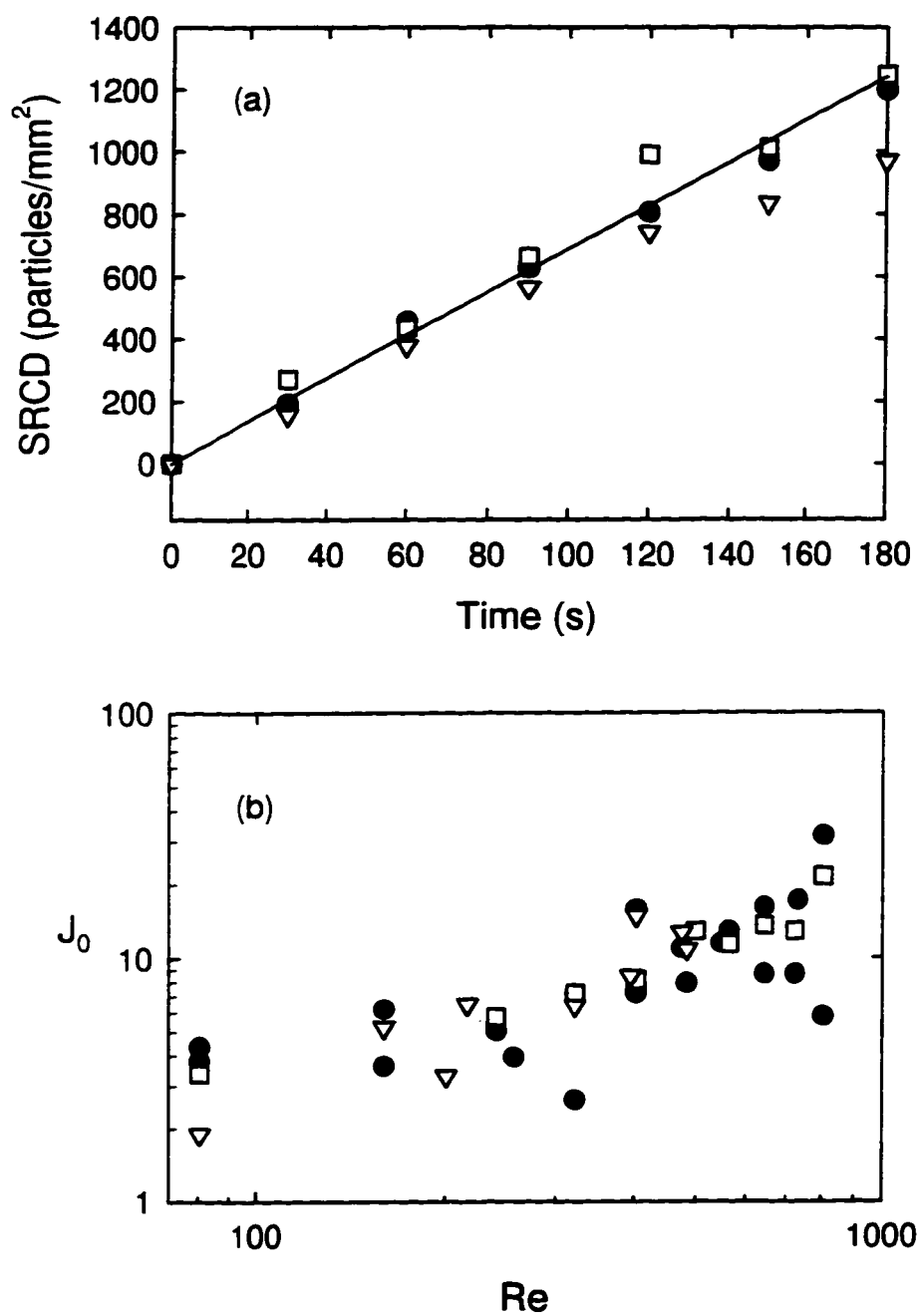


**Figure 8-3.** Variation of (a) stagnation region coating density curves for  $Re=320$  and (b) initial flux to the collector surface as a function of  $c_0$  and  $b_0$  for water-in-hydrocarbon deposition experiments. Experimental conditions listed in Table 8-2. (●) - set A-1; (□) - set A-2; (▽) - set A-3.

surface is approximately equal for each of the three sets. Because the water droplet concentration differs among the three sets, but the initial flux and droplet size are similar, the dependence of Sherwood number on Reynolds number is different for the three sets of experiments, as illustrated in Figure 8-2.

The results of sets A-4 through A-6 are shown in Figure 8-4. The observed values of Sherwood number are nearly 3 orders of magnitude larger than the results obtained in the first three sets. As the data presented in Figure 8-4 show, the observed values of Sherwood number are independent of water droplet concentration for sets A-4, A-5, and A-6. Once again, the theoretical values of Sherwood number as a function of Reynolds number are indicated by the solid line  $\{a = \mu/2\}$  and the two dashed lines  $\{a = (\mu \pm \sigma)/2\}$ . The experimentally determined mass transfer rates are significantly higher than those predicted from mass transfer theory. Figure 8-4 also shows that the experimental results do not vary with Reynolds number in the way that the theoretical results do. The experimentally determined values of Sherwood number do not appear to depend as strongly on Reynolds number as the predicted values of Sherwood number do. The observed mass transfer rates range from  $Sh=32.8$  at a Reynolds number of 80.5 to a maximum value of  $Sh=144$  at a Reynolds number of 725. Predicted values of Sherwood number range from  $Sh=1.60$  at a Reynolds number of 70 to  $Sh=46.7$  at a Reynolds number of 1000. The relatively flat profile exhibited by the experimental data shown in Figure 8-4 suggests that mass transfer due to convection may not be as important as theoretical predictions would indicate.

The final diagram shown in this section, Figure 8-5, provides further evidence suggesting that the experiments are dependent on some factor not yet considered. Figure 8-5 shows the results of set A-1, A-4, and A-5. Sets A-4 and A-5 represent the same experimental conditions. The Sherwood number dependence on Reynolds number follows a similar trend for the three sets, but the experimental data are offset by nearly two orders of magnitude for the results of sets A-4 and A-5. The water droplet concentrations were almost identical for each set of experiments {see Table 8-2}. The continuous phase bitumen concentration differed by a factor of 5 between set A-1 and the other two sets (A-4 and A-5). The lines shown in Figure 8-5 represent

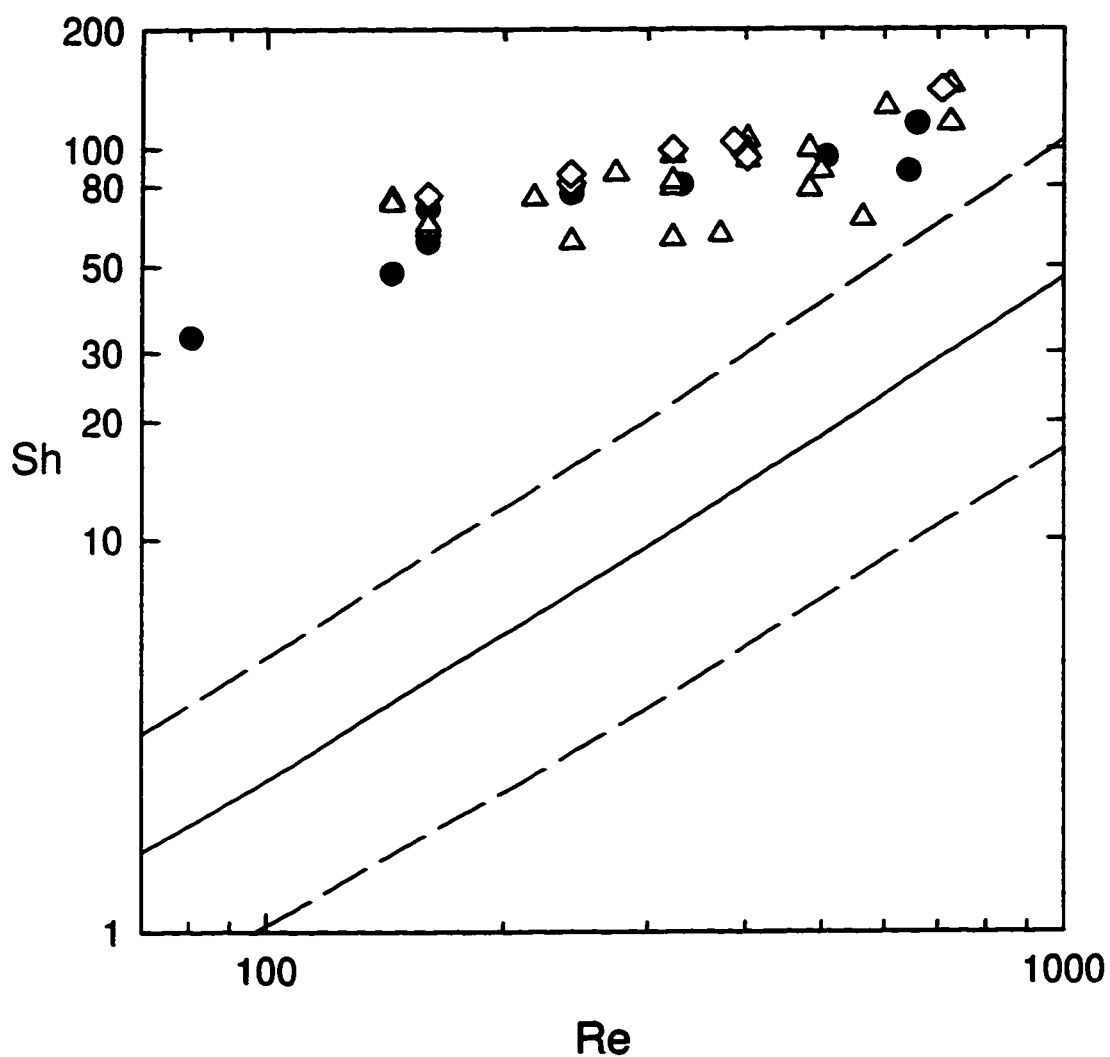


**Figure 8-4.** Dimensionless mass transfer rate (expressed as Sherwood number) as a function of Reynolds number for 1.39  $\mu\text{m}$  water droplets suspended in 4:1 toluene/hexane (by volume) with added bitumen. Experimental conditions described in Table 8-2. (●) - set A-4; (◇) - set A-5; (Δ) - set A-6. Lines show theoretical mass transfer, obtained by solving Equation (3-30):  $Ad=0.007$ , (—)  $a = 0.695 \mu\text{m}$ ; (— —)  $a \pm \sigma/2$ ,  $\sigma = 0.340 \mu\text{m}$ .

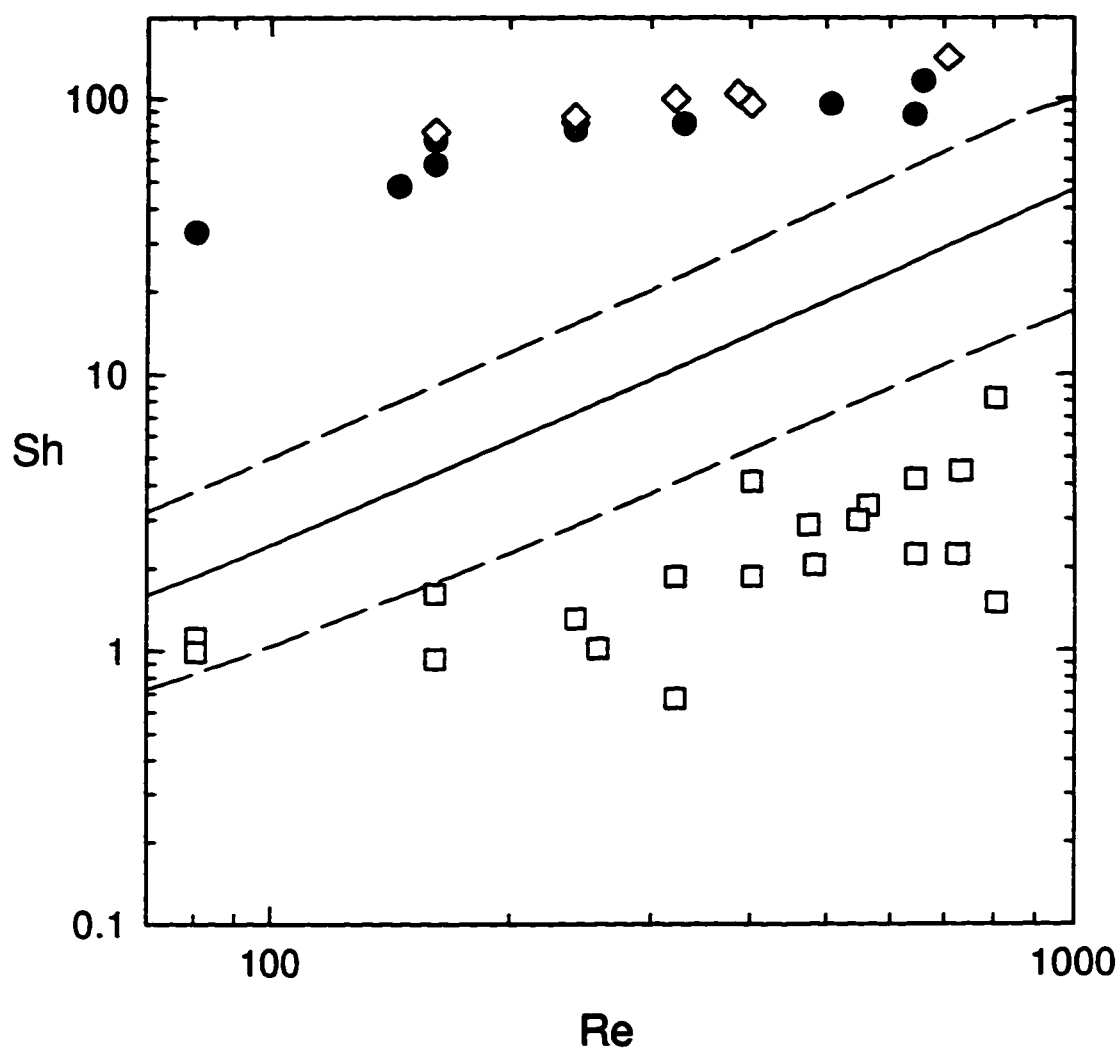


**Figure 8-5.** Dimensionless mass transfer rate (expressed as Sherwood number) as a function of Reynolds number and continuous phase bitumen concentration ( $b_0$ ) for  $1.39 \mu\text{m}$  water droplets suspended in 4:1 toluene/hexane (by volume) with added bitumen. Experiments possessed similar water droplet concentrations. ( $\square$ ) - set A-1 ( $b_0=6.4 \text{ g/L}$ ); ( $\bullet$ ) - set A-4 ( $b_0=1.22 \text{ g/L}$ ); ( $\diamond$ ) - set A-5 ( $b_0=1.22 \text{ g/L}$ ). Lines show theoretical mass transfer, obtained by solving Equation (3-30):  $Ad=0.007$ , (—)  $a = 0.695 \mu\text{m}$ ; (— —)  $a \pm \sigma/2$ ,  $\sigma = 0.340 \mu\text{m}$ .

theoretical predictions of droplet deposition rates. The predicted values of Sherwood number are independent of droplet concentration and continuous phase bitumen concentration. Consequently, all the experimental results shown in Figure 8-5 can be modelled using the same set of parameters ( $a$ ,  $Ad$ ,  $DI$ ,  $\bar{\alpha}$ ). The mass transfer rates for sets A-4 and A-5 are significantly higher than the predicted mass transfer rates, which are shown in Figure 8-5 as the solid line (calculation of Sherwood number using the average droplet radius) bounded by the two dashed lines (calculation of Sherwood number using values of droplet radii that are one standard deviation above and below the mean). The mass transfer rates for set A-1 are significantly lower than the predicted mass transfer rates. The data presented in Figure 8-5 clearly show the effect of continuous phase bitumen concentration on the droplet deposition rates. Set A-1 exhibited low rates of droplet deposition and had the highest bitumen concentration. Sets A-4 and A-5 are characterized by much lower bitumen concentrations than set A-1, but yielded droplet deposition rates that were much greater than rates predicted from mass transfer theory.

Based on the results depicted in Figures 8-2 through 8-5, it was decided that further experiments were required in order to investigate the effect of continuous phase bitumen concentration on the deposition rates.

### **8.5 Effect of continuous phase bitumen concentration**

In the next sets of experiments that were conducted, both the water droplet concentration ( $c_0$ ) and the continuous phase bitumen concentration ( $b_0$ ) were controlled. The bitumen concentration was calculated from Equation (8-1). As Equation (8-1) shows, the bitumen concentration could be increased by adding bitumen to the 4:1 toluene/hexane diluent.

Table 8-3 lists the water droplet concentrations and the continuous phase bitumen concentrations for this group of experiments, labelled B-1 through B-7.

**Table 8-3.** Water droplet concentration ( $c_0$ ) and continuous phase bitumen concentration ( $b_0$ ) for nonaqueous deposition experiments, Set B.

Set #	Water concentration $c_0$ (droplets/ml)	Bitumen concentration $b_0$ (g/L)
B-1	$7.2 \times 10^6$	1.22
B-2	$7.2 \times 10^6$	1.22
B-3	$2.9 \times 10^6$	1.22
B-4	$7.2 \times 10^5$	1.22
B-5	$7.2 \times 10^6$	3.00
B-6	$7.2 \times 10^5$	3.00
B-7	$1.3 \times 10^7$	3.00

Sets B-1 and B-2 are simply repeat runs of experiments A-4 and A-5. Sets B-3 and B-4 have the same bitumen concentration in the hydrocarbon continuous phase ( $b_0=1.22$  g/L) but different water droplet concentrations than sets B-1 and B-2. Experiments labelled B-5 through B-7 have the same bitumen concentration ( $b_0=3.00$  g/L), but three different water droplet concentrations.

The results of sets B-1 through B-4 appear in the upper portion of Figure 8-6. These results are for experiments with a bitumen concentration of  $b_0=1.22$  g/L. The results of sets B-5, B-6, and B-7 are also shown in Figure 8-6. Sets B-5 through B-7 had a bitumen concentration of 3.00 g/L. These data are grouped in a band across the bottom portion of Figure 8-6. Comparison of the results shown in Figure 8-2 and Figure 8-4 with the results shown in Figure 8-6 reveals that there is good agreement between the previous set of experiments (Set A) and this set of experiments (Set B). The solid line shown in Figure 8-6 represents the theoretical values of Sherwood number, determined using the numerical model described in Section 3.5. The single line shown in Figure 8-6 represents all the data. As Figure 8-6 shows, the observed

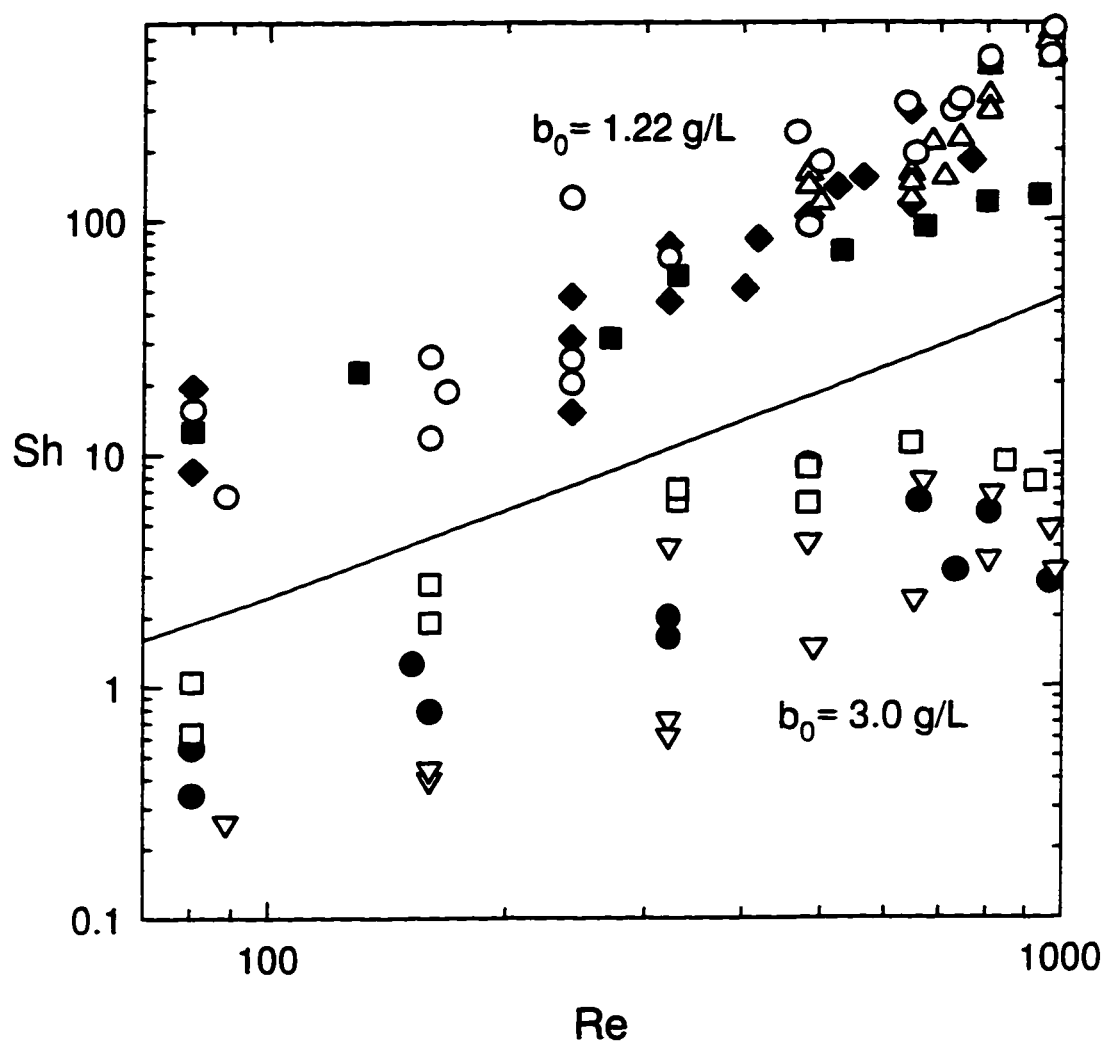


**Figure 8-6.** Effect of continuous phase bitumen concentration ( $b_0$ ) on the dimensionless mass transfer rates (expressed as Sherwood number) of water droplets suspended in 4:1 toluene/hexane with added bitumen. For the upper band of results,  $b_0=1.22$  g/L: ( $\blacklozenge$ ) - set B-1; ( $\triangle$ ) - set B-2; ( $\circ$ ) - set B-3; ( $\blacksquare$ ) - set B-4. For the lower band of results,  $b_0=3.00$  g/L: ( $\bullet$ ) - set B-5; ( $\square$ ) - set B-6; ( $\nabla$ ) - set B-7. Solid line shows theoretical mass transfer, obtained by solving Equation (3-30):  $Ad=0.007$ ,  $a = 0.695$   $\mu\text{m}$ .

mass transfer rates were significantly higher than predicted rates of mass transfer for all Reynolds numbers from 80 to 800, for all experiments characterized by a continuous phase bitumen concentration of 1.22 g/L. Conversely, the experimentally determined Sherwood numbers were significantly lower than predicted Sherwood numbers for all Reynolds numbers from 80 to 800, for all experiments characterized by a continuous phase bitumen concentration of 3.00 g/L.

The observed values of Sherwood number do collapse into two discrete bands on the Sherwood number - Reynolds number diagram shown in Figure 8-6. The two discrete bands represent experiments conducted using systems with two different continuous phase bitumen concentrations. Figure 8-6 clearly shows that the Sherwood number is a strong function of bitumen concentration,  $b_0$ , at least for the weight fractions of bitumen used in these experiments. There is more scatter in the results of the  $b_0=3.00$  g/L experiments because the Sherwood numbers are quite small. The Sherwood number for diffusion of a sphere as  $Pe \rightarrow 0$  is usually taken to be  $Sh=1$  [27]. Figure 8-6 shows that for the  $b_0=3.00$  g/L experiments, the Sherwood number is only weakly dependent on Reynolds number. It appears that some mechanism, such as a steric stabilization or other non-DLVO interaction, acts on the system in a way that compensates for the convective mass transfer component of the mass transfer process, resulting in the small values of Sherwood number that are normally associated with diffusive processes.

All of the results of the water-in-hydrocarbon emulsion deposition experiments can be combined to show the effect of continuous phase bitumen concentration on Sherwood number. This effect is illustrated in Figure 8-7, which shows values of Sherwood number as a function of bitumen concentration for a constant Reynolds number ( $Re=320$ ). As Figure 8-7 shows, the maximum values of Sherwood number correspond to the lowest values of bitumen concentration,  $b_0$ . As the bitumen concentration increases past 1.22 g/L, the Sherwood number decreases rapidly, becoming nearly constant at the highest bitumen concentrations.

It should be noted that emulsions with bitumen concentrations less than 0.600 g/L were not stable enough to use in the impinging jet cell. Although droplets could

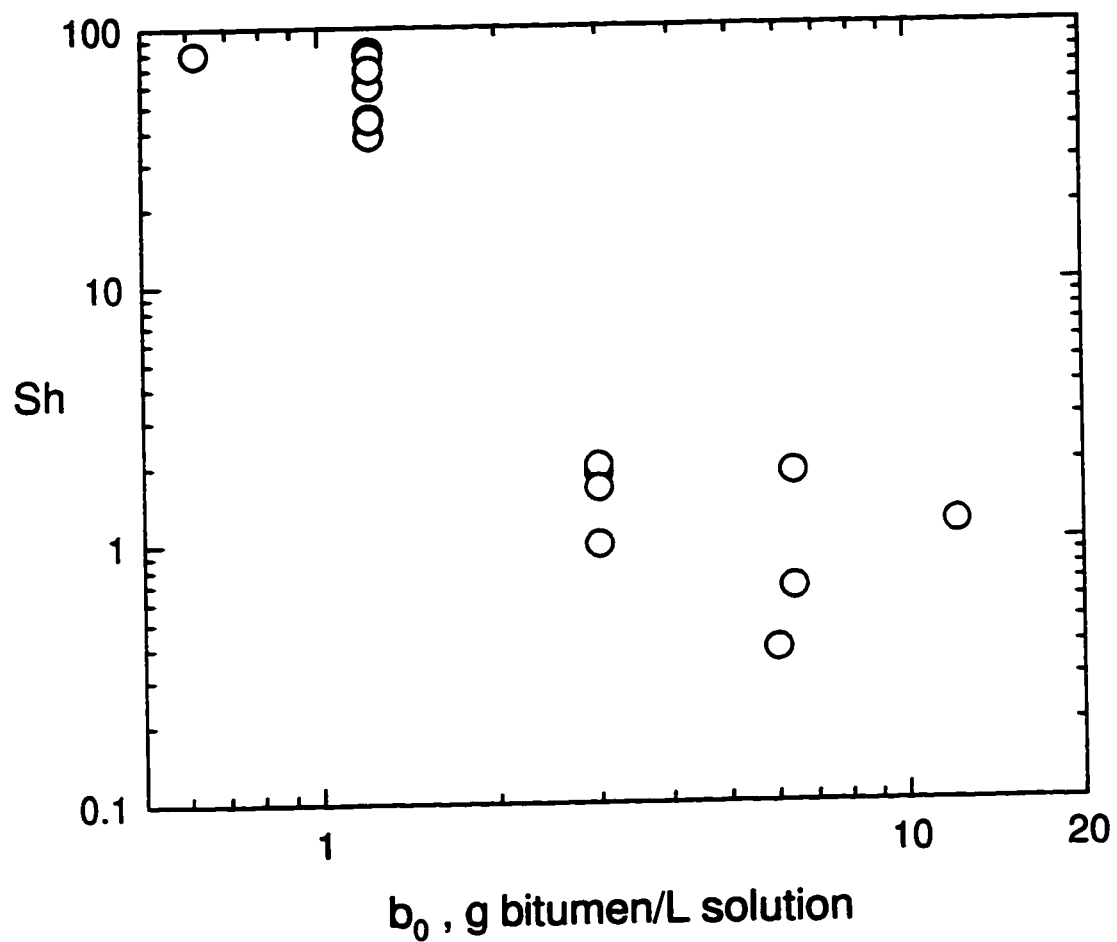


**Figure 8-7.** Variation of dimensionless mass transfer rate (expressed as Sherwood number) with continuous phase bitumen concentration ( $b_0$ ) for water-in-hydrocarbon emulsion deposition experiments;  $Re=320$ .

be observed under the microscope for an emulsion with  $b_0=0.6$  g/L. no deposition was observed when deposition experiments were conducted with this emulsion. A sample of the emulsion was taken from the impinging jet cell reservoir and placed under the microscope, but no droplets could be found, indicating that the emulsion had broken under the shear forces placed on it during flow. Bitumen concentrations above 12.2 g/L could not be used in the impinging jet cell because the emulsion became too opaque.

Figures 8-6 and 8-7 indicate that the deposition rate of the water droplets is strongly influenced by the bitumen concentration. Many studies have shown that bitumen contains natural surfactants known as asphaltenes that reside at the oil-water interface, thereby stabilizing the dispersed phase [62,58,59,100,101]. It is almost certain that the stabilization mechanism involved in these experiments is the same as the mechanism described above. The uncertain part of the analysis revolves around the relationship between bitumen (or asphaltene) concentration and the stability of the emulsions, as indicated by the droplet deposition rates. The steep rise in deposition rates, as shown in Figure 8-7, that occurs between  $b_0=3.00$  g/L and  $b_0=1.22$  g/L could represent a transition from monolayer coverage of a droplet to random, scattered coverage. An analysis of the amount of asphaltenes required for monolayer coverage shows that, even at  $b_0=1.22$  g/L, there are at least ten times more asphaltenes than would be nominally required for monolayer coverage. These calculations are presented in Appendix A. Evidently, the role of the asphaltene concentration is more complicated than simply calculating the monolayer coverage concentration.

Research conducted by Yarranton and Masliyah [98] has produced similar trends between emulsion stability and asphaltene concentration as those shown here. The relationship between asphaltene concentration and emulsion stability is unclear. One interesting but unproven hypothesis points to the role played by unadsorbed asphaltenes in the continuous phase. In this hypothesis, it is put forth that so-called 'free' asphaltene molecules that are present in the continuous phase physically separate the droplet from the collector surface. A schematic diagram of this process is given in Figure 8-8. Work conducted by Varennes and van de Ven [18] concerning the

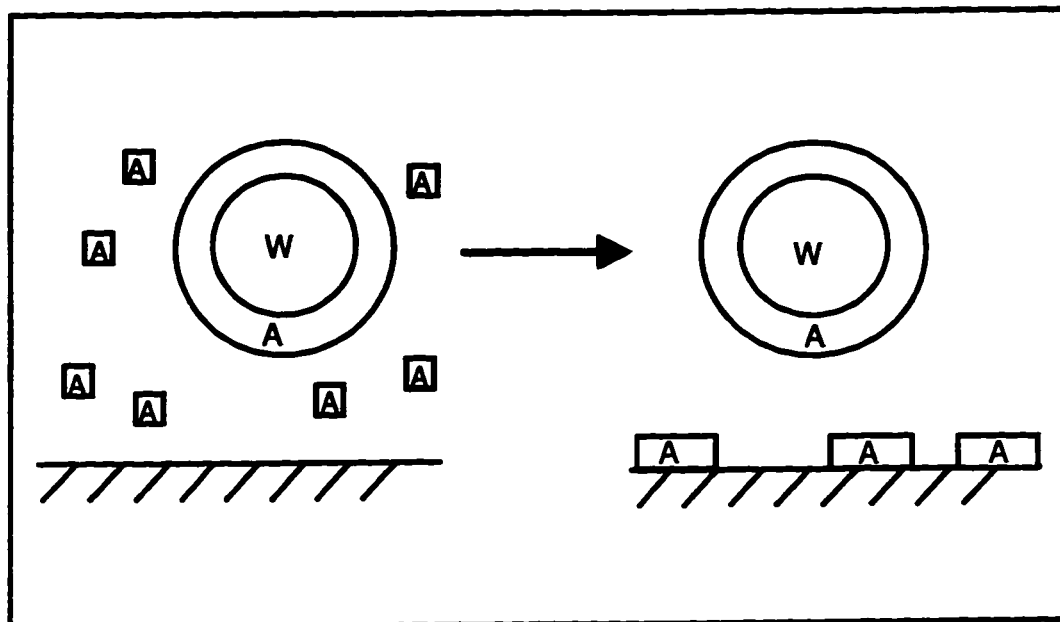


**Figure 8-8.** Schematic representation of possible mechanism to explain the deposition of water droplets (W) coated with asphaltene molecules (A) in the presence of 'free' asphaltenes (A), showing competition for collector adsorption sites between adsorbed and free asphaltenes. From [18].

detachment of latex particles from a collector surface in the presence of free polymer lends credibility to this hypothesis. In their work, Varennes and van de Ven showed that detachment rates increased and deposition rates decreased with increased concentrations of free polymer in the continuous phase.

The nature of the active groups on asphaltene molecules may also play an important role. The active groups are known to be predominantly hydrophilic [37,39,95]. In the water-in-hydrocarbon emulsion deposition experiments discussed above, no deposition was observed when hydrophobic collectors were used. Obviously, the water droplets are more likely to attach to a hydrophilic surface, but what about water droplets surrounded by a layer of asphaltene molecules? Since the 'coated' water droplets still attach to a hydrophilic collector, it is possible that some adsorption reaction takes place between the 'free' asphaltene molecules and the collector surface. It is possible that there is competition for adsorption sites on the collector surface between the 'free' asphaltenes and the asphaltene-coated water droplets. This mechanism was discussed by Varennes and van de Ven [19].

## 8.6 Summary

In Section 8-2, it was shown that a stable emulsion could be prepared, using water as the dispersed phase and a 4:1 (by volume) solution of toluene to hexane, with a small amount of bitumen added to act as the stabilizing agent, as the continuous phase. The resulting emulsion was found to be stable for at least 72 hours after its preparation. The droplets were well-suited for use in impinging jet cell studies: they were stable even after the original emulsion was diluted and were reasonably monodisperse with an average droplet diameter of less than 1.5  $\mu\text{m}$ .

Initial experiments (sets A-1 through A-3) showed that the observed values of Sherwood number varied with droplet concentration,  $c_0$ , while droplet flux to the collector surface,  $J_0$ , did not vary with  $c_0$ , which is exactly the opposite of what is required to ensure that measurement consistency is obtained {see Section 8.4}.

Reproducibility of the results became the immediate concern, so more experiments were conducted (sets A-4 through A-6). Experiment sets A-4 through A-6 were very different from the first three sets, in that (i) Sherwood numbers that were at least two orders of magnitude larger than for the first three sets of experiments were obtained; and, (ii) the consistency criteria based on the ratio of  $J_0/c_0$  was met. Theoretical predictions indicated that there should be no difference among any of the six sets of experiments. There seemed to be no reason for the difference in observed mass transfer rates until a detailed analysis of the experimental conditions was conducted. It was determined that sets A-1 through A-3 had a higher bitumen concentration than sets A-4 through A-6. Seven new sets of experiments were conducted. The continuous phase bitumen concentration,  $b_0$ , and the water droplet concentration,  $c_0$ , were both controlled in these experiments. Sets B-1 through B-7 showed that the results obtained from the first group of experiments (set A) were valid and reproducible, and that the deposition rates are highly dependent upon the continuous phase bitumen concentration of the water-in-hydrocarbon emulsions.

It is believed that the asphaltenes present in the bitumen reside at the water/hydrocarbon interface, thereby stabilizing the emulsions. The specific relationship between asphaltene concentration and droplet deposition rates is unclear. Calculations showed that the transition from small to large values of Sherwood number, which occurred for  $3.0 \text{ g/L} > b_0 > 1.22 \text{ g/L}$ , does not correspond to a change in the monolayer coverage of the water droplets with asphaltenes.

Finally, although DLVO theory can be applied to nonaqueous systems, it cannot be used to predict changes in mass transfer rates with changing bitumen concentration. As a result, there was poor agreement between observed and predicted values of Sherwood number for these experiments. Deposition experiments conducted using emulsions with values of  $b_0 \geq 3.00 \text{ g/L}$  resulted in droplet deposition rates that were much lower than predicted. Deposition experiments conducted using emulsions with values of  $b_0 \leq 1.22 \text{ g/L}$  resulted in Sherwood numbers that were nominally five times larger than values calculated from mass transfer theory.

## 9. Summary and Recommendations

### 9.1 Validity of model: application of DLVO theory to oil-in-water emulsions

The application of DLVO theory to deposition experiments involving the attachment of emulsion droplets to a collector surface can be summarized as follows:

1. Six different oil-in-water emulsions were studied using a range of experimental conditions. Two types of experiments were conducted for each emulsion in order to assess: (i) the variation of dimensionless droplet deposition rate (Sherwood number) with Reynolds number; and, (ii) the variation of Sherwood number with dimensionless double layer thickness ( $\kappa a$ ).
2. Excellent agreement was observed between theory and experiment for the bitumen emulsion deposition experiments conducted using a hydrophilic collector. Experimental results differed from theoretical predictions by less than 20%.
3. Experiments involving two similar mineral oil emulsions (Cannon standard viscometry oils) with different dispersed phase viscosities indicated that the droplet deposition rates were not dependent upon dispersed phase viscosity. Calculation of the Capillary number for the different emulsions studied indicated that the primary effect of dispersed phase viscosity, droplet deformation, would not occur in these experiments.
4. For the Cannon standard viscometry oil-in-water emulsions, droplet deposition rates were higher when the droplet and collector zeta potentials had opposite signs, indicating an attractive double layer force. Predictions of droplet deposition rates based on DLVO theory did not account for the difference between the experimental results.

5. A study of the collector surface coverage during high Reynolds number ( $Re=800$ ) bitumen deposition experiments and high Reynolds number Cannon mineral oil deposition experiments revealed that neither system followed a random deposition pattern. The bitumen droplets spread out over the collector surface, indicating either a heightened interdroplet repulsive force or an enhanced affinity between the droplets and the collector that could not be explained using DLVO theory. The Cannon mineral oil droplets exhibited the opposite trend: they tended to cluster in high concentrations near the stagnation point. The clustering effect exhibited by the Cannon mineral oil droplets partially explains the lower-than-predicted deposition rates. The effective area of deposition is much smaller than the total area available for deposition in this case, which means that particle blocking effects occur at much lower coating densities.

6. The results of Bayol oil-in-water emulsion deposition experiments were not predicted by DLVO theory. Observed deposition rates were similar to predicted values at low and intermediate Reynolds numbers, but differed significantly at high Reynolds numbers. The observed deposition rates decreased sharply with Reynolds number for values of Reynolds number greater than 300. This trend was not predicted by the numerical model. Further analysis of the experiments suggests that the decreased deposition rates at high Reynolds numbers is due to the large induction time exhibited by the Bayol oil droplets. Induction times refer to the characteristic length of time it takes for a droplet to strongly attach to the collector surface after initial impact. Induction times cannot be predicted using DLVO theory. The nonionic surfactant used to stabilize the Bayol oil emulsions may be related to this system's long induction times and low deposition rates at high Reynolds numbers.

7. Pentadecane emulsions, stabilized with a small concentration of asphaltenes, were found to follow DLVO theory.

8. The results of the low viscosity oil deposition experiments, which include the Cannon mineral oils, the Bayol oil, and the pentadecane, reveal one of the major fallibilities of DLVO theory. DLVO theory is unable to explain differences in deposition behavior unless the difference is due to surface charge. Consequently, two systems such as the pentadecane emulsions and the Cannon mineral oil emulsions, which possess similar surface charges but different deposition rates, cannot be adequately described using DLVO theory.

## **9.2 Significance of results of hydrophobic/coated collector deposition experiments**

The significance of the experiments conducted to study the deposition of bitumen droplets on both silane-treated (hydrophobic) and bitumen-coated microscope slides can be summarized as follows:

1. Experiments using both types of collectors revealed that no attractive hydrophobic forces occurred in these systems. In fact, bitumen droplet deposition rates were five to six times lower than predicted by DLVO theory.
2. The results of the bitumen deposition experiments onto a bitumen-coated slide were nearly an order of magnitude lower than was predicted using DLVO theory. These results do not agree with the results of bitumen droplet-droplet coagulation studies conducted by Takamura, Chow, and Tse [60] and Chow and Takamura [61] even though the bitumen droplet - bitumen coated surface interactions should be analogous to bitumen droplet - droplet interactions.
3. The observed bitumen droplet deposition rates onto both the silane-treated and the bitumen-coated collector, as well as the apparent absence of any significant hydrophobic interactions, can be partially explained by the presence of carboxyl

groups at the bitumen-water interface. These surface groups, which impart surface charge to the bitumen, also give the bitumen a partly hydrophilic character. Attractive hydrophobic interactions only occur between strongly hydrophobic materials.

4. Both sets of deposition experiments involving different collectors show the importance of characterizing any surface active agents that are present in a colloidal system. In other words, more than just the surface charge and the Hamaker constant need to be considered when modelling deposition or flotation processes.

### **9.3 Significance of nonaqueous emulsion deposition experiments**

The significance of the water-in-hydrocarbon emulsion deposition experiments conducted as part of this study can be summarized as follows:

1. The experiments involving the deposition of water-in-hydrocarbon emulsions in an impinging jet cell are some of the first of their kind ever conducted.
2. Theoretical mass transfer rates for the water-in-hydrocarbon emulsion deposition experiments were calculated using the numerical model. Only van der Waals and hydrodynamic interactions between the water droplets and the collector surface were considered. Electrostatic interactions were negligible because of the low dielectric constant of the continuous phase.
3. Comparison of observed and calculated mass transfer rates for the water-in-hydrocarbon emulsion deposition experiments indicates that the continuous phase bitumen concentration,  $b_0$ , has a tremendous effect on the observed mass transfer rates. For large values of  $b_0$ , observed mass transfer rates were much lower than calculated mass transfer rates. For small values of  $b_0$ , observed mass transfer rates were significantly higher than was predicted using mass transfer theory.

4. The observed effect of continuous phase bitumen concentration on the rate of water droplet mass transfer to the collector surface can be classified as follows:

(i)  $b_0 \leq 0.6$  g/L: the water-in-hydrocarbon emulsion is not stable. The water droplets break up because of the hydrodynamic forces that occur in the impinging jet cell.

(ii)  $0.6 < b_0 \leq 1.22$  g/L: high rates of water droplet deposition are observed. The values of Sherwood number are independent of water droplet concentration,  $c_0$ , and continuous phase bitumen concentration,  $b_0$ . Observed mass transfer rates were significantly higher than calculated mass transfer rates.

(iii)  $1.22 < b_0 < 3.0$  g/L: droplet deposition rates decrease sharply in this range. Calculations indicate that the transition from high to low mass transfer rates does not correspond to transition from monolayer to sub-monolayer asphaltene coverage of water droplets.

(iv)  $b_0 \geq 3.0$  g bitumen / L solution: the water droplet deposition rate is a function of Reynolds number and water droplet concentration. The deposition rates do not change with increasing  $b_0$ . Observed mass transfer rates were much lower than calculated mass transfer rates, and nearly 2 orders of magnitude lower than the observed mass transfer rates in (ii). The behavior of emulsions with  $b_0 \geq 3.0$  g/L cannot be predicted using DLVO theory. Emulsions with  $b_0 > 12.2$  g/L were too opaque to study in the impinging jet cell.

5. The increase in water droplet deposition rate when  $b_0$  is decreased from 3.0 g/L to 1.22 g/L may be a result of a decrease in competition between free asphaltene molecules present in the continuous phase and the asphaltene-coated water droplets. This theory does not explain the instability of the water droplets when  $b_0 < 0.6$  g/L.

6. The results presented here are potentially very important to the development of efficient demulsification processes.

## **9.4 Recommendations for future work**

Based on the results presented in this thesis, the following recommendations can be made:

1. Further studies should be conducted to correlate surface characteristics of emulsions with deposition rates and characteristic induction times. The results of the oil-in-water deposition experiments indicate that the interaction between surface groups on the droplets and on the collector will often dominate the interactions described by DLVO theory.
2. Future studies of deposition behavior should be concerned with the interactions that occur at the collector surface rather than with the short-range forces that transport a particle to the collector. This type of study would be facilitated by the development of good analytical models that would adequately describe the bulk transport of a particle to the collector surface, thereby eliminating the need to solve the governing fluid flow and mass transfer equations numerically.
3. A more comprehensive description of the hydrophilic/hydrophobic nature of bitumen needs to be pursued. The characteristics that allow bitumen to attach to hydrophobic air bubbles and to hydrophilic collector surfaces under the same solution conditions need to be more fully understood.
4. The results of the water-in-hydrocarbon emulsion deposition experiments discussed in this thesis should be complemented with more extensive deposition experiments, in which the ratio of toluene/hexane in the continuous phase is varied.
5. The study of nonaqueous emulsion behavior is still in its infancy. Many different areas of research need to be addressed. Perhaps the most important first step involves the accurate characterization of nonaqueous emulsions, including zeta potential

measurements in low conductivity media, dissociation of electrolytes and the possibility of electrostatic stabilization in nonaqueous systems. For example, more deposition experiments could be conducted to study the effect of continuous phase dielectric constant on droplet deposition rates.

### **9.5 Major contributions made by this study**

The major contributions made by this study can be summarized as follows:

1. This work consists of an extensive system of tests that reveal a great deal about the behavior of emulsions. The benefits of this are threefold: (i) the experimental work presented here can be used by others who may be in pursuit of better theoretical models; (ii) the results presented here provide insight into the behavior of emulsions in general; and, (iii) the methods used here to characterize and study emulsions could easily be used to determine the degree of complexity required to model any emulsion. For example, the results of this study show that the behavior of bitumen droplets can be modelled using DLVO theory under certain conditions. If a process were operating under similar conditions, then it is known that a model of the process based on DLVO theory would be adequate.

2. The theoretical analysis presented in this work represents a novel synthesis of a number of existing fundamental models, including

- (i) DLVO theory;
- (ii) numerical solution of the continuity, Navier-Stokes, and general convection-diffusion equations;
- (iii) Interfacial Surface Group (ISG) model;
- (iv) Lifshitz' theory for calculation of Hamaker constant; and,
- (v) analytical expressions representing the universal hydrodynamic

correction coefficients (UHCC's).

3. Experiments involving the variation of Sherwood number with dimensionless double layer thickness ( $\kappa a$ ) are first presented in this study.
4. The deposition of water-in-nonaqueous media emulsions using an impinging jet cell has never before been studied. The relationship between the amount of bitumen present in the continuous phase and the rate of droplet adhesion represents a significant contribution to the study of water-in-naptha and water-in-dilute bitumen emulsions that are found in the course of oil sands processing and upgrading.

## REFERENCES

1. Dabros, T. and T.G.M. van de Ven, *Colloid Polym. Sci.*, **261** (1983) 694.
2. Brenner, H., *Chem. Eng. Sci.*, **16** (1961) 242.
3. Goren, S.L., and M.E. O'Neill, *Chem. Eng. Sci.*, **26** (1971) 325.
4. Goren, S.L., *J. Fluid Mechanics*, **41** (1970) 619.
5. Goldman, A.J., R.G. Cox, and H. Brenner, *Chem. Eng. Sci.*, **21** (1966) 1151.
6. Spielman, L.A., and J.A. Fitzpatrick, *J. Colloid Interface Sci.*, **42** (1973) 607.
7. Gosman, A.D., W.M. Pun, A.K. Runchal, D.B. Spalding, and M. Wolfshtein, "Heat and Mass Transfer in Recirculating Flows", Academic Press, London, 1969.
8. Swanton, S.W., *Adv. Colloid Interface Sci.*, **54** (1995) 129.
9. Marshall, J.K., and J.A. Kitchener, *J. Colloid Interface Sci.*, **22** (1966) 342.
10. Hull, M., and J.A. Kitchener, *Trans. Faraday Soc.*, **65** (1969) 3093.
11. Prieve, D.C., and M.M.J. Lin, *J. Colloid Interface Sci.*, **76** (1980) 32.
12. Bowen, B.D., and N. Epstein, *J. Colloid Interface Sci.*, **72** (1979) 81.
13. Adamczyk, Z., and T.G.M. van de Ven, *J. Colloid Interface Sci.*, **80** (1981) 340.
14. Sjollem, J., and H.J. Busscher, *J. Colloid Interface Sci.*, **132** (1989) 382.
15. Sjollem, J., and H.J. Busscher, *Colloids Surfaces*, **47** (1990) 323.
16. Meinders, J.M., H.C. van der Mei, and H.J. Busscher, *J. Colloid Interface Sci.*, **176** (1995) 329.
17. Dabros, T., and T.G.M. van de Ven, *PhysicoChem. Hydrodyn.*, **8** (1987) 161.
18. Varennes, S., and T.G.M. van de Ven, *PhysicoChem. Hydrodyn.*, **9** (1987) 537.
19. Varennes, S., and T.G.M. van de Ven, *PhysicoChem. Hydrodyn.*, **10** (1988) 415.
20. Adamczyk, Z., T. Dabros, J. Czarniecki, and T.G.M. van de Ven, *Adv. Colloid Interface Sci.*, **19** (1983) 183.

21. Boluk, M.Y., and T.G.M. van de Ven, *PhysicoChem. Hydrodyn.*, **11** (1989) 113.
22. Albery, W.J., R.A. Fredlein, G.R. Kneebone, G.J. O'Shea. and A.L. Smith. *Colloids Surfaces*, **44** (1990) 337.
23. Deshpande, M.D. and R.N. Vaishnav, *J. Fluid Mech.*, **114** (1982) 213.
24. Roache, P.J., "Computational Fluid Dynamics", Hermosa Publishers, Albuquerque. NM, 1972.
25. Law, H.S. and J.H. Masliyah, *Ind. Eng. Fundam.*, **23** (1984) 232.
26. van de Ven. T.G.M., "Colloidal Hydrodynamics", Academic Press, London. 1989.
27. Masliyah, J.H., "Electrokinetic Transport Phenomena", AOSTRA Technical Publication Series No. 12. AOSTRA, Edmonton, Alberta, 1994.
28. Klahn, J.K., W.G.M. Agterof. F. van Voorst Vader. *et al. Colloids Surfaces*. **65** (1992) 151.
29. Hamaker, H.C., *Physica*. **4** (1937) 1058.
30. Mahanty, J. and B.W. Ninham, "Dispersion Forces". Academic Press, London. 1976.
31. Israelachvili, J.N. and D. Tabor. *Prog. Surface Membrane Sci.*, **7** (1973) 1.
32. Israelachvili, J.N., "Intermolecular and Surface Forces", 2nd. Edition. Academic Press, London. 1992.
33. Gregory, J., *J. Colloid Interface Sci.*, **84** (1981) 138.
34. Suzuki, A., N.F.H. Ho, and W.I. Higuchi, *J. Colloid Interface Sci.*, **29** (1969) 552.
35. Derjaguin, B.V., *Kolloid. Z.*, **69** (1934) 155.
36. Hogg, R., T.W. Healy, and D.W. Furstenuau, *Trans. Faraday Soc.*, **62** (1966) 1638.
37. Takamura, K. and R.S. Chow, *Colloids Surfaces*, **15** (1985) 35.
38. Healy, T.W. and L.R. White, *Adv. Colloid Interface Sci.*, **9** (1978) 303.
39. Buckley, G. and K. Takamura, SPE #16964, 62<sup>nd</sup> Annual Tech. Conf., Dallas, Texas, 1987.

40. van der Hoeven, Ph. C., and J. Lyklema, *Adv. Colloid Interface Sci.*, **42** (1992) 205.
41. Morrison, I.D., *Colloids Surfaces A*, **71** (1993) 1.
42. Parfitt, G.D. and J. Peacock, in "Surface and Colloid Science", vol. 10, E. Matijevic (Ed.), Plenum Press, New York, 1978.
43. Fuoss, R.M., *J. Am. Chem. Soc.*, **80** (1958) 5059.
44. Barenev, G. M., "The Structure and Mechanical Properties of Inorganic Glasses." Wolters-Noordhoff, Groningen, 1970.
45. Araujo, Y.C., P.G. Toledo, V. Leon, and H.Y. Gonzalez, *J. Colloid Interface Sci.*, **176** (1995) 485.
46. Sermon, P.A., M.A. Yates, and C.A. Koh, *Colloids Surfaces*, **63** (1992) 55.
47. Chow, R.S., and K. Takamura, *J. Colloid Interface Sci.*, **125** (1988) 226.
48. Redford, K.W., *M. Sc. Thesis*, University of Alberta, Edmonton, 1993.
49. American Petroleum Institute (API), "Technical Data Book - Petroleum Refining". 4th. Edition, T.E. Daubert and R.P. Danner (Eds.), American Petroleum Institute, Washington, 1983.
50. Takamura, K. and R.S. Chow, *J. Can. Pet. Technol.*, **22** (1983) 1.
51. Chow, R.S., Personal Communication, 1992.
52. Yan, Y., R. Pal, and J.H. Masliyah, *Chem. Eng. Sci.*, **46** (1991) 985.
53. Yan, Y. and J.H. Masliyah, *Colloids Surfaces A*, **75** (1993) 123.
54. Tadros, Th. F., and B. Vincent, in "Encyclopedia of Emulsion Technology", Vol. 1, P. Becher (Ed.), Marcel Dekker, Inc., New York, 1983.
55. Carroll, B.J., in "Surface and Colloid Science", vol. 4, E. Matijevic (Ed.), Plenum Press, New York, 1978.
56. Berkley, J.B. , in "Criteria for Quality of Petroleum Products", J.P. Allinson (Ed.), John Wiley and Sons, Toronto, 1973.
57. Schulman, J.H., and Leja, J., *Trans. Faraday Soc.*, **50** (1954) 598.

58. Menon, V.B, and D.T. Wasan, *Colloids Surfaces*, **19** (1986) 89.
59. Yan, N. and J.H. Masliyah, *Colloids Surfaces A*, **75** (1993) 123.
60. Takamura, K., R.S. Chow and D.L. Tse, in "Flocculation in Biotechnology and Separation Systems", Y.A. Attia (Ed.), Elsevier Science Publishers B.V., Amsterdam, 1987.
61. Takamura, K. and R.S. Chow, *Energy Process. Can.*, **74**, no. 7 (1982) 29.
62. Takamura, K., and D. Wallace. *J. Can. Pet. Technol.*, **27** (1988) 98.
63. CRC Handbook of Chemistry and Physics, 77th. Edition, D.R. Lide (Ed.), CRC Press, New York, 1996.
64. Mousa, H., and T.G.M. van de Ven, *Colloids Surfaces*, **60** (1991) 19.
65. Mousa, H., and T.G.M. van de Ven, *Colloids Surfaces*, **60** (1991) 39.
66. Mahé, M., M. Vignes-Adler, A. Rousseau, C.G. Jacquin, and P.M Adler, *J. Colloid Interface Sci.*, **126** (1988) 315.
67. Pugh, R.J., and R.-H. Yoon, *J. Colloid Interface Sci.*, **163** (1994) 169.
68. Claesson, P.M., *Prog. Colloid Polymer Sci*, **74** (1987) 48.
69. Churaev, N.V., and B.V. Derjaguin, *J. Colloid Interface Sci.*, **103** (1985) 542.
70. Israelachvili, J.N., *Faraday Discuss. Chem. Soc.*, **65** (1978) 20.
71. Israelachvili, J.N., *Adv. Colloid Interface Sci.*, **16** (1982) 31.
72. Pashley, R.M., *J. Colloid Interface Sci.*, **80** (1981) 153.
73. Pashley, R.M., *J. Colloid Interface Sci.*, **83** (1981) 531.
74. Pashley, R.M, *Adv. Colloid Interface Sci.*, **16** (1982) 57.
75. Pashley, R.M. and B.W. Ninham, *J. Phys. Chem.*, **91** (1987) 2902.
76. Pashley, R.M. and J.N. Israelachvili, *J. Colloid Interface Sci.*, **97** (1984) 446.
77. Rabinovich, Y.I., B.V. Derjaguin, and N.V. Churaev, *Adv. Colloid Interface Sci.*, **16** (1982) 63.

78. Yotsumoto, H., and R.-H. Yoon, *J. Colloid Interface Sci.*, **157** (1993) 426.
79. Israelachvili, J.N., *J. Colloid Interface Sci.*, **98** (1984) 500.
80. Rabinovich, Y.I., and B.V. Derjaguin, *Colloids Surfaces*, **30** (1988) 243.
81. Claesson, P.M., and H.K. Christenson, *J. Phys. Chem.*, **92** (1988) 1650.
82. Rabinovich, Ya. I., and R.-H. Yoon, *Langmuir*, **10** (1994) 1903.
83. Xu Z., and R.-H. Yoon, *J. Colloid Interface Sci.*, **132** (1989) 5.
84. Xu Z., and R.-H. Yoon, *J. Colloid Interface Sci.*, **134** (1990) 427.
85. Claesson, P.M., C.E. Blom, P.C. Herder, and B.W. Ninham, *J. Colloid Interface Sci.*, **114** (1986) 234.
86. Christenson, H.K., *J. Dispersion Sci. Technol.*, **9** (1988) 1.
87. Lee, C.Y., and J.A. McCammon, *J. Phys. Chem.*, **80** (1984) 4448.
88. Varadaraj, R., J. Bock, N. Brons, and S. Zushma, *J. Colloid Interface Sci.*, **167** (1994) 207.
89. Silberzan, P., L. Leger, D. Ausserre, and J.J. Benattar, *Langmuir*, **7** (1991) 1647.
90. Goodwin, J.W., R.S. Harbron, and P.A. Reynolds, *Colloid Polym. Sci.*, **268** (1990) 766.
91. Dabros, T., Q. Dai, H. Hamza, and J. Czarnecki, Proc. 1st. UBC - McGill Bi-annual International Symp. Fundamentals of Mineral Processing, Vancouver, BC, Aug. 20-24, 1995, pp. 413-424.
92. Alexander, K.L., and D. Li, *Colloids Surfaces A*, **106** (1996) 191.
93. Anderson, W.G., *J. Pet. Technol.*, (1986) 1246.
94. Vincent, B., *J. Colloid Interface Sci.*, **42** (1973) 270.
95. Takamura, K., and E.E. Isaacs, in "AOSTRA Technical Handbook on Oil Sands, Bitumens, and Heavy Oils", L.G. Hepler and C. Hsi (Eds.), AOSTRA Technical Publication Series No. 6, AOSTRA, Edmonton, 1989.

96. Yaminsky, V.V., B.W. Ninham, H.K. Christenson, and R.M. Pashley. *Langmuir*, **12** (1996) 1936.
97. Attard, P., *Langmuir*, **12** (1996) 1693.
98. Yarranton, H., and J.H. Masliyah, *AIChE J.*, in press.
99. Chow, R.S., Personal Communication, 1995.
100. Sheu, E.Y., M.M. De Tar, and D.A. Storm, *Fuel*, **71** (1992) 1277.
101. Kokal, S., T. Tang, L. Schramm, and S. Sayegh, *Colloids Surfaces A*, **94** (1995) 253.

## APPENDIX A

### Calculation of asphaltene concentration and water droplet surface coverage for a water-in-hydrocarbon emulsion, $b_0 = 1.22$ g/L

The asphaltene concentration can be calculated assuming a basis of 1 L of dilute emulsion. If  $b_0 = 1.22$  g bitumen / L solution, then the mass of bitumen in the emulsion is  $m_b = 1.22$  g bitumen. The mass of asphaltenes present in 1 L of dilute emulsion,  $m_a$ , is

$$m_a = m_b x_w \quad (\text{A-1})$$

If the weight fraction of asphaltenes in Athabasca bitumen is taken to be  $x_w = 0.17^1$ , then, from eq. (A-1),  $m_a = 0.2074$  g asphaltenes.

Yarranton<sup>2</sup> has estimated that the surface area occupied by 1 g of asphaltene molecules,  $T$ , is  $T = 145 \text{ m}^2 / \text{g}$  asphaltenes. The surface area that can be covered by 0.2074 g asphaltenes is

$$A_m = m_a T \quad (\text{A-2})$$

or,  $A_m = 30.07 \text{ m}^2$ . If the surface area of the water droplets exceeds the surface area that can be covered by the asphaltenes present in the continuous phase, then sub-monolayer coverage would occur.

The water droplet concentration,  $c_0$ , used in these calculations is taken from experiment set B-1 {see Table 8-3}. For set B-1,  $c_0 = 7.2 \times 10^6$  droplets/ml. Thus, in 1 L of emulsion, the total number of water droplets is  $N = 6.2 \times 10^{10}$  droplets. If the radius of a single droplet is  $a = 0.695 \text{ } \mu\text{m}$  and the surface area of a single droplet is

<sup>1</sup>O.P. Strausz, in "AOSTRA Technical Handbook on Oil Sands, Bitumens, and Heavy Oils", L.G. Hepler and C. Hsi (Eds.), AOSTRA Technical Publication Series No. 6, AOSTRA, Edmonton, 1989.

<sup>2</sup>Yarranton, H., Personal Communication, 1996.

$s = 4\pi a^2$ , then the total surface area of the dispersed phase,  $A_s$ , is

$$A_s = N s = N (4\pi a^2) \quad (\text{A-3})$$

For  $N = 6.2 \times 10^{10}$  droplets and  $a = 0.695 \mu\text{m}$ ,  $A_s = 0.3763 \text{ m}^2$ .

These calculations show that  $A_m \gg A_s$ . Clearly, there are at least 10 times more asphaltenes present in the continuous phase than would be required for monolayer coverage of the water droplets.

## APPENDIX B

### Computer code for numerical solution of flow field equations

AFLOW.FOR

\*Written by Sean Sanders (May 1991)

\*Fortran program to solve N-S equations for flow field in an  
\*impinging jet cell.

\*

\*  $\bar{\omega}^*(i,j) = a(i,j,nw)$ ; where  $nw=1$

\*  $\bar{\psi}(i,j) = a(i,j,nf)$ ; where  $nf=1$

\*  $i$ = z-direction grid node labels

\*  $j$ = r-direction grid node labels

\*  $in$ = no. of grid points in z-direction

\*  $jn$ = no. of grid points in r-direction

\*\*\*\*\*

\*Purpose of program: determine  $\bar{\omega}^*(in,1)$ , which is equal to

\*the value of  $\bar{\alpha}$ . where  $\bar{\alpha}$  = strength of stagnation point flow.

\*\*\*\*\*

\*

\*Program based on program given by Gosman et. al. in "Heat and Mass Transfer in

\*Recirculating Flows". Academic Press, London, 1969.

\*

\*\*\*\*\*

dimension a(41,31,2), be(41),bw(41),bn(31),bs(31)

common / cvrble/ a

common / cnumbr/ nw,nf,nv1,nv2,ie,iv,h0,re,sl

common / cgeo/ in,inm,jn,jnm,x1(41),x2(31),r(31),ncord

common / cgen/ nmax, nprint,ip,cc,rp(2),rsdu(2)

\*\*\*\*\*

\* subroutine for initialization and program control

\*\*\*\*\*

\*

\*ensure that dimensions of arrays above correspond with

\*values assigned to n1,n2,n3 below!!

data n1,n2,n3/ 38,31,2/

inm=in-1

jnm=jn-1

\*call initialization subroutines

call grid (n1,n2,n3,be,bw,bn,bs)

call init (n1,n2,n3,a)

\*write problem specification information

```

open (unit=7, file='aflow.out')
write (7,*) 'Reynolds no. =', re
write (7,*) 'separation distance =', h0
write (7,*) 'convergence criterion =', cc
write (7,*) 'maximum iterations =', nmax
write (7,*) 'no. of z-dir grid lines =', in
write (7,*) 'no. of r-dir grid lines =', jn
*iteration- and printout- control loop
niter=0
1  niter=niter+1
*cause one cycle of iteration to be performed
call eqn (n1,n2,n3,a,be,bw,bn,bs)
*test to see if printout is produced
if(((niter+nprint-ip)/nprint).ne.(niter/nprint)) go to 10
call print (n1,n2,n3,a,in,jn,1.ie)
write(6,*)'Iteration # ', niter
write(6,*)'alpha = ', a(in,1.nw)

10  write (7,*)'ITERATION NO. =', niter
write (7,*)'max. resid vorticity =', rsdu(1)
write (7,*)'max. resid str. function =', rsdu(2)
write (7,*)'-----'
*test if maximum no. of iterations (nmax) performed
if(niter.eq.nmax) go to 8
res=0.
do 71 k=1.ie
if(abs(res).lt.abs(rsdu(k))) res=rsdu(k)
rsdu(k)=0.
71  continue
*test if convergence criteria satisfied
if(abs(res).gt.cc.or.niter.le.5) go to 1
*end of loop
go to 9
8  continue
write (7,*)'the soln did not converge in',niter
9  continue
*final printout
do 31 i=1,in
write(7,408)i,a(i,1,nw),a(i,5,nw),a(i,7,nw),a(i,10,nw)
write(7,408)i,a(i,15,nw),a(i,17,nw),a(i,21,nw),a(i,31,nw)
31  continue
write (7,*)'-----'
write (7,*)'i      phi(i,1)      phi(i,2) phi(i,3)      l phi(i,21)'
do 32 i=1,in

```

```

        write(7,408)i,a(i,1,nf),a(i,2,nf),a(i,3,nf),a(i,21,nf)
32    continue
408    format (i3,4f15.4)
        stop
        end

*****BLOCK DATA
:
        block data
        common/ cnumbr/ nw,nf,nv1,nv2,ie,iv,h0,re,sl
        common / cgeo/ in,inm,jn,jnm,x1(38),x2(31),r(31),ncord
        common / cgen/ nmax. nprint,ip,cc,rp(2),rsdu(2)
*****
*    input of numerical data for the problem
*****
*
*****program- and printout- control data
        data nw,nf,nv1,nv2,ie,iv/1,2,3,4,2,2/
        data nmax.nprint,ip,cc/3.50,2,0.0010/
        data rp/2*1 /
        data ncord/2/in,jn/38,31/
*IMPORTANT PARAMETERS! INPUT Re. sl AND h0 HERE!!
        data h0,re,sl/1.7,40..5 /
        end

*****BOUND

        subroutine bound(n1,n2,n3,a)
        dimension a(n1,n2,n3)
        common/ cnumbr/nw,nf,nv1,ie,iv,h0,re,sl
        common/ cgeo/ in,inm,jn,jnm,x1(38),x2(31),r(31),ncord
*****
*    subroutine for iteration on boundary nodes
*****
        d1x1=1/(x1(2)-x1(1))
        d2x1=1/(x1(inm)-x1(in))
        do 42 j=2,jnm
*vorticity at z=0 (upper plane)
        if (r(j).le.1.0) then
            a(1,j,nw)=4.0
        else
            phid=a(1,j,nf)-a(2,j,nf)
            a(1,j,nw)= 3.*phid*d1x1*d1x1/r(j)**2
            a(1,j,nw)=a(1,j,nw)-0.5*a(2,j,nw)

```

```

endif
*vorticity at z=ho (impingement plane)
  phid=a(in,j,nf)-a(inm,j,nf)
  a(in,j,nw)= 3.*phid*d2x1*d2x1/r(j)**2
  a(in,j,nw)=a(in,j,nw)-0.5*a(inm,j,nw)
42  continue
  do 82 i=2,in
*vorticity at r=0 (plane of symmetry)
  arc=1./(r(3)**2-r(2)**2)
  ba2=a(in-2,3,nf)/r(3)**2-a(in-2,2,nf)/r(2)**2
  ba1=a(inm,3,nf)/r(3)**2-a(inm,2,nf)/r(2)**2
  ba0=a(in,3,nf)/r(3)**2-a(in,2,nf)/r(2)**2
  d2bdz2=arc*d1x1**2*(ba0-2*ba1+ba2)

  phid=r(3)**2*a(i,2,nf)/r(2)**2-r(2)**2*a(i,3,nf)/r(3)**2
  a(i,1,nw)= -8.*arc*phid-d2bdz2
*vorticity at r=L (exit plane, vz=0)
  a(i,jn,nf)=a(i,jnm,nf)
  a(i,jn,nw)=a(i,jnm,nw)
82  continue
  return
end

```

#### \*\*\*\*\*CONVEC

```

subroutine convect (n1,n2,n3,a,ae,aw,an,as,i,j,k)
dimension a(n1,n2,n3)
common/cnumbr/ nw,nf,nv1,nv2,ie,iv,h0,re,sl
common/ cgeo/ in,inm,jn,jnm,x1(38),x2(31),r(31),ncord
*****
*  subroutine for calculation of ae,aw,an,as
*****
*
*calculate mean mass flow rate over node
  dv=r(j)*(x1(i+1) - x1(i-1)) * (x2(j+1) - x2(j-1))
  glpw=(a(i,j+1,nf)-a(i,j-1,nf)+a(i-1,j+1,nf)-a(i-1,j-1,nf))/dv
  glpe=(a(i,j+1,nf)-a(i,j-1,nf)+a(i+1,j+1,nf)-a(i+1,j-1,nf))/dv
  g2ps=(a(i-1,j,nf)-a(i+1,j,nf)+a(i-1,j-1,nf)-a(i+1,j-1,nf))/dv
  g2pn=(a(i-1,j,nf)-a(i+1,j,nf)+a(i-1,j+1,nf)-a(i+1,j+1,nf))/dv
*compute ae,aw,an,as
  app=r(j)*r(j)
  ae=0.5*app*(abs(glpe)-glpe)
  aw=0.5*app*(abs(glpw)+glpw)

```

```

an=0.5*app*(abs(g2pn)-g2pn)
as=0.5*app*(abs(g2ps)+g2ps)
return
end

```

\*\*\*\*\*EQN

```

subroutine eqn (n1,n2,n3,a,be,bw,bn,bs)
dimension a(n1,n2,n3), be(n1),bw(n1),bn(n2),bs(n2)
common/ cnumbr/ nw,nf,nv1,nv2,ie,iv,h0,re,sl
common / cgeo/ in,inm,jn,jnm,x1(38),x2(31),r(31),ncord
common / cgen/ nmax, nprint,ip,cc,rp(2),rsdu(2)
*****
*   iteration subroutine
*****
*
*vorticity sub-cycle
source=0.
do 11 j=2,jnm
do 12 i=2,inm
*obtain ae,aw,etc.
call convect (n1,n2,n3,a,ae,aw,an,as,i,j,nw)

*compute bbe,bbw,bbn,bbs
rcub=r(j)*r(j)*r(j)
bbe=2.*rcub/re*be(i)
bbw=2.*rcub/re*bw(i)
bbn=(r(j+1)*r(j+1)*r(j+1)+rcub)/re*bn(j)
bbs=(r(j-1)*r(j-1)*r(j-1)+rcub)/re*bs(j)
anum=(ae+bbe)*a(i+1,j,nw)+(aw*bbw)*a(i-1,j,nw)+
%(an*bbn)*a(i,j+1,nw)+(as*bbs)*a(i,j-1,nw)+source
adnm=ae+aw+an+as+bbe+bbw+bbn+bbs
if (adnm.eq.0.) go to 12
*store old value of vorticity
z=a(i,j,nw)
*calculate new value
a(i,j,nw)=anum/adnm
*calculate residual
rs=1. - z/a(i,j,nw)
*under- or over- relax if specified
a(i,j,nw)=z+rp(nw)*(a(i,j,nw)-z)

```

```

*store maximum residual
  if(abs(rs).gt.abs(rsdu(nw))) rsdu(nw)=rs
12  continue
11  continue
*stream function subcycle
  do 21 j=2,jnm
    do 22 i=2,inm
*obtain source term
      source=a(i,j,nw)*r(j)
*average value of r used for evaluation of bbn,bbs,bbw, bbe
      bbe=2.*1/r(j)*be(i)
      bbw=2.*1/r(j)*bw(i)
      bbn=4./(r(j+1)+r(j))*bn(j)
      bbs=4./(r(j-1)+r(j))*bs(j)
      anum=bbe*a(i+1,j,nf)+bbw*a(i-1,j,nf)+bbn*a(i,j+1,nf)
      l+bbs*a(i,j-1,nf)+source
      adnm=bbe+bbw+bbn+bbs
      if(adnm.eq.0.) go to 22
      z=a(i,j,nf)
      a(i,j,nf)=anum/adnm
      rs=1.-z/a(i,j,nf)
      a(i,j,nf)=z+rp(nf)*(a(i,j,nf)-z)
      if(abs(rs).gt.abs(rsdu(nf))) rsdu(nf)=rs
22  continue
21  continue
*initiate iteration on boundary nodes
  call bound(n1,n2,n3,a)
  return
end

```

\*\*\*\*\*GRID

```

  subroutine grid(n1,n2,n3,be,bw,bn,bs)
  dimension be(n1),bw(n1),bn(n2),bs(n2)
  common/ cnumbr/ nw,nf,nv1,nv2,ie,iv,h0,re,sl
  common / cgeo/ in,inm,jn,jnm,x1(41),x2(31),r(31),ncord
  open(unit=11,file='grid.out')
*****
*   subroutine for calculation of be,bw,bn,bs
*****
*
*compute grid coordinates
  x1(1)=0.

```

```

do 10 i=2,11
  x1(i)=x1(i-1)+0.005
10  continue
  x1(12)=0.1
  do 11 i=13,27
    x1(i)=x1(i-1)+0.1
11  continue
  x1(28)=1.65
  do 12 i=29,41
    x1(i)=x1(i-1)+0.005
12  continue
  x2(1)=0.
  x2(2)=0.005
  do 50 j=3,14
    x2(j)=x2(j-1)*1.5
50  continue
  x2(15)=1.00
  do 51 j=16,30
    x2(j)=x2(j-1)*1.1
51  continue
  x2(jn)=sl

*calculate r(j) according to coordinate system
  if(ncord.eq.1) go to 14
  if(ncord.eq.2) go to 15
14  flag=0
  do 110 j=1,jn
    r(j)=1.
110  continue
  go to 17
15  flag=1
  do 111 j=1,jn
    r(j)=x2(j)
111  continue
*compute be,bw,bn,bs
17  do 21 i=2,inm
    dx1=1/(x1(i+1)-x1(i-1))
    bw(i)=dx1/(x1(i)-x1(i-1))
    be(i)=dx1/(x1(i+1)-x1(i))
21  continue
  do 22 j=2,jnm
    dx2=0.5/(x2(j+1)-x2(j-1))
    bs(j)=(1.+r(j-1)/r(j))/(x2(j)-x2(j-1))*dx2
    bn(j)=(1.+r(j+1)/r(j))/(x2(j+1)-x2(j))*dx2

```

```

22  continue
*print out coordinates
    write (11,*)'i          z'
    do 68 i=1,in
    write (11,106)i,x1(i)
68  continue
    write (11,*)'j          r'
    do 69 j=1,jn
    write(11,106)j,x2(j)
69  continue
106 format (i3,10x,f15.7)
    return
    end

*****INIT
    subroutine init(n1,n2,n3,a)
    dimension a(n1,n2,n3)
    common/ cnumbr/ nw,nf,nv1,nv2,ie,iv,h0,re,sl
    common / cgeo/ in,inm,jn,jnm,x1(38),x2(31),r(31),ncord
    common / cgen/ nmax, nprint,ip,cc,rp(2),rsdu(2)
*****
*subroutine for cal'n of initial values and fixed boundary *conditions
*****
*
*set values in store to zero
    do 20 k=1,n3
    do 30 j=1,jn
    do 40 i=1,in
    a(i,j,k)=0.0
40  continue
30  continue
20  continue
*at the inlet, z=0, r<R, and along the top surface, z=0, r>R
    do 35 j=1,jn
    if (r(j).le.1.0) then
    a(1,j,nf)=r(j)**2*(1-0.5*r(j)**2)
    a(1,j,nw)=4.0
    else
    a(1,j,nf)=0.5
    endif
35  continue
    return
    end

```

## APPENDIX C

### Computer code for numerical solution of mass transfer equations

SHRE1.FOR

\*Fortran program written by Sean Sanders (September 1993)

\*

\*\*\*\*\*

\*\*            VARIATION OF SH WITH RE: NUMERICAL SOLUTION OF  
\*            IMPINGING JET DEPOSITION EXPERIMENTS

\*\*\*\*\*

\*\*This program solves the two first order ODE's

\*\*             $dc/dH = f(Pe, H, f2, Fz, c, X, f1)$  and

\*\*             $dX/dH = f(Pe, f3, H, c)$

\*\*using the Runge-Kutta Fourth Order Method.

\*\*

\*\*\*\*\*

double precision SK(4),SL(4),Cz(2),xz(2)

double precision C,X,SH,COLD,ERR1,ERR2,MU

double precision h,hh,h1,h2,h0,dh,dh0

double precision KA,NINF,DL,DA,AD,KT,NA,EEO,M,Z,ZC,ZP

double precision C1,C2,C3,D1,D2,D3,E1,E2,E3

double precision FA,FR,FZ,F1,F2,F3,A1,A2,A3,B1,B2,B3

double precision PE,C0,X0,D0,ALPH,R,NU,SHOLD,ESH,E

double precision AA,BB,CC,DD,EE,DDL,AKA,DDA,FF1,FF2,FF3

double precision PP,XX,a,FAFR,ADH,CM,DH1,cerz

INTEGER I,J

aforce(adh,hh)=-adh\*(0.2\*(0.2+22.232\*hh)/(hh\*\*2.\*(0.2+  
%11.116\*hh)\*\*2))

rforce(ddl,aka,dda,hh)=ddl\*aka\*(dexp(-aka\*hh)/(1+dexp(-aka\*hh))-  
%dda\*dexp(-2\*aka\*hh)/(1-dexp(-2\*aka\*hh)))

UHCC(AA,BB,CC,DD,EE,HH)=1.00+AA\*DEXP(-BB\*HH)+CC\*  
%DEXP(-DD\*HH\*\*EE)

EQN1(HH,CC,XX,PP,FF1,FF2,FAFR)=-0.5\*PP\*(HH+1)\*\*2.\*FF2\*CC+  
%FAFR\*CC+XX/FF1

EQN2(HH,CC,PP,FF3)=PP\*FF3\*(HH+1)\*CC

\*\*\*\*\*CONSTANTS\*\*\*\*\*

EEO=8.85E-12\*78.3

KT=1.381E-23\*298.

NA=6.022E23

```

      E=1.602E-19
* PARAMETERS FOR CALCULATING F1,F2,F3
      A1= -0.44323
      B1= 1.2991
      C1= -0.55677
      D1= 0.31983
      E1=0.75
      A2= 1.4547
      B2= 1.2588
      C2= 0.79508
      D2= 0.55969
      E2=0.50
      A3= -0.4873
      B3= 5.4228
      C3= -0.50954
      D3= 37.834
      E3=0.50
*****OPEN RESULTS FILES*****
      OPEN (UNIT=7, FILE='bit1.res')
*****SYSTEM DEFINITION*****
      do 347 in=1,3
      if (in.eq.1) a=0.59e-6
      if (in.eq.2) a=0.42e-6
      if (in.eq.3) a=0.76e-6
      WRITE (7,*)'Bitumen emulsion'
      ZC=-0.045
      ZP=-0.027
      MU=0.000956
      M=0.1000
      Z=1.
      R=6.985e-4
      NU=9.528e-7
      AD=0.440
      D0=KT/(6*3.1416*MU*A)
      NINF=1000*NA*M
      DA=0.5*(ZC-ZP)**2/(ZC*ZP)
      DL=EEO*ZC*ZP*A/KT
      KA=A/(EEO*KT/(2*E**2*Z**2*NINF))**0.5
*
**WRITE SYSTEM VARIABLES TO RESULTS FILE
*
      WRITE(7,*)'Ap ='A
      WRITE(7,*)'Do ='D0
      WRITE(7,*)'Zp ='ZP

```

```

WRITE(7,*)'Zc =' ,ZC
WRITE(7,*)'Ad =' ,AD
WRITE(7,*)'NaCl =' ,M
WRITE(7,*)'DI =' ,DL
WRITE(7,*)'Da =' ,DA
WRITE(7,*)'Ka =' ,KA
WRITE(7,*)' Re           Hinf           Sh'
*****ALGORTITHM START*****
DO 21 KK=1,2
DO 29 AKRE=10.,100.,10.
IF (KK.EQ.2) THEN
  RE=10.*AKRE
ELSE
  RE=AKRE
ENDIF
*
*INITIAL CONDITIONS AND PARAMETERS
*****
X0=10.00
H0=0.001
DH0=1.0e-6
C0=0.0
*****
**CALCULATE PE
*****
ALPH=0.52*RE**0.5
PE = 2.*A**3.*ALPH*RE*NU/(D0*R**3.)
*****
50  I=1
    H=H0
    C=C0
    COLD=1.
    ERR2=1.
    X=X0
    DH=DH0
* RUNGE-KUTTA
DO 100 J=1,120000
DO 101 I=1,1000
57  DH1=DH
DO 102 IL=1,2
IF(IL.EQ.1) THEN
  DH=DH
ELSE
  DH=DH/2.

```

```

ENDIF
H1=H+DH/2.
H2=H+DH
FA=AFORCE(AD,H)
FR=RFORCE(DL,KA,DA,H)
FZ=FA+FR
F1=UHCC(A1,B1,C1,D1,E1,H)
F2=UHCC(A2,B2,C2,D2,E2,H)
F3=UHCC(A3,B3,C3,D3,E3,H)
SK(1)=EQN1(H,C,X,PE,F1,F2,FZ)
SL(1)=EQN2(H,C,PE,F3)
FA=AFORCE(AD,H1)
FR=RFORCE(DL,KA,DA,H1)
FZ=FA+FR
F1=UHCC(A1,B1,C1,D1,E1,H1)
F2=UHCC(A2,B2,C2,D2,E2,H1)
F3=UHCC(A3,B3,C3,D3,E3,H1)
SK(2)=EQN1(H1,C+DH/2.*SK(1),X+DH/2.*SL(1),PE,F1,F2,FZ)
SL(2)=EQN2(H1,C+DH/2.*SK(1),PE,F3)
SK(3)=EQN1(H1,C+DH/2.*SK(2),X+DH/2.*SL(2),PE,F1,F2,FZ)
SL(3)=EQN2(H1,C+DH/2.*SK(2),PE,F3)
FA=AFORCE(AD,H2)
FR=RFORCE(DL,KA,DA,H2)
FZ=FA+FR
F1=UHCC(A1,B1,C1,D1,E1,H2)
F2=UHCC(A2,B2,C2,D2,E2,H2)
F3=UHCC(A3,B3,C3,D3,E3,H2)
SK(4)=EQN1(H2,C+DH*SK(3),X+DH*SL(3),PE,F1,F2,FZ)
SL(4)=EQN2(H2,C+DH*SK(3),PE,F3)
Cz(IL)=C+DH/6.*(SK(1)+2.*SK(2)+2.*SK(3)+SK(4))
Xz(IL)=X+DH/6.*(SL(1)+2.*SL(2)+2.*SL(3)+SL(4))
102  CONTINUE
    CERZ=ABS(CZ(1)-CZ(2))
    IF(CERZ.LE.1.0E-4) GO TO 199
    DH=DH1/2.
    GO TO 57
199  H=H+DH1
    C=Cz(1)
    X=Xz(1)
    DH=2.*DH1
101  CONTINUE
    ERR1=ABS(COLD-C)
    WRITE(6,99)J,H,C,DH1
99   FORMAT(i4,f15.9,f15.7,5x,e10.4)

```

```
IF((ERR1.LT.0.0001).AND.(ERR2.LT.0.0001).AND.(H.GT.50.0)) GO TO 500
COLD=C
ERR2=ERR1
100 CONTINUE
SH=X0/C
WRITE(6,*) RE,A,SH
WRITE (6,*)'Iterations completed before Concn stabilizes.'
GO TO 15
500 SH=X0/C
WRITE(7,92) RE,H,SH
92  FORMAT(F7.2,5X,F10.4,5X,F10.7)
WRITE (6,*) RE,H,SH
15  CONTINUE
29  CONTINUE
21  CONTINUE
347 CONTINUE
GO TO 900
900 STOP
END
```

## **APPENDIX D**

### **Raw Data: SRCD Data Tables**

Note: All stagnation coating densities listed as particles/mm<sup>2</sup>.



















Time (s)								Slope	Sh
Re	0	30	60	90	120	150	180		
22	0	104.8	235.8	288.2	401.7	462.9	550.2	3.319	0.0565
22	0	218.3	366.8	576.4	733.6	1030.6	1353.7	6.259	0.1066
30	0	174.7	427.9	585.2	698.7	838.4	1048.0	6.696	0.1141
30	0	69.9	139.7	192.1	253.3	323.1	366.8	2.154	0.0367
45	0	323.1	593.9	1065.5	1441.0	1650.7	2052.4	11.557	0.1966
45	0	262.0	410.5	585.2	768.6	1056.8	1100.4	6.346	0.1081
74	0	925.8	1502.2	2890.8	3781.7	4899.6	5764.2	30.830	0.5251
74	0	113.5	235.8	331.9	427.9	532.8	620.1	3.726	0.0635
118	0	663.8	1607.0	1947.6	2524.0	3109.2	4087.3	22.620	0.3853
118	0	637.6	1144.1	1938.9	2323.1	2663.8	3554.6	21.077	0.3590
134	0	497.8	1231.4	1484.7	1834.1	2218.3	2637.6	17.293	0.2946
134	0	559.0	1283.8	1738.0	2235.8	2593.9	3406.1	19.796	0.3372
134	0	829.7	1493.4	2192.1	3196.5	3956.3	4698.7	24.134	0.4111
267	0	1799.1	3266.4	4314.4	6174.7	7161.6	9013.1	48.035	0.8182
267	0	524.0	1283.8	2008.7	2462.9	2917.0	3607.0	22.620	0.3853
401	0	1353.7	3257.6	4541.5	5545.9	6410.5		51.761	0.8817
401	0	1371.2	3187.8	4628.8	5362.4			52.344	0.8916
Time (s)								Slope	Sh
	0	15	30	45	60	75	90		
534	0	1083	2314.4	3572	5144.1	5231.44	5362.4	79.651	1.3567
534	0	1432.3	3563.3	5485	6279.5	6462.88	6890.8	123.901	2.1105
668	0	2567.7	5973.8	8445	11694	13126.6	13572	191.616	3.2639
668	0	2506.6	4218.3	7581	9746.7	9938.86	10498	163.028	2.7770
802	0	3930.1	7039.3	9389	11590	13432.3	14131	208.501	3.5515
802	0	1589.5	3816.6	5336	6934.5	7493.45	7580.8	121.572	2.0708
802	0	3406.1	6227.1	8742	11362	11903.9	12192	193.654	3.2986
935	0	2585.2	5126.6	8830	12611	14069.9	15144	193.537	3.2967
935	0	2209.6	4716.2	6393	8821	9056.77	9187.8	144.571	2.4626
935	0	2174.7	5013.1	7755	11013	11528.4	11904	174.032	2.9644
Cannon viscometry emulsion (figure 6-13c)									
System C (Table 6-3)									
a=0.475 μm									
Do = 4.8079 e-13 m^2/s									
Co = 5.8 e7 particles/ml									
A=0.1145 mm^2									

			Time (s)														Slope	Sh
Re	0	30	60	90	120	150	180											
22	0	52.4	104.8	157.2	200.9	279.5	331.9										1.747	0.0298
22	0	113.5	235.8	305.7	401.7	559.0	672.5										3.464	0.0590
30	0	61.1	165.9	209.6	253.3	314.4	358.1										2.445	0.0417
30	0	78.6	131.0	218.3	262.0	305.7	358.1										2.358	0.0402
30	0	34.9	69.9	96.1	131.0	157.2	183.4										1.077	0.0183
45	0	157.2	384.3	497.8	593.9	812.2	1030.6										5.735	0.0977
45	0	235.8	419.2	655.0	890.8	1013.1	1170.3										7.162	0.1220
74	0	209.6	454.1	602.6	716.2	934.5	1091.7										6.841	0.1165
74	0	305.7	646.3	969.4	1388.6	1746.7	2034.9										10.830	0.1845
74	0	288.2	445.4	593.9	1004.4	1397.4	1641.9										6.463	0.1101
74	0	157.2	384.3	497.8	655.0	829.7	943.2										5.735	0.0977
130	0	218.3	506.6	628.8	952.0	1231.4	1362.4										7.249	0.1235
130	0	270.7	637.6	917.0	1318.8	1554.6	1834.1										10.393	0.1770
270	0	550.2	960.7	1641.9	2034.9	2681.2	3275.1										17.787	0.3030
270	0	812.2	1266.4	1729.3	2576.4	3519.7	4209.6										18.806	0.3203
400	0	698.7	1056.8	2104.8	2445.4	2917.0	0.0										22.242	0.3789
400	0	611.4	1379.9	2183.4	2471.6	2890.8	0.0										24.396	0.4156

			Time (s)						Slope	Sh
[NaCl]	ka	0	30	60	90	120	150	180		
0.1 M	494	0	471.6	733.6	1414.8	1903.9	2524.0	3109.2	15.022	0.2559
0.1 M	494	0	585.2	1161.6	1528.4	2314.4	3196.5	4069.9	17.205	0.2931
0.1 M	494	0	541.5	1231.4	1869.0	2646.3	3388.6	4174.7	20.990	0.3575
0.1 M	494	0	489.1	1179.0	1738.0	2131.0	2646.3	3004.4	19.680	0.3352
0.1 M	494	0	471.6	1083.0	1633.2	1982.5	2358.1	2768.6	18.370	0.3129
0.05 M	156	0	1144.1	2026.2	3528.4	4812.2	6183.4	6899.6	38.224	0.6511
0.05 M	156	0	1834.1	3886.5	5502.2	7152.8	8899.6	10157.2	61.863	1.0538
0.05 M	156	0	480.3	864.6	1371.2	1703.1	2384.3	2742.4	14.993	0.2554
0.05 M	156	0	585.2	934.5	1633.2	1973.8	2288.2	3083.0	17.496	0.2980
0.05 M	156	0	419.2	908.3	1135.4	1379.9	1703.1	2165.9	12.984	0.2212
0.05 M	156	0	296.9	550.2	864.6	1039.3	1266.4	1615.7	9.491	0.1617
0.01 M	351	0	689.96	1152.8	1852	2288.2	2724.89	2995.6	20.058	0.3417
0.01 M	351	0	436.68	995.63	1590	1834.1	1991.27	2209.6	17.758	0.3025
0.01 M	351	0	410.48	882.1	1397	1545.9	1842.79	2061.1	15.546	0.2648
0.01 M	351	0	401.75	978.17	1319	1458.5	1606.99	1729.3	15.109	0.2574
0.005 M	111	0	899.6	2096.1	3196.5	4017.5	4716.2	5222.7	35.953	0.6124
0.005 M	111	0	17.5	34.9	43.7	69.9	87.3	122.3	0.495	0.0084
0.005 M	111	0	8.7	26.2	34.9	43.7	52.4	61.1	0.408	0.0069
0.005 M	111	0	34.9	96.1	113.5	139.7	165.9	200.9	1.339	0.0228
0.005 M	111	0	26.201	52.402	69.87	87.336	104.803	122.27	0.786	0.0134
			Cannon viscometry emulsion (figure 6-14)							
			Re = 118, pH = 9							
			a=0.475 $\mu\text{m}$							
			Do = 4.8079 e-13 m <sup>2</sup> /s							
			Co = 5.8 e7 particles/ml							
			A=0.1145 mm <sup>2</sup>							

































